THE UNIVERSITY OF HULL

Image based analysis of visibility in smoke laden environments

being a Thesis submitted for the Degree of Doctor of Philosophy

in the University of Hull

by

Qihui Zhang, BSc, MSc

March 2010

To my parents

Abstract

This study investigates visibility in a smoke laden environment. For many years, researchers and engineers in fire safety have criticized the inadequacy of existing theory in describing the effects such as colour, viewing angle, environmental lighting etc. on the visibility of an emergency sign. In the current study, the author has raised the fundamental question on the concept of visibility and how it should be measured in fire safety engineering and tried to address the problem by redefining visibility based on the perceived image of a target sign. New algorithms have been created during this study to utilise modern hardware and software technology in the simulation of human perceived image of object in both experiment and computer modelling. Unlike the traditional threshold of visual distance, visibility in the current study has been defined as a continuous function changing from clearly discernable to completely invisible. It allows the comparison of visibility under various conditions, not just limited to the threshold. Current experiment has revealed that different conditions may results in the same visual threshold but follow very different path on the way leading to the threshold. The new definition of visibility has made the quantification of visibility in the pre-threshold conditions possible. Such quantification can help to improve the performance of fire evacuation since most evacuees will experience the pre-threshold condition. With current measurement of visibility, all the influential factors such as colour, viewing angle etc. can be tested in experiment and simulated in numerical model.

Based on the newly introduced definition of visibility, a set of experiments have been carried output in a purposed built smoke tunnel. Digital camera images of various illuminated signs were taken under different illumination, colour and smoke conditions. Using an algorithm developed by the author in this study, the digital camera images were converted into simulated human perceived images. The visibility of a target sign is measured against the quality of its image acquired. Conclusions have been drawn by comparing visibility under different conditions. One of them is that signs illuminated with red and green lights have the similar visibility that is far better than that with blue light. It is the first time this seemingly obvious conclusion has been quantified.

In the simulation of visibility in participating media, the author has introduced an algorithm that combines irradiance catching in 3D space with Monte Carlo ray tracing. It can calculate the distribution of scattered radiation with good accuracy without the high cost typically related to

zonal method and the limitations in discrete ordinate method. The algorithm has been combined with a two pass solution method to produce high resolution images without introducing excessive number of rays from the light source. The convergence of the iterative solution procedure implemented has been theoretically proven. The accuracy of the model is demonstrated by comparing with the analytical solution of a point radiant source in 3D space. Further validation of the simulation model has been carried out by comparing the model prediction with the data from the smoke tunnel experiments.

The output of the simulation model has been presented in the form of an innovative floor map of visibility (FMV). It helps the fire safety designer to identify regions of poor visibility in a glance and will prove to be a very useful tool in performance based fire safety design.

Acknowledgements

I feel much indebted to my wife, Guiqiu, for her unreserved support and endurance of hardship in the last few years. She has been a great company and hopefully I can make her up with the rest of my life.

Many colleagures have made this work possible. First of all I would like to thank my supervisor, Dr Philip Rubini, for offering me the opportunity of taking on this interesting project. His support and encouragement over the last few years has been proven valuable.

I would also like to thank the other members of the department for their contribution in various ways. Peter, Simon and Chris have built the smoke tunnel and helped in setting up the experimental rig. Dr Lukaschuk and Dr Rybchenko have kindly lent their own optical equipments and made many of the experiments possible. David has offered his time for some much needed accounting and logistic support.

I gratefully acknowledge the financial support of the Engineering and Physical Sciences Research Council in the UK for this project (EP/D037840/1) and the award of Yorkshire Enterprise Fellowship from Yorkshire Forward (YEF67/2009).

Table of Contents

Nomenclature

English

A	Surface area (m^2)
$\acute{A}$	Unit of light wavelength (10^{-10}m)
$\vec{B}$	Magnetic field (Tesla)
c	Speed of light in medium (m/s)
c_o	Speed of light in vacuum (m/s)
c_{lens}	Efficiency of camera lens
C_i	Colour of a pixel, i=R, G or B or extinction cross section
$\vec{D}$	The dielectric displacement (Coulomb/m^2)
D_f	Fractal dimension of particle aggregate
E	Irradiance (W/m^2)
$\vec{E}$	Electric field (Volt/m)
F	Surface view factor or aperture of camera lens
h	Contrast
$\vec{H}$	The magnetic field intensity (Ampere/m)
i	Luminance (cd/m^2) or pixel reading of camera sensor
I	Light intensity (W/sr)
I_0	Intensity of Light source (W/sr)
$\vec{J}$	Free current density (Ampere/m^2)
L	Radiance (W/sr*m^2)
m	Complex refractive index
M	Radiant exitance (W/ m^2)
n	Refractive index

OD	Optical density (m^{-1})
Q	Radiant power (W) or
	extinction efficiency
$\overline{R}_g$	Mean radius of gyration of particle aggregate
x_p	Particle size parameter
Y_a	Modifier of soot aggregate scattering

Greek

ε	Efficiency of lens or
	threshold of contrast or
	electric constant (Farad/m)
η	Colour channel
κ	Wave number (m^{-1})
λ	Wavelength (m)
μ	Magnification of lens or
	Magnetic constant (Newton/Ampere^2)
ν	Frequency (s^{-1}, Hz)
ρ	Albedo of media or
	free charge density (Coulomb/m^3)
σ	Extinction coefficient (m^{-1})
	Electrical conductivity (Siemens/m)
σ_{mass}	Mass specific extinction coefficient (m^2/kg)
σ_{abs}	Absorption coefficient (m^{-1})
σ_{ref}	Reflectance of surface
σ_{sca}	Scattering coefficient (m^{-1})
σ_{std}	Standard deviation
τ	Optical depth
Φ	Radiant flux (W)
ψ	Camera response function

ω	Solid angle (sr)
$\vec{\omega}$	Unit vector in 3D space for solid angle

Subscript

$_{abs}$	Absorption variable
$_{i,j,k}$	Coordinate index or index of summation
$_{sca}$	Scattering variable
$_{ray}$	Variables defined on light ray
$_{\eta}$	Colour channel of a digital camera
$_{v}$	Photometric variable
$_{\lambda}$	Spectra variable

Chapter 1. Introduction

Fire is an inseparable part of human existence. However it is also merciless in rage. Fire safety probably has been an issue before we have learnt how to use it. Our animal instinct tells us to run away from it. Part of modern fire safety measure facilitates the escape from fire. Most fires are accompanied by smoke that can cover a much larger space than the flame itself. Helping people to find the direction and route for speedy evacuation before being burnt or poisoned is the first and most important life saving measure.

The current thesis reports the experimental and numerical modelling research by the author studying the visibility in a smoke laden environment.

1.1 Fire safety and visibility in smoke

In 2004, fire claimed 508 lives and 14,600 injuries in the UK alone. The direct cost on the economy of England and Wales is over £4.26bn, equivalent to approximately 0.47% of GVA (Gross Value Added) of the year (Office of the Deputy Preminister, UK, 2004). Similar or worse statistics can be seen in the United States, Japan (Sekizawa, 1994) and China (Weicheng & Li, 1994). In the developed world, every year fire causes 15 fatalities per million populations on average. Considerable research and engineering efforts have been made in fire protection and prevention. In domestic fire, the population of fire detector among domestic home has significantly reduced casualties in the United States (Sekizawa, 1994). Fires in public buildings such as stations, hospitals, shopping malls, dancing halls and road tunnels do not occur as often as in domestic dwellings but the consequence can be much more devastating. The most recent incident was the Perm nightclub fire in Russia. 112 people were reported dead and more than 120 others wounded (BBC News, 07/12/2009). In 2000, 155 people were killed in the tragic Alpine Gletscherbahn 2 tunnel fire in Kaprun, Austria (Beard & Carvel, 2005). In November 1987, the fire in King's Cross St. Pancras station, London, killed 31 people and injured more than 60. The causes of the fires are accidental and some of them such as the fire of World Trade Center on 9/11 of 2001 are unforeseeable, but good safety design can still reduce the number of casualties.

There are four kind of risk imposed by fire and may lead to casualty:

- exposure to heat either radiant or/and convective,
- inhalation of toxic gases,
- oxygen depletion,
- exposure to sensory/upper respiratory irritants, and
- visual obscuration due to smoke.

Although the last 2 factors may not directly contribute to injury and fatality, they can significantly delay evacuation and increase the risk of casualty from heat and toxic gases. The ultimate goal of fire safety design is to minimize people's contact with heat and smoke during evacuation.

There are two different ways to achieve such goal. One is reducing the intensity of heat and the concentration of smoke via effective ventilation of the building. Large amount of money has been invested into the emergency ventilation system of modern buildings, passenger carries and underground structures. The other way is to reduce the duration of egress so that people would have left the fire affected region before the environment in it becomes untenable.

Starting from 1970's, fire safety regulation has gradually changed from the traditional prescriptive regulatory approach towards performance based approach. The prescriptive approach is based on prescribing unambiguous requirements that are assumed to achieve the implicit, often unstated, safety objectives. Design engineers have found them clear and simple to implement but also restrictive and constantly out of date facing the fast advance of technology and increasing complexity of building design. It often results in excessive conservatism and limits the application of more innovative fire engineering technology.

The performance based approach requires the demonstration of a proposed design to meet the defined objectives but does not prescribe the solution therefore it promotes design innovation. The designer is free to implement the most cost effective, state of the art design technique. A comprehensive performance based approach necessitates the ability to translate the objectives into quantifiable parameters, to set limits for these parameters and validate its compliance with the required performance. It normally comprises three separate components (Beck, 1997):

- Codes, which specify societal goal, functional objectives and performance requirements to reflect society's expectations for the level of health and safety provided in buildings; for example, items such as acceptable access, egress, ventilation, fire protection, electrical services and so on. Such codes do not specify how the requirements would be met.

- Guidelines that are spate documents, adopted by reference, that describes accepted methodologies for complying with the requirements of the codes.
- Evaluation and design tools, which provide accepted methods to assist in the development, review and verification of designs in accordance with engineering standards and guidelines.

An important measure of fire safety performance is the comparison between the required safe escape time (RSET) and the available safe escape time (ASET). RSET is the time required for occupants to travel from their location at the time of ignition to a place of safe refuge[1]. As occupants are exposed to heat and fire effluent, their escape behavior, movement speed, and choice of exit route are also affected, reducing the efficiency of their actions and delaying their escape.

Figure 1-1 Flashover of fire (Vincent, 2009)

ASET is the interval between the time of ignition and the time after which conditions become untenable, after that the building occupants can no longer take effective action to accomplish their own escape (ISO, 2007). ASET may be treated as a time limit for survivability.

[1] In the opinion of the author, RSET should be counted from the time when the fire alarm is raised. The exact time when fire starts is not easy to estimate. The time between the start of fire and the triggering of alarm can vary considerably. Secondly, the majority of building occupants only react to fire alarm.

In a large building fire, flashover occurs when fire grows from its ignition point to engulfing the surrounding parts of the building as shown in Figure 1-1. Figure 1-2 shows the point of flashover on a typical temperature curve of an apartment fire (Walton & Thomas, 2008). Flashover represents the rapid increase of temperature, total heat release and mass of smoke. In fire fighting, flashover is regarded as a point of no return. After this point, the possibility of finding any survivor, including professional fire fighter who is still trapped in fire, would be very small (Vincent, 2009). Flashover is a very important factor in determining ASET. In the case of King's Cross underground fire in London, a few people who were still in the ticket hall at the time of flashover survived. Those who did survive were seriously injured (Fennell, 1988).

Generally ASET depends on the fire size, type of fuel (the amount of smoke it can generate as well as its toxicity), the emergency ventilation system, building structure, local meteorological condition as well as the location of occupants related to the fire site. A safe design should ensure

$$RSET < ASET$$

with adequate margin for the occupants. In achieving this goal, various smoke management systems are designed to extend ASET. In the case of King's Cross underground fire, the time from the start of the fire to the point of flashover was about 18 minutes. It was not enough for the people who were perished by the fire in the ticket hall (Fennell, 1988). In other cases shown later in this section, at some level of smoke intensity, occupants can no longer discern signs and boundaries becoming unaware of their location relative to doors, walls, windows, etc., even if they are familiar with the premises. When this occurs, the occupants would be disoriented and unable to effect their own escape. The time at which this occurs represents the ASET due to smoke obscuration.

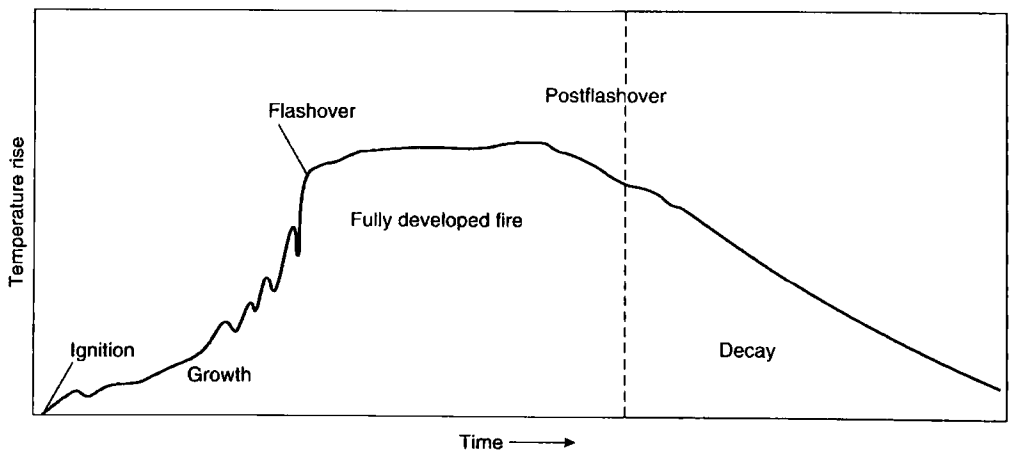

Figure 1-2 Fire curve (SFPE, 2008)

For the RSET time line, the major contributor is the time required to travel through the escape route. It is a fact that in fires people remain for too long in the smoke and breathe in excessive dosages of CO because they cannot find their way out. The most important factors that make people turn back or give up trying to escape are poor visibility and irritation of the eyes by smoke. Tests of evacuations in smoke have demonstrated that the visual characteristics of wayfinding systems can be of decisive importance for their usefulness in smoke (Vincent, 2009).

The reduction of visibility is also a hazard that often first onsets after fire starts in an enclosed building or underground station. Disorientation may lead to prolonged period of staying in toxic environment or even fatality. Generally, if the visibility through smoke is good enough for people to see the emergency exits, toxic products are unlikely to prevent them from escape (Clark, 1988). Therefore any smoke management design should give visibility serious consideration.

In the early morning of 7th April 1990, a fire broke out on board of the Scandianvian Star and left 158 people died. The fire started on deck 3 (the car deck) of the 9 deck ferry. Within 5 minutes, smoke had filled decks 3, 4 and 5. 148 people died from smoke inhalation. Despite of the fact that the fire occurred at 2:00am in the morning therefore the majority of the 148 people were dead in their own cabin during sleep, 49 died in corridors. Among them, 13 bodies were found near the dead end of a non-through corridor. The cause of their death is obviously the inability to find the right escape route. If adequate wayfinding system was provided, many lives could be saved (Robinson & Burgoyne, 1999).

The Daegu subway fire of February 18, 2003 in South Korea killed 198 people and injured at least 147. Many victims became disoriented in the dark, smoke-filled underground station and died of asphyxiation looking for exits. The interview and questionnaires to the survivors after the accident revealed that bad visibility due to smoke and the lack of egress guidance were the main obstacles of evacuation. Only 12% of the survivors evacuated through appropriate escape routes and exits (Jeon & Wonhwa, 2009).

Even in modern, well designed tunnel, the visibility of egress sign may not be as good as expected. During the evacuation of channel tunnel fire in 1996, passengers had difficulty finding the escape passage due to smoke (Kirkland, 2002).

Although in modern building design, efforts have been made to limit the spread of smoke and the escape route such as stair case is isolated from smoke whenever possible. In certain type of building structures such as tunnels, high risers and atria, the reduction in visibility is still a major hazard as it affects occupants who are not located in the immediate fire area but have to evacuate through the smoke affected area.

The visibility of egress sign under smoke condition has been a research subject as early as 1951 (Rasbash, 1951). A wide range of acceptable levels of visibility has been suggested in the fire protection literature. According to the research, being able to see a distance of 3-5m for the occupants familiar with a building layout may be sufficient to evacuate in fire emergency. For those less familiar with the building, a distance of up to 25m has been recommended (Lougheed, 2000). The recent NFPA 130 standard requires that the smoke level of egress should be kept below the point at which a sign internally illuminated at 80lx is discernible at 30m and doors and walls are discernible at 10m (NFPA 2007).

A key part in performance based safety design is performance verification. Experimentally verifying fire safety even at modest scale would be very expensive if possible. As building architecture and lighting becomes increasingly sophisticated, empirical and theoretical verification becomes very important and some time the only method in building design.

The most cited and also much criticized work in the estimation of visibility was by Jin (1978) who presented a simplified visibility calculation based on the conventional wayfinding systems with normal lighting environment. The correlation 4-1 has revealed the very basic relationship between smoke concentration and the visibility of an illuminated sign according to Lambert-Beer's law and used as the base for current design code. Jin has also found that smoke irritation will significantly impair the capability of human objects to find a target sign as shown in Figure 4-5. Further details of Jin's work can be found in Chapter 4 of the current thesis.

The simplicity of Jin's theory and the lack of alternative have made it very popular in the fire safety community. Critics point to its failure in addressing the variety of illuminating conditions and viewing directions (HSE, UK, 1998). As the interior of buildings becomes architecturally more elaborate, such issues have caused concern. In order to compensate the deficit in the understanding of visibility in smoke, design engineers are taking conservative measures to ensure the visibility of signage along the egress passage even under the worst design scenario. Apart from reducing the distance between safety signs and using internally illuminated instead of simple reflect sign, more proactive measures such as flashing sign and photoluminescent wayguidance systems are also considered (Proulx, Kyle, & Creak, 2000). Such conservatism unavoidably results in high construction and operation cost. Certain system such as the handrail is not suitable for buildings such as departmental store, supermarket, atria and stations. In these areas, safety signs often have to compete with other commercial or non-commercial signs. Even under normal condition, finding the exit sign in a multistory departmental store often requires some effort. Other technology, such as the sprinkler system for fire extinction, may complicate the visibility issue either during evacuation or for fire service to access the fire site. Such complication is beyond the capability of existing analysis.

The current study is an effort to address such issues. Combining results from other related research area such as the simulation of smoke movement and human behavior under smoke condition, it can provide more accurate ASET and RSET estimation for architectural and fire engineering communities. Experience has shown that very small improvements in visibility or reductions in smoke irritation can save many lives in fire situations (Vincent, 2009). It is also true that over conservative measures would significantly increase the cost of construction.

1.2 Visibility

The word visibility literally means the ability to be seen or the distance that is possible to see (something) (Microsoft Encarta). The later explanation is widely adopted in the meteorology and aviation industry. There, the meteorologist chose a number of distances, and limited himself to observing and reporting whether features of the landscape at these distances could or could not be distinguished. The "features" which are to be distinguished have to be such that they are visible in a clear atmosphere and under normal daylight illumination. Whether an object can be distinguished or not is a matter of whether its outlines can be seen sufficiently clearly against its background. If the object is a tree the observer must be able to say that it is a tree and not a house. More scientific definition and measurement is given by Koschmieder's theory in 1924.

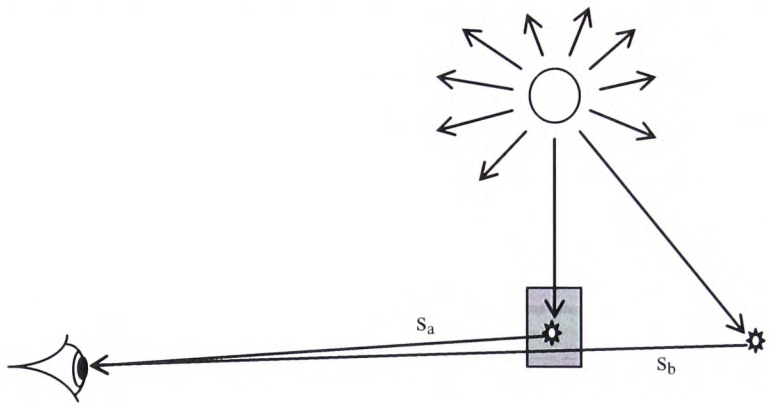

Figure 1-3

Koschmieder (Simpson, 1948) dealt with the simplest form of visual object, namely a perfectly black screen seen against the sky on the horizon. The natural light is scattered by the air molecules (Rayleigh scattering) and aerosol suspended in air. Some of the scattered light reaches the eye of the observer and appears to come from the screen so giving it an apparent surface brightness. This brightness depends on the amount of light scattering between the eye and the screen. In Figure 1-3, it is the total scattering along line s_a toward the eye. As line s_a is interrupted by the screen, assuming air distribution is homogeneous, the total amount of light

scattering increases with the length of s_a. In Figure 1-3, light scattered along line s_b also reaches the eye. As line s_b extends to infinite therefore the scattered light from the direction of s_b appears to be constant and brighter than that from the direction of s_a. As the screen recedes from the eye, the difference between the scattered light from the direction of s_a and that from s_b decreases and eventually becomes unrecognisable. To the observer, the screen has disappeared. The threshold value of s_a, at which the screen disappears, has been defined as the local visibility of air.

Let i_l and i be the apparent brightness (in cd/m^2, candela per square meter) of the sky and screen respectively[1], then as the screen recedes i_l will remain constant and i will increase; the contrast between them is defined as

$$h = \frac{i_1 - i}{i_1} \qquad \text{1-I}$$

It is a physiological law that the eye ceases to recognise this contrast when it falls below a small value ε, called the threshold of contrast. At this point the screen becomes indistinguishable from the sky and the visibility range is reached. Koschmieder assumed that the value of ε is a constant of 0.02. Substituting ε in the place of the ratio for light intensity in Lambert-Beer law

$$\varepsilon = \frac{I}{I_0} = e^{-\alpha x} \qquad \text{1-2}$$

Then the visibility, in terms of visible distance, can be defined as

$$x = \frac{3.91}{\sigma} \qquad \text{1-3}$$

where σ is the extinction coefficient of air in the atmosphere. This formula is widely adopted in meteorology till today (Werner, Jurgen, Leike, & Munkel, 2005).

In fire safety, Jin (1978) has proposed a formula for visibility in smoke as

$$x = \frac{1}{\sigma} \ln\left(\frac{i}{\varepsilon \rho i_0}\right) \qquad \text{1-4}$$

[1] Here the apparent brightness of the surface is not due to the reflectance of the surface but the scattering of air including aerosol.

where i is the luminance of the sign being tested and i_0 is the average luminance of the environment, ρ is the albedo of smoke and ε is the contrast threshold. Expression 1-4 is based on 1-2. Isotropic and homogeneous environmental lighting has been added into 1-4. When $\varepsilon=0.02$, replacing smoke with air and the tested sign with a black screen, equation 1-4 becomes equation 1-3.

1.3 The issues of visibility in fire emergency

In fire emergency, the current design code such as NFPA 130 (NFPA, 2007) sets the ASET visibility criteria according to Jin's threshold. Such criteria ensure reasonable visual distance in the egress path during evacuation. What Jin's theory and any of the existing design guidance can't provide is the way to improve the visibility of emergency sign before the smoke reaches its visual threshold. It is a condition that most evacuee experience and therefore determines the real evacuation time. The current study proposes an image based approach that is different from Jin's theory. It measures visibility not in terms visual threshold but a continuous function from clearly visible to completely disappeared from the observer. It can be used to compare the visibility of two different egress conditions even both are equal and non-critical according to Jin's theory.

The above NFPA code requires that during evacuation smoke obscuration levels should be continuously maintained below the point at which a sign internally illuminated at 80lx is discernible at 30m and doors and walls are discernible at 10m. There is no clear explanation on what can be regarded as discernible. In experiments, two visibility criteria have been referred to: detectability and readability (legibility). It was found that greater smoke density is required for detectability threshold than the readability threshold (Rea, Clark, & Ouellette, 1985). Such uncertainty prompted the current research on quantifying how discernible an object is under smoke condition.

As building interior comes in different forms and layout, fires may be due to different kind of fuel and smoke may move as the result of ventilation, weather, movement of equipment and people, computer simulation has been proven to be a powerful tool in the verification of modern safety. Widely used CAD tool can provide most architectural details. CFD simulation has been proven to be very useful in simulating smoke movement and heat transfer in fire. Computer simulation of visibility in fire is an area that requires more research. The prevailing models are based on Jin's theory that is a simple and effective approach for fire engineers in the past when they have to manually estimate visibility for relatively simple situation. The theory can't take complex environmental conditions into account. Unfortunately, some of the conditions such as

smoke variation in time and space as well as environmental lighting can have dominant effects on the visibility of emergency sign. In order to utilise the more detailed field data from CFD simulation, there are models based on local optical density (OD) (e.g. Gandhi, 1994; Hultquist, 2000). As a local scalar, OD is effectively a different way of expressing the field of smoke concentration. The model failed to address visibility as an integral and directional issue that depends on the viewing direction, the context of the objective as well as the integral of the optical property of the media between the observer and the target object. The current study provides a more sophisticated model that assesses local visibility by taking the spatial/time distribution of media as well as the characteristics of the viewer and the objective into account in order to satisfy the requirements of modern performance based design.

1.4 Contribution of the current study

The current study is the first attempt to quantitatively predict visibility in a smoke laden environment based on comprehensive 3-D numerical model of radiation and digital image. Both theoretical and experimental researches have been carried out by the author in order to create and verify the numerical model. During the process, the author has made a number of contributions to the scientific development of this research area.

1.4.1 Introduction of image based measurement of visibility

In order to compare visibility under conditions other than the visual threshold, the measurement of visibility is redefined in the current study. In principle, the new measurement is based on human perceived image and closely linked to acuity. With this measurement the visibility of a target object becomes a continuous function from clearly discernable till completely obscured by the media (the threshold). Such measurement has made it possible to compare the visibility under pre-threshold condition as well as to simulate visibility based on computer generated virtual images.

1.4.2 Development of image based simulation model for visibility

The image based measurement of visibility has naturally leads to the creation of a computer model on the same principle and serving the same purpose. Based on the transport theory of radiation, a new hybrid zonal and Monte Carlo ray tracing model has been introduced in the current study to simulate the visibility in a smoke laden enclosure with arbitrary 3D geometry. The new method has removed the costly computation of view factors in traditional zonal method and the unstructured cache of the Monte Carlo (photon-mapping) method. The distribution of smoke concentration can be read in as the result of CFD simulation and the simulation domain is divided into cubic cells that can be dynamically adapted to smoke concentration, cache of scattered radiance or any other field variables. Adaptive surface mesh

has been applied in order to catch the details of surface geometry as well as the shadows of illumination. The results from the model simulation have been validated against experimental data and also verified with theoretical solution.

1.4.3 Novel structured irradiance caching for light scattering

A great difficulty in applying Monte Carlo ray tracing to radiation transfer in participating media is to organise the distribution of rays in space so that rapid changes of light scattering can be calculated accurately. Traditionally, all rays are issued from surfaces and their paths are impossible to be pre arranged due to multiple reflections on complex geometry surfaces as well as the random nature of the method itself. In many cases, it has unnecessarily increased the cost of simulation. The author has extended the traditional surface irradiance caching algorithm into 3D space and new expression for irradiance cache has been proposed. Unlike the expression used in photon-mapping method (Jensen H. , 1996), the new expression addresses the issue of light scattering in continuous heterogeneous media. Similar to the zonal method, the volume irradiance is cached in the structured mesh. Combined with the dynamic mesh adaptation, the algorithm is capable of catching severe 3D heterogeneous scattering pattern through caching the scattered light and reissuing rays at the point of scattering.

1.4.4 Smoke tunnel experiments in determining the visibility of illuminated signs

Experiments have been carried out in a purpose built smoke tunnel. The visibility of illuminated signs in different legend formats was measured under various smoke, illuminating intensity and ambient light conditions. The result has been reported in the current thesis.

1.4.5 Estimation of visibility based on digital camera images

Although commercial digital cameras can produce high resolution and very realistic images, but are not very easy to be applied in scientific measurement. It is mainly due to the rapid development of the photo sensor technology and the commercial secrecy behind it. The result is the significant differences in sensor characteristics and data processing algorithm between manufactures. In the current study, an innovative numerical procedure has been created that post processes the image data from a camera and produces an approximation of the human perceived image. Such images are used in measuring the visibility of the target signs as well as in comparing the measurement with model prediction.

1.4.6 First quantitative conclusion that red and green signs are similar in visibility

The current experimental study has revealed that under the same conditions, the signs illuminated with red and green monochromatic light showed very similar visibility. Comparing with them, the visibility of the blue light is much poorer. It is the first time that such common and intuitive knowledge has been put in quantitative form. It has shown that the performance of

the red emergency signs used in North America is, not only conventionally but also quantitatively, equivalent to the green ones used in Europe.

1.4.7 Introduction of visibility map

A floor map that shows the contours of visibility at a given height from the floor has been introduced. The map can be used to judge the visibility of a specific object, or the best visibility of multiple objects, from any point on the map. It can provide a safety overview for a given floor area of a building complementary to the smoke concentration contours.

1.4.8 Model for the extinction coefficient of combustion soot

Due to the change of laboratory condition, combustion smoke was replaced by non-combustion smoke in the experiment. By the time of the change, the study for the optical property of smoke soot was already carried out and important results have been obtained.

A comprehensive review of the past experimental work has put the non-comparable data scattered in reports from different research groups and over two decades of the last century (it seems to be the most important period in the experimental research on this subject) in a single, normalised graph. The graph clearly shows the common and important trend of light extinction verses particle size parameter, the different regimes of scattering as well as the validity range of existing models. Further theoretical research into multiple scattering by soot aggregates has lead the current author proposing an improved model for light extinction by soot aggregates. The model compares favourably with experimental data particularly within the particle size parameter range of 0.2-0.4 where multiple values of extinction efficiency exist for each particle size parameter but only a single value can be predicted with any of the existing models.

1.4.9 New practical zoom camera model

In order to generate photo realistic images from the current numerical model, a virtual zoom lens camera model has been created. It can simulate most of the important features of modern optical camera including zoom, focus, finite aperture, depth of field, lens efficiency as well as $cos^4\theta$ effect without the knowledge of detailed camera structure.

Unlike most camera models used in computer graphic that post process images to fake camera effect, the current model is completely based on optics principles. All the synthetic images in this study are directly generated with the camera model.

1.5 Organisation of the thesis

The main body of the current thesis is divided into 3 parts. Part I introduces the basics of light transportation, perception as well as the optical properties of participating media. Part II

describes how visibility has been measured in the current study and the experimental results. Numerical modelling of visibility in smoke and the comparison between the model prediction and the experimental data are presented in Part III.

Following this introduction, the relevant radiometry concepts, definitions and expressions will be briefly presented at the beginning of Chapter 2. Afterward the theory and previous research work on light transport in participating media are reviewed. The radiation transport equation (RTE) and its boundary conditions are presented forming the base of the subsequent numerical simulation on visibility. In the light of the deficiencies of the extinction models reviewed previously in this chapter, a new model of light extinction by fire smoke is proposed by the current author. It takes into account the effect of multiple scattering by the aggregate of soot particles. Chapter 3 introduces the basics of photometry and visibility. There the author points out the drawbacks of existing visibility definition and opens the discussion of how visibility should be defined in fire safety engineering.

Chapter 4 is a review on the previous research work of visibility in smoke. A summary of the influential factors for visibility in smoke, based on the reviewed researches, is given by the end of the chapter.

Chapter 5 introduces the current experimental study. Its objective, scope, limits as well as the basic components (except the camera) are presented in this chapter. The camera, its calibration and the creation of perceived image from the photographs taken with the camera are the subjects of Chapter 6.

The question of how to define visibility in fire smoke environment is revisited in Chapter 7. The image based definition of visibility and the way that it is measured in the current experiment are described there.

The results and findings from the current experiments are presented in Chapter 8. The experiments have been carried under different smoke, illumination, colour conditions with various different signs.

Chapter 9 starts Part III of the thesis with a review of existing literature on the solution of radiation transfer. Each solution technique is described in its own section and the relative merits and drawbacks are compared. From the understanding of the existing models and the special requirements of visibility simulation, the current author has proposed a new hybrid simulation algorithm based on irradiance caching in space and Monte Carlo ray tracing. The details of the model as well as other aspects of numerical simulation such as grid adaptation and two pass computing procedure employed in the model are presented in Chapter 10. Chapter 11 presents

the verification of the numerical model against a simple theoretical case for radiation transfer. The predicted results are also compared with the measured visibility data given in Chapter 8.

Finally Chapter 12 concludes the current thesis. It summarises the major outcome of the current work and point out the needs of future research in this area.

This chapter is an introduction to the thesis. It has described the social implication of fire safety through real fire examples. The importance of improving visibility in smoke environment as a safety measure has been presented together with the basic concept and current status of research and engineering application. Then the contribution of the current author toward this topic has been summarised. By the end of the current chapter, a brief description of the structure of the thesis has also been given.

Part I The Fundamentals

In the first part of the thesis, the physical and physiological concepts relevant to the transportation and human perception of light are introduced. These concepts are used in the experiment (Part II) and numerical simulation (Part III). Chapter 2 concerns the nature of light, its measurement and its interaction with surface as well as media. Chapter 3 describes the way light is perceived by human as brain stimuli. The combination of the physical and the physiology processes form the base of human visibility. Its concept and measurement are introduced in the later parts of this thesis.

Chapter 2. Light transport in participating media

Light, or electromagnetic radiation in general, is a form of energy that exist in the forms of both particle and travelling wave. As particle, it holds energy in the multiple of basic unit travels alone a straight line in vacuum and interacts with specula surface elastically. As wave, light refracts when travels through media and shows different colour when its frequency changes. This chapter introduces the basic physics concerning the nature of light, its propagation in vacuum as well as its interaction with surface and media. As light is a kind of electromagnetic radiation and the current thesis only concerns with waves within the visible range, the words light and radiation are used interchangeably in this thesis.

2.1 The nature of light

As energy carrying particles, light travels across vacuum space in straight line and shows elastic bounce on specula surfaces. Its speed of travelling in vacuum is a constant of 299,792,458m/s. When light beam hits the interface of a vacuum and a medium or between two different media in a direction other than the normal of the interface, it changes its direction and speed. This phenomenon is called refraction. The travelling direction and speed of the light after the refraction depends on the refractive index of the medium n ($n \geq 1$). In vacuum, n=1.

As wave, the speed(c), frequency(v) and wavelength(λ) of light satisfy the following relation

$$\nu = \frac{c}{\lambda} \qquad 2\text{-}1$$

When light is travelling within a medium other than the vacuum, its speed is determined by

$$c = \frac{c_o}{n} \qquad 2\text{-}2$$

where c_o is the speed of light in vacuum. According to quantum mechanics, each light particle called photon carries with it an amount of energy

$$\varepsilon = h\nu \qquad 2\text{-}3$$

where $h = 6.626 \times 10^{-24} J$ is Planck's constant. It can be seen that the higher the frequency of light, the higher the energy a photon possesses.

2.2 Basic radiometry concepts

Radiometry is the science of measuring electromagnetic radiation. In practice, the term is usually limited to the measurement of infrared, visible, and ultraviolet light (10^{-8}m < λ < 10^{-3}m) using optical instruments. Like any other form of energy, radiant energy Q is measured in joules (J).

2.2.1 Spectral radiant energy

As has been said above, light is energy kept in the form of electromagnetic wave. Most natural light sources emit electromagnetic radiation over a spectrum instead of a single wavelength. Spectral radiant energy is the amount of radiant energy per unit wavelength interval at wavelength λ. It is defined as:

$$Q_\lambda = dQ / d\lambda \qquad 2\text{-}4$$

In the current study, the unit would be kept as J/m. In practice, J/nanometer would be more common.

2.2.2 Radiant flux

Radiant flux is the time rate of radiant energy flow from a source of radiation. It has dimension of power and measured in watts (W) as

$$\Phi = dQ / dt \qquad 2\text{-}5$$

where t is time.

2.2.3 Radiant flux density

The radiant flux density is defined at a point on a surface (real or imaginative) as

$$E = d\Phi / dA \qquad 2\text{-}6$$

When surface A is illuminated by incident light, the radiant flux density is referred to as irradiance. If surface A is emitting/reflecting light, the total radiant flux density is referred to as radiant exitance or radiosity (Figure 2-1).

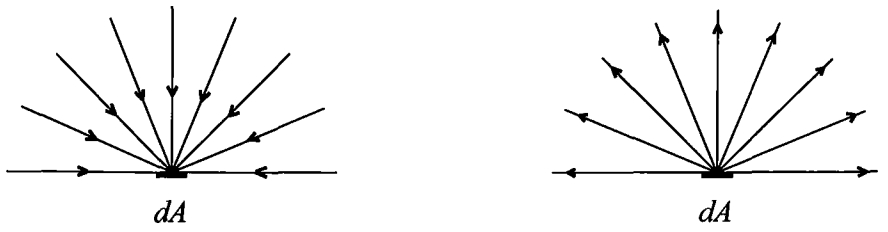

Figure 2-1 Irradiance and radiosity

In the current study, a sign is assigned to Φ so that energy flux density has the opposite sign as the surface normal. Therefore radiosity is a negative flux density and irradiance is a positive flux density. More about the sign convention used in the current study can be seen in the next section.

Although the word radiosity is in fact obsolete, as it is linked to an important approximation method in radiative transfer therefore we retain it here for the time being.

2.2.4 Radiant intensity and radiosity

The amount of radiant flux emitted in a given direction can be represented by a ray of light contained in an infinitesimal solid angle $d\omega$. The radiant intensity within the solid angle can be defined as

$$I = \frac{d\Phi}{d\omega} \qquad 2\text{-}7$$

The relation between irradiance and radiant intensity is

$$E = \frac{\cos\theta}{r^2}\frac{d\Phi}{d\omega} = \frac{I}{r^2}\cos\theta = -\frac{I}{r^2}(\vec{n}\cdot\vec{\omega}) \qquad 2\text{-}8$$

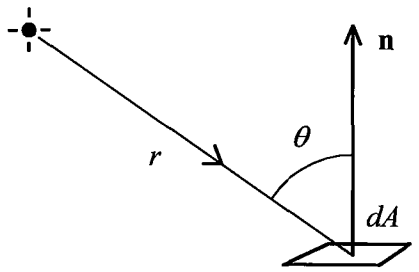

Figure 2-2

It is the inverse square law of a point source. $\vec{\omega}$ is a unit vector in the direction of the incident light and $\vec{n}$ is the surface normal. The introduction of vector notation is to identify the direction of energy flux (incident or exitance). The negative sign in equation 2-8 sets the energy flow of the incident light on a surface as positive. This convention is inherited from radiative heat transfer (a positive radiant flux heats up the surface) and will be used throughout this thesis.

2.2.5 Radiance

Radiance is concerned with the radiant power within an infinitesimal solid angle arriving (leaving) a point on a surface (real or imaginative). It is defined as

$$L = -\frac{d^2\Phi}{d\vec{\omega}\cdot d\vec{A}} = -\frac{dI}{\vec{\omega}\cdot d\vec{A}} \qquad 2\text{-}9$$

dω and dA are defined in Figure 2-3. $d\vec{\omega} = \vec{\omega} d\omega$. For illumination, radiance is the radiant power arriving (leaving) the unit projected area through unit solid angle. Again, the negative sign sets the incident radiance as positive.

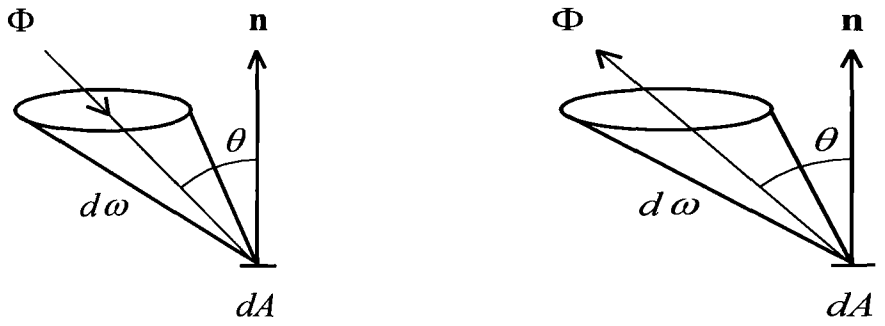

Arriving leaving

Figure 2-3 Surface radiance

In section 2.6 it can be seen that radiance is invariant along a fixed direction in vacuum (Modest, 2003).

In radiative heat transfer, radiance L is often called intensity (Modest, 2003). Here we follow the convention of radiometry in the lighting industry (Ashdown, 1994).

2.2.6 The spectra dependence of radiometry quantities

As mentioned in 2.1, radiant energy is carried by waves over a spectrum. Sometimes it is important to know not only the total radiant energy being transferred but the spectra distribution of the energy. Following spectra radiant energy defined by equation 2-4, the spectra counter parts of the above quantifies in the current section can be defined as

$$d\phi_\lambda = \frac{d\phi}{d\lambda} \qquad 2\text{-}10$$

where ϕ represents *E, M, L* or *I*. λ represents the wavelength.

2.3 Electromagnetic wave and Maxwell's equation

In the last section the basic concepts and quantities in radiometry have been introduced. The space between reflective surfaces is in vacuum. In this section, attention is turned to light transport within a medium. Light travelling in media may loss its energy on the way through scattering and absorption. The theory governing such phenomena is well understood in physical optics and presented here to guide the experimental and simulation work in later chapters.

In 1865 Maxwell published his famous set of equations which formalized the results of the accumulated research on electromagnetism. Electromagnetic phenomena had been recognized as originating in a distribution of electric charge and current which gives rise to the electromagnetic field. This field in turn is the domain of four field vectors, $\vec{E}$, the electric field, $\vec{D}$, the dielectric displacement, $\vec{B}$, the magnetic field and $\vec{H}$, the magnetic field intensity. At every point in space where the physical properties are continuous in its neighbourhood, the field vectors satisfy Maxwell's equations (Kerker, 1969):

$$\begin{aligned}
\nabla \times \vec{E} &= -\partial\vec{B}/\partial t \\
\nabla \times \vec{H} &= \vec{J} + \partial\vec{D}/\partial t \\
\nabla \cdot \vec{D} &= \rho \\
\nabla \cdot \vec{B} &= 0
\end{aligned} \qquad 2\text{-}11$$

where ρ is the free charge density. These equations are supplemented by the material equations to uniquely determine the electromagnetic field.

$$\vec{J} = \sigma\vec{E}$$
$$\vec{D} = \varepsilon\vec{E}$$
$$\vec{B} = \mu\vec{H} \qquad 2\text{-}12$$

The factors σ, ε and μ here (not anywhere else in this thesis) are the medium specific conductivity, the electric constant and the magnetic inductive capacity, respectively. When these factors are independent of direction, the medium is isotropic. If the factors are independent of spatial position, the medium is homogenous. For dielectric medium, σ is zero. The velocity of light in the medium is given by

$$c = (\varepsilon\mu)^{-1/2} \qquad 2\text{-}13$$

2.4 Refractive index

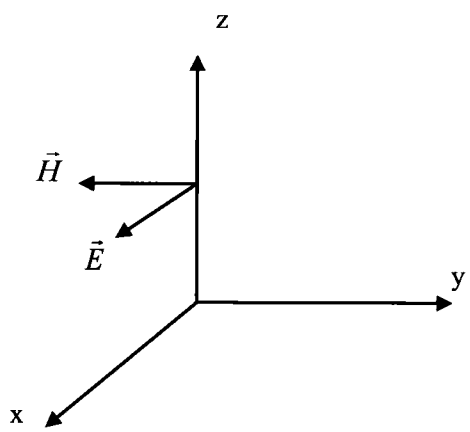

Figure 2-4

For light transport in participating media (ρ=0), the most important property of a medium is its refractive index. Considering a plane, monochromatic wave, harmonic in time and propagating in an unbounded, isotropic, homogeneous medium in the positive z-direction of a Cartesian coordinate system (Figure 2-4), the general solution of Maxwell's equation for the x-component of the electric field $\vec{E}$ can be expressed as

$$E_x = A\exp[i(\omega t - k_0 mz)] \qquad 2\text{-}14$$

where k_0 is the propagation constant in vacuum related to the wavelength in vacuum λ_0 by

$$k_0 = \frac{2\pi}{\lambda_0} \qquad 2\text{-}15$$

The complex refractive index m of the medium is defined as

$$m = k/k_0 = n(1 - i\kappa) \qquad 2\text{-}16$$

The real refractive index n determines the propagating speed or wavelength of E_x as

$$n = \lambda_0/\lambda = c_0/c \qquad 2\text{-}17$$

In Snell's law, n determines the refractive angle when light is passing the interface of two different media

$$\frac{\sin\theta_1}{\sin\theta_2} = \frac{n_2}{n_1} \qquad 2\text{-}18$$

where the subscripts represent the two media (Figure 2-5).

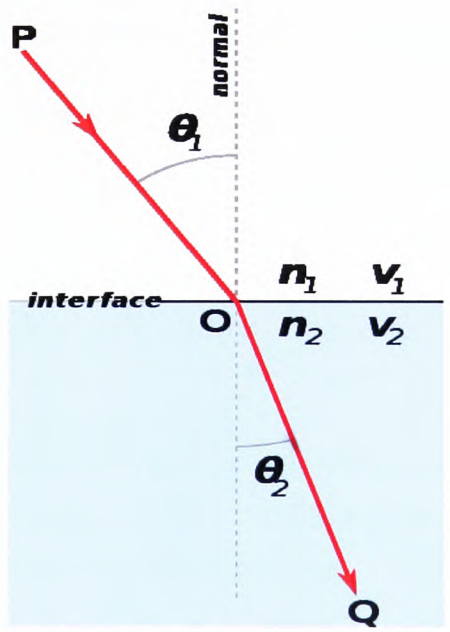

Figure 2-5 Snell's law

The complex part of the refractive index $n\kappa$ is the damping factor while κ is called the index of absorption.

2.5 Light extinction and Lambert-Beer's law

In electromagnetic theory, Poynting vector

$$\vec{S} = \vec{E} \times \vec{H} \tag{2-19}$$

specifies the energy flux at all points in space. Based on the plane wave analysis in the last section, the magnitude of $\vec{S}$ is in proportion to $|E_x|^2$ that is

$$S = \frac{1}{2}\mathrm{Re}\left(\sqrt{\frac{\varepsilon}{\mu}}\right)|A|^2 \exp\left(-\frac{4\pi\kappa z}{\lambda}\right) \tag{2-20}$$

As the wave traverses the medium, the energy flux is exponentially attenuated:

$$L = L_0 e^{-\sigma_{abs} z} \tag{2-21}$$

Here 2-20 has been written in terms of radiance and

$$\sigma_{abs} = \frac{4\pi\kappa}{\lambda} \tag{2-22}$$

is the absorption coefficient. Expression 2-21 is known as Lambert-Beer's law.

The more general differential form of Lambert-Beer's law is

$$dL = -\sigma L dz \tag{2-23}$$

When the medium is homogeneous, integration along a beam gives

$$L = L_0 e^{-\sigma z} \tag{2-24}$$

where $\sigma = \sigma_{abs} + \sigma_{sca}$. Equation 2-20 is the result of infinite plan wave in homogeneous media where the only loss would be absorption. The product of extinction coefficient σ and distance z is called optical depth and denoted as τ in the current thesis.

2.6 Radiative transfer equation (RTE)

From Maxwell's equations, radiant energy is transferred along the direction of the Poynting vector. In vacuum, if an infinitesimal solid angle $d\omega$ is extended from a point source, then there

would be no energy flux across the boundary of $d\omega$. In other words, energy flux within $d\omega$ is a constant, say $d\Phi$. Therefore $d\Phi/d\omega$=constant within $d\omega$.

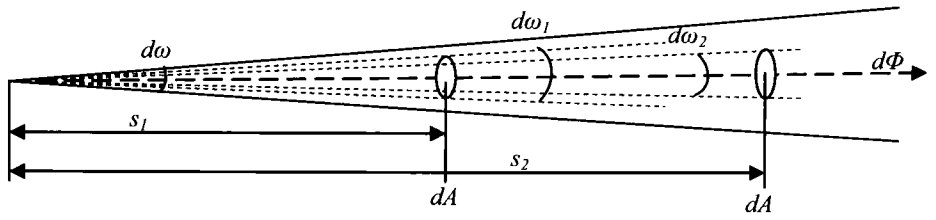

Figure 2-6

In Figure 2-6, the same area dA is placed at two places s_1 and s_2 along the path of the light beam and the energy fluxes through it are

$$d\Phi_1 = L_1 dA d\omega_1$$

$$d\Phi_2 = L_2 dA d\omega_2$$

but within $d\omega$, we also have

$$\frac{d\Phi_1}{d\omega_1} = \frac{d\Phi_2}{d\omega_2} = \frac{d\Phi}{d\omega}$$

Therefore

$$L_1 = L_2 \qquad 2\text{-}25$$

In vacuum, along a light ray radiance is a constant. It is the basic property of radiometry for ray tracing algorithm in part IlI.

When participating medium exists between s_1 and s_2, radiance along a light ray would no longer be constant. The variation of radiance L along the path of ray s depends on the emission, absorption and scattering properties of the medium and can be expressed as (Modest, 2003)

$$\frac{dL_\lambda}{ds} = \vec{s} \cdot \nabla L_\lambda = \sigma_{abs,\lambda} L_{b,\lambda} - \sigma_\lambda L_\lambda + \frac{1}{4\pi} \int_\Omega \sigma_{sca,\lambda} p_{\omega \to s,\lambda} L_{\omega,\lambda} d\omega \qquad 2\text{-}26$$

where $L_{b,\lambda}$ is the emission of the medium and Ω is the entire 4π spherical solid angle. $\vec{s}$ is a unit vector along the direction of propagation (energy flux). The last term ($\sigma_{sca,\lambda} p_{\omega \to s,\lambda} L_{\omega,\lambda} d\omega$) is

the in-scattering from direction ω. p is the phase function. Comparing with isotropic scattering, it can be seen that

$$\frac{1}{4\pi}\int_{\Omega} p_{\omega\to s,\lambda} d\omega = 1 \qquad 2\text{-}27$$

Equation 2-26 is the basic equation to be solved in part III.

2.7 Boundary conditions and BRDF

When light encounters opaque surface or the interface between two different media, it may be reflected, refracted or absorbed. In the current study, only the absorption and reflection types of boundary conditions will be encountered and discussed. In such case the energy balance on the surface should be written as (Figure 2-7)

$$\Phi_{inc} = \Phi_{ref} + \Phi_{abs} \qquad 2\text{-}28$$

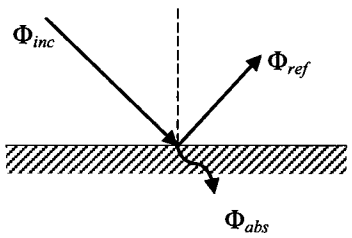

Figure 2-7 Surface reflection and absorption

The subscripts represent incident, reflected and absorbed light respectively.

Exactly how the incoming energy is distributed between the reflection and absorption as well as what is the angular distribution of the reflected light depends on the property of the surface. The simplest model for energy distribution is to define reflectance σ_{ref} and absorptivity σ_{abs} of the surface as

$$\sigma_{\lambda,ref}(\vec{x}) = \frac{\Phi_{\lambda,ref}}{\Phi_{\lambda,inc}}$$

$$\sigma_{\lambda,abs}(\vec{x}) = \frac{\Phi_{\lambda,abs}}{\Phi_{\lambda,inc}} \qquad 2\text{-}29$$

From equation 2-28, the following identity is obvious

$$\sigma_{\lambda,ref} + \sigma_{\lambda,abs} = \mathrm{I} \qquad 2\text{-}30$$

The implicit assumption in the spectra form of 2-29 and 2-30 are that there is no change of wavelength during light reflection on the surface.

The spatial distribution of the reflected light is discussed in the section 2.7.2.

2.7.1 Surface absorption

As the current study is about light transmission among surfaces of an enclosure and the media within it, once the radiant energy has been transformed into a form other than visible light (heat for example), it is regarded as lost and will be taken out of the computational domain. This is what would happen with absorption. In equation 2-28, Φ_{abs} is treated as energy loss and deducted from the incident light.

2.7.2 Surface reflection

Although equation 2-28 addresses the overall radiant energy balance when light impinging a surface point, it cannot tell how light is reflected or, in other word, the spatial distribution of the reflected energy Φ_{ref}.

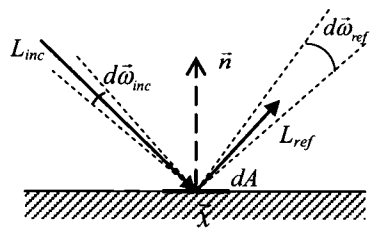

Figure 2-8

In Figure 2-8, the incident radiant energy within solid angle $d\vec{\omega}_{inc}$ falling on surface point $\vec{x}$ is reflected. Part of the reflection is within the infinitesimal solid angle $d\vec{\omega}_{ref}$. The contribution of reflection in the direction $\vec{\omega}_{ref}$ from the incident light in direction $\vec{\omega}_{inc}$ can be expressed as

$$dL_{\lambda,ref,\vec{\omega}_{inc}} = f_{\lambda} L_{\lambda,inc} \vec{n} \cdot d\vec{\omega}_{inc} \qquad 2\text{-}31$$

where $f_\lambda = F(\lambda, \vec{x}, \vec{\omega}_{inc}, \vec{\omega}_{ref})$ is called Bidirectional Reflectance Distribution Function (BRDF). It is the basic optical property of an opaque surface. According to Kirchhoff's law, the BRDF f_λ is reciprocal, that is (Siegel & Howwell, 1992).

$$f_\lambda(\vec{x}, \vec{\omega}_{inc}, \vec{\omega}_{ref}) = f_\lambda(\vec{x}, \vec{\omega}_{inc} \rightarrow \vec{\omega}_{ref}) = f_\lambda(\vec{x}, \vec{\omega}_{ref} \rightarrow \vec{\omega}_{inc})$$

Determination of f_λ is generally very difficult in experiment due to the fact that it changes with material, oxidisation, polish process and so on. In many practical applications, surface can be approximated as one of two kinds of ideal reflector: specular and Lambertian.

In specula reflection, the BRDF f_λ is defined as

$$f_\lambda = F(\lambda, \vec{s})\delta(\vec{\omega}_{inc} \cdot \vec{n} + \vec{\omega}_{ref} \cdot \vec{n}) \qquad 2\text{-}32$$

where δ is Dirac delta function and $F(\lambda, \vec{x}) \leq 1$. The reflection forms the image of the incident light. Surfaces of polished metal, plain mirror as well as large crystal are good examples of specula reflector.

At the other end, the Lambertian surface is assumed to be perfectly diffusive therefore f_λ is independent of direction $\vec{\omega}_{ref}$. On an infinitesimal non-absorptive surface area dA, the reflected radiance can be expressed with the incident energy flux as

$$L_{ref} = \frac{E_{ref}}{\pi} = -\frac{1}{\pi}\frac{d\Phi_{inc}}{dA} \qquad 2\text{-}33$$

where the minus sign is the result of the sign convention set in section 2.2.4. In the current study, the surfaces concerned are made from building material and unlikely to be machine polished therefore should be quite diffusive (Modest, 2003). As the light reaching the surfaces has passed smoke region, the angular distribution of the incident light would also be much more even than that directly from the light source. It effectively makes the overall reflection rather evenly distributed. From the above consideration all the surfaces in the current study are treated as Lambertian surfaces.

2.7.3 Light source

Any surface that emits radiant energy within the visible wavelength range is treated as a light source. At each point on the surface of the light source, radiance in the direction $d\vec{\omega}$ at the point is given as L. The total radiant flux of the light source would be

$$\Phi = \int_A \int_\Omega \int_0^\infty L d\lambda \left(d\vec{\omega} \cdot d\vec{A} \right) \qquad 2\text{-}34$$

where $L = L(\lambda, \vec{x}, \vec{\omega})$ is known and Ω is the hemisphere defined in the $d\vec{A}$ direction. As the simplest case, L is assumed to be a constant over the entire range of visible wavelength and independent of direction and position. Then

$$L = \frac{\Phi}{\pi \Delta\lambda A} \qquad 2\text{-}35$$

Here A is the surface area and $\Delta\lambda$ is the range of wavelength.

More often, light output are defined in terms of luminous flux instead of radiant flux Φ. For a given light source, the luminous flux Φ_v is defined as the following (see section 3.3)

$$\Phi_v = 683 \int_A \int_\Omega \int_0^\infty L_\lambda \bar{y}_\lambda d\lambda \left(d\vec{\omega} \cdot d\vec{A} \right) \qquad 2\text{-}36$$

where the subscript v is to identify a photometric variable from its radiometry counterpart and $\bar{y}_\lambda$ is the luminosity function (see section 3.3). The unit for Φ_v is lumen. In lighting industry, the ratio between Φ_v and the total input power P of the lighting device is defined as the luminous efficacy (lm/W)

$$e_v = \frac{\Phi_v}{P} \qquad 2\text{-}37$$

By keeping all the assumptions of 2-35, the emitting radiance L of our simplest light model would be

$$L = \frac{P e_v}{683 \pi \Delta\lambda A} \qquad 2\text{-}38$$

The value of efficacy for the common lighting devices can be found in Table 2-1 (Pritchard, 1999).

Light source	Average efficacy (lm/W)
Low-pressure sodium lamp	200
High-pressure sodium lamp	110
Natural sun light	80
White fluorescent tube	90
Tungsten-halogen lamp	22

Table 2-1 The average efficacy of common lights

2.8 Light scattering by smoke particles

In the last two sections, the media and their properties such ε, μ, σ and m were assumed continuous. In reality, most media consist of particles that are much larger than the molecules of the matter. The optical characteristics of such particles determine the overall light scattering and absorption of the media. The optical characteristics of individual particle can be investigated from the solution of the Maxwell's equation 2-11 around the particle when it is illuminated by monochromatic parallel plane wave. In 1908, Gustav Mie obtained the solution in his effort to understand the varied colours in absorption and scattering exhibited by small colloidal particles of gold suspend in water. The theory is now commonly known as Mie theory. Details of the theory can be found in Kerker (1969), Bohren (1998) and Hulst (1981). An important contribution of the theory is the establishment of the dependency of extinction cross section on particle size, wave length and refractive index for a spherical particle.

For $x_p|m-1|<2$ (Jones, 1999)

$$Q_{sca}=\frac{8}{3}x_p^4\left|\frac{m^2-1}{m^2+2}\right|^2 \qquad 2\text{-}39$$

$$Q_{ext}=4x_p\,\mathrm{Im}\left\{\frac{m^2-1}{m^2+2}\left[1+\frac{x_p^2}{15}\left(\frac{m^2-1}{m^2+2}\right)\frac{m^4+27m^2+38}{2m^2+3}\right]\right\}+\frac{8}{3}x_p^4\,\mathrm{Re}\left\{\left(\frac{m^2-1}{m^2+2}\right)^2\right\} \qquad 2\text{-}40$$

$$Q_{abs}=Q_{ext}-Q_{sca} \qquad 2\text{-}41$$

where Im{} and Re{} represent the imaginary and real part of a complex function respectively. x_p is called the size parameter of the particle defined as

$$x_p = \pi \frac{d_p}{\lambda} \qquad 2\text{-}42$$

and d_p is the size of the particle. Qs are the efficiencies of absorption, scattering and extinction defined as the ratios

$$\begin{aligned} Q_{sca} &= C_{sca}/s \\ Q_{abs} &= C_{abs}/s \\ Q_{ext} &= C_{ext}/s \end{aligned} \qquad 2\text{-}43$$

where C_{sca}, C_{abs} and C_{ext} are the scattering, absorption and extinction cross sections and s is the geometrical cross section of the particle.

The extinction coefficients are given by

$$\sigma_i = NC_i \qquad 2\text{-}44$$

The subscript i represents scattering, absorption and extinction respectively. N is the number of particles in a unit volume of the medium.

In combustion related studies, the mass specific extinction coefficient σ_{mass} is more often quoted instead of σ. The two are related by the smoke mass concentration ρ_{smoke} as

$$\sigma_{mass} = \frac{\sigma}{\rho_{smoke}} \qquad 2\text{-}45$$

Numerous researchers have carried out experimental work on light extinction by soot of smoke. The results were presented in different ways, with different parameters, different fuel or in different range of wavelength. It was difficult to compare and draw general conclusion from them. The current author has collected them and put all the data that can be reliably expressed in the form of $Q_{ext}=f(x_p)$ into Figure 2-9. Alongside the experiment data (in symbols) are the predictions with various existing models (in lines). The two limiting refractive indices $m=1.3+0.3i$ and $m=2.0+1.5i$ are chosen from Table 2-3. On average $m=1.57+0.56$, for soot in the visible wavelength range, seems to be the most popularly quoted value in the more recent

literature (e.g. Charalampopoulos 1987[1], Dobbins 1990-1994, Wu 1997, Köylü 1994, Smyth 1996).

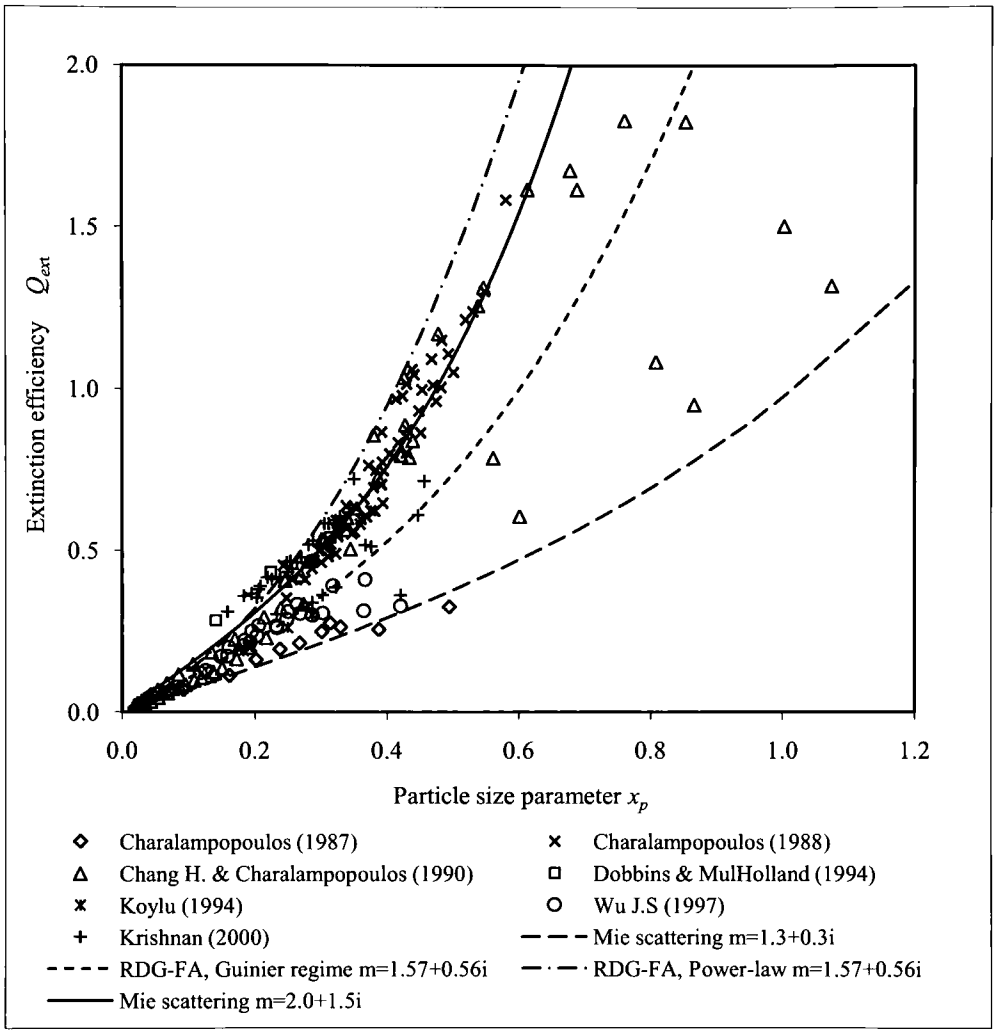

Figure 2-9 Extinction efficiency via size parameter

As can be seen in Figure 2-9, no single model presented there can cover the range of variation of the experimental data. The RDG-FA model as presented in section 2.8.3 puts soot scattering into 2 different regimes (Guinier and Power-law) according the size of soot particle aggregation and modelled each of them separately. The model has identified the two distinctive groups of the experimental data as shown in Figure 2-9 but failed to explain the significant overlapping of the two regimes between 0.2 and 0.4 of x_p. The model also failed in predicting the wide slop change of the extinction curve in the infrared region ($x_p < 0.2$).

[1] Although Charalampopoulos quoted this value as from Dalzell & Sarofim, the value of k in the original paper by Dalzell & Sarofim (1969) was 0.44 – 0.53 for soot illuminated by visible light.

2.8.1 Particle size distribution of smoke

For soot from fire smoke, $|m-1|$ is in the order of 1.0 (see next section), therefore the condition $x_p|m-1| < 2$ requires that the particle size of smoke should not be much larger than the wavelength of the incident light, Bankston has measured the size distributions of smoke under different combustion conditions and with different materials (Bankston, Zinn, Browner, & Powell, 1981). The results have been summarised by Mulholland in the SFPE handbook (SFPE, 2008) as shown in Table 2-2[1].

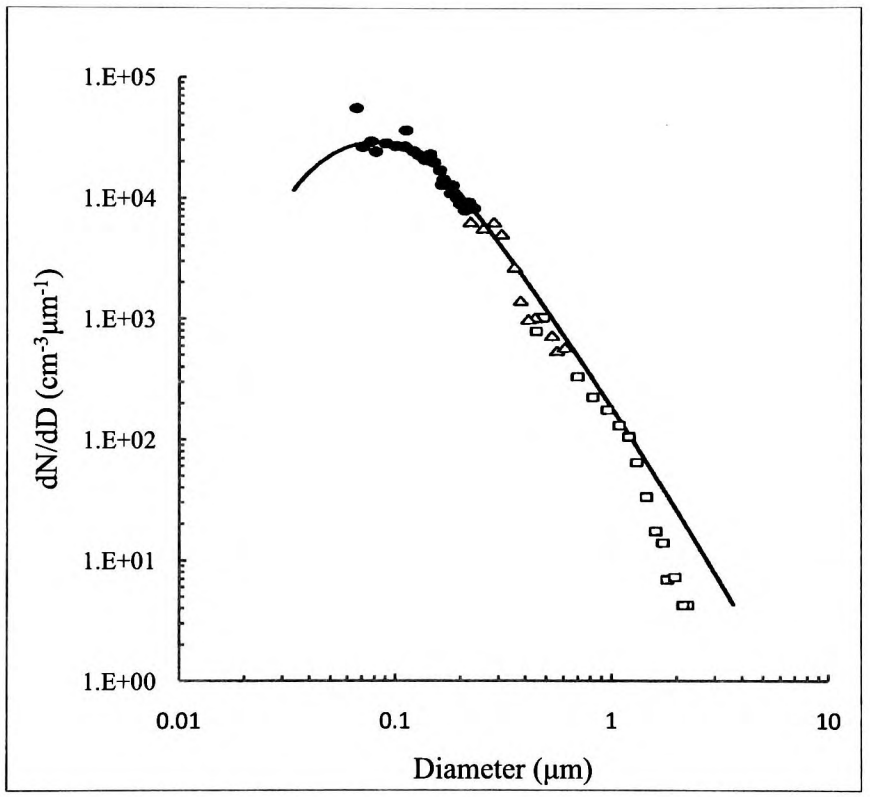

Figure 2-10 Number size distribution of smoke particles (Mulholland, 2008)

[1] In the current section, D has been used in the place of d_p for clarity.

Type	D_{gm}	D_{32}	σ_g	Combustion condition	Reference
Douglas fir	0.5-0.9	0.75-0.8	2.0	Pyrolysis	(Bankston, Zinn, Browner, & Powell, 1981), (Bankston, Cassanova, Powell, & Zinn, 1978)
Douglas fir	0.43	0.47-0.52	2.4	Flaming	(Bankston, Cassanova, Powell, & Zinn, 1978), (Bankston, Zinn, Browner, & Powell, 1981)
Polyvinylchloride	0.9-1.4	0.8-1.1	1.8	Pyrolysis	(Bankston, Zinn, Browner, & Powell, 1981)
Polyvinylchloride	0.4	0.3-0.6	2.2	Flaming	(Bankston, Zinn, Browner, & Powell, 1981)
Polyurethane (flexible)	0.8-1.8	0.1-1.0	1.8	Pyrolysis	(Bankston, Zinn, Browner, & Powell, 1981)
Polyurethane (flexible)		0.5-0.7		Flaming	(Bankston, Zinn, Browner, & Powell, 1981)
Polyurethane (rigid)	0.3-1.2	1.0	2.3	Pyrolysis	(Bankston, Zinn, Browner, & Powell, 1981)
Polyurethane (rigid)	0.5	0.6	1.9	Flaming	(Bankston, Zinn, Browner, & Powell, 1981)
Polystyrene		1.4		Pyrolysis	(Bankston, Zinn, Browner, & Powell, 1981)
Polystyrene		1.3		Flaming	(Bankston, Zinn, Browner, & Powell, 1981)
Polypropylene		1.6	1.9	Pyrolysis	(Bankston, Zinn, Browner, & Powell, 1981)
Polypropylene		1.2	1.9	Flaming	(Bankston, Zinn, Browner, & Powell, 1981)
Polymethylmethacrylate		0.6		Pyrolysis	(Bankston, Zinn, Browner, & Powell, 1981)
Polymethylmethacrylate		1.2		Pyrolysis	(Bankston, Zinn, Browner, & Powell, 1981)
Cellulosic insulation	2-3		2.4	Smoldering	(Mulholland & Ohlemiller, Aerosol Characterization of a Smoldering Source, 1981)

Table 2-2 Particle size of smoke from burning wood and plastics (Mulholland, 2008)

In Table 2-2, D_{gm} is the mass mean number diameter and D_{32} is the Sauter mean diameter of smoke defined as

$$\log(D_{gm}) = \int_0^\infty \log(D) m dD \qquad 2\text{-}46$$

$$D_{32} = \frac{\int_0^\infty D^3 n dD}{\int_0^\infty D^2 n dD} \qquad 2\text{-}47$$

where D is the particle size (diameter). *m(D)* and *n(D)* are the mass and number distribution of the particles. The geometric standard deviation σ_g is defined with the geometric mean number diameter D_{gn} of the particles as

$$\log(\sigma_g) = \left[\int_0^\infty (\log D - \log D_{gn})^2 n dD\right]^{1/2} \qquad 2\text{-}48$$

and

$$\log(D_{gn}) = \int_0^\infty D n dD \qquad 2\text{-}49$$

Figure 2-10 shows a typical size distribution of the particles of smouldering smoke. It can be seen that the particle size is between 0.01 and 3.0μm with the majority of particles having diameter less than 1.0μm. The condition for Mie scattering requires that $D < 0.2\mu m$ for blue light and $D < 0.5\mu m$ for red light. This fact needs to be kept in mind when analysing light scattering by fire smoke with Mie theory.

No	Real part	Imaginary part	Source
1	1.56 – 4.8	0.44 – 3.82	Dalzell (1969)
2	1.9 – 2.1	0.4 – 0.8	Lee & Tien (1981)
3	1.2 – 1.45	0.1 – 0.27	Batten (1985)
4	1.37 – 1.6	0.41 – 0.52	Charalampopoulos (1987)
5	1.52 – 1.82	0.65 – 0.88	Charalampopoulos (1988)
6	1.2 – 2.0	0.08 – 1.0	Habib & Vervisch (1988)
7	0.78 – 4.09	0.32 – 3.37	Chang & Charalampopoulos (1990)
8	1.2 – 2.0	0.1 – 1.0	Horvath (1993)
9	1.55 – 2.10	0.55 – 1.0	Dobbins (1991, 1994)
10	1.57	0.56	Wu (1997)
11	1.95 – 2.5	0.45 – 0.51	van-Hulle (2002)
12	1.55 – 1.9	0.55 – 0.8	Suo-Anttila (2005)

Table 2-3 Refractive indices found in literature

2.8.2 Refractive index of soot

In applying Mie scattering theory, one needs to accurately estimate the value of the complex refractive index *m*. Numerous research activities have been taken around it. Table 2-3 gives some examples of the values cited by different researchers. For soot particles, the refractive index may be affected by factors such as soot temperature, the hydrogen to carbon (H/C) ratio of fuel, particle size distribution, the form of aggregation of particles and the wavelength of illuminating light. Among them, the influence of temperature has been found to be very weak (Stull & Plass, 1960). Charalampopoulos and Felske (1987) carried out in-situ measurement of *m* at different height of premixed methane/oxygen flame. With the geometric width of the particle distribution up to 1.24, no significant influence of particle size distribution on *m* has been observed. This may be due to two reasons. The first is that the measured refractive index of polydisperse particles was compared with that of a quasi-monodisperse particle set. The monodisperse particle diameter is assumed to be the most probable diameter of the corresponding polydisperse set and the geometric width was set to 1. Such comparison may not truly reflect the influence of particle size distribution on light scattering by soot particles. The other, may be more likely cause of the insensitivity of refractive index to the particle size distribution, is the aggregation of soot particles in smoke. As the small soot particles aggregate, the size of individual particle becomes less influential to the result of light scattering/absorption. The insensitivity of the refractive index on the size distribution of soot particles can also be found in the paper by Habib & Vervischi (1988).

Based on the Drude-Lorentz dispersion model, Dalzell & Sarofim (1969) argued that an increase in H/C in soot results in the decrease in the number of free electrons and a decrease in both the real and the imaginary part of *m*. Their experiment with acetylene (H/C=1/14.7) and propane (H/C=1/4.6) has not shown significant difference to support such argument. More recent experiment by Wu (1997) has confirmed that within the visible wavelength range, refractive index does not vary significantly between different fuel types.

Outside the visible wavelength range Habib & Vervischi (1988) have found that with high H/C ratio (>0.2), the *k*-curve representing the imaginary part of the refractive index exhibits a slop change when λ>1.0μm. It has effectively provided support to Dalzell and Sarofim's argument.

The dependence of refractive index on wavelength is evident in both experiment and theoretical model as shown in Figure 2-11 where the lines represent the theoretical values from Drude-Lorentz dispersion model (Lee and Tien 1976) with different number density and damping constants (Zhang & Rubini, To be published in 2010). The solid lines are that for the real part of refractive index *m* and the dashed lines are that for the imaginary part of *m*. The symbols on the

same graph are the experimental data by different research groups. Among them, the model from Dalzell (1969) has shown the best fit to the experimental data.

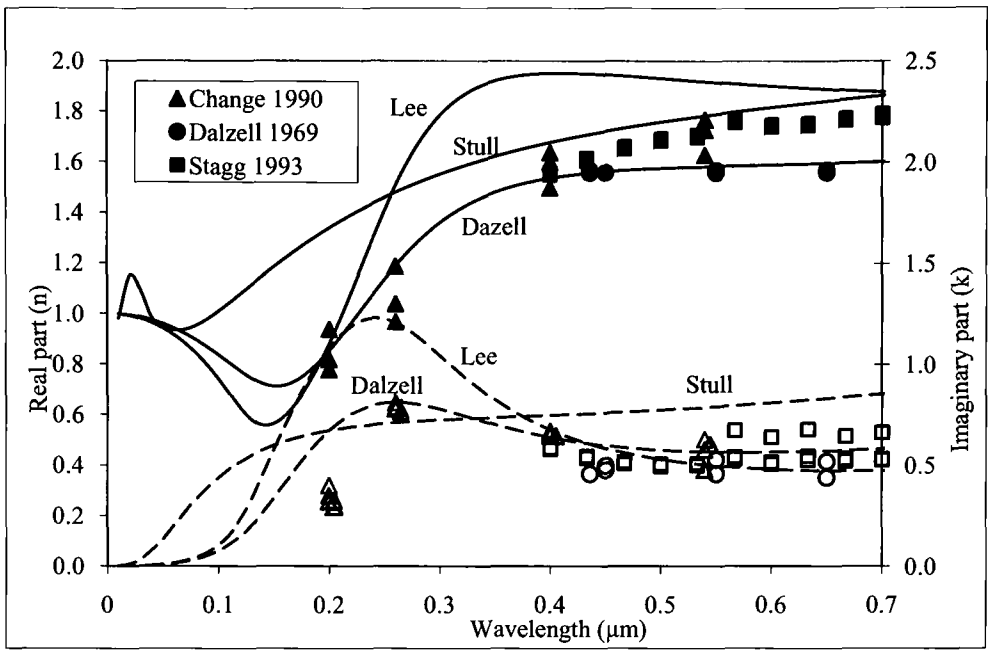

Figure 2-11 Change of refractive index with wavelength

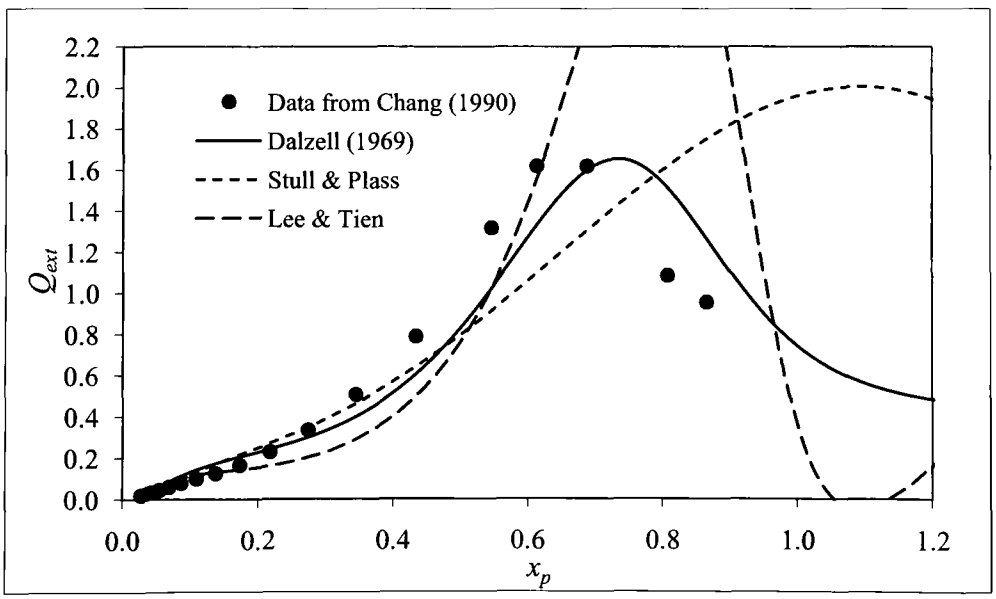

Figure 2-12 Change of extinction efficiency via size parameter

Figure 2-12 shows the prediction of extinction efficiency from Mie theory with the refractive indices from Drude-Lorentz dispersion models. Again, Dalzell's model offers the best prediction.

2.8.3 Aggregation of soot particles

In combustion generated smoke, soot particles are rarely exist in isolation. They link together forming chain-like aggregation (Williams & Gritzo, 1998). A practical and common model, known as RDG (also called RDG-FA or RDG-PFA model) for light scattering by soot particle aggregation was proposed by Dobbins and Megaridis (1991). The soot aggregation had been modeled as porous sphere. According to Dobbins and Magridis, particle aggregation in soot only affects light scattering. When the size of the primary particle satisfies Rayleigh condition $x_p << 1$ and $x_p|m-1| << 1$, the absorption efficiency of the smoke is the same as that for the prime particles

$$Q_{abs} = 4x_p E(m) \tag{2-50}$$

But the scattering efficiency needs to be modified by a factor Y_a as

$$Q_{sca} = \frac{8}{3} x_p^4 F(m) Y_a \tag{2-51}$$

The values of Y_a depends on the morphological regime of the aggregation. There are two regimes that have been identified according to the size of the aggregate relative to light wavelength (Köylü & Faeth, 1994): the Guinier regime ($\kappa^2 \overline{R_g^2} \le 3D_f/8$) and the power-law regime ($\kappa^2 \overline{R_g^2} > 3D_f/8$). Here $\kappa = 2\pi/\lambda$ is the wave number of the incident light. $\overline{R}_g^2$ is the mean radius of gyration of the aggregates and D_f is the fractal dimension of the aggregates. The corresponding Y_a are

$$\begin{cases} Y_a = k_f \left(\dfrac{3D_f}{16 x_p} \right)^{D_f/2} & \kappa^2 \overline{R_g^2} \le 3D_f/8 \\ Y_a = k_f (4x_p)^{-D_f} \left[\dfrac{3}{2-D_f} - \dfrac{12}{(6-D_f)(4-D_f)} \right] & \kappa^2 \overline{R_g^2} > 3D_f/8 \end{cases} \tag{2-52}$$

As can be seen in Figure 2-9, when x_p is less than 0.2, most of the measured values are around the curve of Guinier regime. When x_p is larger than 0.3, most of the measured values are close

to the curve of power-law. As can be seen in the next section, the extinction efficiency between 0.2 and 0.3 depends on the mean particle size.

2.8.4 Multiple scattering by soot particles

All theories being considered so far are based on the assumption that a single ray of incident light will at maximum hit one particle before disappearing from the domain. The particles are considered either in isolation staying far apart from each other or stick together to form a bigger separate entity (aggregate). Experiments have shown that soot particle aggregation results in clusters of non-coalescent particles close but still geometrically independent to each other (e.g. Köylü 1995 and Williams 1998).

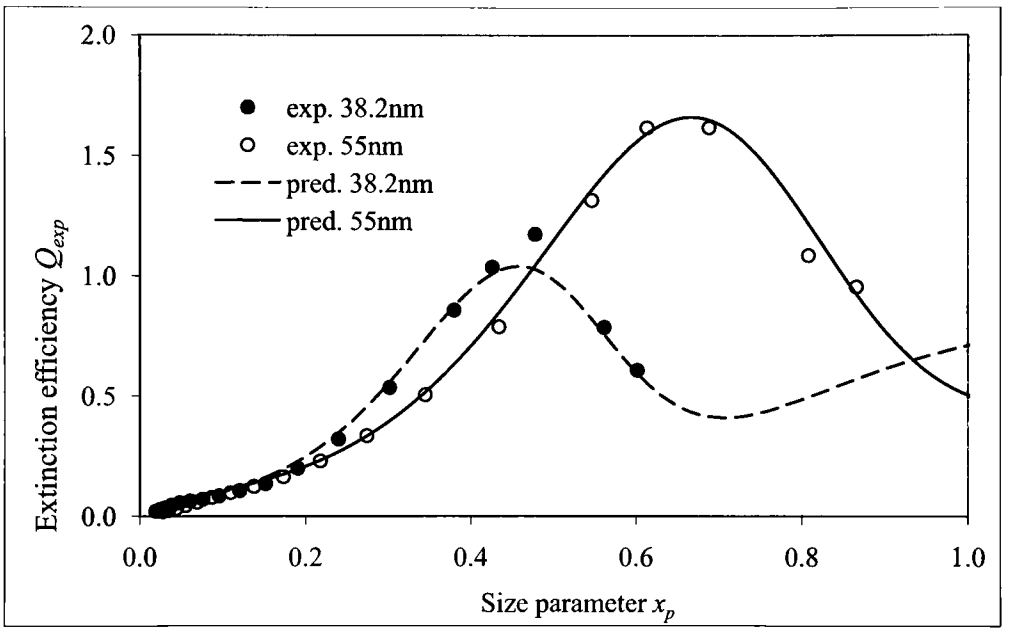

Figure 2-13 Extinction efficiency of particles with different size

By performing multipole analysis of the scattered electric field from such particle cluster, Mackowski (1991, 1994 and 1995) has found that the conventional dipole approximation used in the RDG theory may result in error of more than 20% in the predicted absorption cross section for small x_p. Under constant refractive index, Mackowski defined the ratio of absorption cross sections between that of a particle in an aggregate and that of an independent particle. He found that the ratio increases significantly as the number of particles in aggregate increases from 1 to 20. Further increase of the number of particles in an aggregate, the ratio gradually turns to a constant (Mackowski 1991, 1994, 1995). Based on Mackowski's analysis, the current author has proposed a modifier to the particle extinction efficiency. The modifier is a logarithmic function of the number of particles in a soot aggregate n_p and expressed as

$$Q'_{ext} = Y_a Q_{sca} + \log(n_p) Q_{abs} \qquad 2\text{-}53$$

where Q_{sca} and Q_{abs} are from Mie theory as defined by equation 2-39 and 2-41 respectively. In the correction of scattering with the RDG model, only the Y_a value for the Guinier regime is included. Figure 2-13 shows the comparison between the measured extinction efficiency (Chang & Charalampopoulos, 1990) and the prediction with equation 2-53.

The change of Q'_{ext} with different n_p is shown in Figure 2-14. It can be seen that the closest prediction is the one with $n_p = 20$. It is consistent with Mackowski's analysis.

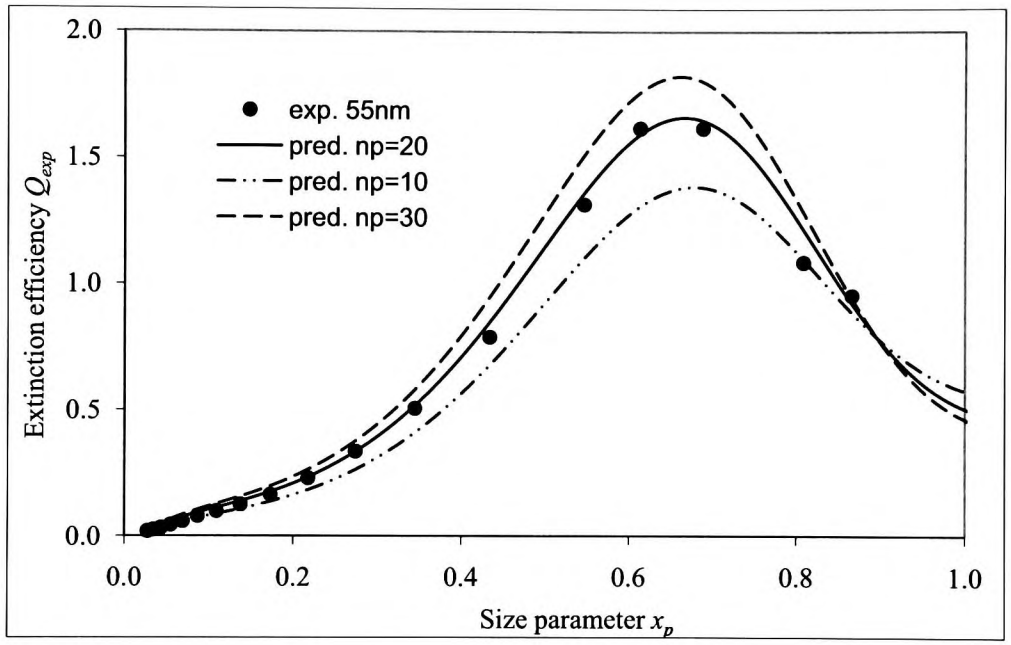

Figure 2-14 Change of extinction efficiency with number of particles in an aggregate

Further details of the new scattering model for soot aggregates can be found in the paper by Zhang and Rubini (To be published in 2010)

2.9 Summary

This chapter has presented the concepts and equations in classic optics that will be used in the rest of the thesis. The basic radiometry describes how light travels between surfaces over vacuum space. In media, light attenuates over distance according to Lambert-Beer's law. More details of light extinction by a small particle have been shown in the Mie theory as a solution of Maxwell's equation. The theory has revealed the dependence of light extinction on the wavelength.

In soot of fire smoke, the aggregation of particles has changed its optical property differing from Mie theory. In the current study the author has carried out a comprehensive survey of previous research on light extinction by soot aggregation. The survey has revealed that the aggregation of soot particles not only alters the scattering but also absorption behaviour of smoke. This is contrary to the previous belief that particle aggregation only affects scattering and leaves absorption behaviour unchanged.

By modifying Mie extinction for both scattering and absorption, the current study has shown that the prediction of the extinction curve has been significantly improved and the power law regime introduced previously to fit the extinction curve for $x_p > 0.3$ is no longer necessary.

Chapter 3. Vision and photometry

Vision, also known as visual perception, is the ability to interpret information and surroundings from visible light reaching the eye. The last two chapters described the transmission of light in space and through media as well as its measurement. After light has reached human eyes, it is interpreted by the physiological vision system. Such interpretation is the subject of photometry (Mather, 2009).

3.1 Human eye

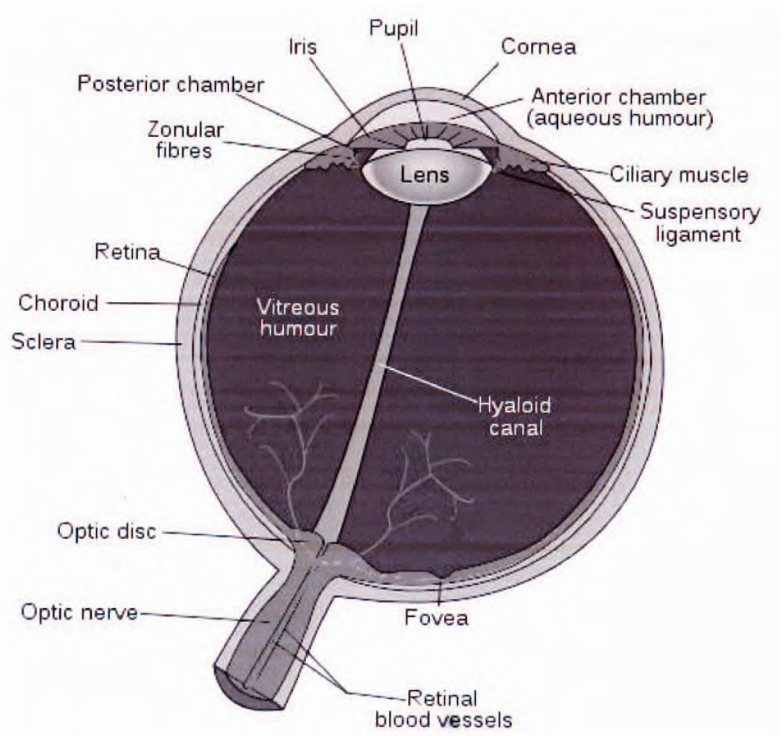

Figure 3-1

Figure 3-1 (wikipedia/eye) is a schematic diagram of the human eye. The important parts here is the iris that adjust the amount of light allowed passing into the eye and the lens that focuses light passing it to form an image on the retina. The retina converts the image into brain stimuli. These components are analogy to the aperture, lens and sensor in a modern digital camera.

There are mainly two types of photoreceptor cells on the retina, the rods and cones. Rods function mainly in dim light and provide black-and-white vision, while cones support daytime vision and the perception of colour.

3.2 Colour

In the spectrum of electromagnetic wave, only the range between 370nm 700nm would be visible by human eye. The stimulation of human eye by the light of different wavelength within the visible range produces the sense of colour. Light with different wavelength or different mixture of wavelengths produce different colour sense. It was suggested that human eye is capable of distinguishing about 10 million different colours (Hunt, 1992).

3.3 Colour sensibility of human eyes

The sensitivity of human eyes changes with different colour or the wavelength of light. It is the subject of photometry. The foundations of photometry were laid in 1729 by Pierre Bouguer. In his *L'Essai d'Optique*, Bouguer discussed photometric principles in terms of the convenient light source of his time: a wax candle. This became the basis of the point source concept in photometric theory (Hunt, 1992).

It should be kept in mind that photometry measures light in terms of both radiometry quantities and the sensitivity of human eyes. The difference between radiometric and photometric theory is in their units of measurement.

3.3.1 Luminous intensity

Today the international standard for luminous intensity is a theoretical point source that has a *luminous intensity* of one *candela*(cd). It emits monochromatic radiation with a frequency of 540 x 10^{12} Hertz (or approximately 555 nm, corresponding to the wavelength of maximum photopic luminous efficiency) and has a radiant intensity (in the direction of measurement) of 1/683 watts per steradian. The relation of the spectral luminous intensity and the radiant intensity can be expressed as

$$I_{v,\lambda} = 683 y_\lambda I_\lambda \qquad 3\text{-}1$$

where the subscript v represents the photometrical counter part of radiometric variable. In 3-1, y_λ is the luminosity function (luminous efficacy) defined in the CIE photometric curve (Figure 3-2). It provides the weighting factor needed to convert between radiometric and photometric measurements. Considering, for example, a monochromatic point source with a wavelength of

510 nm and a radiant intensity of 1/683 watts per steradian, Figure 3-2 shows that the photopic luminous efficiency at 510nm is 0.503. The source therefore has a luminous intensity of 0.503 candelas.

3.3.2 Luminous flux

Luminous flux is photometrically weighted radiant flux (power). Its unit of measurement is *lumen* (lm), defined as 1/683 watts of radiant power at a frequency of 540 x 10^{12} Hertz. As with luminous intensity, the luminous flux of light with other wavelengths can be calculated using the CIE photometric curve. Similar to luminous density, the relation between luminous flux and radiant flux is

$$\Phi_{v,\lambda} = 683 y_\lambda \Phi_\lambda \qquad 3\text{-}2$$

A point source having a uniform (isotropic) luminous intensity of one candela in all directions (i.e., a uniform *intensity distribution*) emits one lumen of luminous flux per unit solid angle (steradian).

3.3.3 Luminance

Luminance is photometrically weighted radiance. It is an approximate measure of how "bright" a surface appears when it is viewed from a given direction. The value of luminance is defined with luminosity function as

$$L_{v,\lambda} = 683 y_\lambda L_\lambda \qquad 3\text{-}3$$

The unit of luminance is cd/m^2.

The important point to remember is that in terms of visual perception, human eyes perceive luminance (Hunt, 1992).

3.3.4 Luminosity function

For a give light source, the luminous flux Φ_v is defined as the following

$$\Phi_v = 683 \int_0^\infty \bar{y}_\lambda \Phi_\lambda d\lambda \qquad 3\text{-}4$$

The subscript λ indicates that both $\bar{y}$ and Φ are the functions of wavelength. Within narrow band, both $\bar{y}$ and Φ can be determined experimentally therefore the value of the luminosity function $\bar{y}_\lambda$ can be calculated. Figure 3-2 shows the luminosity functions included in CIE 1924

standard (Wyszecki & Stiles, 1982). The two curves are for photopic and scotopic vision[1] respectively. Since photopic vision represents visual sensitivity under normal lit condition, unless being mentioned specifically, the photopic curve would be referred as the luminosity function in the current study.

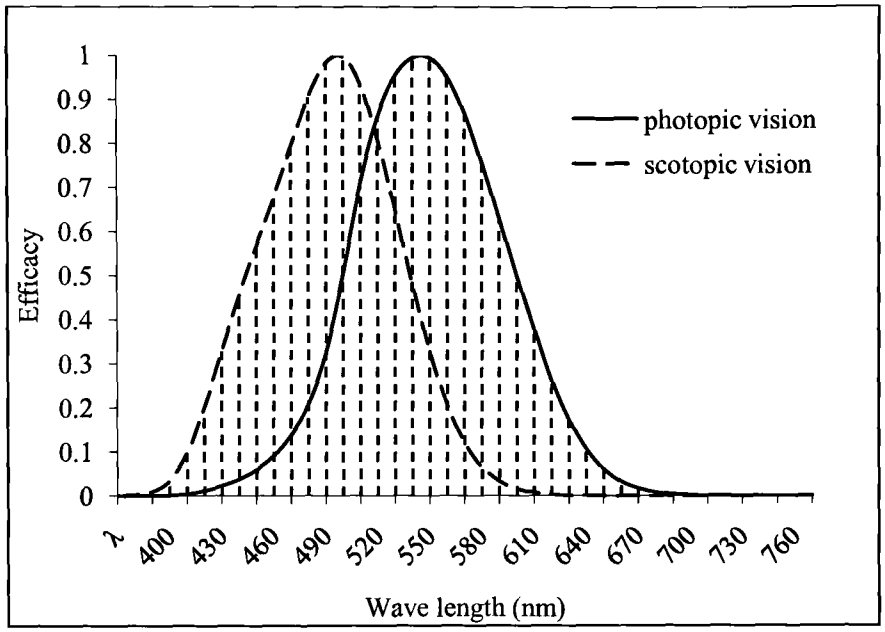

Figure 3-2 Luminosity function (Wyszecki & Stiles, 1982)

The standard luminosity function is normalized to a peak value of unity at 555nm. The unit of luminous flux Φ_v is lumen. It is defined as unity for a radiant power Φ_λ of 1/683 watt at wavelength of 555 nm, which is the peak of the luminosity curve[2]. It is the reason for the constant 683 in the equations of this section.

3.4 Contrast

Contrast is the difference in visual properties that makes an object distinguishable from other objects and the background. In visual perception of the real world, contrast is determined by the

[1] Photopic vision is the vision of the eye under well-lit conditions. In humans and many other animals, photopic vision allows color perception, mediated by the cone cells of the eye. Scotopic vision is the vision of the eye under low light conditions. Scotopic vision is produced exclusively through rod cells which are most sensitive to wavelengths of light around 498nm.

[2] The real peak of the luminosity curve is at λ=555.015nm and the value of the constant should be 683.002.

difference in the colour and brightness of the object and other objects within the same field of view. Because the human visual system is more sensitive to contrast than absolute luminance, we can perceive the world similarly regardless of the changes in illumination over the day or from place to place (Mather, 2009).

Various definitions of contrast are used in different situations. Here, luminance contrast is used as an example, but the formulas can also be applied to other physical quantities. In many cases, the definitions of contrast represent a ratio of the type

$$\frac{\Delta L_v}{\bar{L}_v} \qquad 3\text{-}5$$

where ΔL_v is the difference of luminance between the target sign and its background. $\bar{L}_v$ is a nominal luminance. The rationale here is that a small difference would be negligible if the nominal luminance is high, while the same difference matters if the nominal luminance is low. The following are few common definitions of contrast based on 3-5.

3.4.1 Weber contrast

The Weber contrast is defined as

$$h_w = \frac{L - L_b}{L_b} \qquad 3\text{-}6$$

with L and L_b representing the luminance of the sign and the background respectively. The nominal luminance is the background luminance. Expression 3-6 is commonly used in cases where small features are present on a large uniform background, i.e. the average luminance is approximately equal to the background luminance. The typical application of 3-6 is in aviation as shown in section1.2.

3.4.2 Michelson contrast

The Michelson contrast is commonly used for patterns where both bright and dark features are equivalent and take up similar fractions of the area. The Michelson contrast is defined as

$$h_m = \frac{L_{\max} - L_{\min}}{L_{\max} + L_{\min}} \qquad 3\text{-}7$$

with L_{max} and L_{min} representing the highest and lowest luminance. The nominal luminance is $L_{\max} + L_{\min}$ and represents twice the average of the luminance. With image of digital camera, $L_{\max}$ and $L_{\min}$ may be severely affected by noise and the result would be very unreliable.

3.4.3 RMS contrast

The root-mean-square (rms) contrast is commonly used in image processing and defined as the standard deviation of pixel intensity (Peli, 1990):

$$h_{rms} = \frac{\sigma_{std}}{L_n} = \frac{1}{L_n}\sqrt{\frac{1}{N}\sum_{i=1}^{N}(L_i - \bar{L})^2} \qquad 3\text{-}8$$

where L_n is a factor that normalizes the maximum value of L_i/L_n to 1. N is the total number of pixels in the image, and $\bar{L}$ is the average luminance across the image. σ_{std} is the standard deviation of L_i.

3.5 Visibility

In section 1.2, it has been seen that visibility can be defined in terms of threshold visual distance. It is a meteorological definition used in homogeneous media and background lighting condition. The purpose of measuring visibility there is to know the maximum distance that a given object is still discernable by the observer. Such distance is a vital condition for aviation and shipping industry. In fire protection engineering, by adopting the above visibility definition from meteorology, design code such as NFPA 130 was able to establish visibility criteria that controls the minimum visual distance during fire evacuation that is a necessary safety condition. What needs to be mentioned is that in the case of fire emergency, visibility concerns the discernability of egress path under often heterogeneous smoke and lighting condition. Unlike in meteorology, as long as the target is identifiable, the distance between the evacuee and the target is unlikely to be an issue. It raises a question if the distance based definition of visibility is the best choice for fire protection engineers.

In defining visibility during emergency egress, consideration should also be given to the smoke condition before it reaches the visual distance threshold. Most evacuations in fact take place under such condition. The effectiveness of emergency signage under such condition will significantly affect the time of evacuation. Here the existing definition of visibility has shown its limitation in guiding fire safety engineers improve the efficiency of emergency egress. Conditions that have shown significant influence on the effectiveness of emergency signage such as colour, context and viewing angle (see Chapter 4) are not reflected in the existing definition and the measurement based on it.

The current study is the first attempt to address these issues and create the concept of visibility based on perceived image in smoke laden environment. Here the emphasis has been given to "discernability". In this thesis, visibility and "discernability" are synonymous. Since

"discernability" is not in any English dictionary, therefore visibility will be used throughout this thesis although its meaning would be more authentic.

At this point, it has to be said that the current author has no intention to provide a general definition of visibility in the current thesis. However a definition that suites the fire protection engineering is considered necessary and therefore given as the following:

Visibility is the human imaginary perception of a given target.

In this definition, emphasis has been laid on the target and its perception since the objective of the study is to understand the human interpretation of a particular object that has been visually accessed.

In terms of measuring visibility, the following consideration has been given in the current study:

- The higher of the contrast between the target and the rest of the image, the better of the visibility of the target.
- A brighter image would provide better visibility than a darker image.

The first point may be easier to be accepted since it is consistent with existing measures of visibility such as that given by equation 1-3 and equation 1-4. The second point may attract argument as some existing researchers point out that visibility does not depend on light intensity (Schooley & Reagan, 1980) although our common sense tell us otherwise. In the experiment by Collins, Dahir and Madrzykowski (1992), it was found that signs with highter luminance were more visible through smoke. Similar results have been observed by Ouellette(1988) and Ouellette has recommended to remove the limitation on maximum sign luminance from BS2560.

For image based visibility, the above considerations can be expressed as

$$V_\lambda = F(contrast, brightness, colour) \qquad 3\text{-}9$$

where function F depends on how the image has been created and will be defined in the following chapters for photographic and synthetic images respectively.

3.6 Summary

The important aspects of human vision and basic photometry concepts have been presented in this chapter. Among them the luminant efficacy, or photometric function would be the most relevant function to the current study. It has revealed the way that human eye responses to the stimulation of light with different colour. With the help of this function, it has been possible to

mathematically convert a physical image received by the eye into an image that is perceived by the brain. Human visibility can be simulated by interpreting such image. It is called the image based visibility in the current study. Comparing with the prevailing concept of visibility, the new concept is more close to the common understanding of the word itself. In quantifying visibility so defined, the following steps should be followed:

1. Acquisition of physical image (photographic or synthetic).
2. Conversion of the image into human perception (vision).
3. Defining measure to interprete the vision.

The rest of this thesis is concerned with how to realise these steps in experiment as well as in numerical simulation.

Part II Experimental study of visibility in smoke tunnel

This part of the thesis describes the experimental work carried out in a tunnel filled with misty smoke. Various illuminated signs are tested and digital photographs are taken under different smoke, luminance and colour conditions. The experimental procedure demonstrates how to measure visibility from digital photographs. The results of the experiment lead to some useful and interesting conclusions.

Chapter 4. Previous research work

In the second half of the last century, numerous researches in the visibility of emergency exit sign have led to significant improvement on the safety standards in this area. Such research work has been reviewed in this chapter and some requirements for further study have also been pointed out.

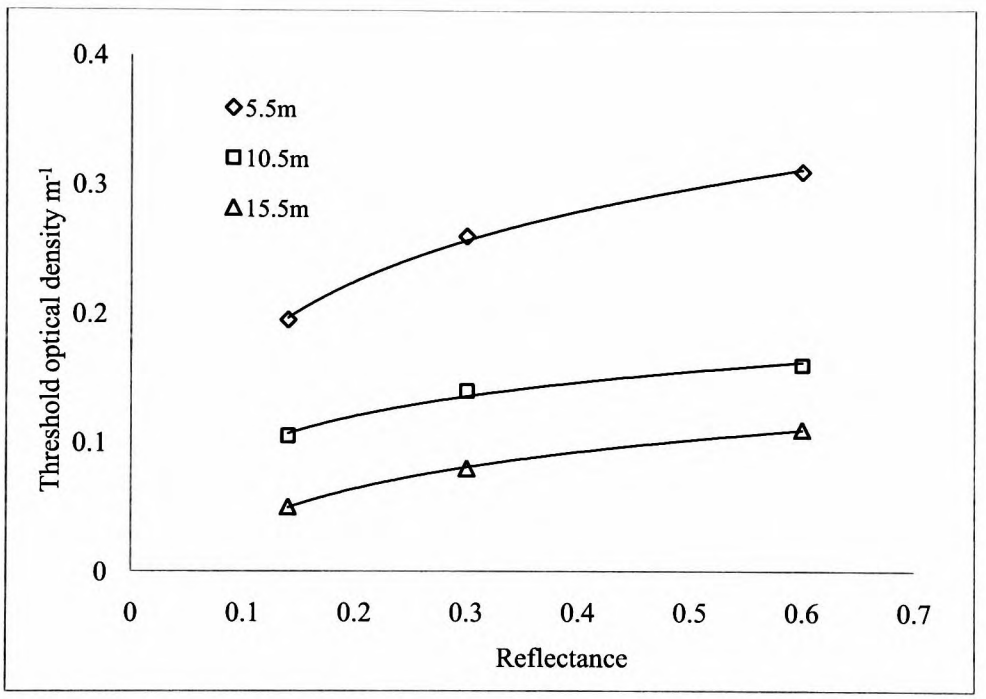

Figure 4-1 The effect of reflectance (HSE, UK, 1998)

Early experiment on the visibility of exit sign in smoke was in 1969 by Jin (HSE, UK, 1998). He studied externally illuminated reflective sign with different reflectance (defined as radiosity/irradiance, see section 2.2.3) on a black background. The circular placards were viewed through a window from 5.5m, 10.5m and 15.5m and the diameter of the placard was changed to 50mm, 100mm and 150mm respectively. Three different placards were tested with reflectance 0.6, 0.3 and 0.14 respectively. The chamber was illuminated by high-mounted fluorescent lamps providing ambient luminance of 60lx. White smoke was generated by burning filter paper. The threshold optical density of the smoke was recorded as shown in Figure 4-1. The lines are the fitting curve. With the placards positioned at 10.5m from the viewer, the

reflectance of the placards was 0.6 and the background reflectance was 0.07 under the illumination of 60lx, Figure 4-2 show the relation between the diameter of the placard and the threshold optical density when the placard could not be distinguished from its background.

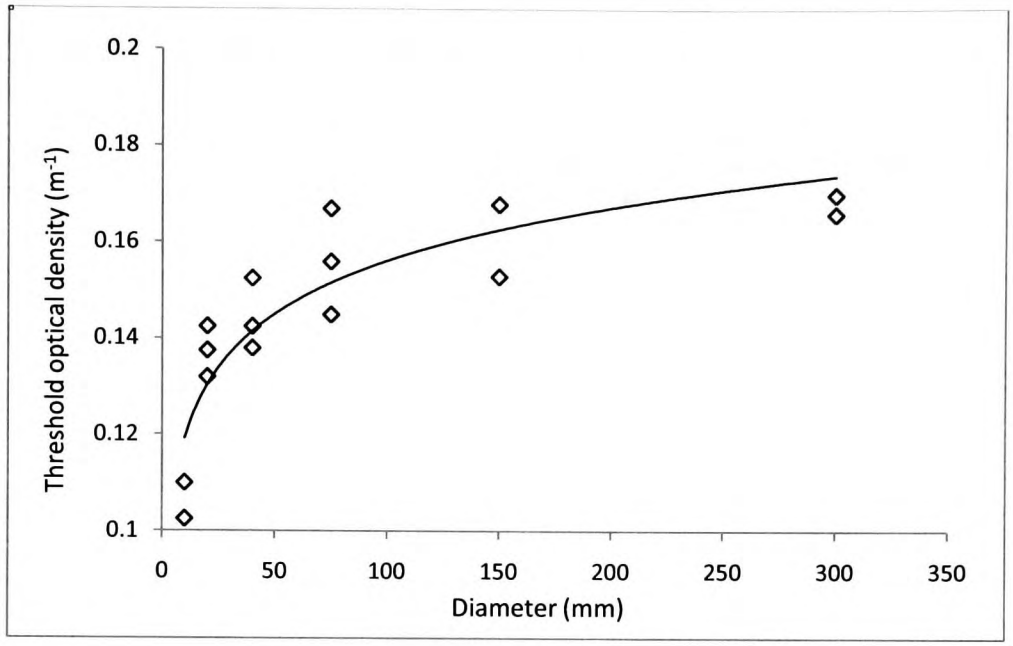

Figure 4-2 The effect of placard diameter (HSE, UK, 1998)

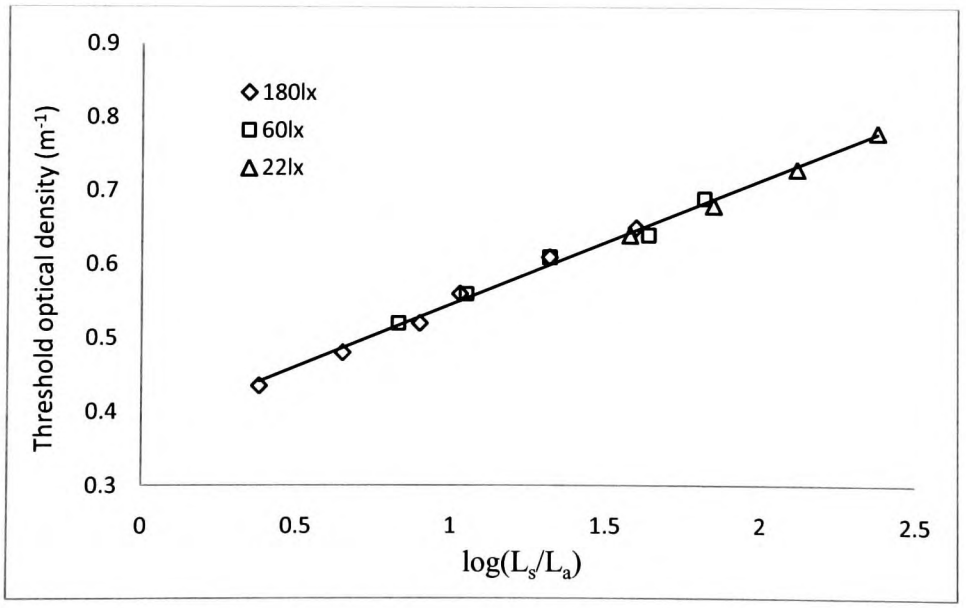

Figure 4-3 The effect of ambient light

The effect of ambient lighting was also investigated by Jin in the same experiment. All the parameters were the same as in Figure 4-1 but the placards were back-illuminated by a projector that can change the luminance of the placards. The chamber was illuminated by high mounted florescent lamps providing luminance ranging from 2lx to 180lx. Figure 4-3 shows the result viewed at 5.5m with 3 different ambient illuminations. In Figure 4-3, L_s is the luminance of the placard and L_a is the luminance of the ambient light.

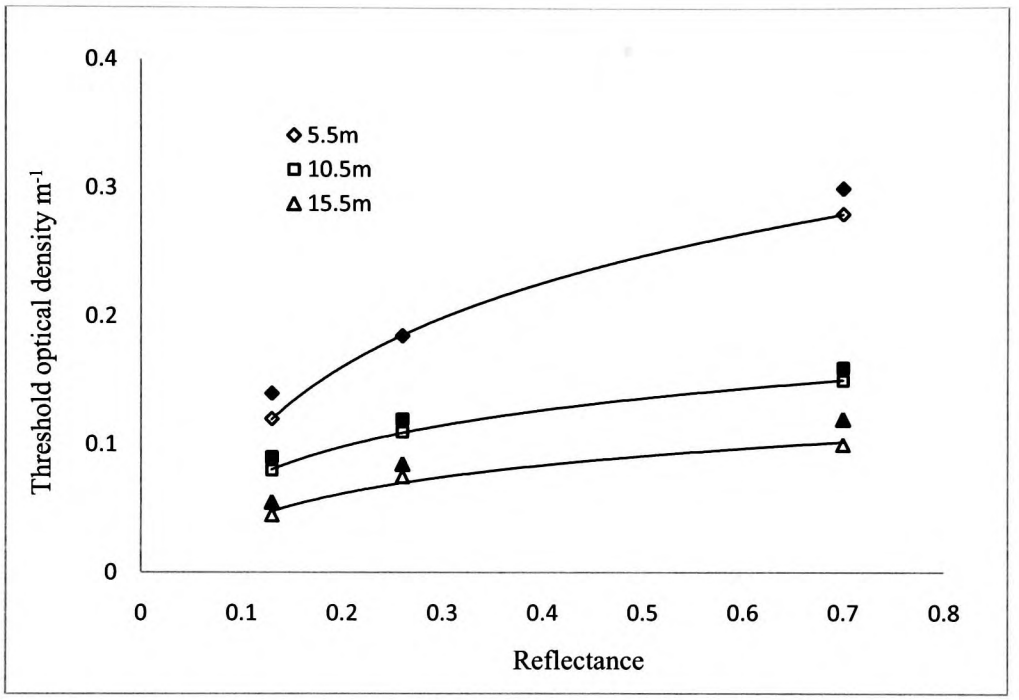

Figure 4-4 The effect of black and white smoke

It can be seen in Figure 4-3 that the threshold optical density increases with the luminance of the sign and decreases with that of the ambient light. Within the tested range, regardless the values of L_s and L_a, the visibility of the placard is uniquely determined by the ratio L_s/L_a. It has prompted Jin to use contrast as a measure of visibility (Jin T. , 2008).

Later, Jin carried further study with black and white smoke. With the similar conditions as in the previous experiment, the reflectance of the placard was changed to 0.7, 0.26 and 0.13 under illumination of 40lx. White smoke was generated by mouldering polystyrene burning at 500°C and black smoke was generated by flaming polystyrene burning at 750°C. Generally the threshold optical density in the white smoke (open symbols) was slightly smaller than that for black smoke (solid symbols) as shown in Figure 4-4 (HSE, UK, 1998) but the differences are insignificant. Therefore the results of white smoke are applicable to black smoke.

The effect of smoke irritancy on visibility was also investigated by Jin and Yamada (1985). They filled a 20m corridor with highly irritant white smoke produced by burning wood cribs and a less irritant black smoke from burning kerosene. The objects were asked to walk from one end of the corridor and read the FIRE EXIT sign at the other end. The locations at where the objects can read the sign were recorded as the obscuration thresholds. For the less irritant smoke, their data correlated according to

$$x * \sigma = const. \qquad 4\text{-}1$$

where σ is the extinction coefficient of the smoke and x is the maximum distance between the sign and location where the objects can read the sign. In irritant smoke, equation 4-1 can not hold and x was rapidly reduced when smoke density increases (see Figure 4-5). Jin and Yamada suggested that the irritating effect of thick smoke would reduce visibility beyond its physical opaqueness.

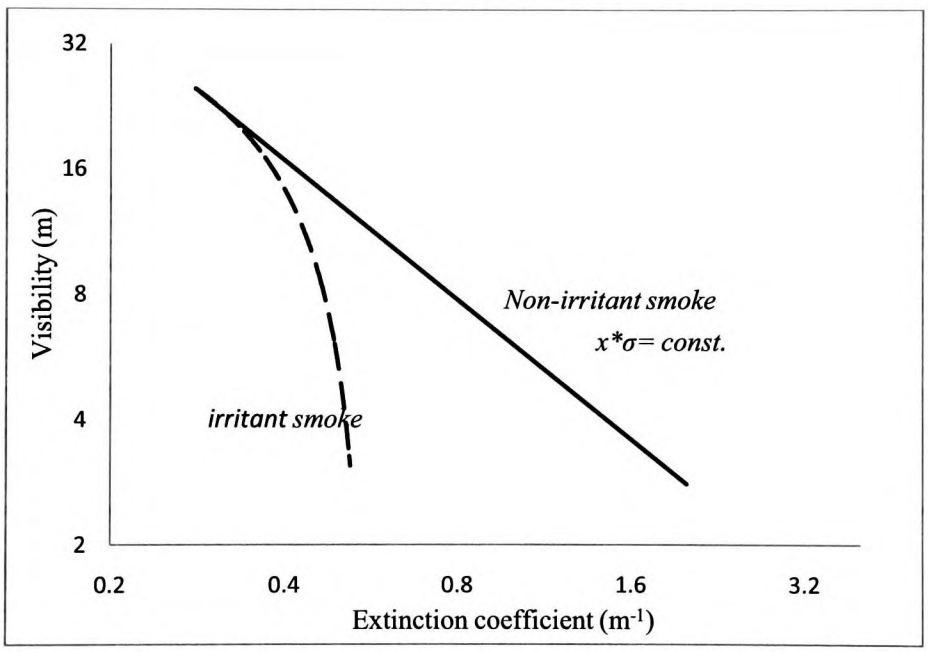

Figure 4-5 The effect of irritant smoke (Jin and Yamada, 1985)

Collins and Lerner (1983) asked 42 people to evaluate 108 different symbols under various luminance conditions. Based on the experiment, they recommended the symbol showing a person and an open door to be considered for use in the United States (Figure 4-6). It has subsequently been adopted in NFPA 170 (NFPA, 1999) .

Rea, Clark and Ouellette (1985) evaluated the visibility of thirteen exit signs using both photometric and psychophysical evaluation procedures. In their experiment, 16 volunteers made

threshold observation of the exit signs in smoke. Two of the signs were self-illuminated, while the remaining eleven were illuminated with either fluorescent or incandescent bulbs. Cosmetic oil smoke was produced by a smoke generator. The effects of sign type, threshold visibility criterion and ambient illumination were tested for 52 different conditions. In terms of the threshold visibility criterion, two visibility criteria: detectability and readability, were used during the experiment. If a sign were judged to be either detectable or readable, smoke was added to the smoke chamber until the sign was obscured. The smoke density for which a sign was just below the threshold was taken as the critical smoke density. Ambient lighting in the chamber was provided by a pair of F40 cool white fluorescent lamps which provided the ambient luminance of 75 lx at 1.5m above the floor. The luminance of the signs was also measured at several points on the sign face.

Figure 4-6 Emergency sign in NFPA 170

By analyzing the data obtained, Rea et al concluded that brighter signs were more visible in smoke. Greater brightness was required for readability than detectability. When ambient illumination was provided, sign visibility was reduced. Such effect is different for different type of signs. The presence of ambient illumination also increased the amount of sign luminance required to reach the readability threshold as compared with the detectability threshold. The authors suggested that scattered light from luminous (background) areas of a sign will reduce its readability more than its detectability. In addition, scattered light seemed to reduce the readability of low contrast signs more than high contrast signs, as well as the readability of smaller text. The red signs were slightly less affected by light scattering in the cosmetic oil smoke.

People with abnormal colour vision performed significantly poorly in the experiment. While protans[1] found the signs with the highest luminance to be more visible, their critical smoke density was markedly lower than for colour-normal observers. Analysis of the data indicated that the reduction in luminous efficiency for red signs on dark backgrounds was about 20% for protans.

In a subsequent study, Ouellette (1988) evaluated the visibility of 3 different illuminated exit signs. The main difference among the signs is the colour combination of their legend and background as shown in Table 4-1.

Sign type	Letters	Background
A	Red transilluminated	Opaque
B	Opaque	Red transilluminated
C	Red transilluminated	White transilluminated

Table 4-1

The experiment was conducted over a cylindrical smoke cavity of 1.52m in length and 0.813m in diameter. Ambient lighting inside the smoke cavity was provided by a single 10W incandescent lamp on the floor of the smoke cavity. 12 volunteers with normal eyesight age between 22 and 48 participated in the experiment. The participants were asked to report the threshold luminance under each designed experimental condition. Based on the data collected, Ouellette concluded that smoke concentration and ambient illumination strongly influence the visibility of the signs. On average, signs with white trasilluminated backgrounds required greater luminance than those with darker backgrounds. Although the 3 signs were very different in text/background combination, all of them were similar in terms of threshold luminance.

Collins, Dahir and Madrzykowski (1990, 1992) tested 12 different exit signs simutanously in smoke chamber of 9.14m x 18.9m. Real fire smoke was produced by a 100kw diffusion flame propane burner. There were 21 adult observers age between 18 and 60 years with normal or corrected eye sight participated in the experiment. Ambient illumination of 5-10lx was provided to simulate the emergency conditon. The participants observered the exit signs through a clear

[1] There are three major classes of color deficiency - protanopia, deuteranopia, and tritanopia. Protan defects are characterized by loss or alteration in the long wavelength (red) photopigment; deutan defects are characterized by loss or alteration in the medium wavelength (green) photopigment; and tritan defects (very rare) are characterized by loss or alteration in the short wavelength (blue) photopigment (Hunt, 1992).

plexiglas window under both clear and smoke conditions. They were asked not only give rating to the visibility of each sign but also making spontaneous comments on their experiences. The comments indicated that red is the preferred the colour for the exit signs. It should be point out that the comments were made by the North Americans who were accustomed to red exit signs. It was also mentioned by the authors that all the red signs had somewhat higher luminance than the green signs. The authors concluded that overall sign luminance is a primary determinant of visibility with higher luminance being associated with greater visibility. Sign configuration is also an important contributor with stencil-faced signs - signs with illuminated letters and opaque backgrounds - being somewhat more visible than panel-faced signs.

Tuomisaari (1997) measured the luminance of electrical powered and photoluminescent signs from various distances and viewing angles under both clear and smoky conditions.

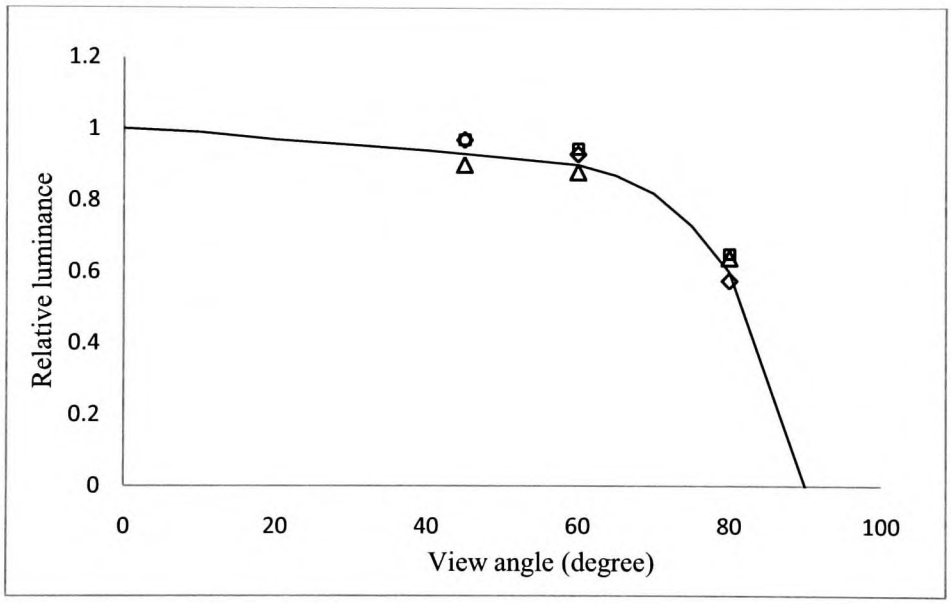

Figure 4-7 The effect of view angle on visibility (Tuomisaari, 1997)

Figure 4-7 shows the change of relative luminance with the view angle. 60% of luminance drop occurred within the last 10 degree of view angle.

The previous research work has established the following facts:

1. In a non-irritant smoke environment, for people with normal eyesight, the threshold of optical depth is a constant.
2. Smoke irritancy significantly reduces the value of the above constant.
3. The present of ambient light can reduce the visibility of a sign.

4. The angle of viewing can affect the visibility of a sign.
5. Visibility of sign can be reduced significantly among people with abnormal colour vision.

The opinions on the effect of the illumination or brightness of the sign are different among the researchers. The effect of sign colour is inconclusive. Tests have only been carried out in North America where people are used to see emergency signs in red. Even though, its effect seems to be less important.

It should be point out that all the previous researches are based on the threshold visual distance.

Chapter 5. The current experiment

5.1 Objective of the experiment

The current experiment was setup to support the concept of image based visibility in smoke laden environment. The designed experimental procedure demonstrates how visibility can be quantitatively defined and measured with physical images in digital form. The measurement has been made under various smoke, luminance and colour conditions and the results were examined to see if it can improve our understanding of visibility in smoke. The experiment also provides the data in validating the computer simulation model given in the next part of the thesis.

5.2 The scope of the experiment

The current experiment has tested the following effects on the visibility of exit sign in smoke

- Smoke concentration

  The smoke concentration various continuously in time but has been kept homogenous. The instantaneous value of smoke extinction coefficient was recorded at the same time when the photographic image was taken.

- Illumination of the exit sign

  Each experiment has been repeated with 3 different level of power input of the illuminating light source for the exit signs.

- The colour of the illuminating light

  Each experiment has also been repeated with 3 different colours: red, green and blue.

- The legend of the exit sign

  Barcodes, text and standard emergency signs have been tested under different smoke, illumination and colour conditions.

5.3 Limitations of the experiment

1. No combustion generated smoke has been tested.

2. Only smoke under homogenous condition has been tested.
3. All signs tested were internally illuminated. No reflective sign has been tested.
4. The dynamic range of digital camera output was limited to 16bit per colour channel. The maximum pixel value is 65504. Any value larger than that would be cut off. For certain light source output, it was necessary to keep the camera exposure short enough to avoid the overflow of pixel value.
5. The LED light source output is intermittent. It requires the camera exposure to be long enough in order to avoid the camera output from fluctuation. It requires the aperture of the camera to be controlled so that the result does not fluctuate and at same time the pixel values are within the dynamic range of the camera.

5.4 The smoke tunnel

A simple rectangular smoke tunnel shown was built to achieve the objective and cover the scope of the current experiment laid out in sections 5.1 and 5.2. The tunnel has been built with aluminium sheets bolted on aluminium frame. The internal dimension of the tunnel is $1.0x1.0x4.0m^3$ so that the longitudinal distance is sufficient to give large optical depth of the smoke and the surface reflection of the aluminium sheets will not affect light scattering around the longitudinal centre line of the tunnel.

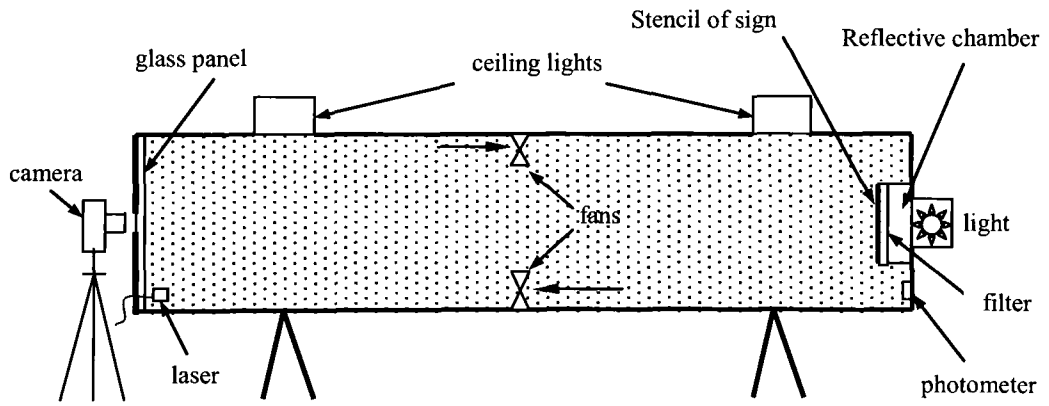

Figure 5-1 The smoke tunnel

At the far end of the longitudinal centre line is the illuminated sign to be tested. The sign consists of a LED light source and a reflective chamber. The size of the reflective chamber was $0.06x0.12x0.15m^3$. In front of the chamber, there were two layers of sanded Perspex-sheet filter to make the luminance over the sign more uniform. The sign is a stencil mask attached to the filter. The light source was mounted outside the tunnel and the light shining in the chamber

through a circular window of 0.12m in diameter. Apart from the circular window and the surface of the filter, the rest area of the chamber was covered with aluminium foil. The foil was made uneven to further diffuse the light. The near end of the tunnel was sealed by glass panel and covered with non-transparent curtain. A small circular window having the same diameter as the camera lens has been opened on the curtain for the camera to see through. Due to the limitation of non-combustion smoke, the tunnel was filled with misty smoke produced with ACME HPLine smoke fluid from a Magnum KAM KSM1100 smoke generator. It should be mentioned that although the experimental results with the misty smoke can serve the purpose of validating simulation model, it should not be expected to be the same as that of soot smoke. Figure 5-2 is a photo of the tunnel without the glass panel.

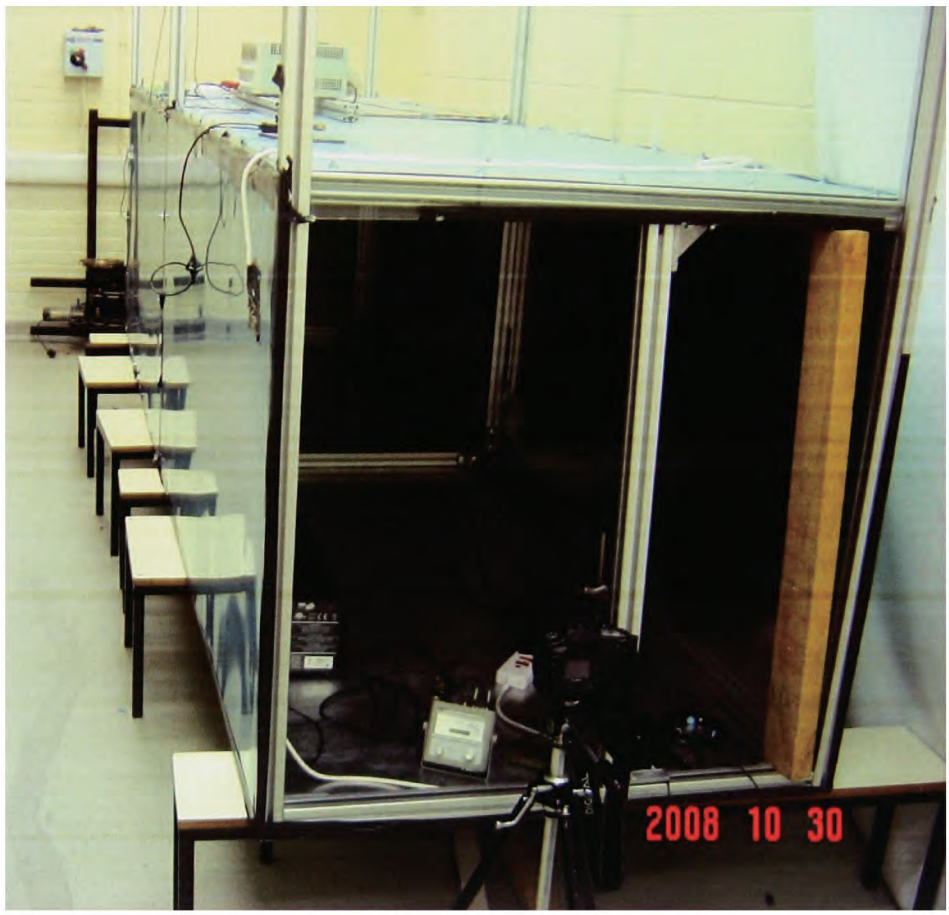

Figure 5-2 The smoke tunnel

The homogeneity of smoke field inside the tunnel has been achieved by fixing two ventilation fans at the bottom left and top right corners of the middle cross section of the tunnel and keeping the smoke well ventilated. The smoke tunnel was incompletely sealed so that the

average smoke concentration inside the tunnel decreased in a very slow pace that was measurable over tens of seconds.

5.5 The light sources

The light source of the sign is a 12W LED stage light with 16 red, 16 green and 16 blue LEDs. The power input of the light source can be set in 3 levels. Level 1 is the full power. Level 2 is about half of it and Level 3 is about a quarter. The light has been filtered through a number of white sanded Perspex-sheet filters to improve the uniformity of its output. Figure 5-3 shows the spectrum of the light source. Each curve in Figure 5-3 represents the spectrum of the light with only the LEDs of a single colour being switched on at full power (level 1). The peak values of red, green and blue light appear at wavelength 638, 523 and 463 nm respectively. The ratio of the areas covered by each spectra curve is 0.23:0.3:0.47. Under clear condition the mixture of the 3 colour is pale white.

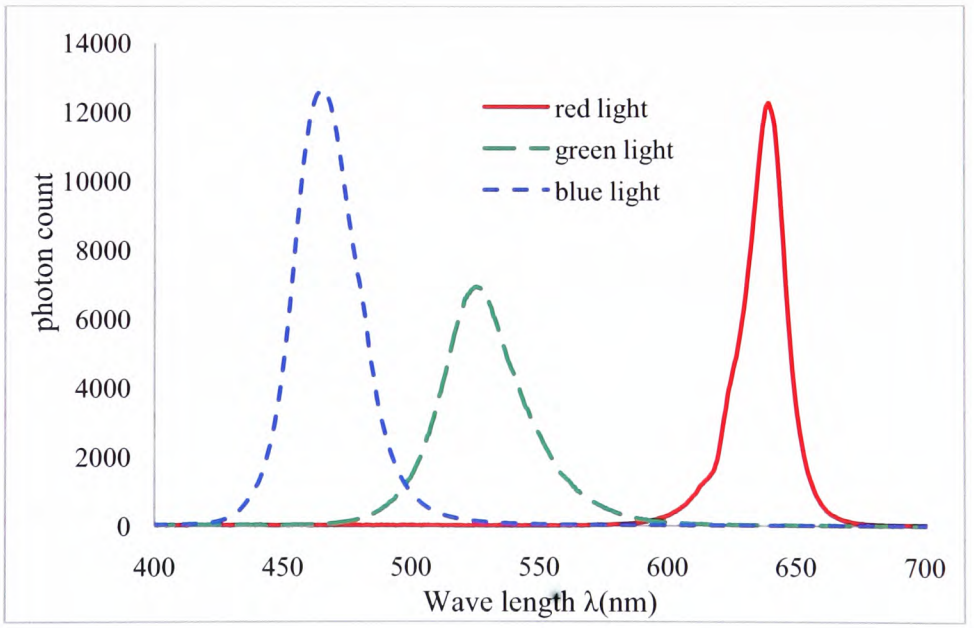

Figure 5-3 Spectrum of the light source of sign

Since light from the LEDs has been filtered with Perspex of unknown optical property, the power output of the light source needs to be measured in order to set the boundary condition. It has been done with the photometer as shown in Figure 5-4. The photometer is located at 4.0 meters at the near end of the empty tunnel without the sealing glass. The surface of the

photometer is parallel to the surface of the sign. The line of sight between the photometer and the sign is perpendicular to both. The lens of the camera is put in front of the photometer. The setup is shown in Figure 6-1(a). The round stencil sign used is also the same as in section 6.1. In total darkness the image of the light source can be focused on the photometer. The following assumptions were made in this measurement.

1. The dimension of the light source is small comparing with the distance between the light source and the camera lens. Therefore the solid angle extended by the surface of the lens and any point on the surface of the sign can be treated as a constant.
2. The light emission of the sign is constant over its surface.

From these two assumptions, the emission of the light source is related to the radiant power measured with the photometer by

$$\phi = c_{lens} e A \Delta\omega \qquad 5\text{-}1$$

where e is the light emission of the sign. c_{lens} is the efficiency of the lens. A is the area of the sign and $\Delta\omega$ is the solid angle defined by the area of the aperture A_{lens} and the distance x between the light source and the surface of the lens.

$$\Delta\omega = \frac{A_{lens}}{x^2} \qquad 5\text{-}2$$

Colour	Red	Green
Power level 2	**0.65**	**0.98**
Power level 3	0.31	0.37

Table 5-1 Power emission of light sources (Watt/sr*m^2)

The result of the measurement is given in Table 5-1. It should be aware that in Table 5-1 only the red and green light at power level 2 and 3 are measured in the experiment due to the limitation of the photometer power range (< 50mWatt).

The ceiling lights are the similar LED stage light but the LED units are bigger and more powerful (16W). Its spectrum is shown in Figure 5-5. There are two peaks for each channel. A single filter has been applied to the ceiling lights in order to make its luminance more uniformly distributed. For each ceiling light, a window of 8x8cm^2 is opened in the middle of the tunnel ceiling. The windows are located at 1.0m from each end of the tunnel (see Figure 5-6).

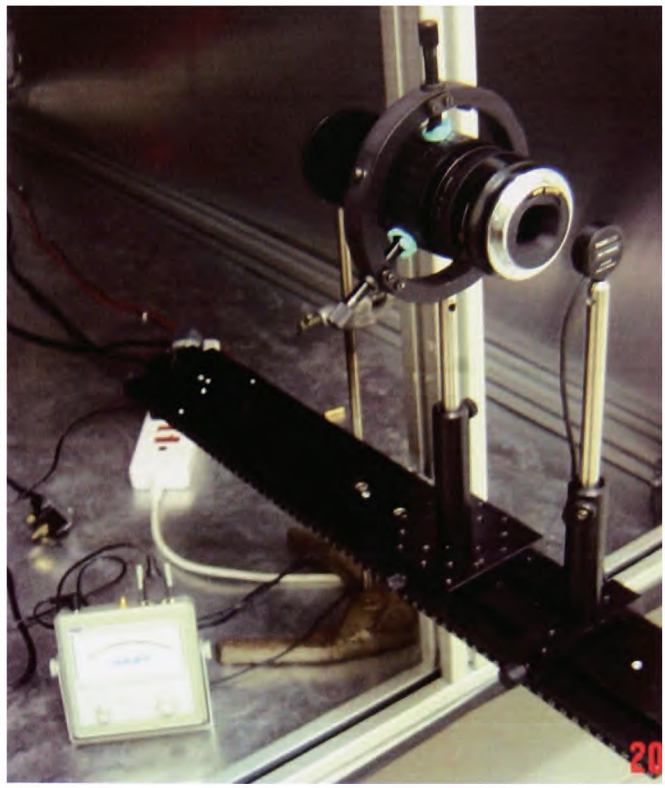

Figure 5-4 Measuring output of light source

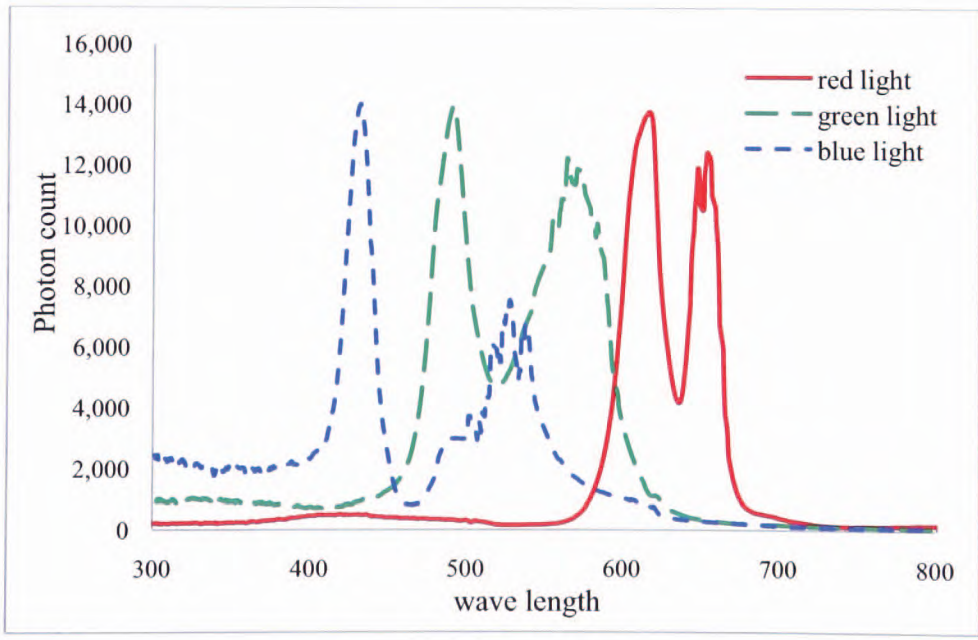

Figure 5-5 Spectrum of ceiling light

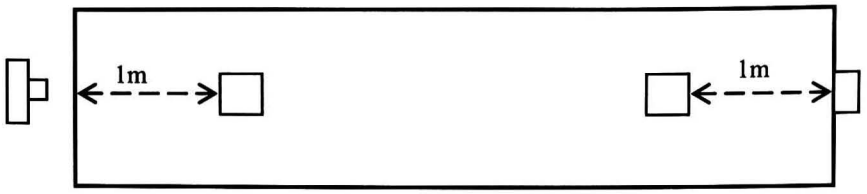

Figure 5-6 Top view of the smoke tunnel

5.6 Measurement of optical depth

As the smoke in the tunnel is homogeneous, it was convenient to measure the optical depth and used it as a parameter in comparing experimental data. A pair of red laser diode and photometer has been used to measure the optical depth defined as

$$\tau = \sigma x = \ln(\Phi_0/\Phi) \qquad 5\text{-}3$$

where Φ is the power of laser beam read from the photometer and Φ_0 is that before smoke was introduced into the tunnel. x is the distance from the laser to the photometer. Lambert-Beer's law has been applied since the laser beam was only attenuated by the smoke.

Chapter 6. Image generation in the current experiment

Digital camera is the most effective equipment to record, store and share images. In the current study, it has been used just for such purpose. This chapter describes how a particular camera should be calibrated and the photographs are converted into the perceived images that are required for measuring visibility. It explains the principle and the procedure of the conversion. The final formulae and the constants might be different from one kind of camera to another.

6.1 Camera calibration

A digital camera is an array of photoelectric sensors. Each of the sensor measures light fallen on it and converts the radiant energy received into electronic signal to be stored as pixel values. In most digital colour cameras, each pixel records light using 3 or more sensors. Each sensor measures light within certain range of wavelength, typically in red, green and blue colour band respectively. It is the so called RGB model. The general form of the model is given by (Fu, et al., 2006)

$$i_\eta = \psi_\eta\left(g\frac{\Delta t}{F^2}\int_0^\infty s_\eta(\lambda)L(\lambda)d\lambda\right)+n_\eta \qquad 6\text{-}1$$

where i_η is the pixel value in channel η (η=R, G or B), $L(\lambda)$ is the spectral distribution of radiance from light source at wavelength λ, g is a geometrical factor. Δt is the camera exposure. F is the aperture. ψ_η is the intensity response function in channel η and $s_\eta(\lambda)$ is the combined spectral sensitivity of image-optics, colour-filter and the sensor in channel η. Camera calibration is to determine ψ_η and $s_\eta(\lambda)$ for a particular camera. n_η in 6-1 is the dark noise in channel η and can be determined by the photograph taken when the lens is covered. In the current study, it has been found that the maximum value of n_η is less than 50 but the minimum visible pixel value is above 5000. Therefore n_η has been ignored in the following discussion.

6.1.1 The camera

The camera used in this experiment is a commercial Canon EOS10D SLR camera with Canon EF 100-300mm zoom lens. The diameter of the lens is 58mm and the maximum aperture is

1:5.6. There is a UV filter in front of the lens for protection. Table 6-1 gives the camera parameters used in the current experiment

Focal length	100-300mm	**ISO**	200
Aperture	5.6 – 22	**Sensor size**	22.7mm x 15.1mm
Image size (output)	3088 x 2056 (6.3million)	**Sensor type**	CMOS
Image size (full)	3152 x 2068		

Table 6-1

The camera image was written in raw format (CRW format for the Canon 10E camera used here) and processed with the freeware image reader ImageJ.

6.1.2 Efficiency of the lens

The lens and the UV filter attached to it cause the attenuation of the incoming light. The loss is determined by the efficiency of the lens. In the experiment, it has been measured with low power red laser (5mWatt, λ=653nm). At first, the intensity I_0 of the laser was directly measured with the photometer. Then the same laser beam was shining through the lens and the photometer reading, say I, was taken on the other side of the lens. The efficiency of the lens is the ratio I/I_0. The result has shown the value of 0.64. In the current study, it was assumed that the efficiency of the lens is independent of wavelength and aperture.

6.1.3 Linearity of intensity response function ψ_η

The parameter ψ_η in expression 6-1 represents the response of camera to the change of light intensity. It would be different for each colour channel. In most applications, what is more important would be to know the linearity of ψ_η instead of its value. In other words, for a fixed light source, the colour spectrum of the light is constant, therefore the sensor of a digital camera should respond linearly to the irradiance of light. In the current experiment, it means

$$\int_0^\infty s_\eta(\lambda)L(\lambda)d\lambda = const. \qquad 6\text{-}2$$

The normalisation factor has been merged into ψ_η. Keeping the spectrum constant can be achieved in different ways with the LED light. One way is to change the number of LEDs. Assuming that all the LED bulbs are the same, changing the number of LED bulb will only change the total output intensity without altering the light spectrum. The LED light installed as the back light of the sign is capable of changing into 3 different levels by switching on/off some of the bulbs. Alternatively this can be achieved by adjusting the combination of aperture and exposure of the camera. The irradiance on the sensor is in proportion to $\Delta t F^{-2}$. Figure 6-1

shows the setup of the experiment. In this setup, a circular sign of 0.09m in diameter was employed as in Figure 6-2.

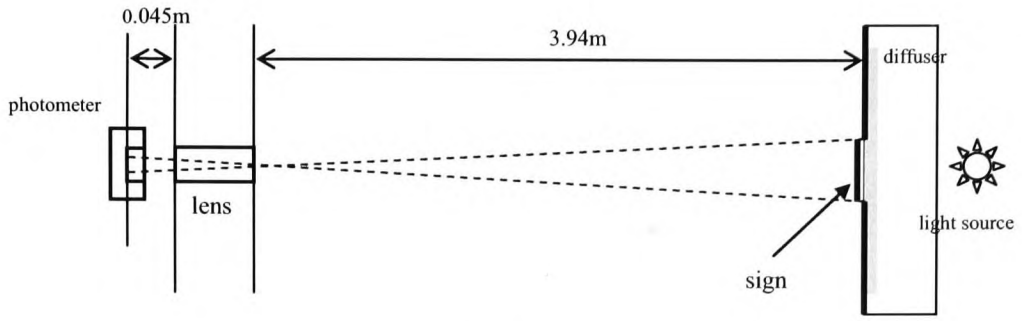

(a)

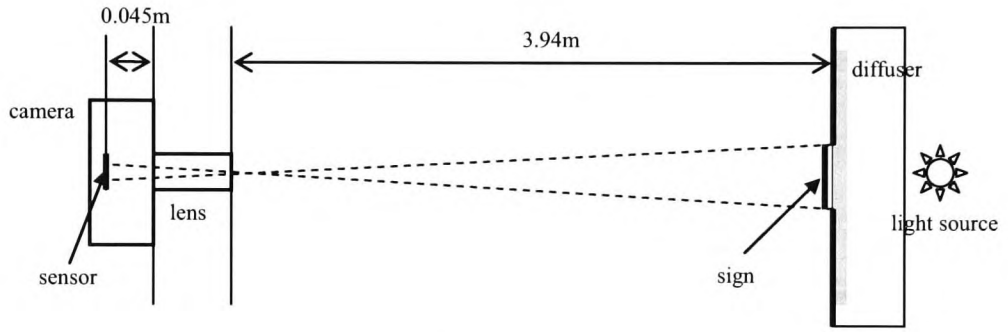

(b)

Figure 6-1 Camera calibration

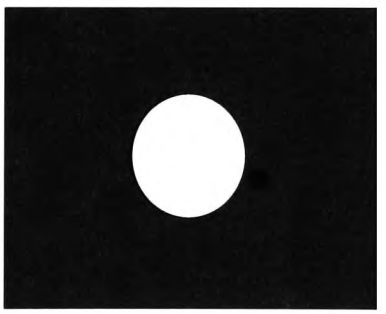

Figure 6-2

In Figure 6-1(a), the camera lens is dismounted from the camera body and held against the sign at a distance of 3.94m. The photometer is positioned at the same location as the sensor of the camera (for Canon EOS10D, it is 0.045m from the mounting surface of the camera lens). With

the maximum focal length of the zoom set to 300mm, the focused image of the target light source falls entirely within the sensor area of the photometer. The photometer records the total power of the incident light.

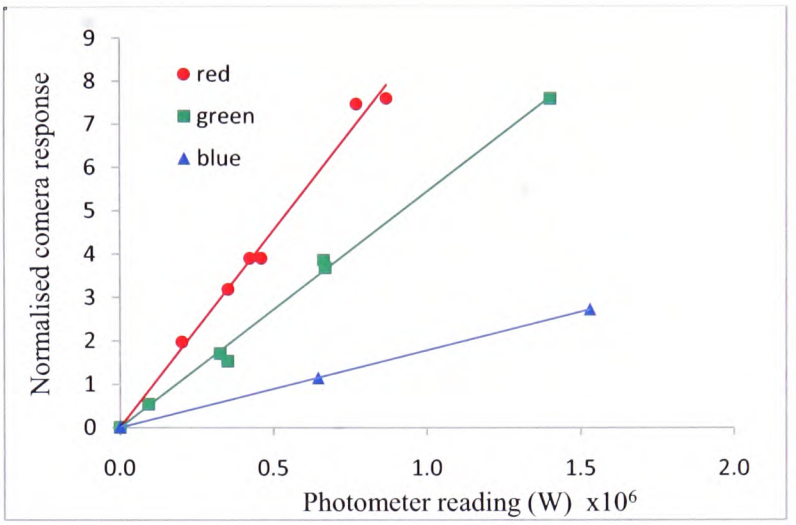

Figure 6-3 Linear response of the camera sensor

In Figure 6-1(b), the body of the camera is reattached to the lens that is held at exactly the same position as in Figure 6-1(a). A digital photograph of the same image is taken. The above procedure was repeated with different power output of the light source and $\Delta t F^{-2}$ values. Figure 6-3 shows the relation between the averaged pixel value and the corresponding photometer reading. The 3 lines represent the results with red, green and blue light respectively.

6.1.4 Spectral sensitivity $s_i(\lambda)$

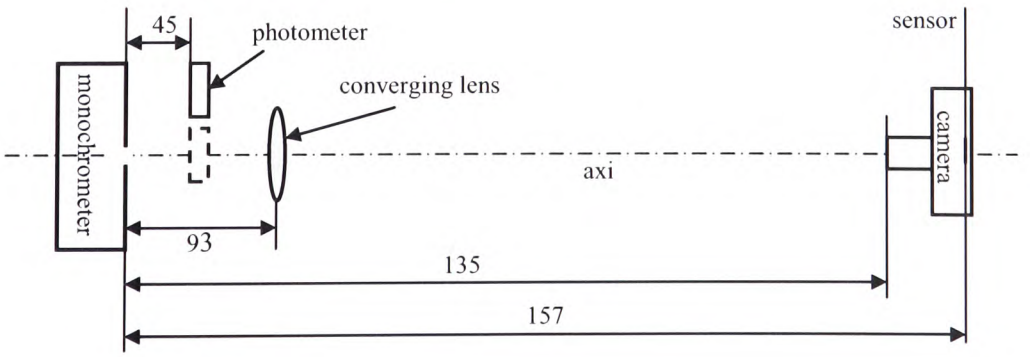

Figure 6-4

Although the intensity response of the camera is linear, its response to the spectral change may not be so simple. In order to understand how the camera sensor responds to light of different colour, a monochromator is used as the light source.

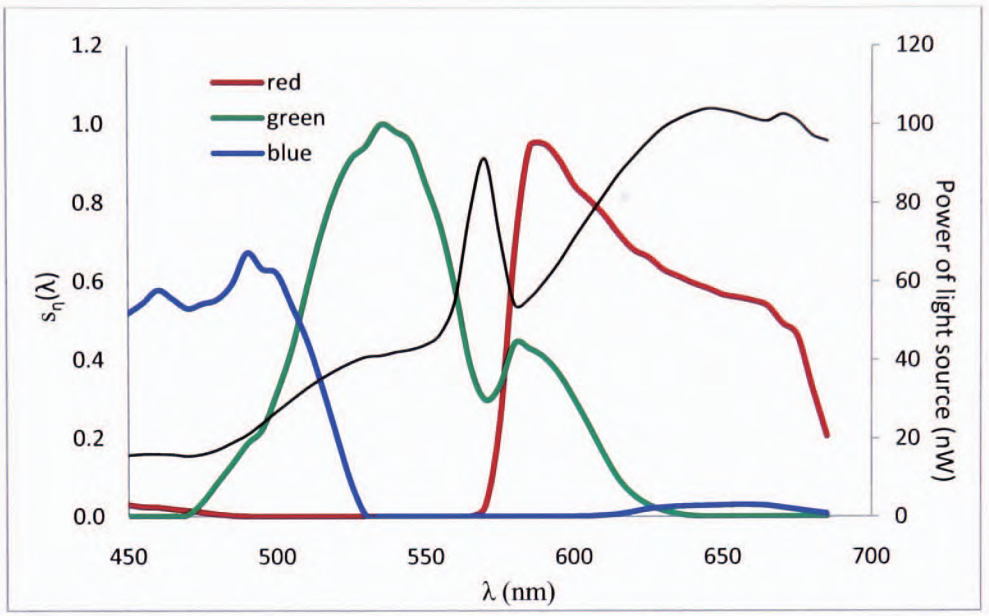

Figure 6-5 Camera calibration curves

The experimental setup is shown in Figure 6-4. A photometer is used to measure the intensity of the light from the slit of the monochromator. When it is positioned in front of the monochromator slit, it measures the output of the monochromator. Otherwise, it measures the background radiation. The converging lens converts the output light of the monochromator so that it would be parallel to the axis. The spectral range of the measurement covers the visible spectrum between 450-685nm. In order to measure $s_i(\lambda)$, equation 6-1 is written over an incremental of wave length $\Delta\lambda_j$ as

$$i_\eta(\lambda_j) = \psi_\eta g \frac{\Delta t}{F^2} s_\eta(\lambda_j) L(\lambda_j) \Delta\lambda_j \qquad 6\text{-}3$$

In the current study, $\Delta\lambda_j$ is uniformly distributed as $\Delta\lambda$=5nm over the entire measured spectrum. The camera ISO number, aperture and exposure are also kept constant as 200, F5.6 and 1/15s respectively. Under such conditions, equation 6-3 can be written as

$$s_\eta(\lambda) = \xi_\eta \frac{i_\eta(\lambda)}{\Phi(\lambda)} \qquad 6\text{-}4$$

Where $\Phi(\lambda)$ is the power measured by the photometer (minus background radiation) that is proportional to $L(\lambda)$. ξ_η is a constant for each channel. The subscript j is omitted.

Expression 6-4 means that for each camera, the difference of $s_\eta(\lambda)$ obtained under different measuring conditions is only the constant ξ_η. Figure 6-5 shows the $s_\eta(\lambda)$ of the Canon EOS10D camera obtained in the current experiment.

6.2 Transformation from photograph to perceived image

In section 3.5, visibility has been defined as human imaginary perception. Its formation could be depicted as the (light source) – (objects) – (perceived image) process in Figure 6-6. The current study is an attempt to simulate such process and quantify the perceived image as brain stimuli. It would be a necessary step toward the prediction of decision making process in the simulation of human behaviour.

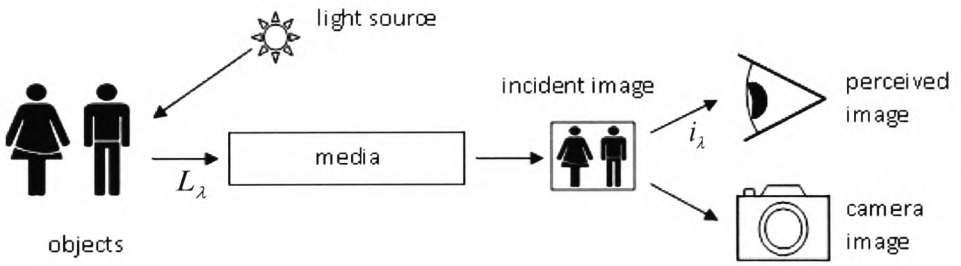

Figure 6-6

The relation between the spectra luminance i_λ reached the eye and the spectra radiance of the light source L_λ can be expressed as

$$i_\lambda = \Gamma_\lambda(L_\lambda) \qquad 6\text{-}5$$

where Γ_λ represents the spectra conversion operator. In equation 6-5, Γ_λ consists of two operators. The first operator $\Gamma_{rad,\lambda}$ represents light transmission through media and the second operator $\Gamma_{eye,\lambda}$ generates the perceived image. The two operators are applied to light in the following sequence.

$$L_{\lambda,i} = \Gamma_{rad,\lambda}(L_\lambda) \qquad 6\text{-}6$$

and

$$i_\lambda = \Gamma_{eye,\lambda}(L_{\lambda,i}) \qquad 6\text{-}7$$

where $L_{\lambda,i}$ is the radiance of the incident light reaching the eye at wavelength λ.

As shown in Figure 6-6, the first operator $\Gamma_{rad,\lambda}$ is a process that is determined by the geometrical/physical conditions of the process regardless who is the observer of the target. However the second process is solely dependent on the observer or the receiver of the transmitted light. In order to make quantitative assessment of visibility, $\Gamma_{eye,\lambda}$ is substituted by the operator representing a quantification device in the experiment. In the case of digital camera, the operator would be $\Gamma_{camera,\lambda}$ and expression 6-7 would be

$$i_{c,\lambda} = \Gamma_{camera,\lambda}(L_{\lambda,i}) \qquad 6\text{-}8$$

where $i_{c,\lambda}$ represents the pixel reading of the camera image. If the inverse operator of $\Gamma_{camera,\lambda}$ exits and is denoted as $\Gamma^{-1}_{camera,\lambda}$ then

$$L_{\lambda,i} = \Gamma^{-1}_{camera,\lambda}(i_{c,\lambda}) \qquad 6\text{-}9$$

offers the opportunity to convert the camera image into a perceived image that can also be quantified if both $\Gamma^{-1}_{camera,\lambda}$ and $\Gamma_{eye,\lambda}$ represent simple (monotonic) image mapping.

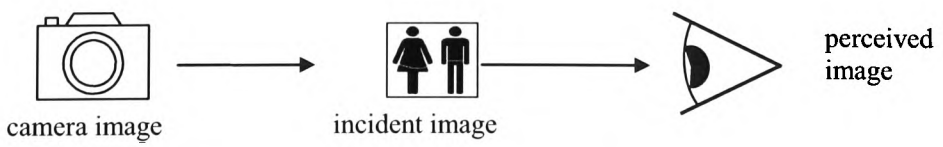

Figure 6-7

Mathematically, the process in Figure 6-6 can be expressed as

$$i_\lambda = \Gamma_{eye,\lambda}\left(\Gamma^{-1}_{camera,\lambda}(i_{c,\lambda})\right) \qquad 6\text{-}10$$

From the discussion in section 3.3, the spectra conversion $\Gamma_{eye,\lambda}$ is the luminosity function $\bar{y}_\lambda$.

$$i_\lambda = \bar{y}_\lambda L_{\lambda,i} \qquad 6\text{-}11$$

[1]

In a real digital camera, the sensor receives the incident light through 3 colour channels. Each channel is sensitive to certain section of the spectrum. Figure 6-5 shows the sensitivity of each channel for the Canon EOS10D camera. Instead of i_λ the image output of the sensor satisfies the following integration

$$i_{c,\eta} = \left[\int_0^\infty \Gamma_{camera,\lambda}(L_{\lambda,i})d\lambda\right]_\eta \qquad 6\text{-}12$$

where the subscript η represents one of the colour channels. $\Gamma_{camera,\lambda}$ is the camera response curves shown in Figure 6-5. There are as many conversion operators like 6-12 as the number of colour channels. In section 6.1.3, it has been experimentally proven that the relation between $i_{c,\eta}$ and $\int_0^\infty L_{\lambda,i}d\lambda$ is linear for the current camera. Therefore there is a constant ψ_η that satisfy the following equation

$$i_{c,\eta} = \left[\int_0^\infty \Gamma_{camera,\lambda}(L_{\lambda,i})d\lambda\right]_\eta = \psi_\eta\left[\int_0^\infty L_{\lambda,i}d\lambda\right]_\eta \qquad 6\text{-}13$$

If none of the conversion operator changes light spectrum, then

$$\frac{\int_0^\infty \bar{y}_\lambda L_\lambda d\lambda}{\int_0^\infty L_\lambda d\lambda} = c_y \qquad 6\text{-}14$$

where c_y is a constant that does not change between the light source and the eye.

[1] A constant of 683 has been omitted here.

The approximation of the perceived luminance reached the eye within colour channel η can be expressed as

$$
\begin{aligned}
i_\eta &= \left[\int_0^\infty i_\lambda d\lambda\right]_\eta \\
&= \left[\int_0^\infty \bar{y}_\lambda L_{\lambda,i} d\lambda\right]_\eta \\
&= \left[c_y \int_0^\infty L_{\lambda,i} d\lambda\right]_\eta \\
&= \frac{c_{y,\eta}}{\psi_\eta} i_{c,\eta}
\end{aligned}
\qquad 6\text{-}15
$$

For polychromatic light, the total perceived luminance would be

$$
i = \sum_\eta i_\eta \qquad 6\text{-}16
$$

In 6-15, ψ_η and $c_{y,\eta}$ can be determined by applying 6-13 and 6-14 to the light source and carrying out numerical integration. For the current light source and camera, $c_{y,\eta}$ and ψ_η are given in Table 6-2.

	Red	**Green**	**Blue**
$c_{y,\eta}$	0.218	0.744	0.1
ψ_η	0.6	0.75	0.5

Table 6-2

It should be mentioned that the value of ψ_η is not fixed but the ratio among all the channel is. Different sets of ψ_η corresponding to lights with the same spectrum but different intensity.

6.3 Summary

Since the response of a digital camera is different from that of human eye, a numerical procedure has been created to extract the perceived image from photograph taken with a digital camera. The procedure has been based on experimental data for camera calibration. Although the result is for Canon EOS10D, the procedure would be generally applicable to most commercial digital camera. The basic requirements are that the camera responds linearly to the change of light intensity and the spectra response function of the camera, $s_\eta(\lambda)$, is known. The

accuracy of the procedure depends on the number of colour channels the camera has. At the moment, it is limited to 3 (the RGB model).

Chapter 7. Measurement of visibility in the current experiment

7.1 Image contrast defined in the context of digital image

Unlike existing visibility measurement, such as that offered by Jin (1978), which relies on the geometry and physical boundary conditions of light transmission, the current study aims at establishing a visibility measurement that is based on the result image regardless how light has been transmitted into the receiver/image generator. Therefore it is important to build a procedure in quantifying the images acquired by the receiver, in most cases, the digital camera.

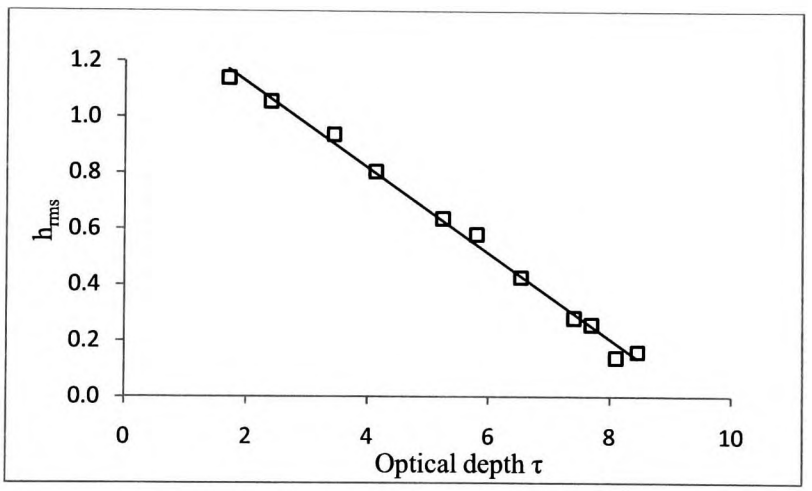

Figure 7-1 RMS contrast for red square viewed through smoke

In processing an image, the first quantity encountered is its contrast. Among existing definitions of contrast as reviewed in section 3.4, the RMS contrast in section 3.4.3 is the only one that satisfies our requirement and therefore adopted in the current study. The radiance in expression 3-8 is replaced with the pixel reading i. In the current study, L_n in 3-8 is taken as the mean pixel value plus a fraction of the standard deviation. In this way, the RMS contrast is expressed as

$$h_{rms} = \frac{\sigma_{std}}{i_{mean} + \alpha\sigma_{std}} \qquad 7\text{-}1$$

where α is a constant. As the first approach, its value is set to 0.5. For signage in fire safety engineering, it is not very interesting to study the case that i_{mean} is close to zero. Therefore a good estimation of the statistic maximum of i would be in the order of $(i_{mean} + 0.5\sigma_{std})$. Figure 7-1 shows the change of h_{rms} vs. optical depth τ for a red square sign (Figure 7-2). It can be seen that h_{rms} is linearly decreasing as τ increases.

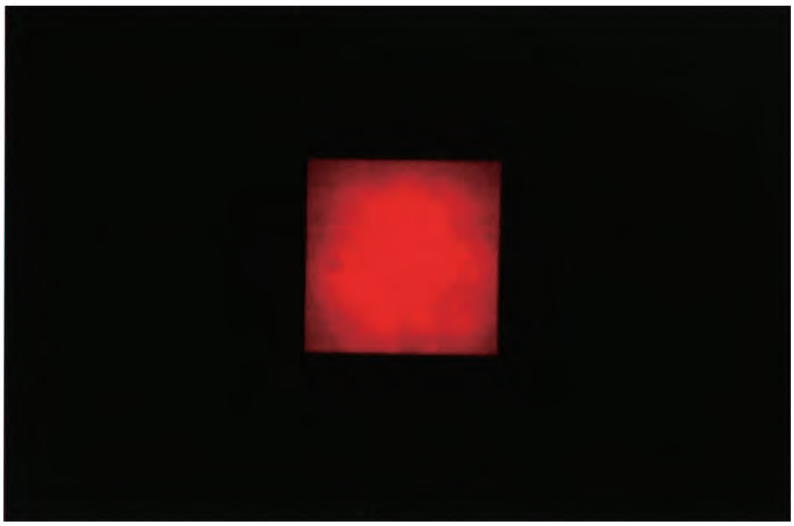

Figure 7-2 A square mask over the light source

According to Lambert-Beer's law, the average image intensity will decrease exponentially with τ. If there is no scattered light reaching the image sensor (e.g. light extinction is purely the result of absorption), σ_{std} should follow exactly the same exponential function as the average image intensity. In the current case, scattered light does exist and reaches the images sensor so that more blurred images are expected. In other words, σ_{std} decreases faster than the average value of image intensity. It is indeed the case as shown by the fitted functions in Figure 7-3 and Figure 7-4.

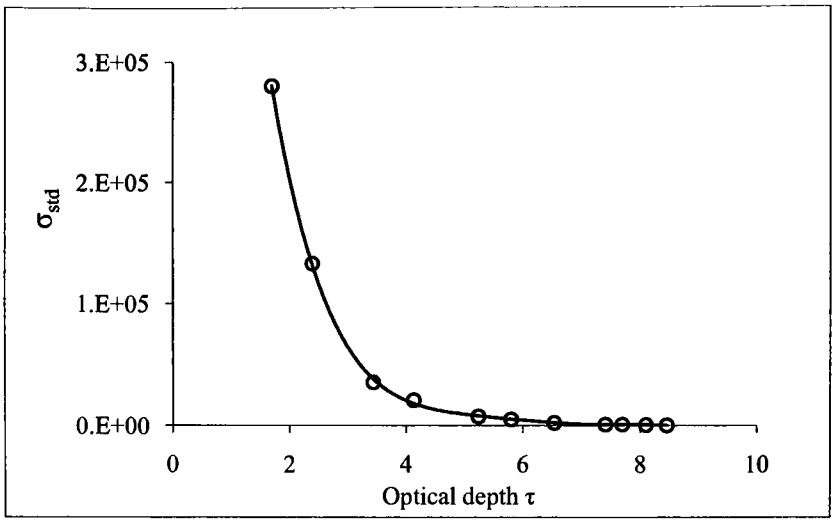

Figure 7-3 Standard deviation of image intensity

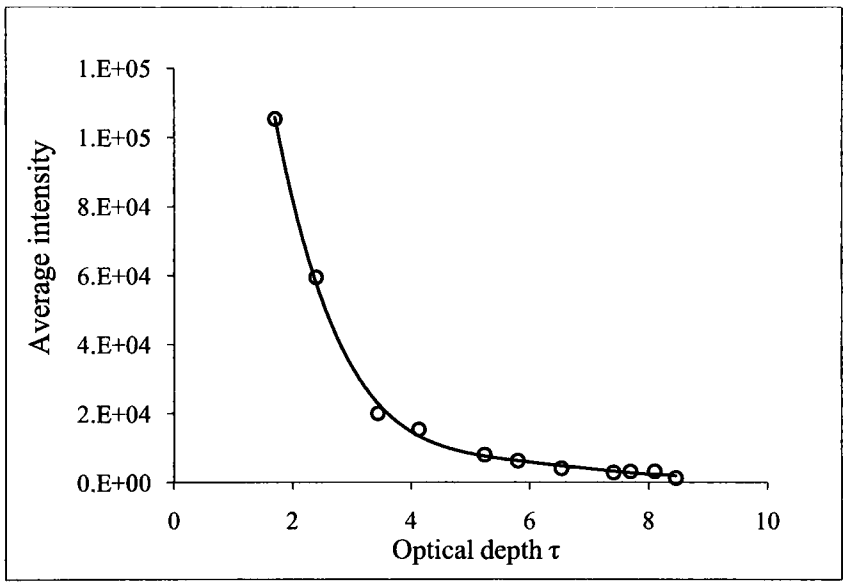

Figure 7-4 Average value of image intensity

7.2 Visibility estimated from images

In section 3.5, it has been seen that visibility can be expressed in terms of a function of the characteristics of the image. Under the current experimental condition, the proposed function F in equation 3-9 for an individual colour channel is given as

$$F_\eta = h_{rms,\eta}\tilde{\phi}_\eta c_{y,\eta} \qquad 7\text{-}2$$

where $\tilde{\phi}$ is the normalised mean brightness (pixel value) of the image. For the images in the current study, the normalised form of $\tilde{\phi}$ is

$$\tilde{\phi}_\eta = \frac{\beta}{\psi_\eta t_{\exp} \Delta D} i_{mean,\eta} \qquad 7\text{-}3$$

where ΔD is the dynamic range of the camera. For most of the modern commercial digital camera, it is 65535 for each colour channel. $t_{\exp}$ is the camera exposure and β is the aperture area ratio of the camera. It is given by dividing the camera aperture stop a by a nominal aperture stop. In the current study it has been taken as the largest aperture f/5.6 (representing an aperture area of $2.254 \times 10^{-03} m^2$). Therefore

$$\beta = \left(\frac{a}{5.6} \right)^2 \qquad 7\text{-}4$$

For images formed by mixed colour, visibility is defined the same way as that for a single colour channel.

$$F = h_{rms} \tilde{\phi} c_y \qquad 7\text{-}5$$

In 7-5, ψ_η and $c_{y,\eta}$ are replaced by ψ and c_y. Both are the results of integrations over the entire spectrum of the light source.

7.3 Measurement of visibility in smoke tunnel

Various signs have been experimentally studied in the current experiment to evaluate the visibility of them under both clear and smoke conditions. Table 7-1 gives an approximated guidance on the relative importance of different factors that influence the visibility of a sign. Based on this guidance, the following parameters are chosen to be tested.

1. Light intensity of the sign.
2. Optical depth τ.
3. Colour of sign.
4. Ambient lighting.
5. The form of the sign:

a. Thickness of sign strokes.

b. Stencil against translucent sign.

In most cases, the performances of the above parameters are expressed in V-τ charts where V is the visibility defined in section 3.5 and τ is the optical depth. Table 7-2 shows the test matrix.

Smoke properties	Sign luminance	Distance	Ambient light	Sign colour	Legend	Sign size	View angle	Stroke width
5	4	4	3	3	2	2	2	1

Table 7-1

Smoke		Yes																	
Ceiling light		No									Yes								
Colour channel of sign		R			G			b			R			g			b		
Intensity of sign(%)		25	50	100	25	50	100	25	50	100	25	50	100	25	50	100	25	50	100
Square sign				x			x			x			x						
Circular sign				x			x			x									
Exit sign				x			x			x									
Bar code	2:1	x	x	x	x	x	x	x	x	x									
	1.5:1	x	x	x	x	x	x	x	x	x					x	x		x	x
	1:1	x	x	x	x	x	x	x	x	x		x	x						
	0.5:1	x	x	x	x	x	x	x	x	x		x	x		x	x		x	x

Table 7-2

7.4 The experimental procedure

Each experiment session starts with the smoke tunnel free from any trace of smoke. The laser-photometer pair would be adjusted to get the maximum photometer reading at the given distance. The sensor of the photometer is fixed to the end panel of the tunnel and the laser is supported by a frame with very heavy base seating on the bottom of the tunnel. The arrangement is to ensure the stable reading of the photometer even under the influence of vibration caused by the smoke generator and ventilation fans.

After close the glass door, black sugar paper blind is used to seal the tunnel from any other light source. A circular window the same diameter as the camera lens is open to the camera. After

switching on the light source of the sign, photo images of the sign under clear condition will be taken for comparison.

The smoke generator and the two ventilation fans are switched on and the tunnel is gradually filled with smoke until the sign has completely disappeared then stop the smoke generator but leave the fans running. Wait for a short while (few seconds) so that the smoke concentration would become uniform. At this point, the laser is switched on and the first photometer reading is taken. Immediately after taking the photometer reading, switch off the laser and take the photograph of the sign. The procedure is repeated for every 10-20 seconds. At each incident, the laser beam must be switched off before the photograph is taken to ensure no light scattering from the laser beam interferes with the photographic image.

7.5 Summary

This chapter describes the details of the experiment procedure in the smoke tunnel. The examined parameters that are believed to be influential for the visibility of an illuminated sign have been listed in the form of test matrix. In section 3.5, the concept of image based visibility was explained and it has been said that its exact expression would be application specific. In this chapter, the expression of visibility in the assessment of digital photographic image has been proposed. This expression will be applied in the analysis of experimental data in the next chapter.

Chapter 8. The experimental results

In this chapter, the measurements of visibility in the smoke tunnel will be presented. The effects of various factors such as the smoke concentration, luminance of sign as well as ambient illumination are examined. Conclusions based on the analysis of the experimental results will be compared with that in previous research.

8.1 Visibility of barcodes sign

Most emergency exit signs are composed with text or the mixture of text and figure as shown in Figure 8-1. Despite illumination, language, colour and size, the texture composition of the sign, or the legend, is also important. It is obvious that under the same environmental condition, the first sign in Figure 8-1, as proposed by Collins and Lerner (1983), is easier to be identified than the second and the last. The difference lies in the pattern, stroke and spaces between the strokes.

Figure 8-1 Examples of emergency sign

In the current study, a series of barcode signs of different stroke thickness and intervals are first studied to see their effect on visibility in combination with colour and luminance. Table 8-1 is the list of the barcodes used in the current study. Each barcode is shown in a row in the table with its aspect ratio, the width of its transparent bar and its opaque interval and the total width of the barcode. The aspect ratio of a barcode is defined as:

$$\frac{Width\ of\ tranparent\ bar}{Width\ of\ opaque\ \text{int}\ erval} \qquad 8\text{-}1$$

All the barcodes are the same height of 9.0cm.

Height	9											
Aspect		■		■		■		■		■		**Total width**
2.0 : 1.0	2.0	1.0	2.0	1.0	2.0							8
1.5 : 1.0	1.5	1.0	1.5	1.0	1.5	1.0	1.5					9
1.0 : 1.0	1.0	1.0	1.0	1.0	1.0	1.0	1.0	1.0	1.0			9
1.0 : 0.5	1.0	0.5	1.0	0.5	1.0	0.5	1.0	0.5	1.0	0.5	1.0	8.5

Table 8-1 Formation of barcode, widths are in centimetre (cm)

Figure 8-2 shows the images of the 4 barcode signs in Table 8-1. The interval between bars is fixed as 1.0cm for the first 3 barcodes and 0.5cm for the last one. Their stencil area (the white area) ratios are 6:6:5:6 and the total widths of the sign are 8, 9, 9 and 8.5cm respectively.

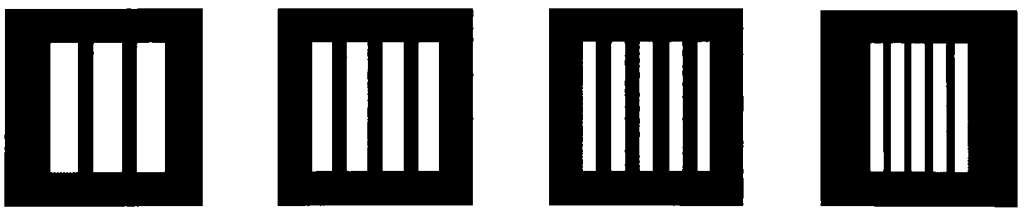

Figure 8-2 Barcode signs with different aspect ratio

Visibility has been measured with 3 different power and 3 different colour settings of the light source. The optical depth of the smoke changes continuously from 0 to 9. According to Jin (2008), when optical depth is greater than 8.0, the sign would become invisible. In the current experiment, each measurement is carried out with the tunnel filled with smoke more than enough to fully obscure the sign. In terms of optical depth, its value would be larger than 12. Measurements are made as the smoke level goes down naturally due to leakage. 5 people age between 19 and 52 with normal eyesight have been asked to observe the optical depth threshold, the observed threshold optical depth were between 7 and 9 for different colour and sign combination.

The complete results of the measurement are presented in Appendix A. In the next few sections the effect of the most influential factors on visibility are compared and discussed.

8.1.1 The aspect ratio of barcode

Figure 8-3 shows the visibility of green barcodes with different aspect ratio. At power level 1, the visibilities of the two bulkier barcodes are clearly better than the other two thinner ones. Results with other colour and power of the light sources are compared in Appendix B. It can be seen from Appendix B that what is shown in Figure 8-3 is a general phenomenon.

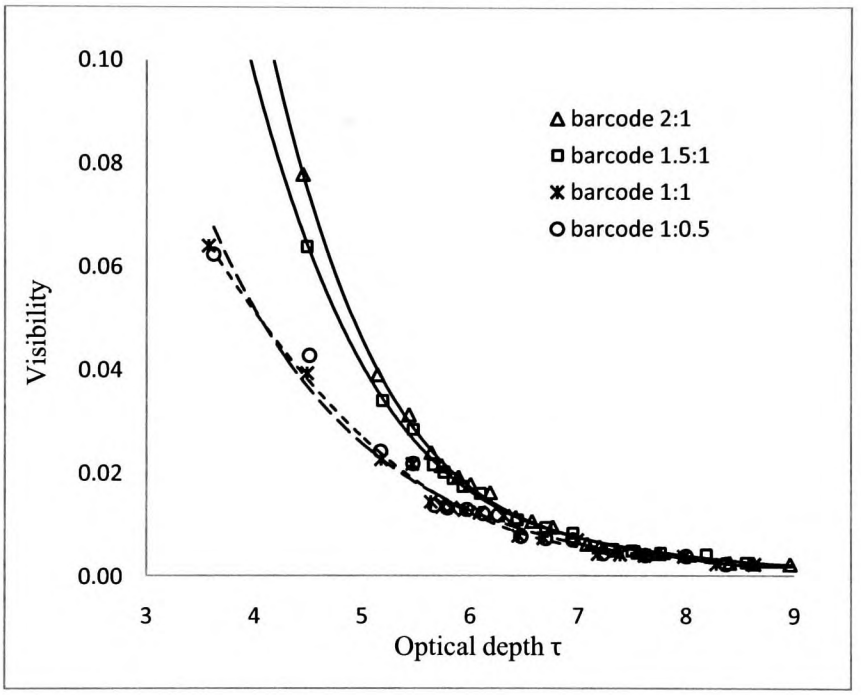

Figure 8-3 Visibility of different barcodes with green light at power level 1

In practice, bulky legend for emergency sign is the preferred choice. What can also be seen in Appendix B is that the advantage of the bulky barcode diminishes if either the power of illumination or the value of the photometric function of the sign decreases as shown in Figure 8-4.

Figure 8-5 shows the images of the same barcodes as in Figure 8-3 with optical depth about 6.5. It is obvious that the two bulky barcodes in Figure 8-5 (c) and (d) are more easy to be identified than (a) and (b).

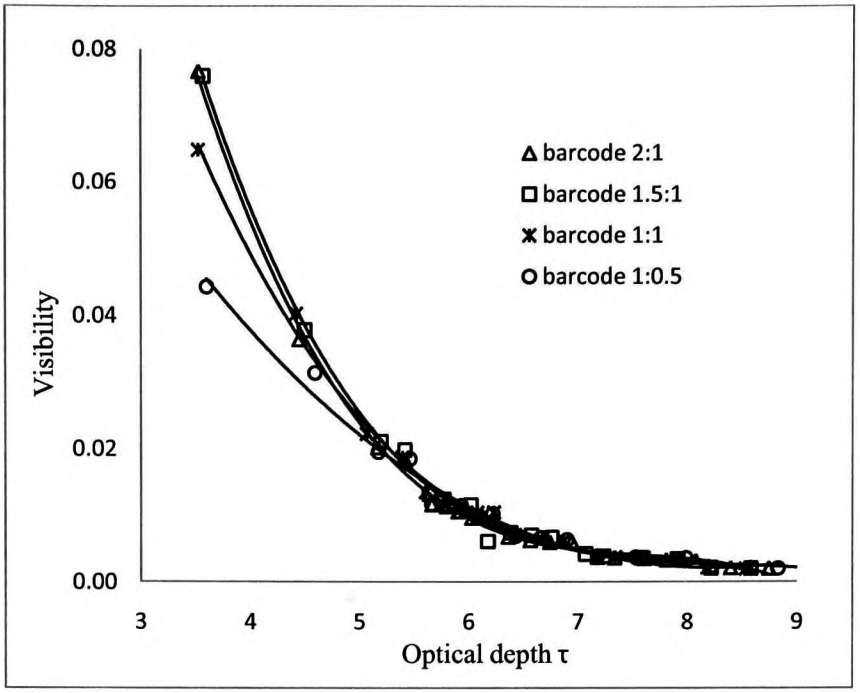

(a) Visibility of different barcodes with green light at power level 2

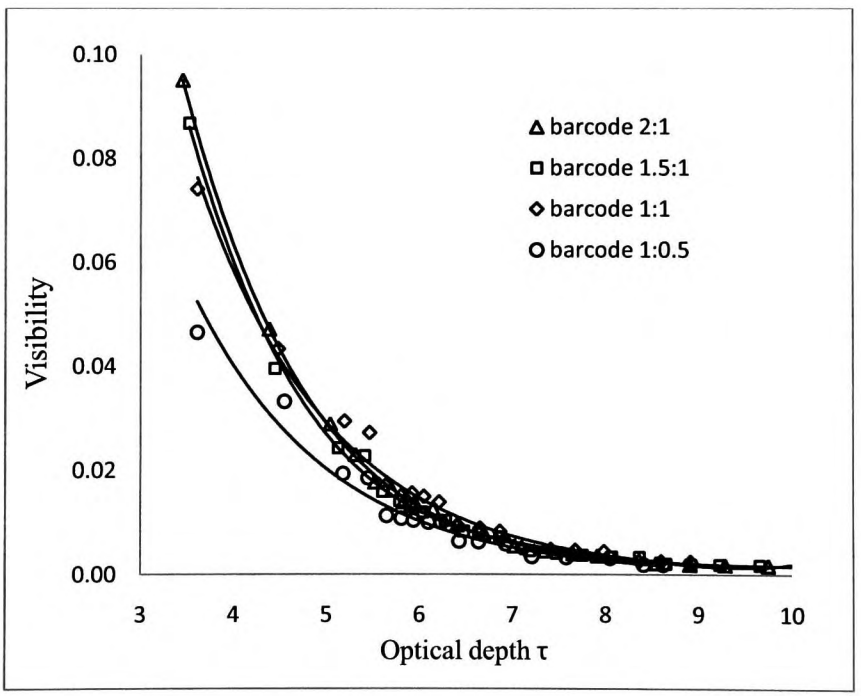

(b) Visibility of different barcodes with red light at power level 1

Figure 8-4

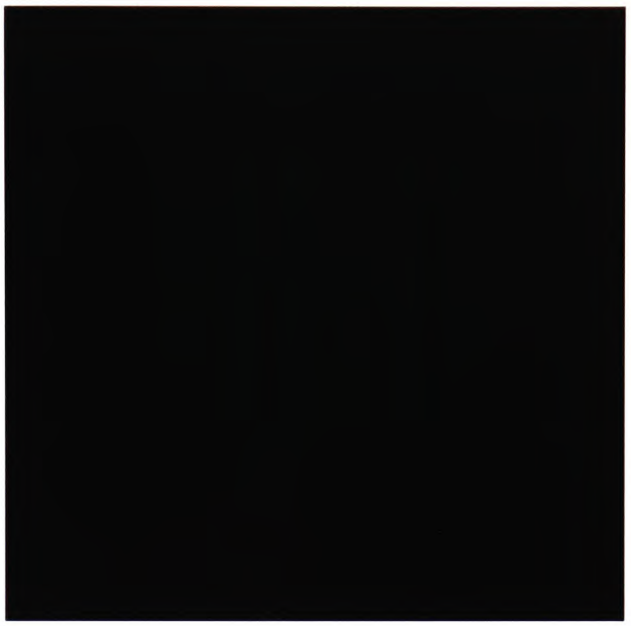

(a) 1:0.5

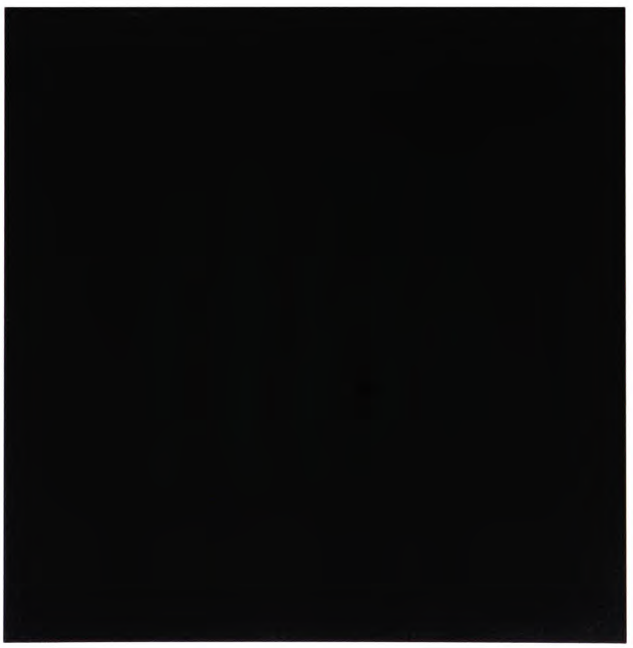

(b) 1:1

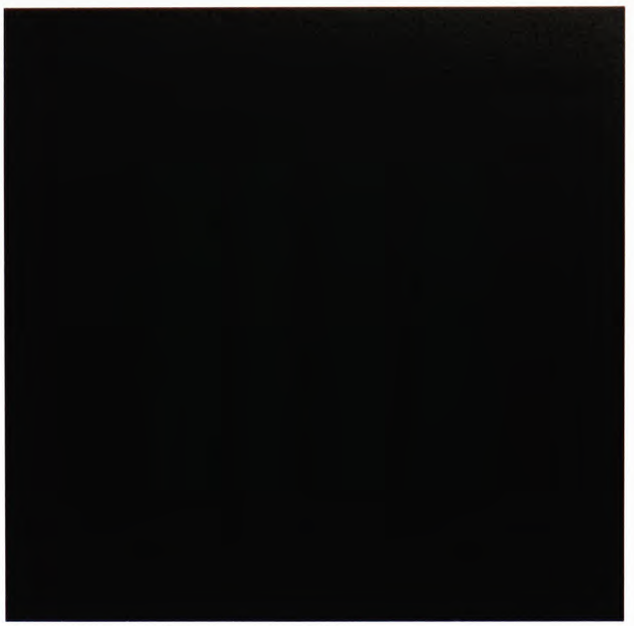

(c) 1.5:1

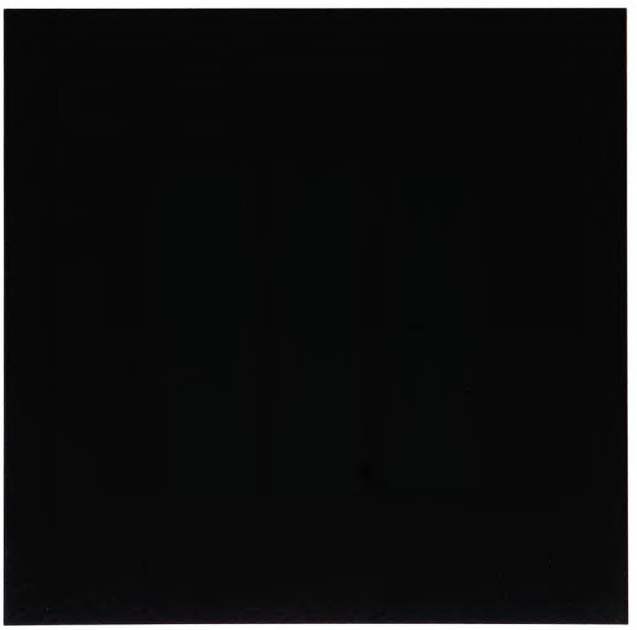

(d) 2:1

Figure 8-5 Images of barcode signs with different aspect ratio

8.1.2 The illuminating power of the light source

As can be predicted with common experience, higher power of the light source will lead to better visibility of a sign. Figure 8-6 shows the measured visibility from the barcode sign with 1.5:1 aspect ratio and green light at 3 different power levels. The visibility of the sign improves with the increase of the power input of the light source. Similar effect can be seen under other colour or aspect ratio conditions in Appendix C.

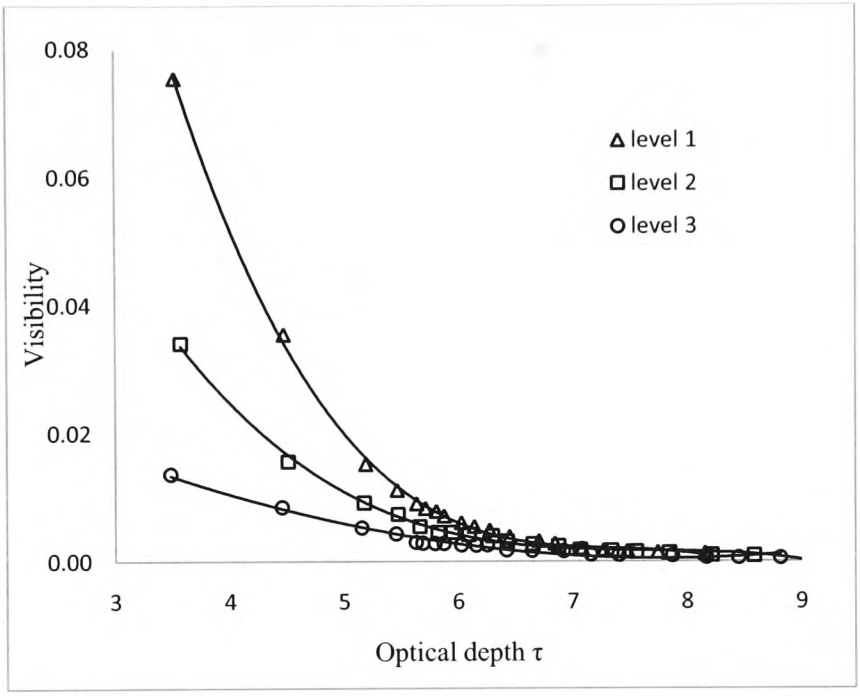

Figure 8-6 Visibility of barcode (1.5:1) with different green light power

Exception does exist in the case of barcodes with small aspect ratio and strong light scattering as in Figure 8-7 where the barcodes of 1:0.5 are illuminated with blue light. In this case, strong scattering has reduced the contrast of the image produced at power level 1 below that at power level 2 when $\tau>5$.

As the optical depth increases, the visibility curves representing different light power converge. At $\tau=8$, the differences become very small. In human field experiment, such difference is unrecognisable by the participants as shown by Jin (1978).

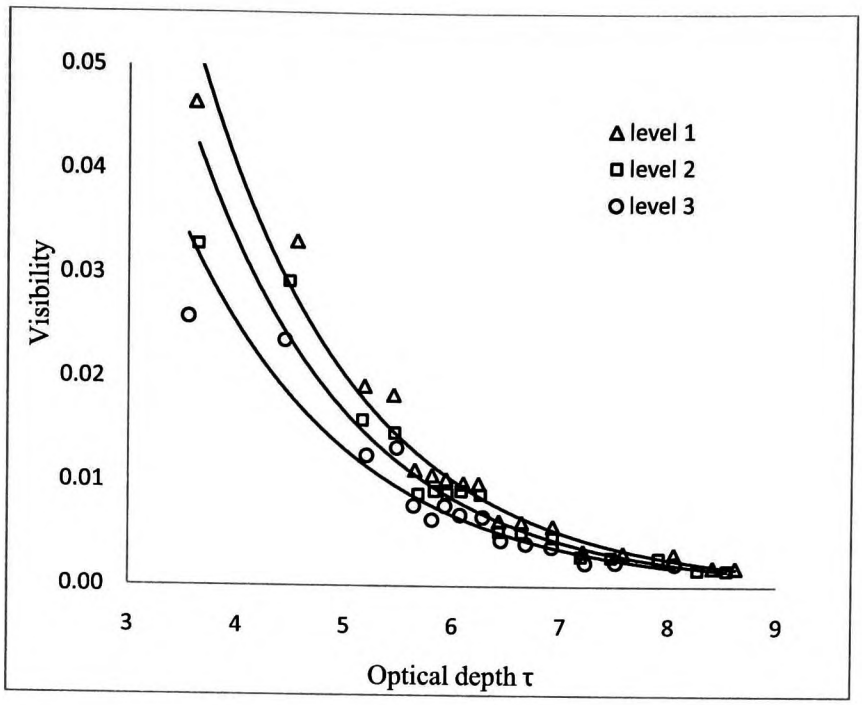

Figure 8-7 Visibility of barcode (1:0.5) with different blue light power

8.1.3 The colour of a barcode sign

It is generally accepted that emergency sign (or any other warning signal) should be in red or green colour. The reason is simply put as that red light suffers less from extinction and the human eye is more sensitive to green colour. There are other reasons such as tradition and history. People in North America have chosen red as the colour for their emergency sign but in Europe, green is the colour that has been used for the same purpose. This issue has been left in the history of fire protection without conclusive preference.

Rea et al (1985) studied coloured EXIT signs which had various combinations of red/black, red/white, green/black and green/red. The signs were view from a distance of 5.5m. Twelve subjects with normal vision observed the red and green signs. Ouellette (1993) later reported (the same study) that there was no statistically significant overall effect of colour: seven subjects did slightly better with red signs, while the remaining five showed a marginal advantage with green signs. It was concluded that the effects of colour of emitted light on visibility, if any, was much less than that of sign luminance, ambient illumination, or smoke density.

In the current study, the results of visibility measurements with 3 different colour light sources are compared and the comparison under various experimental conditions is given in Appendix D. In reference to the measured results in Appendix A, the results in Appendix D are normalised

against the output of the light source which is measured directly as described in section 5.5 and Table 11-1.

The comparison in Appendix D has, for the first time, tried to quantify the argument on the colour of emergency sign. Under the current experimental conditions, signs illuminated with red and green light have shown very similar visibility but that with blue light is significantly poor (Figure 8-8). It means that the performance of red signs used in North America is as good as that used in Europe.

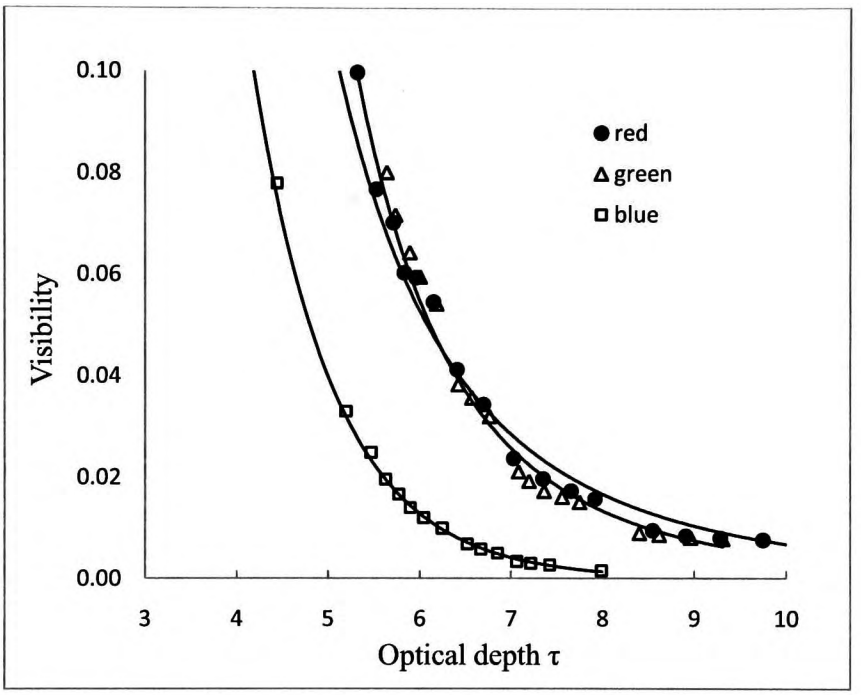

Figure 8-8 Visibility of barcode with aspect ratio 2:1 at power level 1

8.1.4 Ambient light

Jin (2008) has point out that the visibility of placard decreases with the intensity of the ambient light. Rea (1985) presented the relation between the luminance of an exit sign and its critical optical density of smoke. Figure 8-9 shows the visibility curve with and without ambient lights. It is clear that the ambient light has significantly reduced the critical optical density of the smoke.

In the current study, two barcodes with aspect ratio of 1.5:1 and 1:0.5 have been chosen to repeat the measurements shown in Appendix A with the ceiling light near the camera being switched on (see Figure 5-1). Measurements have been done at power level 1 and 2 of the light source. At level 3, the power input is too low for the visibility of the sign to be measured.

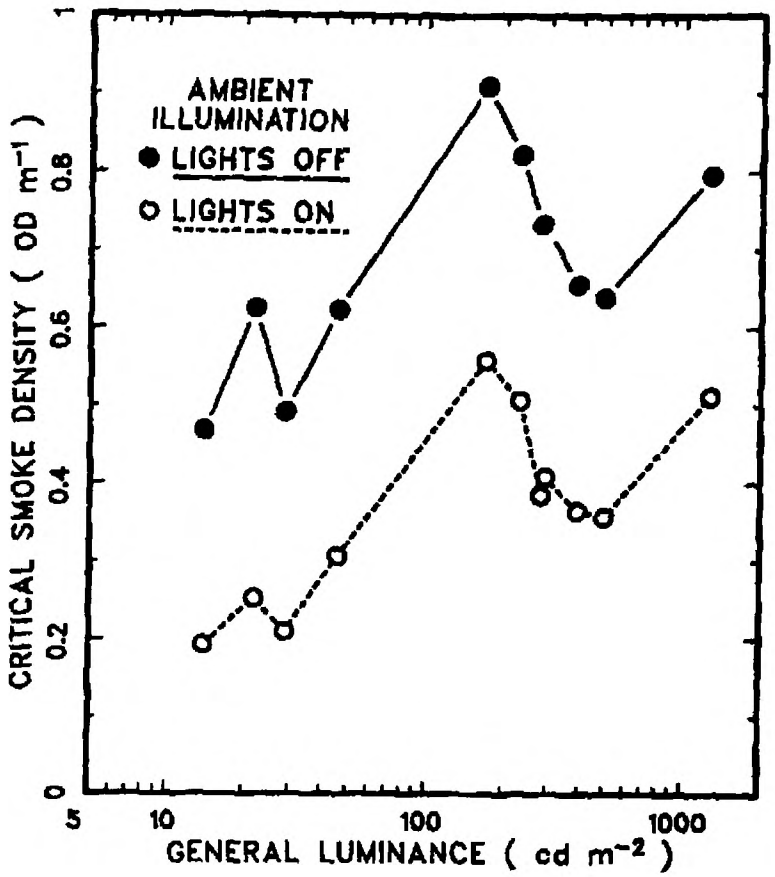

Figure 8-9 The effect of ambient light on the visibility of emergency sign (Rea, 1985)

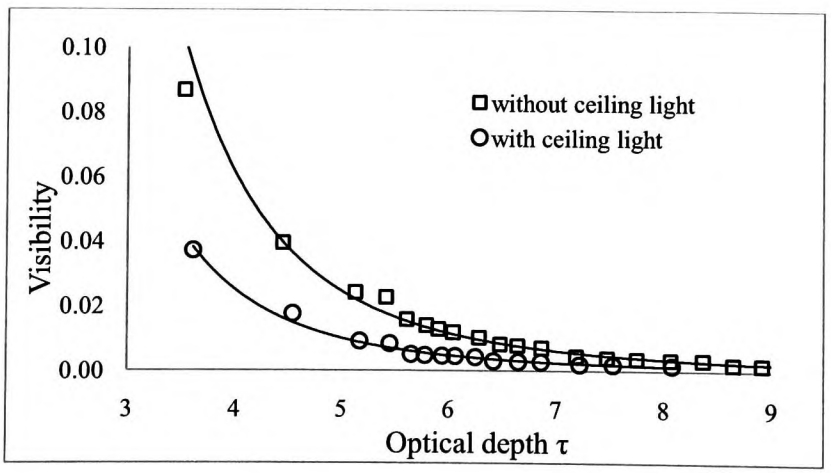

Figure 8-10 Visibility of red barcode with aspect ratio 1.5:1 at power level 1

Figure 8-10 shows the comparison of visibility for red barcode with aspect ratio 1.5:1 at power level 1 with and without the ceiling light. It can be seen that with the ceiling light being

switched on, the visibility of the sign has been significantly reduced. Similar effect can be seen under other experimental conditions as shown in Appendix E.

8.2 Visibility of text stencil

A stencil with the text "EXIT" has been tested with the same LED light source as in the cases of barcodes. The area of the text legend is 12x4cm^2. The font of the characters is bold Arial with stroke width of approximately 0.8cm. The stencils were illuminated at power level 1. Figure 8-11 shows the images of the stencil under clear condition.

Figure 8-11 Exit stencil illuminated with red, green and blue LED light

Figure 8-12 shows the visibility of the stencil normalised by the power of the light source in the same way as in Figure 8-8. As in the cases of barcodes, the visibilities of red and green lights are very similar but that of the blue light is lower.

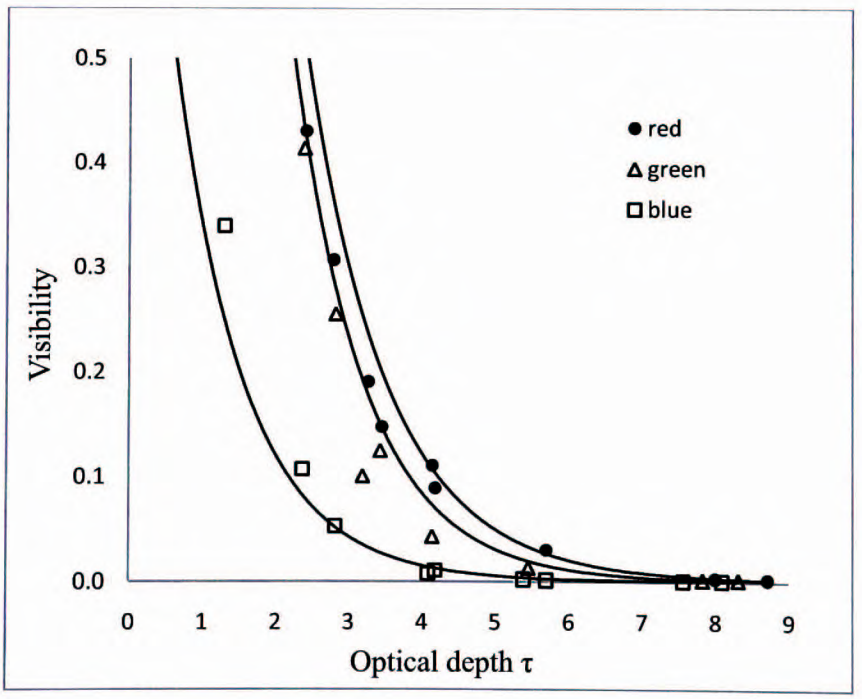

Figure 8-12 Visibility of EXIT stencil

8.3 Visibility of commercial emergency exit sign

8.3.1 The sign and its visibility

The visibility of a European commercial emergency exit sign (Figure 8-13) has also been tested in the current experiment. The sign is the 8WT5 type with dimension of 38x19x6cm^3 powered by one 8W fluorescent lamb.

Figure 8-13 The un-illuminated commercial emergency exit sign in day light

Complying with the requirements of EN60598-2-22 and suitable for incorporation into an emergency lighting system complying with BS5266-1:2005, the sign is fitted with a legend according to the Health and Safety Signs Directive 1996 and BS5499. The entire surface of the sign is translucent with white legend on green background.

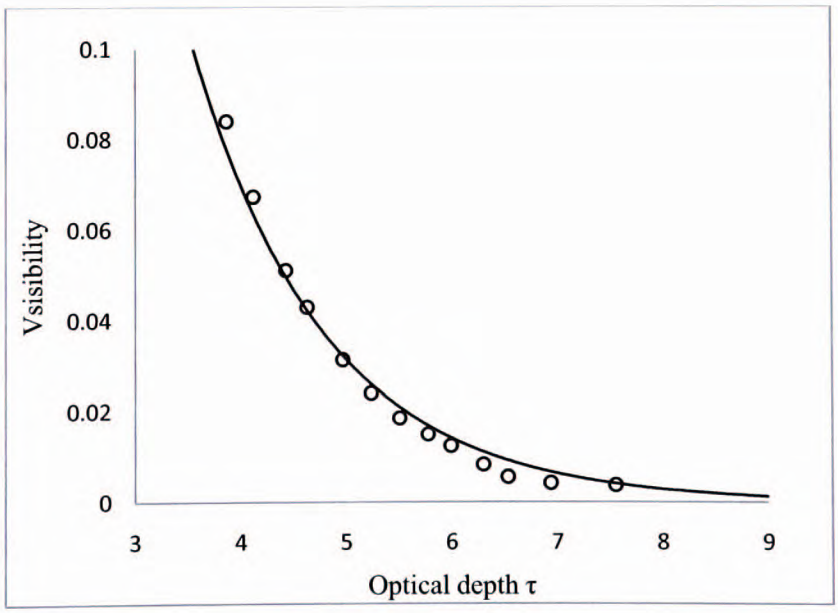

Figure 8-14 Visibility of the real exit sign vs. smoke optical depth

The sign was placed in the middle of the tunnel cross section and 3 meters from the camera. The camera settings are the same as for the barcode signs except that the focal length of the zoom was reduced from 300mm to 200mm.

Figure 8-14 shows the decrease of the visibility of the sign verses the optical depth of smoke. The general trend of the curve is still exponential.

8.3.2 Translucent against opaque background

Figure 8-15 is a photo image of the illuminated sign taken in the smoke tunnel. In order to see the effect of the translucent green background, the sign was masked with a black opaque stencil which converts the sign into white laminated legend on black background as shown in the photo image of Figure 8-16.

Figure 8-15 Photo image of the emergency sign with green translucent background

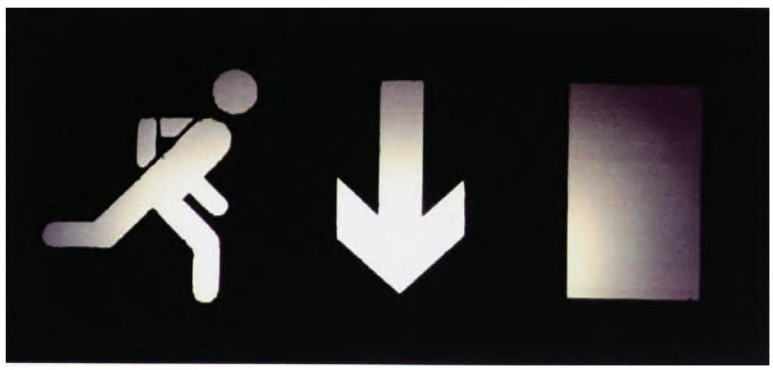

Figure 8-16 Photo image of the emergency sign without background luminance

The comparison between the translucent sign and the stencil sign is shown in Figure 8-17. Although the difference is relatively small, the visibility of the translucent sign is generally better than that of the stencil sign up to the optical depth of 7.0. Afterward the performance of

the two signs is almost the same. It is believed that the reason of better visibility for the translucent sign is due to the fact that visibility in the current study depends on the image contrast between the sign and its background as well as the overall brightness of the image. Both values are higher for the translucent sign than the stencil sign because the former has larger illuminated area. Therefore the improvement of visibility is on the entire sign, not just its legend.

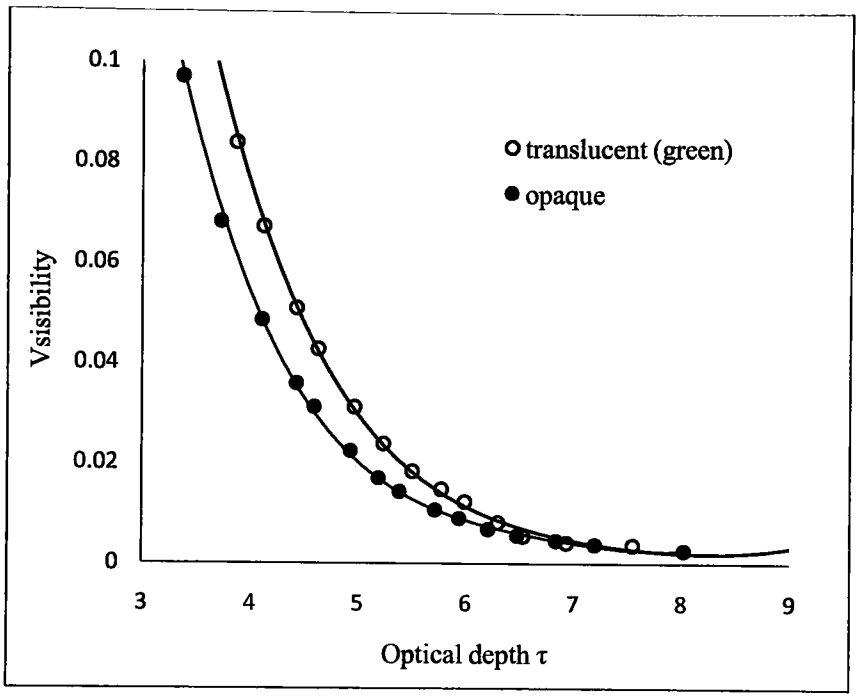

Figure 8-17 Visibility of the sign with and without background luminance

The current conclusion contradicts with the results from Ouellette (1988) and Collins et al (1992). In both of the cases, the sign was formed with thin red text on white translucent background that would be rather dominant in terms of total luminance. What also needs to be pointed out is that visibility defined in the current study is different from the visual threshold used in those experiments.

8.4 The visibility threshold

The commonly accepted visibility threshold given by Jin (2008) is that the optical depth of smoke equals to 8.0 as shown in Figure 8-18. Interestingly this threshold is largely independent of media type and the brightness of light source.

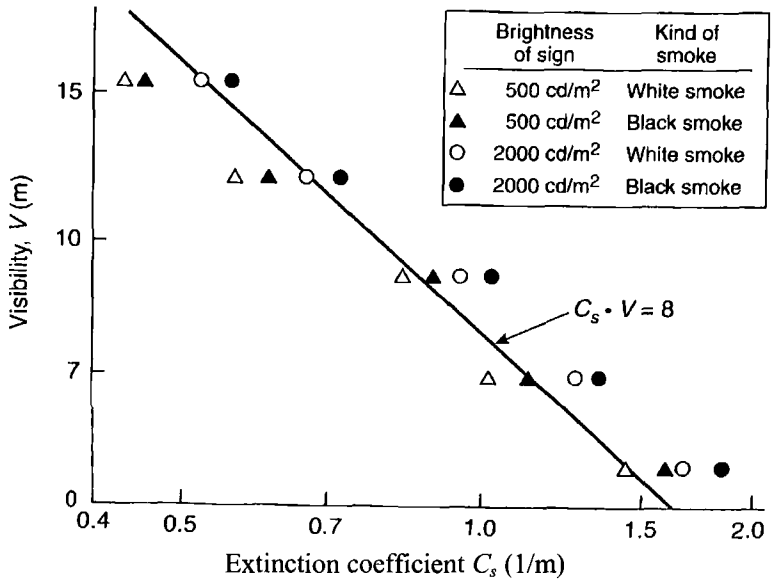

Figure 8-18 Jin's visibility threshold (Jin T. , 2008)

On the visibility curve as defined in the current study, the threshold is a point where the visibility curves under different conditions merges (e.g. Figure 8-3, Figure 8-6, Figure 8-12 and Figure 8-17). Different visual condition leads the visibility curve towards the threshold with different slop. In relatively favourable visual conditions (brighter light source, bulky sign etc.) the disappearance of the target would be rather sudden. If the conditions are less favourable, the image of the target goes blur well before the conditions reach the threshold. It opens the question of how the performance of an emergency sign should be judged. At the moment, judgement is made only on the threshold of visual distance. It is certainly important that the emergency sign should stay visible during the entire period of evacuation. However, the visibility of the sign can be very different under different conditions before the threshold is reached. Should the designers make effort to improve the visibility of emergency sign so that it would be easier for the evacuee to find the egress route even in hurry or panic? The answer is definitely yes.

8.5 Summary

Various internally powered signs were examined in the smoke tunnel under controlled environment. Quantitative visibility measurements of the signs have been made with commercial digital camera. Here are the main findings from the experiment.

- Signs illuminated by red and green light have very similar performance of visibility in a smoke laden environment. The performance of a sign illuminated by blue light would be significantly poor compared with the other two.
- The visibility of an internally illuminated sign can be improved through the increase of its luminance.
- The presence of ambient light could significantly reduce the visibility of a sign.
- An illuminated sign with white legend on green translucent background perform better than that on opaque background.
- The legend of a sign with bulkier stroke and larger interval between the strokes has better visibility than that with thin and compact strokes.
- The difference in visibility due to different visual conditions diminishes as the optical depth of the smoke approaches the threshold value of 8.0 given by Jin.

Most of the above points are arguably known to the fire engineering community but this has been the first time quantitative conclusions have been drawn. In the opinion of the author, more attention should be paid to the pre-threshold conditions that have caused some significant discrepancies and would be experienced by most evacuees during fire evacuation. Improvement of visibility under such condition will certainly improve the performance of emergency egress.

Part III Numerical simulation of visibility in smoke laden environment

Experimental study of visibility in fire smoke is important in order to understand its mechanism and the general principle for improvement. Conditions of real fire in modern public buildings would be more complicated in almost every aspect in comparison with the conditions in the laboratory. It justifies the use of computer simulation for design verification. As part of the current study, a computer model for the visibility in smoke laden environment has been developed. This part of the thesis gives the details of the model and its validation against the experimental data presented in Part II.

Chapter 9. Previous solution methods for the radiative transfer equation

The radiative transfer equation 2-26 is an integro-differential equation. In addition to the 3 spatial dimensions common in other dynamic systems, there are 2 angular and one spectra dimensions. Consequently, exact analytical solutions exist for only a few extremely simple situations such as one-dimensional problem in homogeneous medium with constant optical properties.

Most engineering problems are multi-dimensional and heterogeneous. Frequently the spectral variations of the radiative properties have to be accounted for. Therefore simplified approximations are necessary in the solution of the RTE. Depending on the nature of the specific problem in hand, the degree of accuracy required, and the available computer facilities, solution methods of varying degrees of approximation have been devised. In this chapter, some typical methods that have been developed in astronautics, atmospheric/meteorological science, neutron transport, radiative heat transfer and computer graphic are reviewed.

9.1 Analytical solution

Analytical methods can be applied to radiation transport problems only in the case of highly idealized situations, like problems with simple geometry and homogeneous participating media having spectrally independent radiative properties (gray medium). In such situations, exact analytical solutions can be obtained for the RTE, which is used for determining the variation of intensity in the participating media. The simplest example is equation 2-24. More complex solution involves heterogeneous medium or two dimensional boundary conditions (Heaslet & Warming, 1963). The analytical solutions have received much attention in atmospheric sciences and neutron transport (Viskanta, 1987). In thermal engineering, their application is limited and the procedures of obtaining such solution are already written in text books (see, e.g., Ozisk, 1973; Siegel & Howwell, 1992; Modest, 1993).

Since visual simulation is intrinsically 3 dimensional, no effort has been made to seek analytical solution.

9.2 Numerical solution

9.2.1 Spherical Harmonics method (P_N –Approximation)

Assuming that at a point $\vec{x}$ in space, the spectral radiance field $L_\lambda(\vec{x},\vec{\omega})$ can be expressed as the following series

$$L_\lambda(\vec{x},\vec{\omega}) = \sum_{l=0}^{\infty}\sum_{m=-l}^{l} L_l^m(\vec{x}) Y_l^m(\vec{\omega}) \qquad 9\text{-}1$$

where the subscript λ has been omitted on the right hand side of expression 9-1 for clarity. $L_l^m(\vec{x})$ is position dependent coefficients and $Y_l^m(\vec{\omega})$ is the spherical harmonics given by

$$Y_l^m(\vec{\omega}) = (-1)^{(m+|m|)/2}\left[\frac{(l-|m|)!}{(l+|m|)!}\right]^{1/2} e^{im\psi} P_l^{|m|}(\cos\theta)$$

where θ and ψ are the zenith and azimuth angle describing $\vec{\omega}$ in spherical coordinate system defined at $\vec{x}$. P_l^m is the associated Legendre polynomials.

Similarly, expanding the phase function in expression 2-26 as

$$p(\mu,\mu_\omega) = \sum_{m=0}^{M} A_m P_m(\mu_\omega) P_m(\mu) \qquad 9\text{-}2$$

where $\mu = \cos\theta$ and $\mu_\omega = \cos\theta_\omega$. m is the order of approximation of the phase function.

Further assume that the problem is one dimensional and the local spherical coordinate system can be chosen so that the radiance field is independent of the azimuth angle ψ. It leads to (Modest, 2003)

$$L(\tau,\mu) \approx \sum_{l=0}^{N} L_l(\tau) P_l(\mu)^{1} \qquad 9\text{-}3$$

where the position vector $\vec{x}$ is substituted by the integration along the direction of radiation $\vec{s}$ $\tau = \int_0^s \sigma ds$. The in-scattering integration in 2-26 now can be written in series form as

[1] In this case $L_l^m = 0$ if $m \neq 0$ therefore the superscript m is omitted

$$\int_{\Omega} p_{\omega\to s} L_\omega d\omega = \int_{-1}^{1} p(\mu,\mu_\omega) L(\tau,\mu_\omega) d\mu_\omega = \sum_{l=0}^{N} L_l(\tau) \sum_{m=0}^{M} A_m P_m(\mu) \int_{-1}^{1} P_l(\mu_\omega) P_m(\mu_\omega) d\mu_\omega \qquad 9\text{-}4$$

As Legendre polynomials are orthogonal, therefore

$$\int_{-1}^{1} P_l(\mu_\omega) P_m(\mu_\omega) d\mu_\omega = \frac{2\delta_{lm}}{2m+1}$$

and

$$\int_{\Omega} p_{\omega\to s} L_\omega d\omega = \sum_{l=0}^{N} \frac{2A_l}{2l+1} L_l(\tau) P_l(\mu) \qquad A_l = 0 \text{ for } l > M \qquad 9\text{-}5$$

Substituting 9-1 and 9-5 into 2-26 and exploiting the orthogonality of the Legendre polynomials again lead to N+1 ordinary differential equations for $I_n(\tau)$

$$\frac{n+1}{2n+3} I'_{n+1}(\tau) + \frac{n}{2n-1} I'_{n-1}(\tau) + \left(1 - \frac{kA_n}{2n+1}\right) I_n(\tau) = (1-k) I_b(\tau) \delta_{0n} \qquad 9\text{-}6$$

where $n=0, 1, \ldots\ldots, N$ and the prime denote differentiation with respect to τ. Up to this point the integral-differential equation 2-26 has been converted to a set of ordinary differential equations 9-6. In theory the method can yield solution to the accuracy of any degree but the expression of P_N is very complex even for small N (less than 3) (Ou & Kuo-Nan, 1982; Ratzel & Howell, 1983; Menguc & Viskanta, 1985, 1986). What needs to be remembered is that equation 9-6 is only a one-dimensional solution (the real solution process is far beyond 9-6). In multi-dimensional geometries, attempt to make higher order approximations would be unrealistic. The drawback of the method is that low-order approximations are usually only accurate in optically thick media, and accuracy improves slowly for higher-order approximations while mathematical complexity increases extremely rapidly (Viskanta, 1987). With the higher order terms, boundary conditions are also very complicated. When the media is heterogeneous, the problem becomes too complicated to solve.

9.2.2 Discrete ordinates method (S_N – Approximation)

If the radiative transfer equation 2-26 is solved along a set of n different directions $\vec{s}_i$, i = *1, 2, ...*, n and the scattering integrals over direction are replaced by numerical quadratures, that is

$$\int_{\Omega} L(\vec{x}_i,\vec{\omega})p(\vec{x}_i,\vec{s}_i,\vec{\omega})d\omega = \sum_{j=1}^{n} w_j I(\vec{x}_i,\vec{\omega}_j)p(\vec{x}_i,\vec{s}_i,\vec{\omega}_j)$$

where w_j is a weighting factor. Then the original RTE can be written as

$$\vec{s}_i \cdot \nabla L_\lambda = \alpha_{abs,\lambda} L_{b,\lambda} - \alpha_{ext,\lambda} L_\lambda + \frac{\sigma_{sca,\lambda}}{4\pi} \sum_{j=1}^{n} w_j I(\vec{x}_i,\vec{\omega}_j)p(\vec{x}_i,\vec{s}_i,\vec{\omega}_j) \qquad i = 1,2,\cdots,n. \tag{9-7}$$

The accuracy of 9-7 keeps improving as n increases provided that the direction $\vec{s}_i$ and weighting factor w_i satisfy the following conditions

$$\sum_{i=1}^{n} w_i = \int_{4\pi} d\omega = 4\pi$$

$$\sum_{i=1}^{n} w_i \vec{s}_i = \int_{4\pi} \vec{s}\, d\omega = 0$$

$$\sum_{i=1}^{n} w_i (\vec{s}_i \otimes \vec{s}_i) = \int_{4\pi} (\vec{s} \otimes \vec{s}) d\omega = \frac{4\pi}{3}\delta \tag{9-8}$$

Here δ is the unit tensor and $\otimes$ denotes the dyadic product between two vectors. Since the solution must be symmetrical (radiances in two opposite directions co-exist), an even number of the simultaneous equations must be solved at any spatial point. A solution of this type is denoted as S_N with *N=2, 4, 6, ...* The subscript N is called the order of the solution. The number of discrete ordinates n, the order of the solution N and the physical dimension of the solution space D *(D=1, 2, 3)* form the following relation

$$n = 2^D N(N+2)/8 \tag{9-9}$$

A S_4 solution for a two dimensional radiative transfer problem requires $2^2 \times 4(4+2)/8 = 12$ simultaneous equations to be solved at each point (Siegel & Howwell, 1992).

The discrete ordinate method was first proposed by Chandrasekhar(1960) in his work on stellar atmosphere radiation. Later, Lee(1962) and Lathrop(1966) apply it to neutron transport theory. Fiveland (1984) calculated 2 dimensional radiative heat transfer in enclosures with this method and observed that different sets of ordinates may result in considerably different accuracy. His results of S_4 and S_6 ordinates are generally better than the P_3 solution from Ratzel & Howell (1982).

Later Truelove (1987) improved Fiveland's solution by adding the half-range condition that the set of ordinates and weights should also satisfy the first moment over a half range on the surface of walls:

$$\int_{\vec{n}\cdot\vec{s}<0} |\vec{n}\cdot\vec{s}|d\omega = \int_{\vec{n}\cdot\vec{s}>0} \vec{n}\cdot\vec{s}\,d\omega = \pi = \sum_{\vec{n}\cdot\vec{s}_i>0} w_i \vec{n}\cdot\vec{s}_i \qquad 9\text{-}10$$

Comparing with the P_N method, the S_N method is more flexible. It can be applied to non-isothermal, heterogeneous, anisotropically scattering media in complex geometries. In radiative heat transfer, the implementation of the S_N method can be conveniently accommodated in the CFD mesh readily available for flow and convective heat transfer simulation. It makes it a primary choice within the CFD community.

The discrete ordinates method suffers from two major sources of inaccuracy, the ray effects and false scattering. False scattering is the result of spatial resolution same as the false diffusion in CFD simulation and may be reduced using any discretization scheme that improves field resolution (refined mesh or higher order scheme). The same problems accompanied with such scheme in CFD simulation (over/under shoot, unphysical values etc.) also appear in the radiative simulation. Ray effects are the result of angular resolution and related to the abrupt change of radiation on the boundary. As the discrete ordinates are bound by conditions in equation 9-8, the computational cost of angular refinement is proportional to N^2 and N has to be an even number. Some mitigation schemes have been introduced to reduce the ray effects but they are often restricted (e.g. thin smoke), costy and complicated to implement making a conceptually transparent method rather obscure (Liou & Wu, 1997; Coelho, 2004). Due to such drawbacks, the S_N method is not well accepted by the computer graphics community despite its computational efficiency by solving a single set of linear equations to get the illumination of the entire scene.

9.2.3 Radiosity method

The radiosity method was developed in the late 1950s and early 1960s for surface to surface thermal radiation problems within an enclosure with gray, diffusive walls and without participating media (Oppenheim, 1956). Under such conditions, radiation leaving a finite

surface area A_j and arriving at another finite surface area A_i can be expressed as, assuming radiance on each surface area is constant

$$\Phi_{ji} = -\int_{\Omega}\int_{A_j} L_j p_{ji} \vec{\omega}_{ji} \cdot d\vec{A}_j d\omega_i = -\int_{A_i}\int_{A_j} L_j p_{ji} \vec{\omega}_{ji} \cdot d\vec{A}_j \frac{\vec{\omega}_{ji} \cdot d\vec{A}_i}{\left|\vec{x}_i - \vec{x}_j\right|^2} = E_j \int_{A_i}\int_{A_j} p_{ji} \frac{\left|\vec{\omega}_{ji} \cdot \vec{n}_i\right|\left|\vec{\omega}_{ji} \cdot \vec{n}_j\right|}{\pi\left|\vec{x}_i - \vec{x}_j\right|^2} dA_i dA_j$$

9-11

where the phase functions is in fact a visibility function

$$p_{ji} = \begin{cases} 1 & \text{if } dA_j \text{ is visible from } dA_i \\ 0 & \text{otherwise} \end{cases}$$

The total radiant energy flux arrived at A_i is

$$\Phi_{inc,i} = A_i \sum_{j=1}^{N} E_j F_{ij}$$

Therefore

$$E_i = \rho_i \sum_{j=1}^{N} F_{ij} E_j + \pi L_{emt,i} \qquad 9\text{-}12$$

where N is the total number of surface elements of the enclosure and

$$F_{ij} = \frac{\overline{s_i s_j}}{A_i} \qquad 9\text{-}13$$

is called view factor (or form factor) of A_j viewed from A_i with the exchange area $\overline{s_i s_j}$ defined as

$$\overline{s_i s_j} = \int_{A_i}\int_{A_j} p_{ij} \frac{\left|\vec{\omega}_{ij} \cdot \vec{n}_i\right|\left|\vec{\omega}_{ij} \cdot \vec{n}_j\right|}{\pi\left|\vec{x}_i - \vec{x}_j\right|^2} dA_i dA_j \qquad 9\text{-}14$$

Since $\overline{s_i s_j}$ is symmetrical to the sub scripts, the view factors between A_i and A_j follow the rule of reciprocity

$$F_{ij} A_i = F_{ji} A_j \qquad 9\text{-}15$$

Equation 9-12 for all the elements of the enclosure forms a set of linear equations for the surface radiosity of the enclosure (Oppenheim, 1956).

This method was first introduced into computer graphic for global illumination by Kajiya (1986). Various improvements were made to reduce the computational cost in calculating view factors and reducing the total number of elements without losing the capability of producing visually acceptable images (Cohen & Wallace, 1993).

In surface radiation within enclosure and global illumination for computer graphics, equation 9-12 can be solved implicitly with efficient linear solvers popular in FEA and CFD simulation even though computing view factor 9-13 is still burdensome in 3D cases with complex geometry. In global illumination, small surface elements are required to avoid artefacts along the edges of geometry as well as the boundaries of shadow.

9.2.4 Zonal method

The zonal method is widely applied in calculating radiation heat transfer with participating media in practical engineering systems. It was first developed by Hottel & Cohen (1958) for an absorbing-emitting and non-scattering gray gas with constant absorption coefficients. Hottel & Sarofim (1967), Noble (1975), Smith *et al*(1985) and Nelson *et al*(1986) extended it to deal with non-constant and non-gray absorption coefficients as well as isotropic scattering media.

As a direct extension of the radiosity method (in computer graphics it is often referred as radiosity method), equation 9-12 is replaced by the following equations for surface and volume local energy balance in equilibrium condition (Rushmeier & Torrance, 1987)

$$\begin{cases} A_i E_i = A_i E_{emt,i} + \rho_i \left(\sum_{j=1}^{N} \overline{s_i s_j} E_j + \sum_{j=1}^{M} \overline{s_i g_j} J_j \right) & \textit{for surface zone} \\ 4\sigma_i V_i J_i = 4\sigma_{abs,i} V_i J_{emt,i} + \rho_i \left(\sum_{j=1}^{N} \overline{g_i s_j} E_j + \sum_{j=1}^{M} \overline{g_i g_j} J_j \right) & \textit{for volume zone} \end{cases} \qquad 9\text{-}16$$

where E and J are radiosity defined on surface and volume zone respectively. N and M are the number of surface and volume zones respectively. The exchange areas $\overline{s_i g_j}$ and $\overline{g_i g_j}$ are defined by

$$\overline{s_i g_j} = \int_{A_i V_j} \int p_{ij} \frac{|\vec{\omega}_{ij} \cdot \vec{n}_i| \sigma_j}{\pi |\vec{x}_i - \vec{x}_j|^2} dA_i dV_j$$

$$\overline{g_i g_j} = \int_{A_i A_j} \int p_{ij} \frac{\sigma_i \sigma_j}{\pi |\vec{x}_i - \vec{x}_j|^2} dV_i dV_j \qquad \text{9-17}$$

Same as $\overline{s_i s_j}$, they are also symmetrical to the subscripts i and j.

With participating media, the definition of p_{ij} must include energy loss during transmission from element i to element j regardless it is surface or volume type. This is evaluated according to Lambert-Beer's law as

$$p_{ij} = e^{-\int_{s_i}^{s_j} \sigma ds}$$

The integration is to account the heterogeneity of the media.

Kajiya (1986) introduced this method to the computer graphics community. Rushmeier(1988) applied it in his simulation of global illumination with thin media exhibiting weak anisotropic surface scatter, where volume-to-volume interaction was assumed insignificant. Bhate and Tokuta (1992) extended the method to more general anisotropic media and Bhate also carried out progressive zone refinement (Bhate, 1993) to reduce the overall cost.

The popularity of the zonal method is due to its simplicity in terms of the decomposition of computational domain and nearly analytical solution for the inter-zonal radiant exchange. Such advantage diminishes as the problems to be solved become more complex. In a typical cube filled with participating media and divided into n elements in each principle direction, the cost of computing the exchange areas 9-16 would be $O(n^7)$[1]. In cases that the participating media is constant, this operation needs to be carried out only once per scene. In other cases, such cost is often considered prohibitively high.

9.2.5 Monte Carlo ray tracing

In 1946, following the creation of the world's first electronic computer ENIAC, a team of scientists in Los Alamos Laboratory carried out a series of statistical computation on it

[1] The number of elements would be $O(n^{3x2})$ and the cost of p_{ij} would be $O(n)$.

simulating neutron transport process. Monte Carlo method was formally introduced (and named) in this simulation (Metropolis, 1987).

The method was first introduced into thermal radiation in the early 1960s for one dimensional radiative heat transfer problems (Fleck, 1961; Howell & Perlmutter, 1964) . Later, more complex problems concerning non-gray, anisotropically scattering media confined in various types of enclosures were investigated using this method (Taniguchi, 1967; Taniguchi, 1969; Stockham & Love, 1968; Avery *et al,* 1969; Gupta *et al,* 1983; Abed & Sacadura, 1983; Yang *et al,* 1983; Tiwari & Liu, 1992; Farmer & Howell, 1994 and Liu & Tiwari, 1994). The high computational cost of the Monte Carlo method had prevented it from being widely adopted in its early stage of development. In recognition of its high accuracy and high computing cost, it was recommended as a benchmark for other methods (Viskanta, 1987; Mishra & Blank, 1995). As the hardware capabilities have advanced and more efficient algorithms (e.g. Kobiyama, 1989; Liu, Shang, & Chen, 1999; Modest, 2003) have been introduced, the cost of the method becomes more and more acceptable.

Generally speaking, Monte Carlo methods are a class of computer algorithms that rely on repeated random sampling. It is more of an idea or a principle than a particular computational method. Metropolis gave an excellent explanation of the principle in his original paper (Metropolis & Ulam, 1949). In solving radiative transfer equation, the method has often been used in Monte Carlo integration. The idea is to evaluate the integral

$$L = \int_{\Omega} f(x) d\mu(x) \tag{9-18}$$

with a quadrature

$$L \approx \sum_{i=1}^{N} w_i f(x_i) \tag{9-19}$$

where the weight w_i and the sample location x_i are determined in advance. N is the total number of samples.

The advantage of the Monte Carlo method over other method mentioned so far is its versatility. Regardless the dimension of the problem domain and the smoothness of the integrand, it converges at the rate of $O(N^{-1/2})$ (see next chapter) while the other quadrature based approximations will converge according to Bakhvalov's theorem, at $O(N^{-1/s})$ or worse. Here s is the dimension of the problem domain and the integrand should have a bounded, continuous first derivative (Veach, 1997).

Another advantage of the Monte Carlo method is its simplicity. Only two basic operations are required namely sampling and point evaluation which leads to simple computer software implementation. It is easier to be used in complex problem such as that involving heterogeneous and/or anisotropic media.

The traditional ray tracing technique was introduced into global illumination by Whitted (1980). He described a novel way for extending the ray-casting algorithm to determine visible surfaces in a scene to include perfect specula reflections and refractions. Later Cook et al (1984) extended it into stochastic ray tracing.

Essentially there are two tracing strategies: forward and backward tracing. The former, tracing rays from the source toward the target, is often used in neutron transport (Spanier & Gelbard, 1969) and radiative heat transfer (Tessé, Francis, & Jean, 2004) as well as in nuclear medicine (Bousis, Emfietzoglou, Hadjidoukas, & Nikjoo, 2008). The later, tracking rays from the receiver (image plane) toward the source is extensively used in computer graphics for image generation (Dutré, Bekaert, & Bala, 2003).

Limited extension of the origin of rays will result in very non-uniform convergence rate in the domain. Figure 9-1 demonstrates a camera catching the reflected light from a Lambertian surface. With forward Monte Carlo ray tracing, the probability of a ray issued from the light source being captured by the camera is quite small. It means that to generate a reasonable image, the total number of rays to be introduced from the light source, N, has to be very large since the convergence rate of the Monte Carlo method is $O(N^{1/2})$. On the Lambertian surface, the illumination would have reached its converged value with a sampling number $N' << N$. The same argument can be applied to backward Monte Carlo ray tracing.

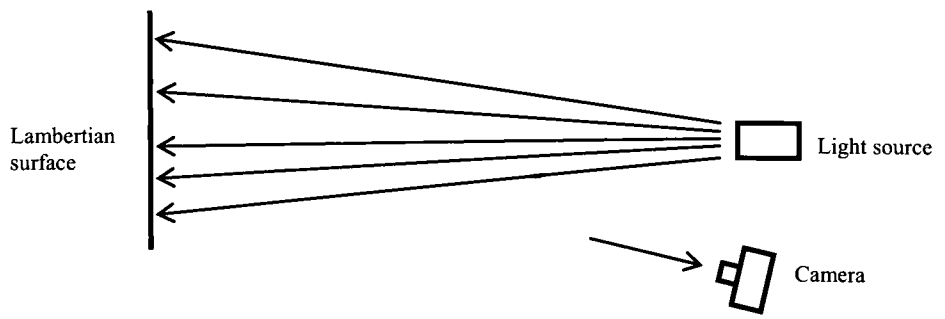

Figure 9-1

The above problem prompts the development of two pass tracing algorithms. In the first pass, rays are introduced from the light source and radiance is cached in space or on the surfaces in the scene. In the second pass, rays are introduced from the receiver (either a camera or eye). The

path of the rays is traced till it reaches a diffusive surface. In the case of specula surface, multi-leg path is traced till the ray either reaches a diffusive surface, absorbed or escaped from the scene. Many Monte Carlo ray tracing based hybrid methods are different from each other in the way that radiance is cached.

Computationally, Monte Carlo ray tracing is the most memory efficient method. Since there is no cohesion among light rays, the computation is naturally parallel and distributable.

9.2.6 Irradiance cache

Among the basic methods in solving the radiation transfer problems, the discrete ordinate method is very efficient in solving problems of thermal energy/temperature distribution but not quite suitable for image creation when the radiance field contains discontinuity as in the cases involving light beams and specula reflection. The spherical harmonic method is too complicated even for single scattering case (equation 9-3). The improvement of accuracy is accompanied with dramatic increase of the complexity of solution by including higher order term of Legendre polynomials. The zonal method can provide comprehensive global illumination solution by solving one set of linear equations but the high cost of computing the view factors causes concern. On the other hand, the Monte Carlo ray tracing solution is independent of the complexity of problem domain and relatively simple to implement. Its converging rate $O(N^{-1/2})$ is generally regarded as slow.

In order to improve both accuracy and efficiency, various hybrid methods have been proposed. Evans (1998) proposed the SHDOM method combining the spherical harmonic method and the discrete ordinate method for atmospheric radiation. Rushmeier et al (Rushmeier & Torrence, 1990; Chen, Rushmeier, Miller, & Turner, 1991) extended their earlier radiosity model by adding Monte Carlo ray tracing to simulate specula reflection and caustics.

The most successful hybrid method is photon-mapping (Jensen H. , 1996). The method employs two Monte Carlo passes: the first is to generate radiance cache on all surfaces (photon-map) and the second is to create image based on the photon-map. As the photon-map is constructed with only points, the method is completely independent from surface tessellation. The basic photon-mapping idea was extended to include participating media (Jensen & Christensen, 1998). The method is very effective in simulating caustics since there is a clear, definite free surface and the rest of the domain is filled with homogeneous medium of one kind or another. For diffusive media such as smoke that has no interface between different media but the spatial distribution of each medium is heterogeneous, the structure of the photo-map could become rather arbitrary. Unless huge number of photons are stored, it would be difficult to produce an accurate description of the field of radiation with photon-map.

9.2.7 Simulation of visibility in smoke

In fire protection engineering, the visibility of smoke, defined as visual distance, is calculated from optical density (SFPE, 2008):

$$OD = \frac{\ln(I_0/I)}{x} \qquad 9\text{-}20$$

where x is the length of optical path. In numerical simulation, optical density can be estimated from smoke mass concentration ρ_{smoke} following Lambert-Beer's law as (Ingason & Persson, 1998)[1]

$$OD = \sigma_{mass}\rho_{smoke} \qquad 9\text{-}21$$

where ρ_{smoke} is often the result of CFD fire simulation. Since OD is a scalar, some simulation packages such as PHOENICS uses (1/OD) as a measure of visibility and present it in a contours plot (CHAM, 2006). Others use it in the line of sight calculation and also for smoke visualisation as in FDS-SmokeView (Forney G. , 2009).

The OD (or rather its inverse) contours is difficult to interpret by fire engineers and often misleading. For example, OD=8 at a point does not means the local visible distance is 1/8 meter. According to Jin (2008), it is in fact 1.0 meter. In heterogeneous smoke field, treating visibility as a local property would be even more problematic.

The line of sight calculation integrates light extinction along its path. The result of the integration is the optical depth of smoke. It can be used to measure visibility. In computer graphics as well as in FDS (McGrattan, Hostikka, & Floyd, 2009), optical depth is linked (arbitrarily) to the transparency of graphic layers to produce the image of smoke as shown in Figure 9-2 (Forney G. , 2009). It only offers an easy way to qualitatively visualise smoke effect.

Husted etc (2004) carried out integration along the line of sight in his CFD fire simulation. By converting the unit of OD into 10m of visual distance, he gave an estimation of visibility in the predetermined directions and at certain floor level as shown in Figure 9-3.

The contours in Figure 9-3 show the visual distance at each point in the simulation domain observing from right to left as indicated by the arrow. In the region painted yellow, the visual distance would be great or equal to 20m so that anything on the left wall would be visible. In the

[1] In Ingason's paper, OD was defined using $\log_{10}$ instead of ln. Here OD is kept consistent with the definition in SFPE handbook (SFPE, 2008).

red region, visual distance is reduced to 10m or less therefore nothing on the left wall would be visible.

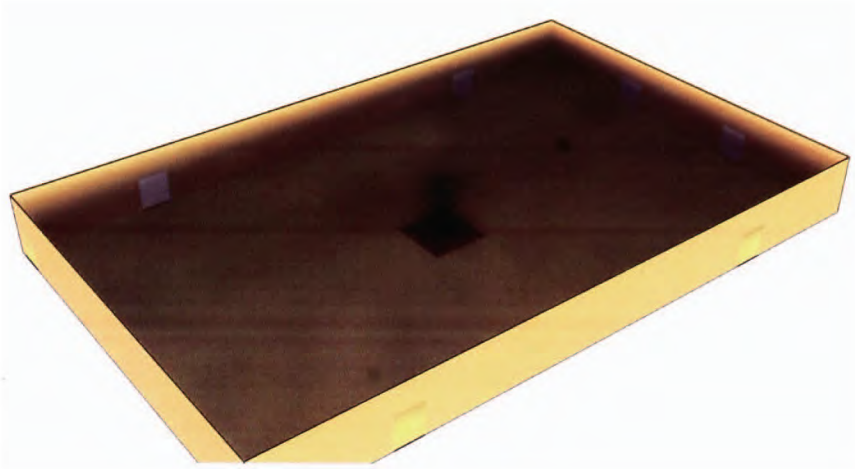

Figure 9-2 Smoke in a hall (generated in SmokeView (Forney G. , 2009))

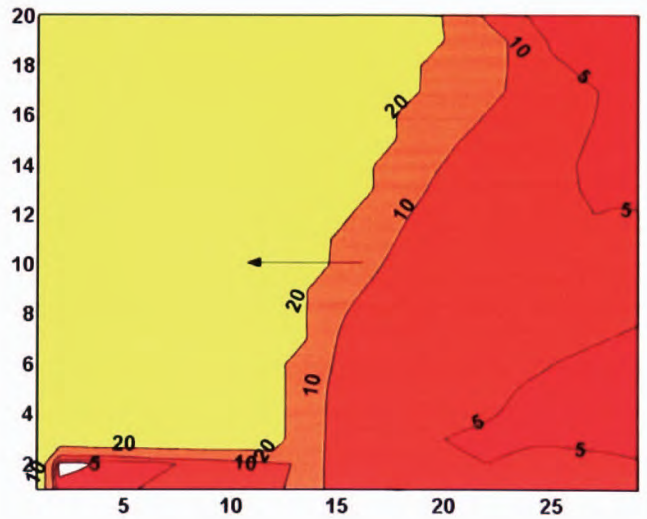

Figure 9-3 Visibility of the left wall (Husted, Carlsson, & Göransson, 2004)

Comparing with optical density contours, the contours of visual distance represents a step forward. It can calculate light extinction in a given direction. What it can't offer is the effect from environmental factors other than the smoke itself. For example, it can't tell the difference of different signs. It also cannot see any ambient light.

In computing graphic, Jensen extended his photon-mapping technique into volume scattering and simulated the images of clouds (Jensen & Christensen, 1998). It solves equation 2-26 directly. In-scattering was included as part of the solution. The result showed white/light gray clouds instead of black smoke as in the output of the line of sight simulation. It has been pointed out in the last section that the photon-mapping method is expensive. When applied to light transport in participating media, the cost becomes even higher. As the output of computer graphics, the results were not validated and no justification has been given as if the solution satisfies the law of physics such as energy conservation.

9.3 Summary

The existing computation of visibility in smoke as a post process of CFD fire simulation is over simplified, inadequate and therefore requires improvement. The difficulty is the high computing cost involved in solving the radiation transport equation. Traditional approximation, based on series expansion such as the P_N method, leads to formulae that are too complicated to solve. The discrete ordinate method or S_N method, although a quite straight forward angular discretization approach, is suffering from numerical error such as ray effect and false scattering. Therefore cannot be applied to image generation. The zonal method is relatively simple in concept but the cost of calculating view factors can be prohibitively high in 3D heterogeneous cases that require high spatial resolution. Applying to image generation, all these methods lead to the problem of aliasing.

On the other hand, the Monte Carlo ray tracing method has been proven to be accurate, versatile and capable to generate high resolution image. It has been linked with long computing time because of its low convergence rate. Recently its efficiency has been improved through combining the method with irradiance caching and multi-pass tracing. A good example in this area of development is the photo-map method. Its success in generating credible synthetic images of caustics has been very impressive. Its unstructured caching algorithm still presents as a cost obstacle in simulating heterogeneous media such as fire smoke. In the next chapter, the current author introduces a new, more efficient hybrid Monte Carlo method that is capable of caching irradiance for fire smoke.

Chapter 10. Numerical simulation model in the current study

Experimental work is necessary in establish various mechanisms relevant to fire protection. Real fire scenarios are too complex and expensive to be verified in the laboratory. This is the area numerical simulation has been proven to be very useful. Although numerical simulation is easy and less expensive relative to laboratory test, some of the simulation work still requires large computer and long running time (days, weeks or even longer). The simulation of image based visibility in fire smoke is one of such case. Among all the algorithms reviewed in the last chapter, the zonal method and the Monte Carlo method are the two best candidates in serving the current objective. Unfortunately both of them are high cost algorithms. In this chapter, the current author introduces a new hybrid algorithm that adds the structured irradiance cache of zonal method into the more accurate and versatile Monte Carlo algorithm. Combining this hybrid algorithm with the dynamically adaptive octree mesh and a two pass tracing procedure, the new simulation model is capable of solving the RTE under any known condition to the required accuracy with reasonable cost.

10.1 Introduction

The aim of the current study is to establish a computer simulation program that can accurately predict the image of an illuminated sign over a distance filled with participating medium, more specifically, smoke. This is somehow different from the aims followed by the previous authors reviewed in the last chapter. They are in two campuses. In the first campus are the scientists and thermal engineers. Their objective is to achieve good accuracy in terms of physical properties such as overall energy balance and local mean temperature and heat fluxes even the results itself may be visually unsmooth. People in the second campus, namely the computer graphics engineers are looking for simulation results that are visually credible and pleasant as well as computationally efficient often at the cost of physical accuracy. The current study is an attempt to establish fire engineering conclusions based on simulated virtual images that is both physically accurate and also visually acceptable since human eye is sensible to image details.

As an engineering tool, the simulation model should satisfy the following requirements.

1. It should include all the main physical processes involved in light transport with participating media.
2. The results of the simulation must accurately reflect physical reality. Certain techniques (tricks, such as 3D texture map, artificial scattering, etc.) used in computer graphics to accelerate the simulation on the expense of numerical accuracy or even physic correctness are not acceptable.
3. The image generated from the simulation should be both physically and visually realistic.
4. The algorithm developed should be easily parallelisable to take the advantage of multiprocessor/distributed computing.
5. The algorithm should be easy enough to allow data import/export from other numerical analysis such as FEA and CFD.
6. Reasonable rendering performance would be advantageous provided that it is not on the expense of accuracy.

In view of the exiting methods and the above requirements, a new hybrid of Monte Carlo ray tracing and zonal method has been developed in the current study.

10.2 Why creating a new model?

From Chapter 9 it can be seen that numerical simulation of radiation transport is linked with high computing cost. In order to achieve the requirement laid out in the last section, the cost would be even higher. Among the existing approaches reviewed in Chapter 9, the closest approximation methods that may satisfy the current requirements are the zonal and photon-mapping (a cached Monte Carlo) methods.

The problem with the zonal method is the high cost in computing view factors. In transient simulation, either static high resolution mesh or dynamic adaptive mesh would be too expensive in generating view factors.

The limitation of Photon-mapping comes from its unstructured nature of photon data. On the surface, it is very flexible since it can dynamically construct any surface with points. In reality, it is a costly process. In simple case such as caustics where the surface is simple and well defined, photon mapping is effective but still expensive (Jensen H. , 1996). In media that has continuous distribution in space, there is no clear surface of the medium or interface between media, the method has difficulty to determine the interaction point where to seed a photon. Although the method has been extended into area such cloud simulation with volume photon

map, the in-scattering calculation requires 3D searching and interpolation among huge number (millions) of unstructured photons, the cost is still high even after special technique such as GPU programming has been implemented (Boudet, Pitot, Pratmarty, & Paulin, 2005).

The method proposed in this chapter is a hybrid of the above two methods. It combines the zonal style cache and the photon-mapping style caching. Irradiance is cached on prescribed mesh via Monte Carlo ray tracing. It does not compute the costly view factors and there is no 3D searching and unstructured data interpolation involved. The implementation of dynamic mesh adaptation technique means the total number of mesh points can be controlled according to the required accuracy therefore the overall computing cost would be reduced further.

10.3 Scene or domain

A scene or domain is the subspace to be simulated in a numerical model. Scene is often used when the physical or visual aspect of the simulated space is referred and domain may be used to refer to the computational aspect. In the current study they can be used interchangeably.

10.4 The two pass procedure

The current method generate images in two passes: shading and rendering. In the shading pass a 3D radiosity map (the irradiance cache) will be built on the prescribed mesh. In the rendering pass, backward path integration for rays issued from each pixel of the image will be carried out. The main advantage of a two pass algorithm is preventing excessive number of rays being introduced in order to improve image accuracy therefore speeding up the convergence. A view independent radiosity map is also for reuse when multiple images from different point and direction are required such as the task of building a floor map of visibility (section 11.8).

10.5 Spectra model

The spectra distribution of light has been discretized into colour channels so that

$$\int_{\lambda_a}^{\lambda_b} L_\lambda d\lambda = \sum_{\eta=0}^{\eta=n-1} \left[\int_{\lambda_\eta}^{\lambda_{\eta+1}} L(\lambda) d\lambda \right] = \sum_{\eta=0}^{\eta=n-1} L_\eta \Delta\lambda \qquad 10\text{-}1$$

L_η is the radiance of channel η. Typically, also in the current study, 3-channel representation is used. They are called R, G, B named after the wavelength of their peak radiance as depictured in Figure 10-1

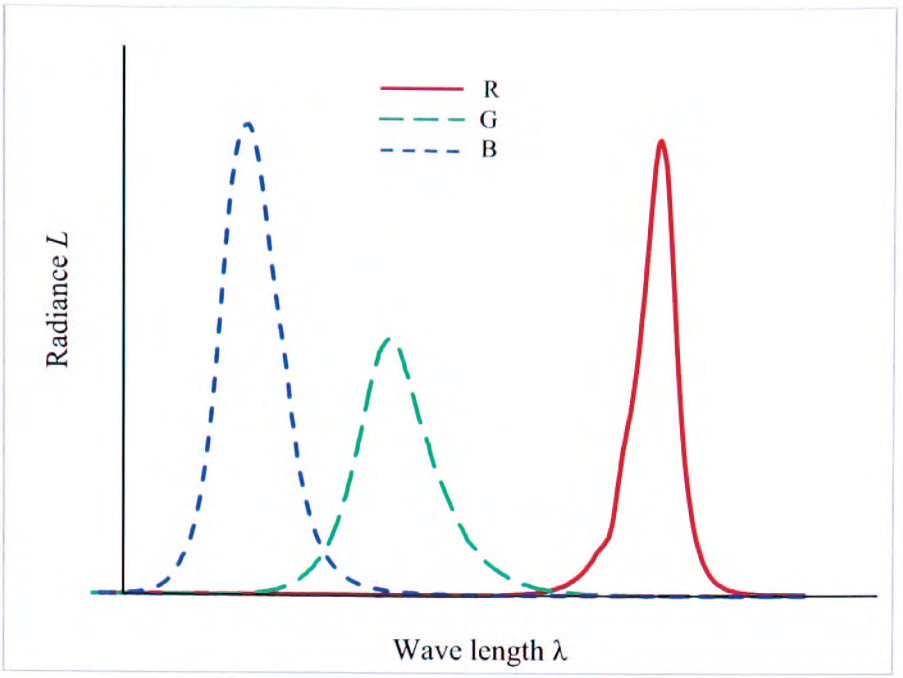

Figure 10-1

In this study, the subscript η is often omitted so that the un-subscripted L is used to represent any one of the said channels.

10.6 Shading

10.6.1 Light source and surface light emission

Light is introduced from light sources in the form of rays. The simplest light source is a surface area emitting light of each channel as $L(\vec{x},\vec{\omega})$ and

$$\int_S \int_\Omega L(\vec{n}\cdot d\vec{\omega})ds = \Phi_0$$

where $\vec{n}$ is the surface normal and Φ_0 is the illumination energy flux or power in watt. For convenience here the unit of lumen is not used to avoid unnecessary conversion. Ω is the hemisphere in the direction of $\vec{n}$ and S represents the illuminating surface of the light source.

The corresponding ray representation of the light source is

$$\sum_{j=1}^{N} \phi_j(\vec{x}_j,\vec{\omega}_j) = \Phi_0 \qquad 10\text{-}2$$

There are total N rays introduced for the current colour channel and each ray initially carries energy flux ϕ_j starting from point $\vec{x}_j$ on the surface in direction $\vec{\omega}_j$, a direction within the hemisphere Ω. $\vec{x}_j$ and $\vec{\omega}_j$ are sampled according to given spatial and angular distribution functions.

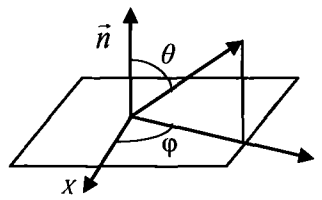

Figure 10-2

Figure 10-2 is a rectangular plain surface emitting light diffusively. $\vec{x}_j$ is uniformly distributed on the surface. At each point $\vec{x}_j$, $\vec{\omega}_j$ is determined by the zenith angle θ and the azimuth angle φ. The zenith angle θ is sampled between 0 and $\pi/2$. It satisfies the importance sampling function $\cos\theta$. The azimuth angle φ is uniformly sampled between 0 and 2π. All rays sampled have the same energy flux

$$\phi_j = \frac{\Phi_0}{N} \qquad 10\text{-}3$$

10.6.2 Surface scattering

In the current study, all surfaces are assumed to be solid and opaque without subsurface scattering of light. Light hits a surface at a point and will be reflected at the same point. Surface reflectance is governed by the bidirectional reflectance distribution function (BRDF) as defined by equation 2-31. In most of the cases concerned, either the surfaces themselves are diffusive or due to the scattering of incident light by smoke, the exitant light from the surfaces would follow diffusive distribution. Therefore a further assumption here is that surface reflectance is always Lambertian. Although not required by the algorithm itself, it makes the treatment of surface scattering much simpler and saves computer storage.

10.6.2.1 Irradiance cache

With Lambertian reflectance assumption, the total incident power in colour channel η falling on a surface element can be defined as

$$\Delta\Phi_{inc} = \sum_{j=1}^{n} \phi_j \qquad 10\text{-}4$$

In the framework of ray tracing, the incident light has been represented by individual ray arrived at the surface element. Each of them possesses radiance power ϕ_j. The subscription η has been omitted since light from all channels and their mixture behave in the same way.

The incident rays can be put into two groups, the ones directly from the light sources and the ones as the result of surface/volume scattering

$$\Delta\Phi_{inc} = \Delta\Phi_{inc,dir} + \Delta\Phi_{inc,sca} = \sum_{j=1}^{m} \phi_j + \sum_{j=1}^{n} \phi_j \qquad 10\text{-}5$$

where m is the number of rays directly from light source and n is that for the rest of the domain. In cases without participating media, $\Delta\Phi_{inc,dir}$ is a constant and $\Delta\Phi_{inc,sca}$ varies till convergence is achieved.

10.6.2.2 Monte Carlo radiosity

Unlike other Monte Carlo ray tracing based methods (Dutré, Bekaert, & Bala, 2003; Jensen, 1996), the current method terminate all incident rays on non-specula surfaces. New rays are issued in the same way as for light emitting from a simple diffuse light source with the energy flux Φ_0 being replaced by $\Delta\Phi_{ref} = \sigma_{ref}\Delta\Phi_{inc}$.

10.6.3 Surface mesh

10.6.3.1 Basic requirements

In fire simulation, the geometry is often generated with CAD software. The geometry surfaces are most likely to be in B-rep (boundary representation) form. For the sick of argument, in the current study it is assumed that only triangulated surface mesh is used in defining geometries. An additional requirement is that within each surface there would be no T-connection of the edges. An edge can only be connected to other edges by nodes at its ends and there should be no open-ended edge. Figure 10-3 illustrates the basic mesh requirements on a surface.

All the meshes in the second row are unacceptable. The first contains T-connection of edges. The second contains non-triangular element and the last one has an open end edge.

A geometry element may be constructed from several surfaces with physical properties such as colour defined on each of them. Surface normal is defined on each node of surface mesh.

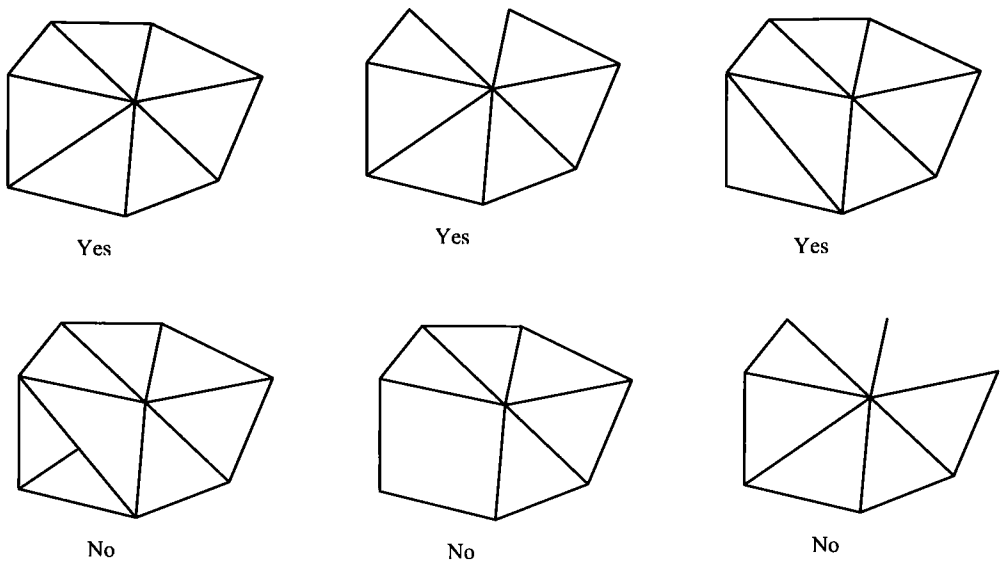

Figure 10-3 Valid and invalid surface mesh element

10.6.3.2 Functions defined on nodes

With tessellated surface representation as used in the current study, certain function such as irradiance would be defined on each surface element. Such functions are convenient in surface caching and assurance of energy conservation but can cause aliasing on image. In order to get smooth surface image, the current method convert the piecewise solution to solution defined on nodal points. The following conversion is used for any function that needs to be converted.

$$f_{node} = \sum_{i=0}^{n} a_i f_i \qquad 10\text{-}6$$

where f is the function to be converted and n is the number of surface elements connected to the node. a_i's are weighting factors defined as

$$a_i = \frac{\Delta A_i}{\sum_{j=1}^{n} \Delta A_j}$$

where ΔA_j is the surface area of element j connected to the node. The area weighted averaging is based on the consideration that $f_{element}$ defined on large elements are statistically more stable than that on the small elements. It will improve the smoothness of the nodal function f_{nodal}. It

also means that the result would be more diffusive. This concern has been addressed through progressive mesh adaptation.

Under the assumption of Lambertian surface, radiance on surface element ΔA_i can be determined by surface irradiance as

$$L_i = \sigma_{ref,i} \frac{\Delta \Phi_{inc,i}}{\pi \Delta A_i} \qquad 10\text{-}7$$

The value at a node can be calculated with expression10-6 as

$$L_{node} = \sum_{i=0}^{n} a_i L_i \qquad 10\text{-}8$$

It should be mentioned that the above conversion operation is only carried out before the final image generation stage and uses temporary memory storage.

10.6.3.3 ***Progressive surface mesh adaptation***

In mesh based approximation as the radiosity method, the characteristics of mesh plays an important role in determine the accuracy of the solution. Cohen (Cohen & Wallace, 1993) has summarised the influential mesh characteristics into four categories: density, order, shape and discontinuity representation. In the current study, the order of the surface mesh element is linear so that it is easier to ensure energy conservation. The only shape of the surface element is triangle. In order to improve the accuracy of the solution, mesh density needs to be controlled.

Assuming f is a function defined on a surface A, at a point $\vec{x}$, f over a distance $\Delta\vec{s}$ can be approximated as

$$f_{\vec{x}+\Delta\vec{x}} = f_{\vec{x}} + \Delta f = f_{\vec{x}} + \Delta\vec{s} \cdot \nabla f$$

The error of the approximation is $O(\Delta s^2)$. In the current study, by keeping the variation of Δf approximately the same within the domain, the mesh size Δs can be controlled by

$$\Delta s = \frac{\xi}{\vec{n}_s \cdot \nabla f} \qquad 10\text{-}9$$

where ξ is a global constant having the same dimension as f and $\vec{n}_s$ is the unit vector in $\Delta\vec{s}$ direction. If there are more than one controlling functions, there would be one constant ξ

corresponding to each of them and the local mesh density is the minimum of all Δs determined by equation 10-9. The local gradient ∇f is estimated from the current value of f by (see Figure 10-4)

$$\begin{vmatrix} \partial f/\partial x \\ \partial f/\partial y \\ \partial f/\partial z \end{vmatrix} = \begin{vmatrix} (x_A - x_o) & (y_A - y_o) & (z_A - z_o) \\ (x_B - x_o) & (y_B - y_o) & (z_B - z_o) \\ (x_C - x_o) & (y_C - y_o) & (z_C - z_o) \end{vmatrix}^{-1} \begin{vmatrix} f_A - f_o \\ f_B - f_o \\ f_C - f_o \end{vmatrix}$$

where

$$f_o = (f_A + f_B + f_C)/3$$

The current control of mesh density leads to a good representation of discontinuity with less number of mesh elements in regions where function f is relatively smooth.

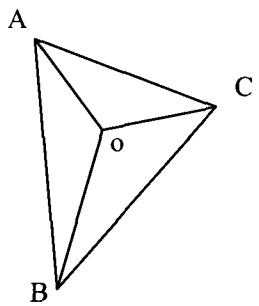

Figure 10-4

Figure 10-5 shows the result of the simulation for the popular benchmark case of Cornell box. The simulation started with the mesh shown at the bottom left. After 3 iterations, the solution converged and the final mesh is shown at the bottom right of Figure 10-5. It can be seen in Figure 10-5 that in the region where luminance is uniform, the surface mesh is coarse. The finest mesh appeared near the edges of shadow.

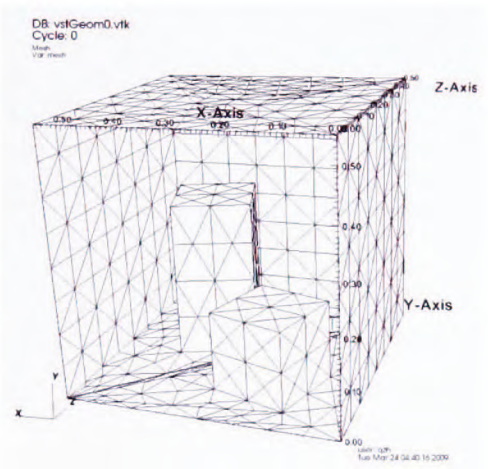

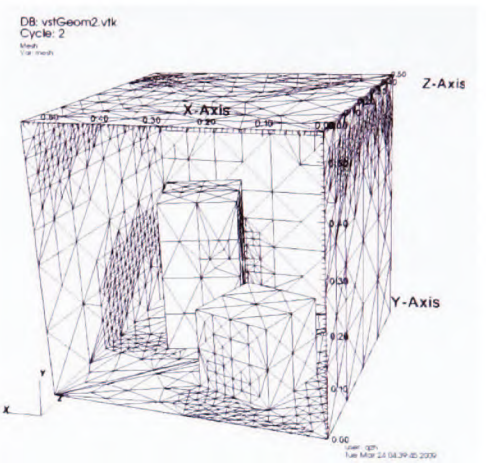

Figure 10-5 Cornell box

10.6.4 Volume scattering

10.6.4.1 Volume cache

In the current model the medium is assumed to be diffusive and heterogeneous. The spatial distribution of medium is almost always given in the form of 3D array related to a mesh system. Therefore it is preferable that the volume scattering calculation utilises the same data structure that is compatible with that used in the zonal method. It has been learned in the last chapter that the zonal method requires high cost computation of view factors. In order to reduce the cost, a new Monte Carlo ray tracing based method has been developed in the current study that caches the irradiance of the media.

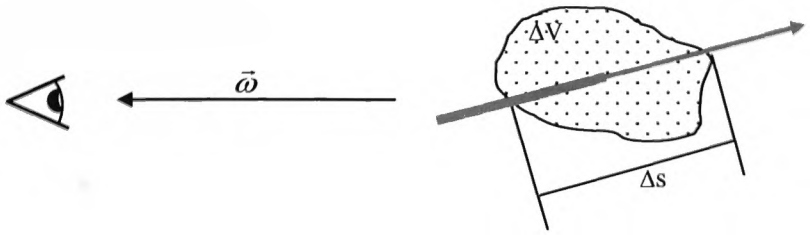

Figure 10-6

Figure 10-6 shows a ray with power ϕ passing through a small volume ΔV in space filled with participating medium. The loss of power due to scattering is $\Delta\phi_{sca}$. If there are n similar rays passing the volume, the scattered light detectable in the $\vec{\omega}$ direction would be

$$dL = \frac{ds}{4\pi}\int_{\Omega} p_{\omega'\to\vec{\omega}} L_{\vec{\omega}} d\omega' \approx \frac{ds}{4\pi\Delta V}\sum_{i=1}^{n} p_{i,\vec{\omega}}\Delta\phi_{sca,i} \quad [1] \qquad 10\text{-}10$$

The power cache

$$\Delta\Phi_{sca}(\vec{\omega}) = \sum_{i=1}^{n} p_{i,\vec{\omega}}\Delta\phi_{sca,i} \qquad 10\text{-}11$$

is defined on ΔV. Under the assumption of isotropic medium, $\Delta\Phi_{sca}$ is a scalar

$$\Delta\Phi_{sca} = \sum_{i=1}^{n}\Delta\phi_{sca,i} \qquad 10\text{-}12$$

Unlike in the case of surface scattering, a ray passes the volume ΔV will continue its course until the total power that it possesses has extinguished. New rays will be introduced from volume ΔV. The power of each ray is

$$\phi = \frac{\Delta\Phi_{sca}}{m} \qquad 10\text{-}13$$

where m is the total number of newly introduced rays.

[1] This is different from Jensen (Jensen & Christensen, 1998). Jensen gave expression of L instead of dL and ds was replaced by $1/\sigma_{sca}$. It is the current author's view that 10-10 is a more proper approximation of in-scattering. Jensen's approach is suitable for single scattering such as that on the liquid – air interface (caustics) but not in continuous heterogeneous media.

10.6.4.2 Volume mesh adaptation

In the current study the domain is divided by Cartesian volume mesh. The participating media is defined on each node of the mesh and rays will be traced within each volume cell. The mesh is organised in an octree as shown in Figure 10-7.

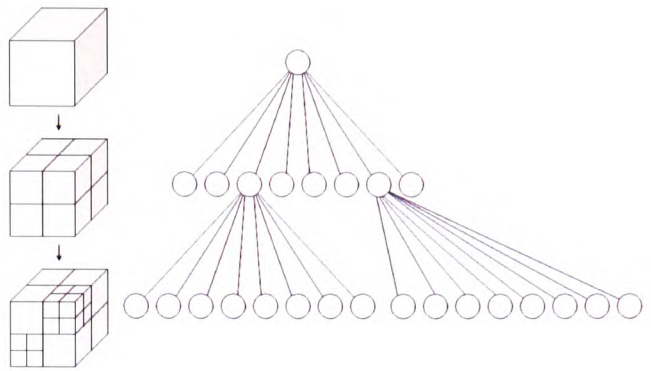

Figure 10-7

Unlike body-fitted meshes, the current mesh will "cover" the entire geometry in the way shown in Figure 10-8(a). Surface scattering still takes place on the surface of geometry regardless its relation with the mesh (Figure 10-8 (b)).

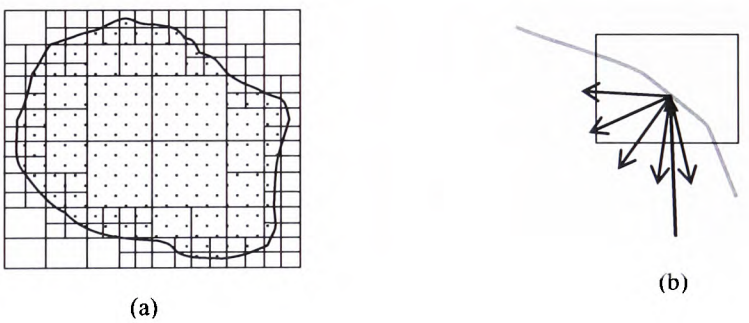

Figure 10-8

The tree structure makes grid refining/coarsening a simple dividing or deleting operation. The Cartesian nature of the cells makes other geometrical operations such as intersection with geometry surface much simpler. Figure 10-9 shows the volume mesh in the same Cornell box simulation as in Figure 10-5. The figure on the right is the bottom view. The red lines mark the geometry surface.

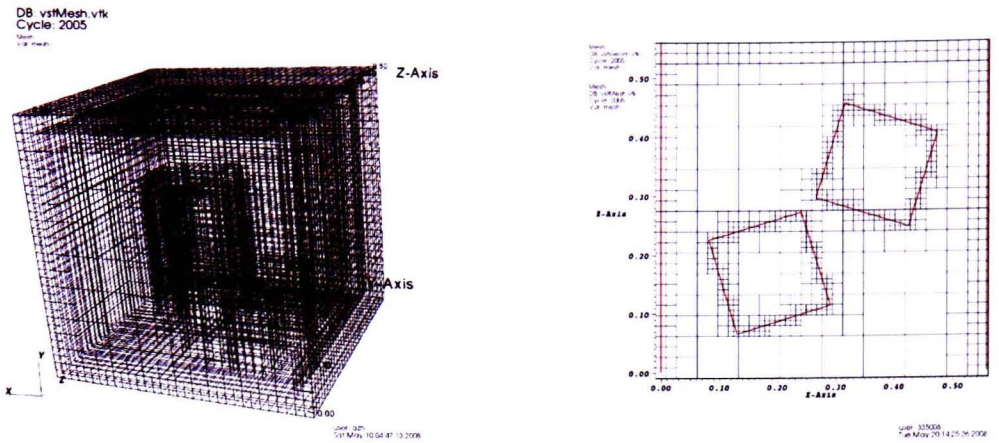

Figure 10-9 Volume mesh adaptation to fit geometry

Figure 10-10 shows how the mesh can be dynamically adapted to the solution in section 11.1. The 3D mesh is shown on the left of Figure 10-10. On the right hand side of Figure 10-10 is the middle cross section of the mesh overlapped by the filled contours of the solution.

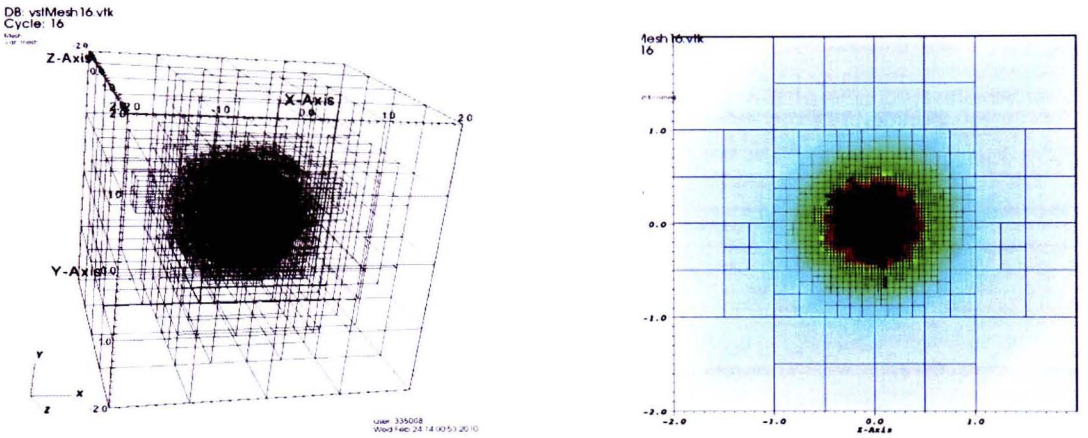

Figure 10-10 Volume mesh adaptation to solution

10.6.4.3 ***Ray tracing***

After leaving a geometry surface, a ray will be traced through the volume mesh on cell by cell base. Starting from a position $\vec{p}_0 = (x_{10}, x_{20}, x_{30})$ in a cell, the exit point of the ray would be on one of the cell boundary. The boundary point is determined by

$$\vec{p}_1 = \vec{p}_0 + t\vec{\omega}$$

$$t = \max[0, \min(t_1, t_2, t_3)] \qquad t_i = \max\left(0, \frac{x_{i1} - x_{i0}}{\omega_i}\right)$$

where the subscript i represents one of the principle coordinate and $\vec{\omega} = (\omega_1, \omega_2, \omega_3)$ is the unit vector in the direction of the ray. After $\vec{p}_1 = (x_{11}, x_{21}, x_{31})$ is determined, the ray will be set in the neighbouring cell and the above process would be repeated. The tracing algorithm is very efficient when combined with mesh adaptation shown in the last section.

In a boundary cell, there is a lookup table listing all surface elements that are either within or intersect with the cell boundary. In this case,

$$t = \max[0, \min(t_1, t_2, t_3, t_b)]$$

where t_b is the minimum parameter for the ray to intersect the nearest surface element from the lookup table. If the ray does intersection a surface element, tracing is terminated and surface scattering takes place.

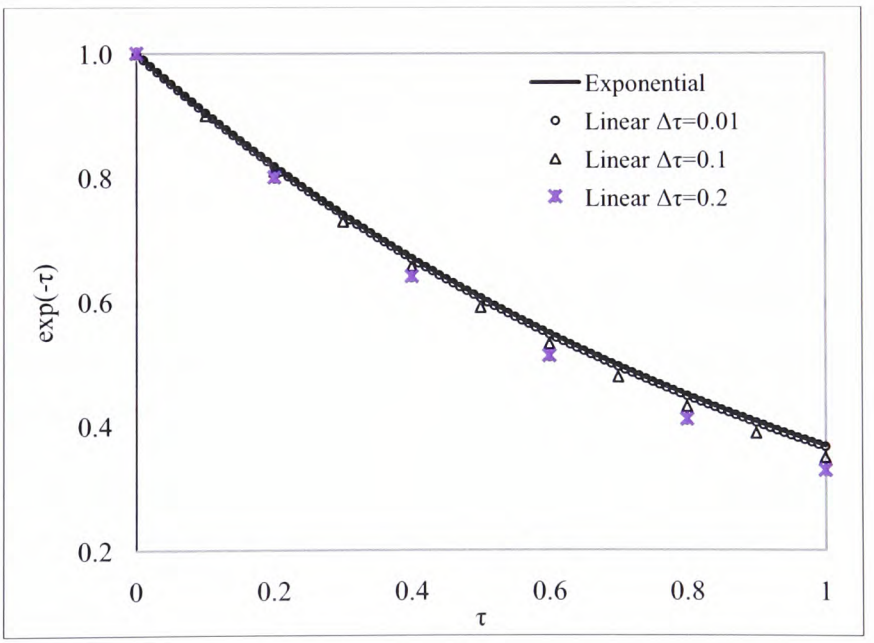

Figure 10-11

With participating media, the power of the ray is updated at the end of each tracing step according to the value of $\Delta\tau = \sigma|\vec{p}_1 - \vec{p}_0|$

$$\begin{cases} \phi_1 = \phi_0 e^{-\Delta\tau} & \Delta\tau > 0.1 \\ \phi_1 = \phi_0(1-\Delta\tau) & \Delta\tau \le 0.1 \end{cases} \qquad 10\text{-}14$$

Figure 10-11 shows the approximation of $e^{-\tau}$ by marching with different $\Delta\tau$. It can be seen that even with $\Delta\tau = 0.2$, the result of numerical integration is still very close to $e^{-\tau}$.

The power loss of the ray due to scattering is

$$\Delta\phi_{sca} = \rho(\phi_0 - \phi_1) \qquad 10\text{-}15$$

where ρ is the albedo of the media. The scattered radiant power $\Delta\phi_{sca}$ is cached and subsequently re-emitted as described in section 10.6.4.1.

10.6.4.4 Energy conservation, convergence and cost

The shading algorithm described above is conservative. For non-absorbing media, at the end of each iteration, the total irradiance on surfaces and in the media of the domain equals to the total emission

$$\sum_{j=1}^{N_v} \Phi_{v,j} + \sum_{k=1}^{N_s} \Phi_{s,k} = \sum \Phi_{emt} \qquad 10\text{-}16$$

where $\sum \Phi_{emt}$ is the total power emission from light sources. N_v and N_s are the total number of volume and surface elements respectively. Φ is the cached power. Equation 10-16 also ensures that the algorithm is bound.

To see that the algorithm does offer converged solution, the following assumptions have been added to simplify the discussion without losing the generality of the conclusion.

1. The medium is isotropic.
2. The number of rays introduced from each surface/volume element is sufficiently large so that the variance due to Monte Carlo sampling is less than the truncation error of irradiance cache.

At any time, the irradiance at a point, regardless it is in the domain or on its surface, would be the total of radiation from all other surface/volume elements toward it.

$$\Phi_i^k = \sum_{j=1, j\neq i}^{N} v_{ij} a_{ij} \frac{n_{ij}}{m_j} \left(\Phi_j + \Phi_{emt,j}\right) \qquad 10\text{-}17$$

Where m_j is the number of rays issued from element j (emission or scattering) and n_{ij} is the number of rays from element j and passing element i. v_{ir} (or $v_{ij} = n_j v_{ir}$) is the visibility function defined as

$$v_{ir} = \begin{cases} e^{-\sigma s_r} & \textit{ray } r \textit{ passes element } i \\ 0 & \textit{otherwise} \end{cases} \qquad 10\text{-}18$$

Here s_r is the distance that ray r has travelled from its origin till hitting element i. It should be noticed that expression 10-17 is equally applicable to both surface and volume elements. a_{ir} depends on the type of elements concerned.

$$a_{ir} = \begin{cases} \sigma_{sca,i} \Delta s_{i,r} & \textit{element } i \textit{ is volume type} \\ k_i & \textit{element } i \textit{ is surface type} \end{cases} \qquad 10\text{-}19$$

Equation 10-17 can be written in matrix form as

$$\Phi = T\Phi + B \qquad 10\text{-}20$$

where Φ is the irradiance vector, T is the scattering operator and

$$t_{ij} = v_{ij} a_{ij} \frac{n_{ij}}{m_j} \qquad i \neq j$$

B is the constant vector representing irradiance from light sources. The solution of 10-17 can be expressed as

$$\Phi = (I - T)^{-1} B \qquad 10\text{-}21$$

where I is the identity matrix and none of the element t_{ij} of T is negative. Therefore $(I - T)$ is invertible and solution 10-21 exists. The physical background of the problem tells that vector Φ is real and 10-16 ensures that it is also bound. The above conditions enable the expansion of $(I - T)^{-1}$ into Neumann series as (Meyer, 2000)

$$(I-T)^{-1}=\sum_{i=0}^{\infty}T^{i} \qquad 10\text{-}22$$

The sufficient condition for 10-22 to converge is $\|T\|<1.0$ (Jiang, Gao, & Wu, 1978). Let's take $\|T\|=\|T\|_1$ then

$$\|T\|_1=\max_j \sum_{i=1,i\neq j}^{n}|t_{ij}| \le \max_j\left(\frac{1}{m_j}\sum_{i=1,i\neq j}^{n}v_{ij}a_{ij}n_{ij}\right) \qquad 10\text{-}23$$

As nothing in the bracket of 10-23 is less than zero, it is not necessary to take absolute value. The summation in the bracket is over all elements that receiving radiant energy emitted from element *j*. It can be expressed in a different form as

$$\frac{1}{m_j}\sum_{i=1}^{n}v_{ij}a_{ij}n_{ij}=\frac{1}{m_j}\sum_{j=1}^{m_j}\sum_{i=1}^{n}v_{ij}a_{ij}\approx\frac{1}{m_j}\sum_{j=1}^{m_j}\sum_{i=1}^{n}\frac{\Delta x}{e^{i\Delta x}} \qquad 10\text{-}24$$

Here n is the number of cells a ray k, issued from element j, passes through along its path. Defining $\Delta x=\sigma_{sca}\Delta s$ therefore $\sigma_{sca}s_r\approx i\Delta x$. According to geometric series theory

$$\sum_{i=1}^{n}\frac{1}{e^{i\Delta x}}=\frac{1-e^{-n\Delta x}}{e^{\Delta x}-1}$$

Therefore

$$\frac{1}{m_j}\sum_{i=1}^{n}v_{ij}a_{ij}n_{ij}<\frac{1}{m_j}\sum_{j=1}^{m_j}\frac{\Delta x}{e^{\Delta x}-1}\approx\frac{1}{m_j}\sum_{j=1}^{m_j}\left|1-\frac{\Delta x}{2}+\frac{1}{12}\Delta x^2\right| \qquad 10\text{-}25$$

The condition for 10-22 to converge has become

$$\left|1-\frac{\Delta x}{2}+\frac{1}{12}\Delta x^2\right|<1$$

or

$$0.0<\Delta x<6.0 \qquad 10\text{-}26$$

On surfaces, condition 10-26 becomes $\sigma < 6.0$ which is guaranteed. For participating media, condition 10-26 imposes a restriction on cell size Δz of

$$\Delta z < \frac{6.0}{\sigma_{sca}} \qquad 10\text{-}27$$

It can be easily satisfied most of the time.

For a $(n \times n \times n)$ cube, the cost of the algorithm would be $O(mn^4)$ where m is the average number of rays issued from each point. Comparing with $O(n^7)$ for the zonal method, it is a very efficient method if the number of cells passed by a ray is assumed to be the same order as n.

There is no formal cost estimation for photon-map method. Due to its global adaptive nature, the cost varies considerably from case to case. Assuming that in the above cube, smoke concentration fluctuate due to eddies that have the same length scale as the cell size, in order to map such heterogeneous field, photon-map needs no less spatial point than the number of vertices in the current method. As 3D photon-map is global and unstructured, all operations must also be global therefore quite expensive. With the current method, once the mesh is created, almost all operations are local. The Cartesian nature of the structured mesh further reduces the complexity of the operations. Photon-map is not designed and therefore unsuitable for continuous heterogeneous field.

10.7 Rendering and the virtual camera

As has been explained in Figure 9-1, in principle image can be generated in the shading pass but the resolution of the image would require far too many rays to be introduced than necessary to get good image resolution. In the rendering pass, rays are introduced from the image surface and tracked back toward the scene. Once a ray hits a non-specula surface, path integration is carried out on the way back.

A virtual camera is a numerical model for image generation. The simplest and most popular model used in 3D computer graphics is the pinhole camera (Foley, Dam, Feiner, & Hughes, 1990). In a pinhole camera, light passes a small "pinhole" of an opaque plate then forms the image on a parallel plane as shown in Figure 10-12

Mathematically, the image of a pinhole camera is the result of a perspective projection transformation as shown in Figure 10-13.

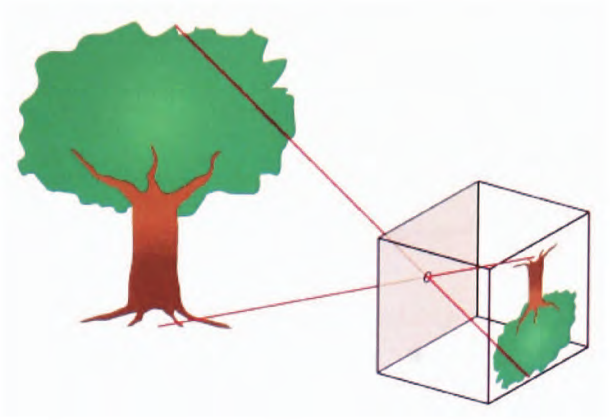

Figure 10-12 A pinhole camera

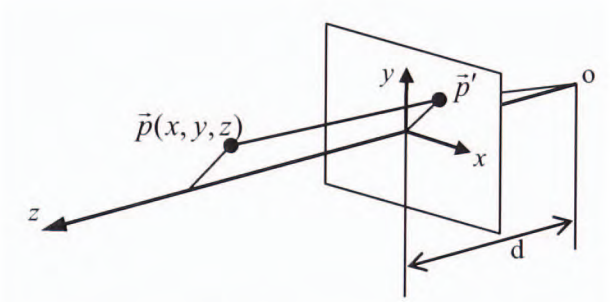

Figure 10-13 Perspective projection

The transformation can be expressed as (Foley, Dam, Feiner, & Hughes, 1990)

$$\begin{bmatrix} x' \\ y' \\ z' \\ w \end{bmatrix} = \begin{bmatrix} 1 & 0 & 0 & 0 \\ 0 & 1 & 0 & 0 \\ 0 & 0 & 1 & 0 \\ 0 & 0 & 1/d & 0 \end{bmatrix} \cdot \begin{bmatrix} x \\ y \\ z \\ 1 \end{bmatrix} \qquad 10\text{-}28$$

Although widely used in computer graphics, pinhole camera is optically inefficient therefore rarely used in practice. Most optical devices utilise lens to collect more light therefore enhance image quality. A lens can generate the image of a point from all light passing its surface instead of just that passing a pinhole as in Figure 10-14

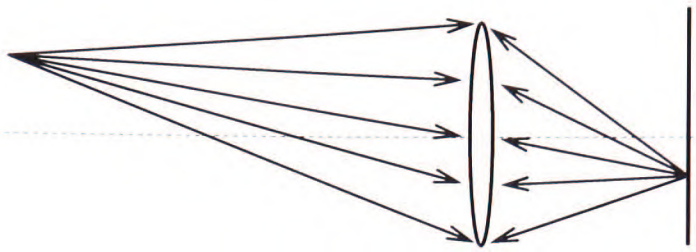

Figure 10-14 The image of a point formed with lens

In the current study, the virtual camera is a model of the lens system.

10.7.1 Model requirements

A real optical system such as the camera to be modelled here often contains more than one group of lenses as shown in Figure 10-15 (WITZ, 2008).

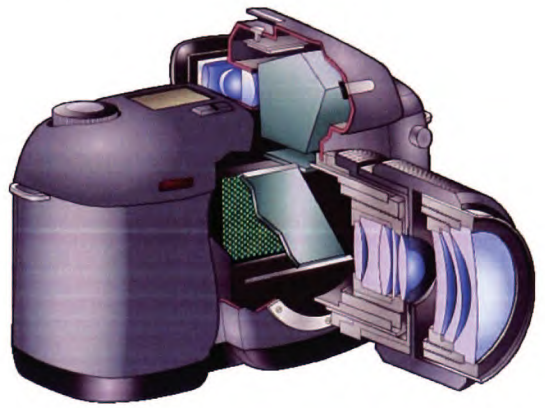

Figure 10-15

Although the thick lens model that covers the complete lens structure exists (Kolb, Mitchell, & Hanrahan, 1995), it is impractical in most cases since the structure of lenses for most commercial systems are not available. As being mentioned before, a pinhole model can generate the image and simple to implement but it can't simulate the effect of lenses on the light intensity of an image. In many computer graphics application, it is more important to get the depth of field of a camera than the true light intensity. Potmesil proposed a method that extends the pinhole model. He assumed that the diameter of the circle of confusion equals to 1/10000 of the object distance from the lens. Therefore the depth of field is determined when the diameter of the circle of confusion is equal to the dimension of the pixel. Potmesil first generated the image with pinhole camera model and then applied the circle of confusion to the image in a post-processing stage (Potmesil & Indranil, 1981). Cook (1984) simulated the depth of field and circle of confusion directly with his fixed focal length thin lens model in the rendering pass.

In the current study, a new abstract camera model is introduced that satisfies the following requirements:

1. The model yields the real light intensity of the image.
2. The lens is a variable focal length zoom.
3. The lens has finite aperture.
4. As an abstract model, no lens characteristics that relates to the material and manufacturing process such as aberration would be modelled.

The parameters given as model input are

1. Focal length.
2. Target plane (the object plane being focused on).
3. Focal plane (image plane).
4. Camera aperture.
5. Lens efficiency.

10.7.2 Lens model

Figure 10-16 depicts the thin lens model in the current study. Unlike Cook's model (Cook, Porter, & Carpenter, 1984), here the lens represents an optical zoom and the position of the principle plane *o* is not fixed.

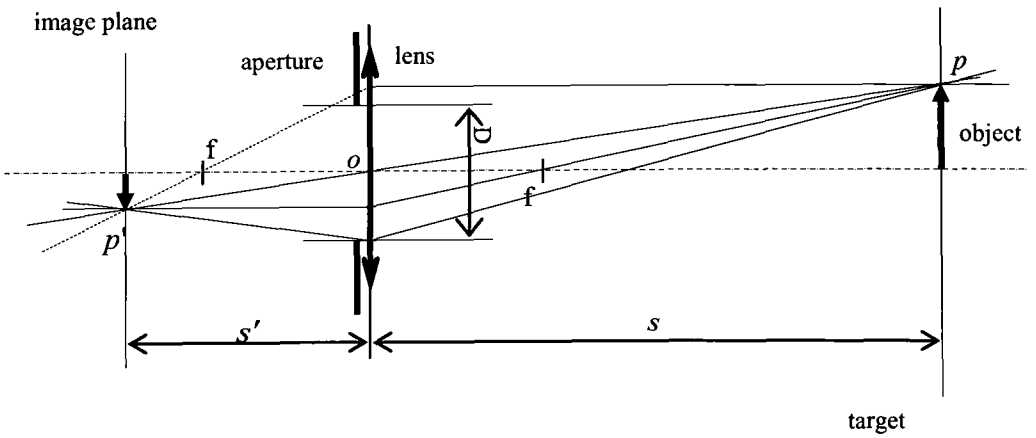

Figure 10-16

The position of the principle plane can be determined by Gaussian lens formula (Blaker & Rosenblum, 1993) . Once the camera position (image plane) and the position of the target plane are given the position of the principle plane would be calculated with

$$\begin{cases} s + s' = S \\ \frac{1}{s'} + \frac{1}{s} = \frac{1}{f} \end{cases} \qquad 10\text{-}29$$

The solution of 10-29 is

$$\begin{cases} s = \sqrt{\left(\frac{S}{2}\right)^2 - fS} + \frac{S}{2} \\ s' = \sqrt{\left(\frac{S}{2}\right)^2 - fS} - \frac{S}{2} \end{cases} \qquad 10\text{-}30$$

Equation set 10-30 offers real solution for s and s' under the condition

$$f \le \frac{S}{4}$$

As the Guassian lens formula is based on a coordinate system originated at point o, s and s' have opposite signs.

[1] The second set solution of equation 10-29 does not generate real image.

10.7.3 Depth of field

When an object is not in the target plane, light from a point on the object will form a circular area on the image plane instead of a point as shown in Figure 10-17. This circular area is called the circle of confusion.

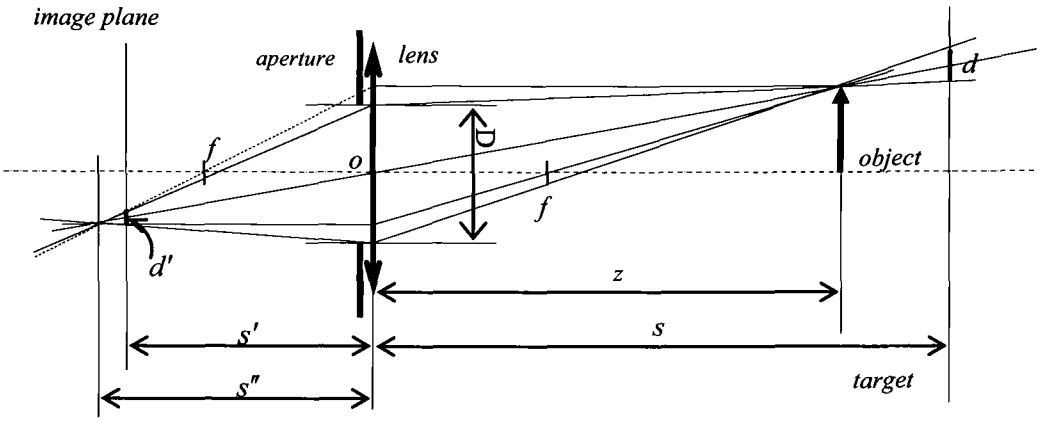

(a)

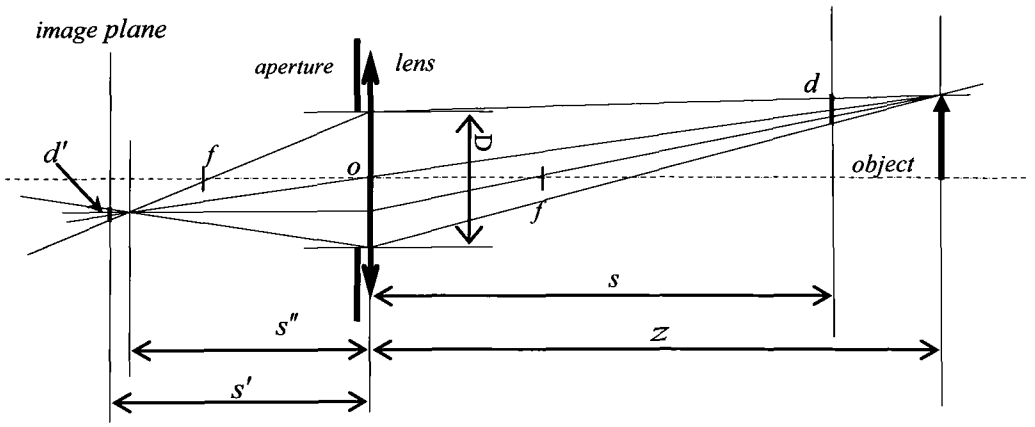

(b)

Figure 10-17 Image of out-of-focus point

Denoting the diameter of the circle of confusion as d' then d' can be determined by

$$d' = \frac{|s-z|}{z}\frac{s'}{s}D \qquad 10\text{-}31$$

where D is the diameter of the aperture and z is the distance of the object from the principle plane. The depth of field (*dof*) would be $|s-z|$ when d' equals to the pixel dimension Δx of the image sensor:

$$dof = \frac{\Delta x s}{D\frac{s'}{s} \pm \Delta x}$$

where the (+) sign corresponds to the case of $s>z$ (Figure 10-17 (a)) and the (-) sign corresponds to the case of $s<z$ (Figure 10-17 (b)).

In rendering pass, a number of rays are issued from each pixel toward the aperture and subsequently tracked through the scene. The result irradiance from each ray is equally distributed within the circle of confusion[1].

(a) Target plane is 4.2m from lens (in focus)

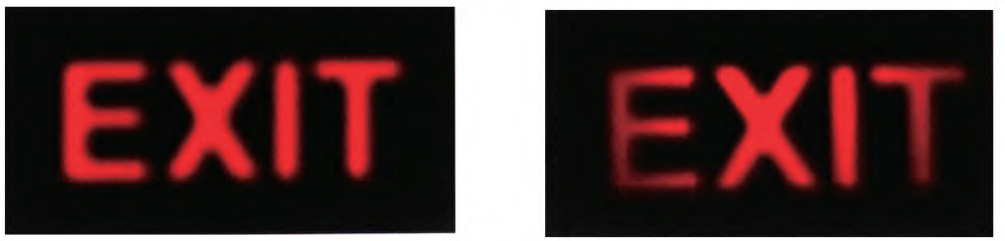

(b) Target plane is 5.0m from lens

[1] The real distribution of irradiance within the circle of confusion depends on the BRDF at the original surface point as well as the characteristic of the lens. Uniform distribution is an assumption used in the current study.

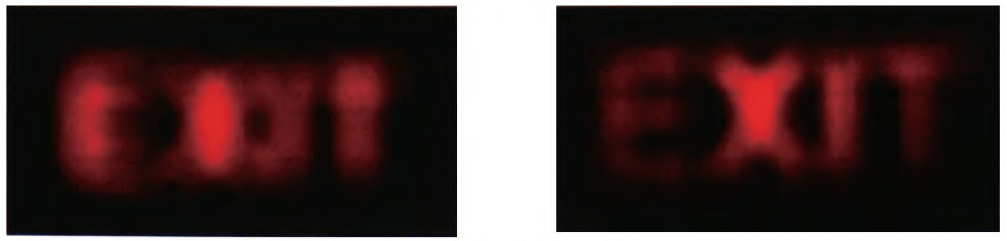

(a) Target plane is 7.0m from lens

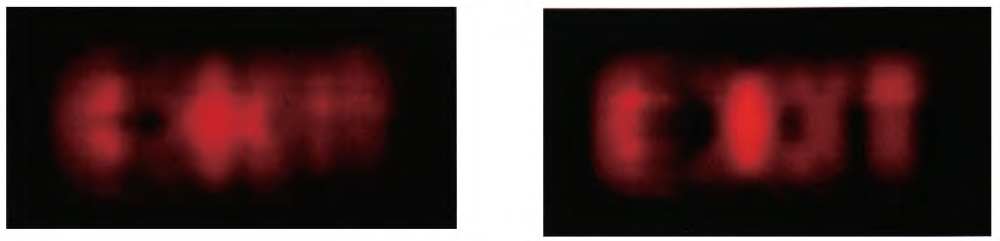

(b) Target plane is 10.0m from lens

Figure 10-18 Simulated (left) and photographic (right) image focusing

Figure 10-18 shows the comparison between the simulated results (on the left) and the photographs from Canon 10E digital camera (on the right). The simulation has reproduced the out-focusing effect of the camera.

10.7.4 Pixel irradiance

As shown in Figure 10-16, the total radiant energy falls on a pixel of the image sensor (p') is equal to the energy transmitted within the cone formed by the surface of the lens and point p on the target plane:

$$E_{pixel} = \int_{A_{pixel}} \int_{A_{lens}} L_p d\omega dA \qquad 10\text{-}32$$

where A_{pixel} and A_{lens} are the pixel and lens surface area respectively. $d\omega$ is defined between the lens surface and point p as in Figure 10-19

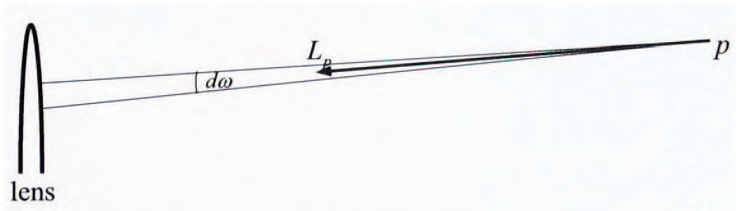

Figure 10-19

Since the size of each pixel is very small, the light falling on it can be treated as uniform, therefore

$$E_{pixel} = A_{pixel} \int_{A_{lens}} L_p d\omega$$

Performing Monte Carlo integration on the surface of the lens gives

$$E_{pixel} = A_{pixel} \int_{A_{lens}} \frac{\vec{L}_p \cdot d\vec{A}}{s^2} = A_{pixel} \frac{1}{N} \sum_{i=1}^{N} \frac{\vec{L}_i \cdot \vec{n}_i}{s_i^2 (1/A_{lens})} = \frac{A_{pixel} A_{lens}}{N} \sum_{i=1}^{N} \frac{\vec{L}_i \cdot \vec{n}_i}{s_i^2} \qquad 10\text{-}33$$

The summation is over the surface of the lens and s_i is the length of the ray issued from the sample location i and in the direction of point p. $\vec{n}_i$ is the surface normal at the same location. The radiance L_i is the result of path integration for the issued ray as given in the next section.

In the rendering pass, there would be N rays tracked from each pixel point p' toward p on the target plane (Figure 10-16). It should be mentioned here that p is a virtual point. Rays tracked toward it may be intercepted by other object in the scene or pass it till hit an opaque surface.

10.7.5 Gouraud shading

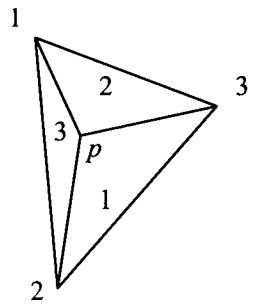

Figure 10-20 Surface interpolation inside a triangle

When the ray hit a surface element ΔA, surface radiance is interpolated from that defined on the nodes as

$$L_p = \frac{1}{\Delta A} \sum_{i=1}^{3} \Delta a_i L_i \qquad 10\text{-}34$$

where Δa_i is the area of the sub-triangle i of ΔA (Figure 10-20) and L_i is given by equation 10-8. L_p is carried by the ray on its way back toward pixel point p'. Since the surface normal is also defined on the nodes of the triangle, the surface normal at p is given by

$$\vec{n}_p = \frac{1}{\Delta A} B[\Delta a]$$

where B is a 3x3 matrix with $\vec{n}_i$ as its ith column.

10.7.6 Path integration

Once the ray has hit a surface at point p and picked up the surface radiance, path integration starts from point p as

$$\int_p^{p''} dL = \sum_{i=1}^{N} \Delta L_{ext,i} + \frac{1}{4\pi} \sum_{i=1}^{N} \frac{\Delta \Phi_{sca,i}}{\Delta V_i} \Delta s_i \qquad 10\text{-}35$$

where p'' is the intersection of the ray with the lens of the camera. N is the number of volume cells that the ray has passed on its way toward the camera lens. $\Delta L_{ext,i}$ represents the extinction of radiance in volume cell i. Similar to equation 10-14, $\Delta L_{ext,i}$ is determined by

$$\begin{cases} \Delta L_{ext,i} = L_{i-1}\left(e^{-\Delta \tau_i} - 1\right) & \Delta \tau_i > 0.1 \\ \Delta L_{ext,i} = -L_{i-1} \Delta \tau_i & \Delta \tau_i \le 0.1 \end{cases}$$

Here $\Delta \tau_i = \sigma \Delta s_i$.

10.8 Summary

A new image based numerical model for the visibility in smoke laden environment has been proposed in this chapter. The model took the advantages of the traditional zonal model and Monte Carlo ray tracing model. Combined with highly adaptive octree mesh, the model can build the field of irradiance very efficiently. The built irradiance field has been reused in image generation using back tracking technique that can offer image of any resolution. The unique virtual zoom camera has been built on sound optical principle and generated synthetic images that are comparable with photograph from commercial digital camera. In the next chapter, the high quality synthetic images produced with this model will be used in the simulation of experimental data presented in Chapter 8.

Chapter 11. Model verification and validation

A new model for numerical simulation of visibility in smoke has been proposed in Chapter 10. Its strength, characteristics of convergence as well as cost of computing were also analysed. In the current chapter, the model will be verified first against a known theoretical solution and then validated with the experimental data presented in Chapter 8. By comparing the prediction with the experimental data, it will reveal the accuracy of the model and point out possible future improvement.

11.1 Model verification with point light source

In a foggy night, a street lamp produces the scattering pattern as shown in Figure 11-1

Figure 11-1 A street lamp in a foggy night

Such a scattering pattern can be idealised as a point light source emerged in a homogenous, isotropic and non-absorbing medium. Further simplification is that the light source itself is monochromatic (not necessary) and also isotropic: the intensity from the light source is the same in all direction. Mathematically, it is a one dimension problem in which the radiance of the scattered light only depends on the distance from the light source but the result is 3 dimensional and point symmetric. Radiant energy balance means that the total radiant energy flux over the surface of an enclosure surrounding the light source would be equal to the power

of the light source emission. For a sphere surface centred at the point of the light source, the total energy flux through the surface can be expressed as (see equations 2-9 and 2-10)

$$\Phi = \int_S \int_{2\pi} L d\omega ds = 4\pi^2 R^2 L \qquad 11\text{-}1$$

where Φ is the power emission of the light source and R is the radius of the sphere.

This particular case has been chosen in the current study to verify the current numerical model and see how the one dimensional, point symmetrical and non-stochastic solution can be obtained with the full 5D (3 spatial and 2 angular), stochastic and finite volume algorithm.

The computational domain is a $2x2x2m^3$ cubic filled with isotropic medium with scattering coefficient 1.0 and zero absorption. The cubic has no wall or, put it in another way, the surfaces of the domain are non-reflective. The point light source is located at the very centre of the cubic with radiant power output of $4\pi^2$Watt. The domain is covered with 3D Cartesian mesh. Monte Carlo rays are introduced from each mesh element with random direction that satisfies uniform distribution over entire 4π space. Light is 100% scattered at each point. The radiance of the scattered light *L(x, y, z)* is a 3D field. Its value on the surface of any sphere centred at the point of light source is given by equation 11-1. For *R=1.0, L(R)=1.0.* Figure 11-2 shows how the radiance field was formed and converged during numerical iteration. In these graphs, the colour spectrum has been set so that any value larger or equal to 1.0 would be red. As the solution converges starting from iteration 10, the radius of the red sphere is stabilised at 1.0 and its surface becomes smoother although there are still small oscillations showing the stochastic nature of the solution. The surface is shown more clearly in Figure 11-3 when the range of the contour colour band is narrowed to 0.01.

Figure 11-4 shows the change of radiance of the scattered light along a radius of the sphere. The symbols are from the model prediction and the curve represents function *L(R)* as given in equation 11-1. The model prediction has closely followed the theoretical result. The rapid change of light scattering in the region of R<1.0 produces the visual effect of solid white circle surrounded by thin veil as in Figure 11-1. The pattern is similar in the prediction as shown in Figure 11-2 at iteration 20.

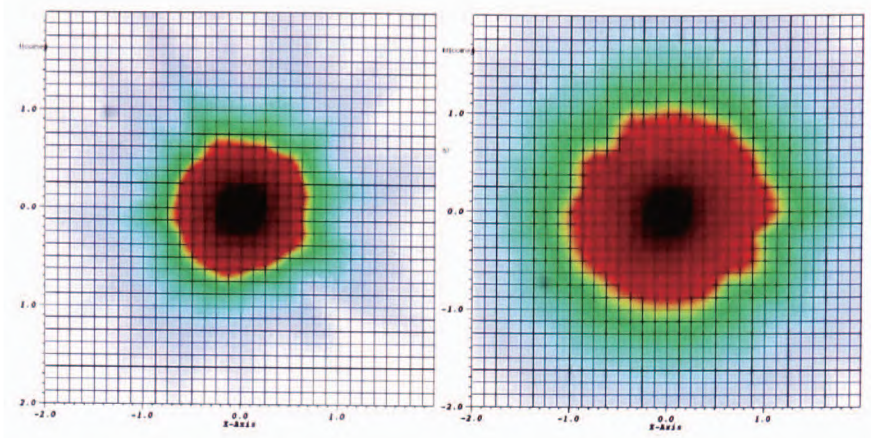

Iteration 1 Iteration 3

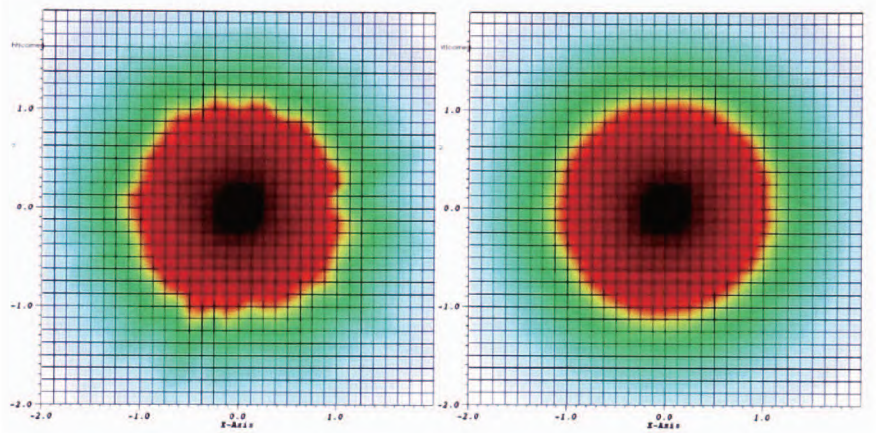

Iteration 5 Iteration 10

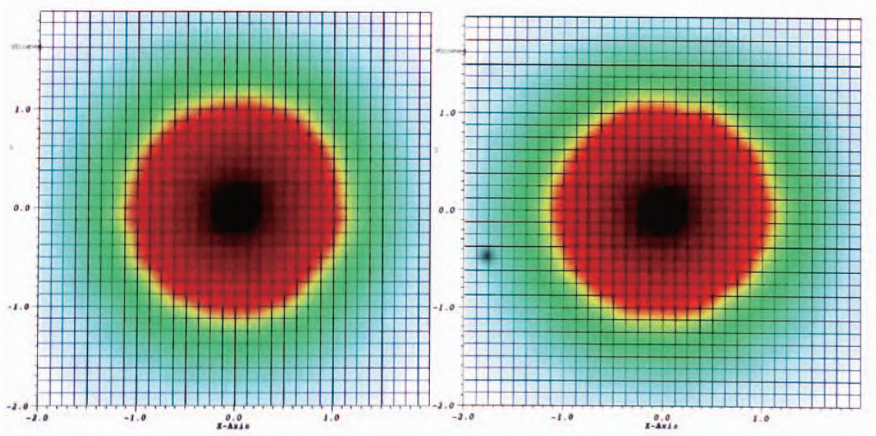

Iteration 15 Iteration 20

Figure 11-2 Radiance distribution of a point light source

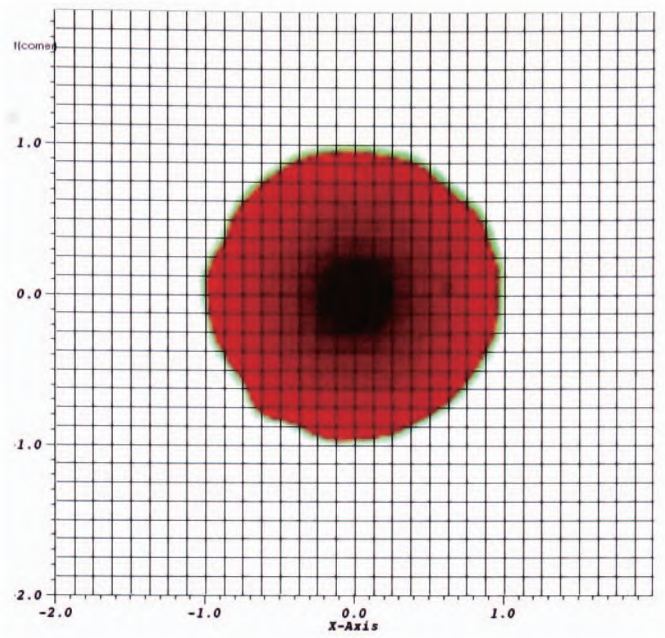

Figure 11-3 Radiance distribution of a point light source with narrow contour colour band

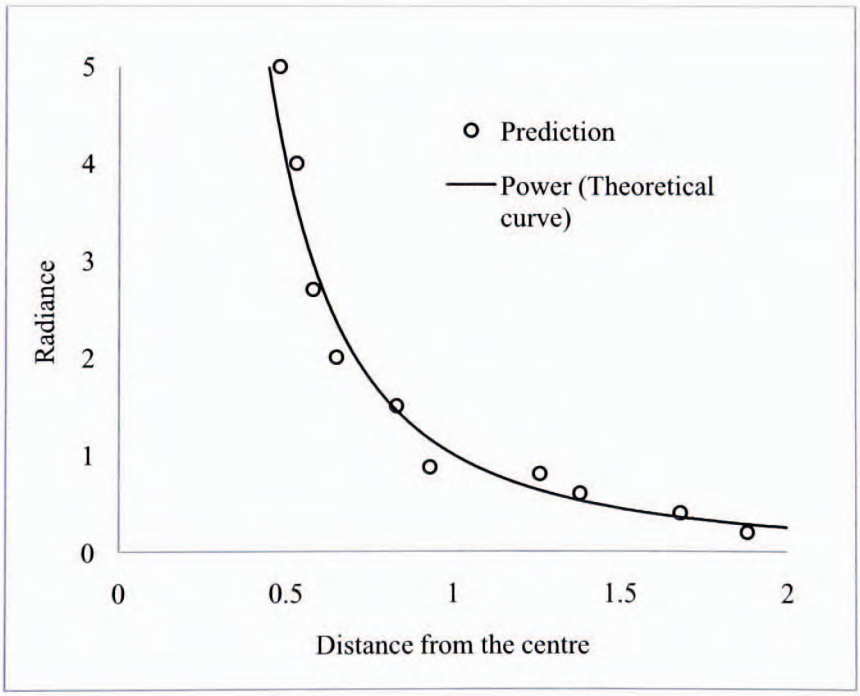

Figure 11-4 Predicted radiance of scattering along a radius of sphere

11.2 Visibility in numerical simulation

Visibility defined in section 3.5 takes a different form for synthetic image from that for the photographic image as in section 7.2. It is not necessary to introduce exposure in the numerical solution and there is no need to carry out camera correction. In expanding expression 7-2 for ϕ_η, the normalised brightness of the synthetic image is given by

$$\tilde{\phi}_\eta = c_\phi \frac{\beta}{\varepsilon_\eta \Delta D} \phi_{mean,\eta} \qquad 11\text{-}2$$

where ϕ is the energy flux falls on a pixel and ε_η is the energy of a photon at the given wavelength as in section 2.1. The reason to convert $\phi_{mean,\eta}$ into photon count is to make the result comparable with that obtained by 7-3 in the experiment since the pixel value in a digital photographic image is proportional to the photon count falls on the pixel during exposure (Dennis, 1986) and c_ϕ is the proportional constant. A value of 1.5 is used in the current study.

11.3 Boundary conditions

The emission of the light source has been measured in section 5.5 for red and green light at power level 2 and 3. The emission under the other conditions in Table 11-1 are extrapolated from that in Table 5-1 with the help of the energy spectrum shown in Figure 5-3. It should be point out that, in Figure 5-3 the area ratio represents the ratio of photon counts but in Table 11-1, the numbers are power emission.

Colour	Red	Green	Blue
Power level 1	1.3	1.96	3.7
Power level 2	**0.65**	**0.98**	1.85
Power level 3	**0.31**	**0.37**	1.05

Table 11-1 Power emission of light sources (W/sr*m^2)

The smoke tunnel is made with aluminium panels. The reflectance of machine polished aluminium is generally above 0.9 when illuminated with visible light (Bartl & Branek, 2004). In the current study, the panels are exposed in air and there is no special surface treatment therefore the reflectance of 0.8 has been used in the prediction. The tunnel at the camera end is sealed with glass and covered by black sugar paper. It is assumed that the reflectance for both the paper and the glass are negligible. None reflective boundary condition has been set at this end of the tunnel.

11.4 Other assumptions

In comparing the model prediction with experimental data, it is assumed that the misty smoke used in the current experiment is both homogeneous and optically isotropic. The homogeneous assumption is justifiable. Particular attention has been paid during the experiment to keep the smoke distribution in the tunnel uniform with the two ventilators (section 5.4).

A common approximation of light scattering pattern is the Henyey-Greenstein phase function (Tuchin, 2007):

$$p = \frac{1}{4\pi} \frac{1-g^2}{\left[1+g^2-2g\cos\theta\right]^{3/2}} \qquad 11\text{-}3$$

where θ is the angle of scattering from the direction of the incident light and g is a parameter that determines the pattern of scattering as shown in Figure 11-5. On the left of Figure 11-5, $g=0$. The scattering is isotropic. On the right hand side of Figure 11-5, scattering pattern changes from extreme back scattering to extreme forward scattering corresponding to different value of g in equation 11-3.

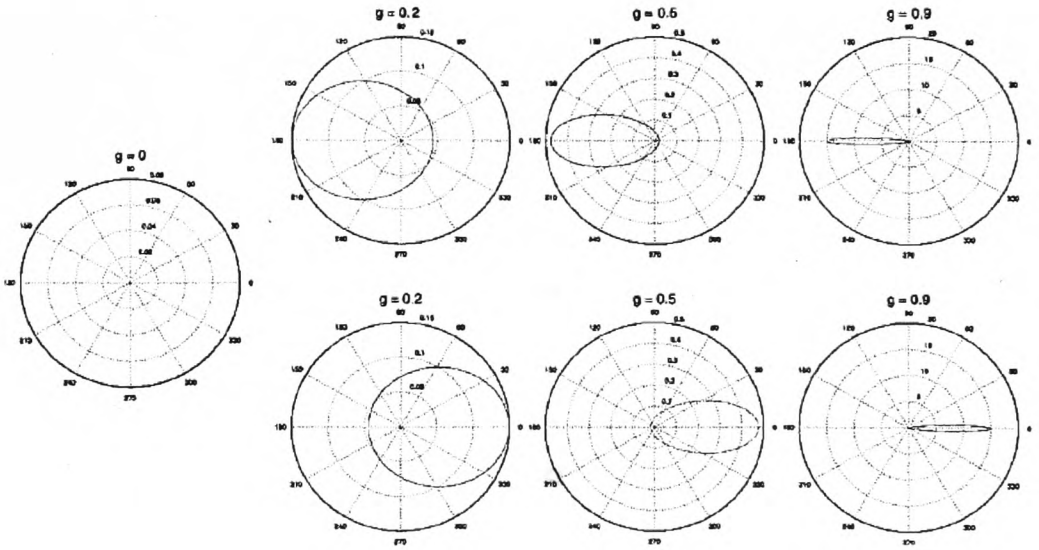

Figure 11-5 Henyey-Greenstein phase function

What needs to be mentioned here is that the pattern shown in Figure 11-5 is for scattering of a single incident light beam: a single light beam hitting an isolated medium particle. In practice, particularly with media of high albedo, multiple incident lights may come from different direction due to surface reflection and scattering by other particles of the medium. The output

from this kind of scattering pattern is likely to be more angularly uniform than that in single scattering as illustrated in Figure 11-6.

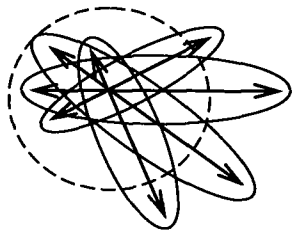

Figure 11-6 Scattering of multiple incident light

Isotropic scattering assumption is introduced here as the first order approximation to the current problem. It would be the main area for improvement in the future. What is worth mentioning here is that the model simplification as the result of this assumption has significantly reduced the computational cost.

Further assumption has been introduced about the optical property of the mist namely its extinction coefficients. Since the mist is highly reflective and transparent, it is assumed that its absorption to visible light can be neglected therefore its extinction coefficient is equal to its scattering coefficient. It implies that light transport through the mist would be lossless.

The estimation of the scattering coefficient is based on the measurement of optical depth with low power red laser (λ=653nm) as described in section 5.4. The value of the scattering coefficient in this case is the same as the optical density of the smoke given by expression 9-20.

The limitation of the single colour (red) laser measurement means that our comparison between the prediction and experimental data would be most significant on the red signs. When comparing results for the cases with green and blue sign, the optical depth quoted should be treated as a reference to smoke condition.

11.5 Visibility of barcodes

Prediction has been made against the barcodes measurements under various conditions. The complete set of results is given in Appendix F. Comparing to the experimental data, the accuracy of the prediction varies. Part of the inaccuracy is from the numerical model such as the assumption of isotropic scattering. Other causes include the inaccurate estimation of boundary conditions and physical parameters such as the power of the light source and the extinction coefficients.

11.5.1 Red barcodes with aspect ratio 2:1

Figure 11-7 shows the comparison between the measured and simulated visibility for barcode of 2:1 illuminated with red light. Good agreement between the prediction and the measurement has been achieved when the luminance of the sign is the highest. As the luminance decreases, the discrepancy between the prediction and the measurement increases. The reason for the discrepancy is not clear at this stage.

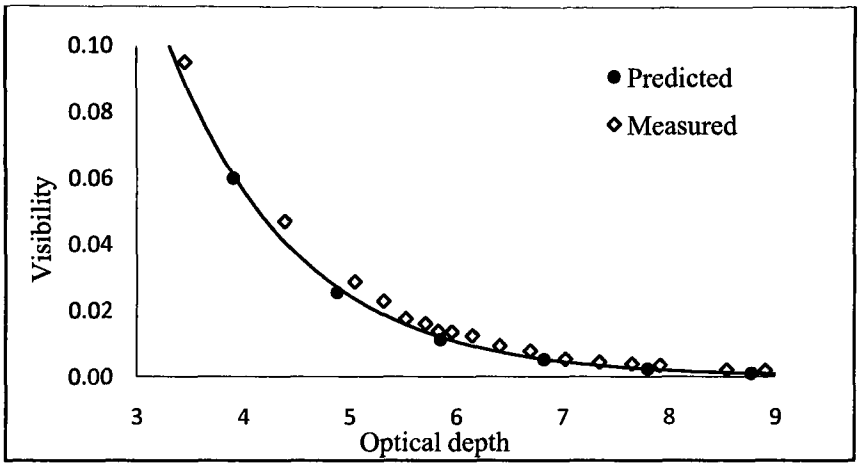

Power level 1

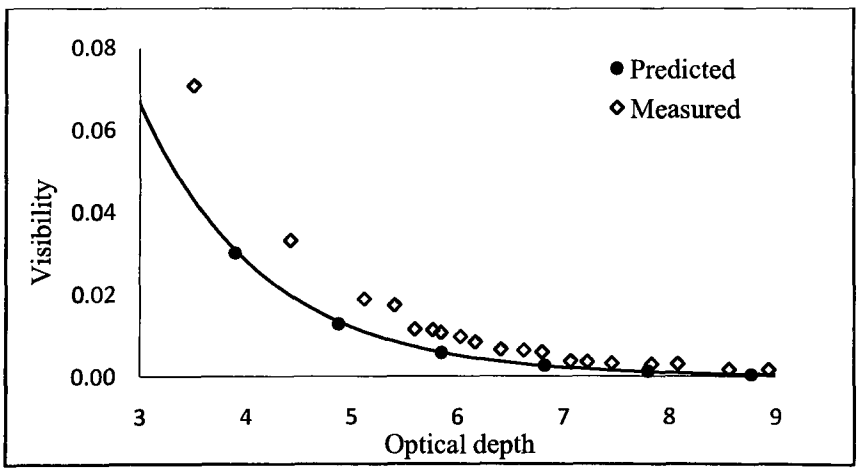

Power level 2

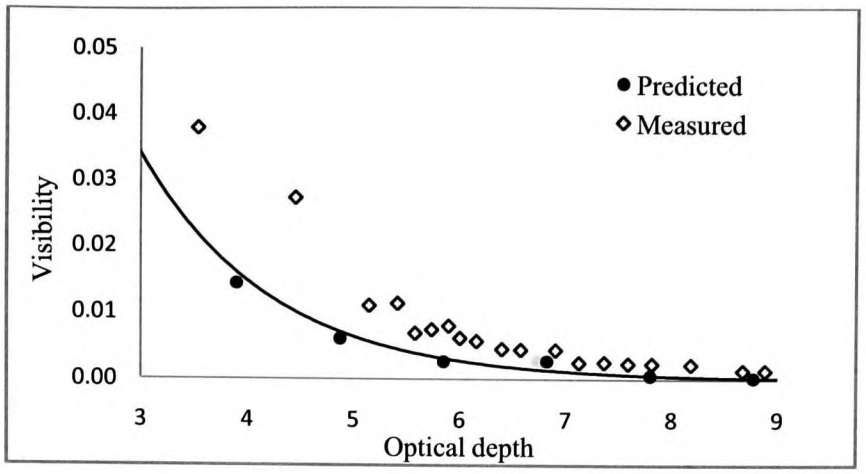

Power level 3

Figure 11-7 Red barcode with aspect ratio 2:1

11.5.2 Red barcodes with aspect ratio 1.5:1

Similar to the last section, the visibility of the barcodes is under predicted in the case of low power signs as shown in Figure 11-8. The excellent agreement between the prediction and the measurement in the case of power level 1 is not surprising since the coefficient c_ϕ in expression 11-2 is calibrated against this case.

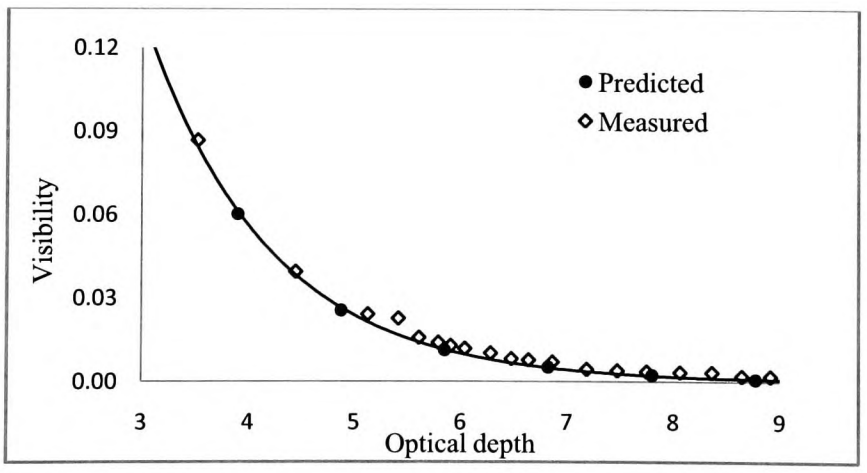

Power level 1

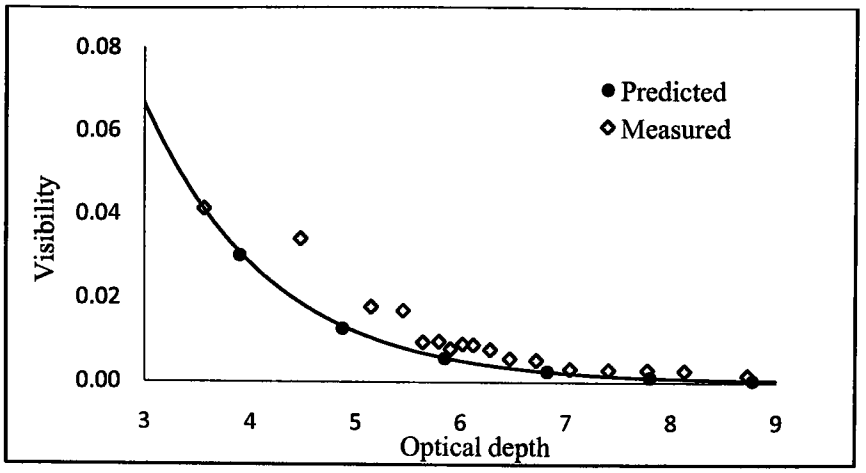

Power level 2

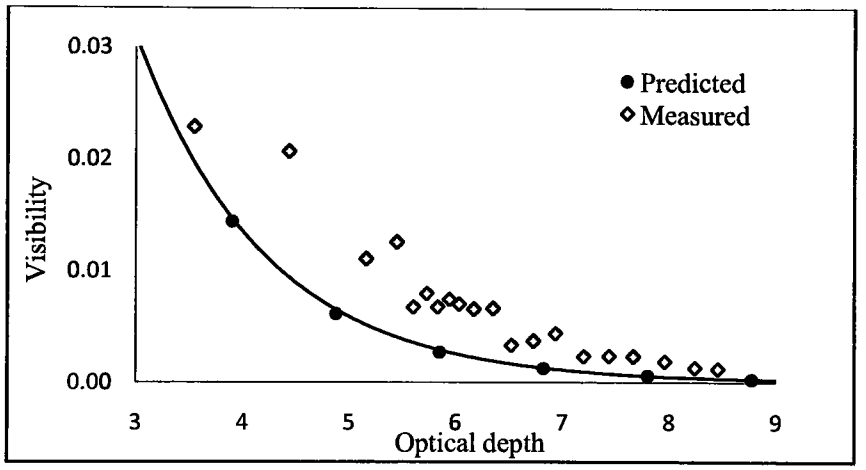

Power level 3

Figure 11-8 Red barcode with aspect ratio 1.5:1

Figure 11-9 shows the comparison of synthetic (left) and photographic (right) images at power level 2 and low smoke concentration. It can be seen that the synthetic image is softer than the photograph. In fact, the true visual effect seen during the experiment was closer to the synthetic image. The sharper image of the photograph may be due to the step change of the integer colour data. In the synthetic image, colours are represented with floating point number therefore changes are continuous.

Figure 11-9 The synthetic (L) and photographic (R) images at low smoke concentration

11.5.3 Red barcodes with low aspect ratio

Figure 11-10 and Figure 11-11 show the comparison between the prediction and experimental data for red barcodes of aspect ratio 1:1 and 1:0.5 respectively. In these cases, the largest discrepancy appears at power level 1 and visibility is over predicted. The unexpected over prediction might be caused by the combination of the uncertainty of input light power as in Table 11-1 and the non-uniformity of the light source as can be seen in Figure 7-2.

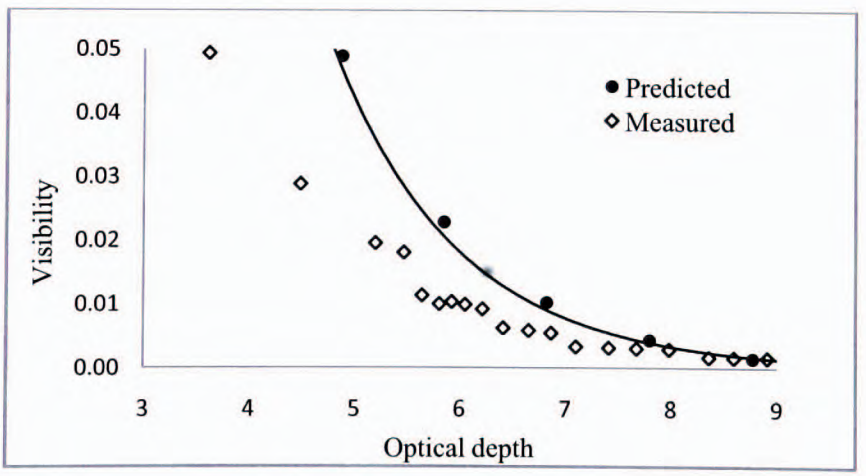

Power level 1

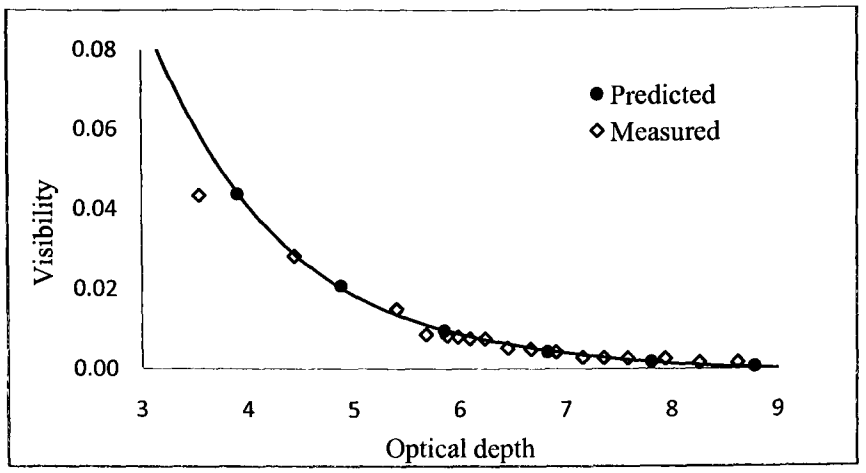

Power level 2

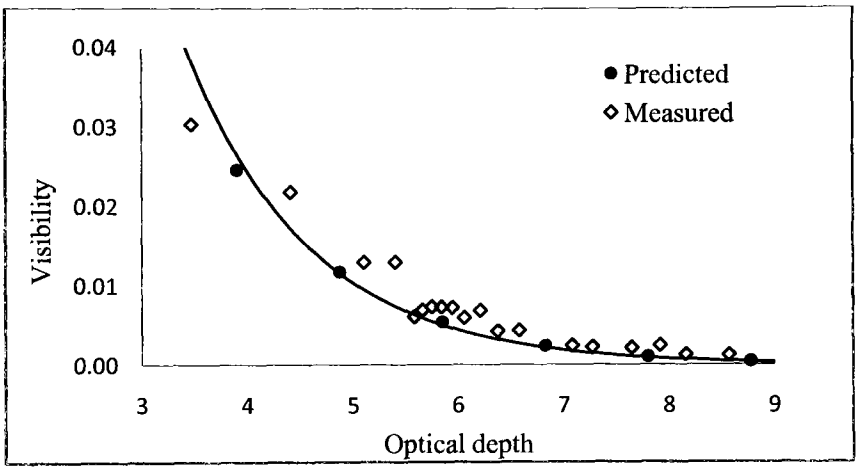

Power level 3

Figure 11-10 Red barcode with aspect ratio 1:1

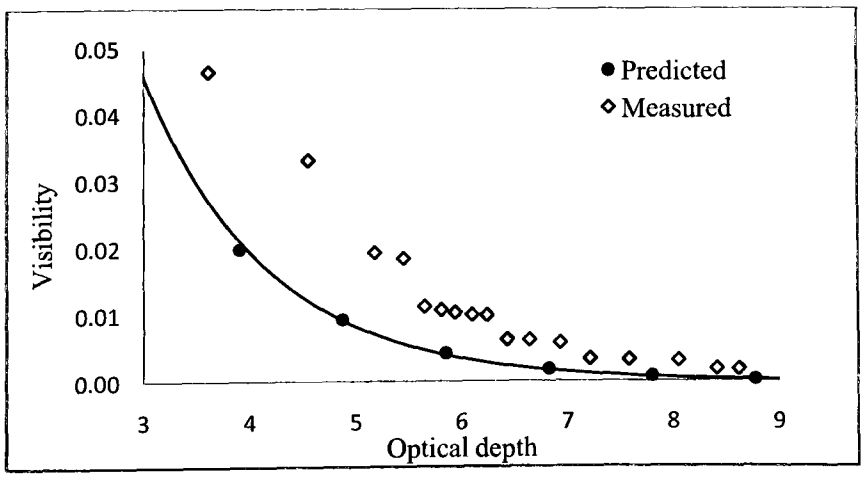

Power level 1

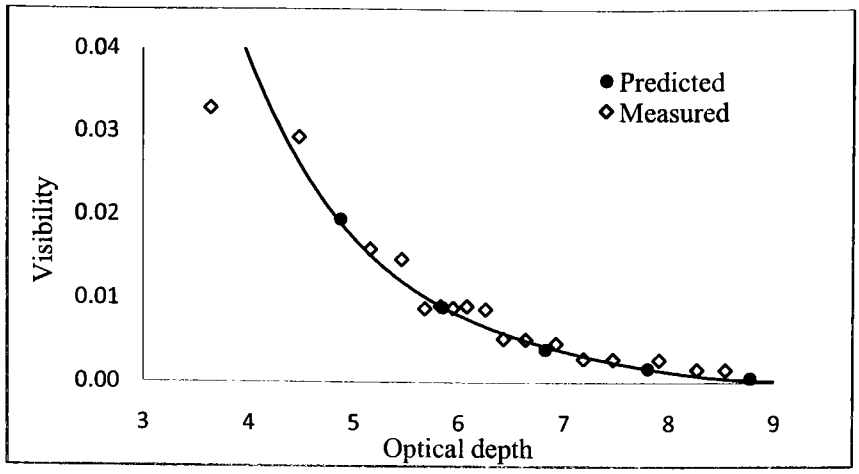

Power level 2

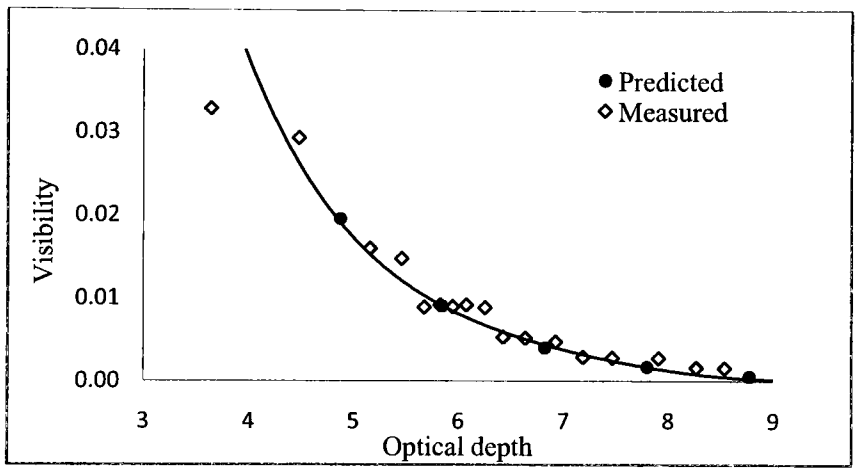

Power level 3

Figure 11-11 Red barcode with aspect ratio 1:0.5

11.5.4 Visibility of barcodes with green and blue colour

As mentioned in the introduction of the current chapter, the measurement of extinction coefficient in the current study was limited to the red colour with wavelength 653nm. With this point in mind all optical depth quoted in this thesis should be read as "optical depth of red light". For colour other than red, the optical depth quoted should be treated only as a reference to the smoke condition. It does not necessarily reflect extinction coefficient that is often a function of wavelength (see section 2.8).

As can be seen in Appendix F, visibility is often over predicted in the cases of green and blue barcodes. It is considered that the extinction coefficients used in these cases are the same as that

for the red barcodes which could be different from their real value. Figure 2-9 shows the spectra variation of extinction coefficient for fire smoke. Within the visible range of wavelength (x=0.3 to 0.6), it is likely that the extinction coefficient will increase when wavelength moves from red to blue. Although Figure 2-9 is for soot, it is expected that the scattering coefficient of mist could follow similar spectra change. A commonly known evidence can be seen in rainbow. If this is true, then it is possible that the problem here is not over prediction but under estimation of the measured value.

In order to see if this is the case, a powerful green laser was employed in the case of green barcodes with aspect ratio of 1.5:1 to measure optical depth directly and the result is shown in Figure 11-12. It can be seen that the predicted visibility becomes much closer to the measurement.

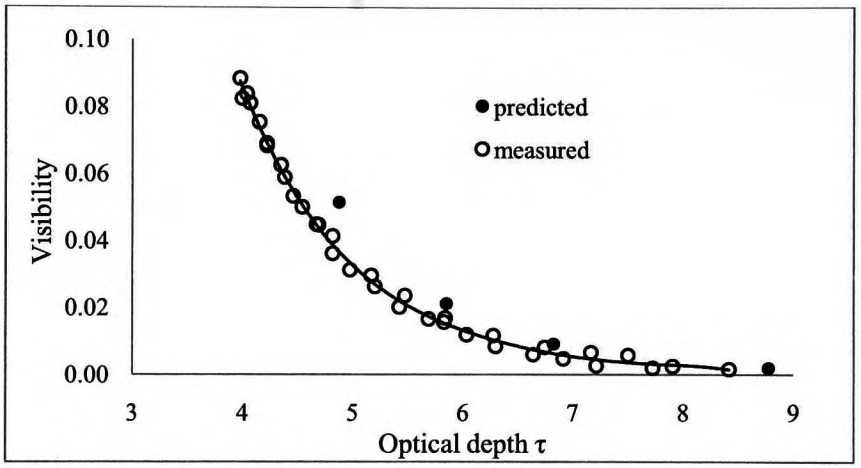

Figure 11-12 The visibility of green barcodes (1.5:1)

11.6 The influence of ambient light

Figure 11-13 and Figure 11-14 show the comparison of the predicted visibility with experimental data when the ceiling light near the camera is switch on. There is no direct measurement of radiance for the ceiling light. Its value is estimated to be the same as the light source of the sign. The agreement between the prediction and the experimental data is generally good. In low scattering case (barcodes 1.5:1, power level 1), visibility is over predicted. On the other hand, in high scattering case (barcode 1:0.5, Power level 2), visibility is under predicted. Only red sign with red ceiling light has been compared as this is the experimental data containing minimum uncertainty.

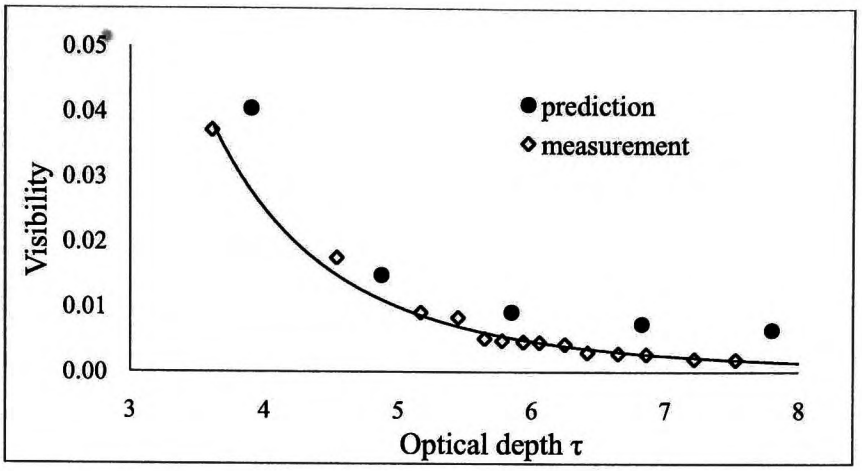

Power level 1

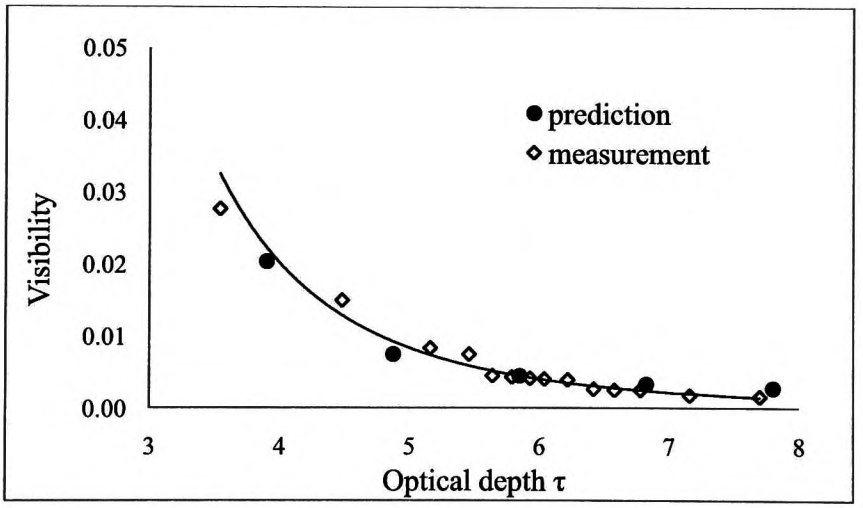

Power level 2

Figure 11-13 Visibility of barcodes (1.5:1) with ceiling light

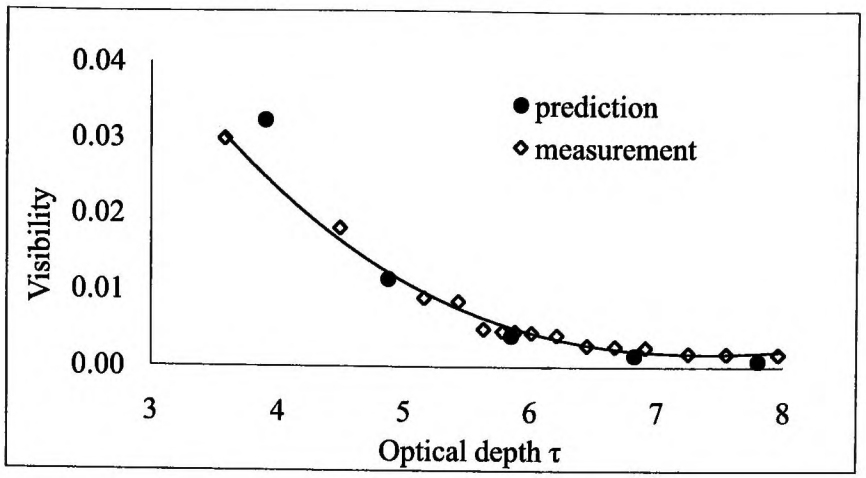

Power level 1

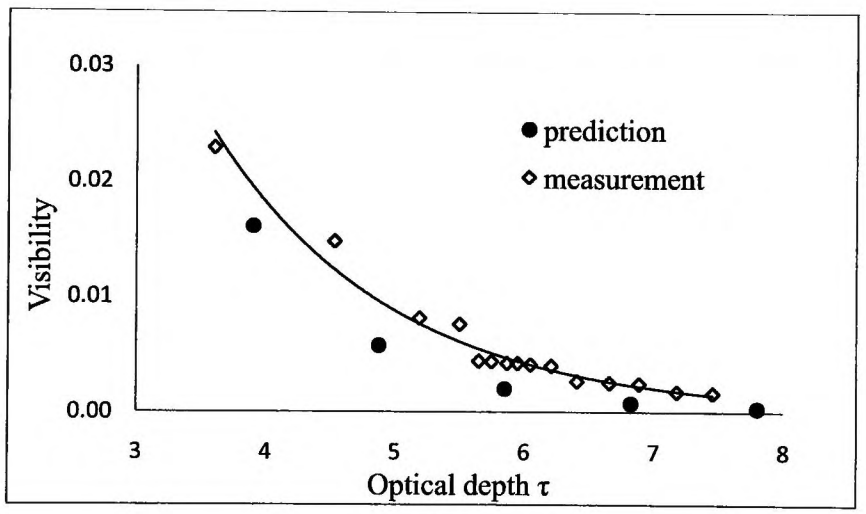

Power level 2

Figure 11-14 Visibility of barcodes (1:0.5) with ceiling light

11.7 The assumption of isotropic scattering

As a first order approach, the current simulation model made an assumption that light scattering by the mist smoke is isotropic. It is the author's belief that this assumption is the main contributor of discrepancy between the model prediction and laboratory measurement.

Table 11-2 shows how the relative quality of model prediction changes as given in section 11.5

Category	Bulky barcode					
Barcode	2:01			1.5:1		
Luminace level	1	2	3	1	2	3
Measured visibility (τ=4)	0.06	0.05	0.03	0.06	0.04	0.022
Prediction	good	under	under	good	under	under

Category	Thin barcode					
Barcode	1:01			01:00.5		
Luminace level	1	2	3	1	2	3
Measured visibility (τ=4)	0.04	0.04	0.025	0.04	0.035	0.04
Prediction	over	good	good	over	good	good

Table 11-2

There is a general trend from over prediction to under prediction when the luminance of the sign goes from high to low.

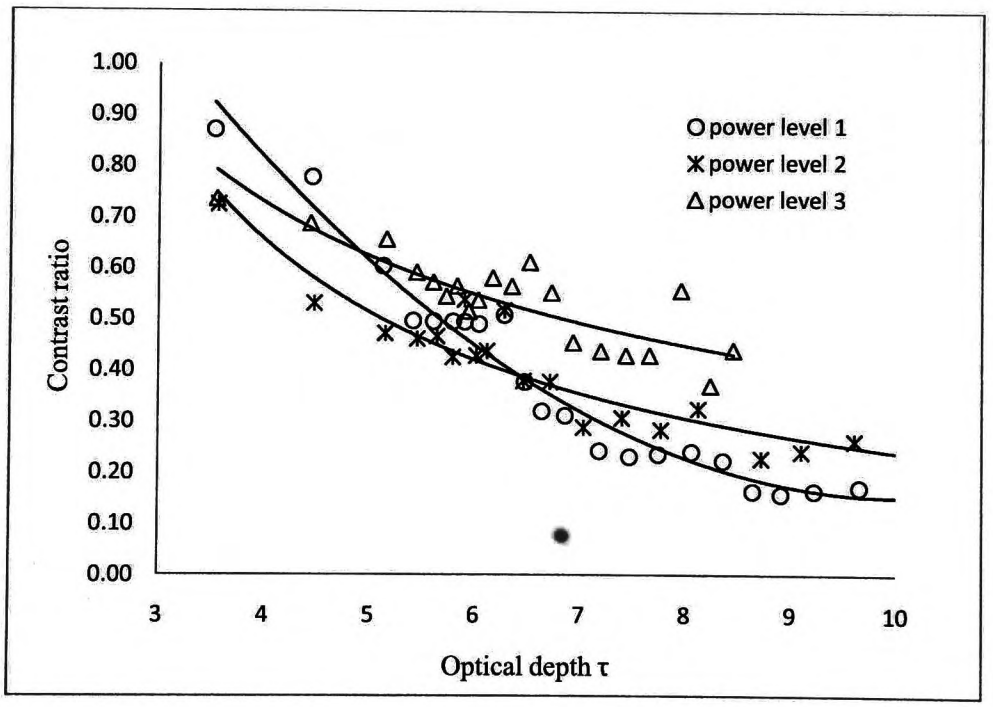

Figure 11-15 Contrast ratio of red barcode (1.5:1) with different power level

It needs to be mentioned that the illuminated sign is the only light source in this case. Therefore only the light from the sign will be scattered. Figure 11-15 shows the contrast ratio as defined by expression 7-1 with 3 different power levels for red barcode of 1.5:1. It can be seen that

when smoke concentration is high, the contrast ratio increases as the luminance of the sign decreases. In other words, the relative light scattering decreases with the luminance of the sign. This is contrary to the assumed isotropic scattering process. In isotropic scattering, the intensity of the scattered light is the same in all direction therefore it is proportional to the incident light (Figure 11-16(b)). In the case of anisotropic scattering it would be possible that the change of luminance is accompanied by the change of scattering pattern as shown in Figure 11-16(a)

high liminance low liminance

(a) Anisotropic scattering

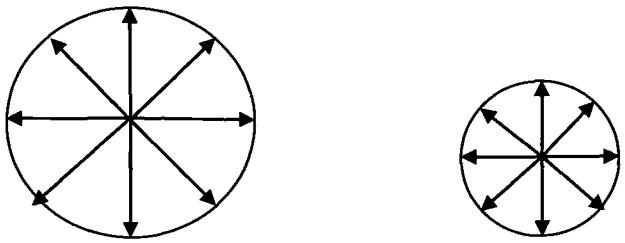

(b) Isotropic scattering

Figure 11-16 Scattering pattern

Such change will result in the disproportional change of visibility when the luminance of the sign changes.

Taking the case of red barcode 1.5:1 as example, at power level 1, the prediction agrees with the measurement data. As the luminance of the sign decreases, the predicted scattering decreases in proportion but the measured scattering decreases more (see Figure 11-15 and equation 7-1). It leads to the under prediction of visibility.

11.8 Floor map of visibility (FMV)

So far the study has been concerned with visibility of a specific target from a given view point. Judgement of fire safety performance for a building design requires the assessment of overall visibility across the building. In the current study, a floor map of visibility (FMV) has been proposed that gives a global and concise picture of visibility for a design under smoke condition.

FMV is defined as a snapshot of two dimensional plane contours at certain vertical level (eye level) that maps out the probability of wayfinding at each location in a structure. It shows the best visibility of all emergency signs viewed from the given location. The visibility is measured with the synthetic images generated from the simulation model. To demonstrate the concept, a hypothetical fire scenario is presented here.

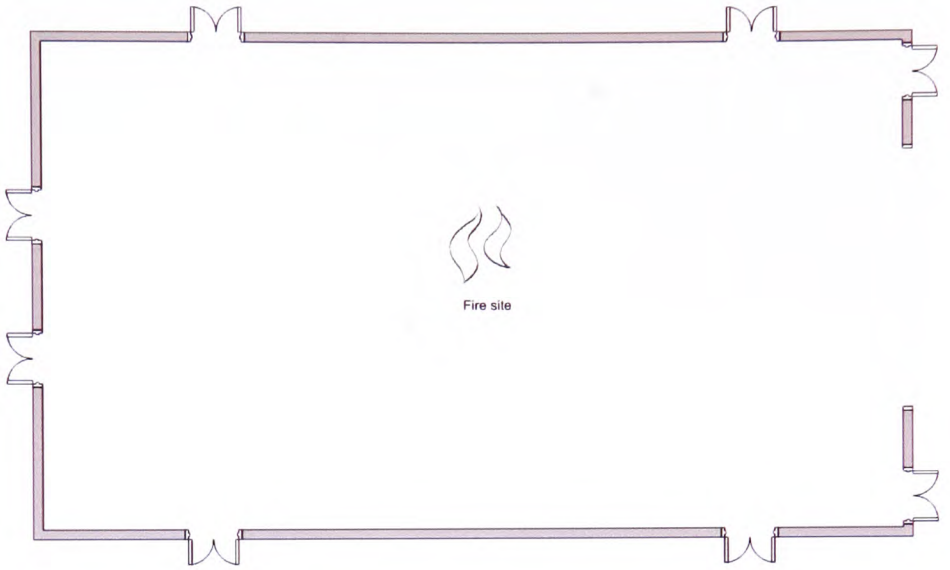

Figure 11-17 Floor plan and the fire site

In this scenario, fire started in the centre of a dancing hall. The dimension of the hall is 55x35x5m^3. There are two doors on each side of the hall. Above each door there is an internally illuminated emergency exit sign. The fire size is 1MW. Figure 11-17 shows the floor plan of the hall and the fire site. Figure 11-18 is the internal of the empty hall before the start of fire.

The smoke distribution in the hall had been simulated with FDS from NIST (McGrattan, Hostikka, & Floyd, 2009). After 3 minutes, the hall has been filled with smoke as shown in Figure 11-19. The same result has also been shown with FDS-SmokeView as in Figure 9-2. In terms of smoke opacity, Figure 11-19 and Figure 9-2 are comparable.

Figure 11-18 The internal of the hall

Figure 11-19 The internal of the hall after 3 minutes from fire starts

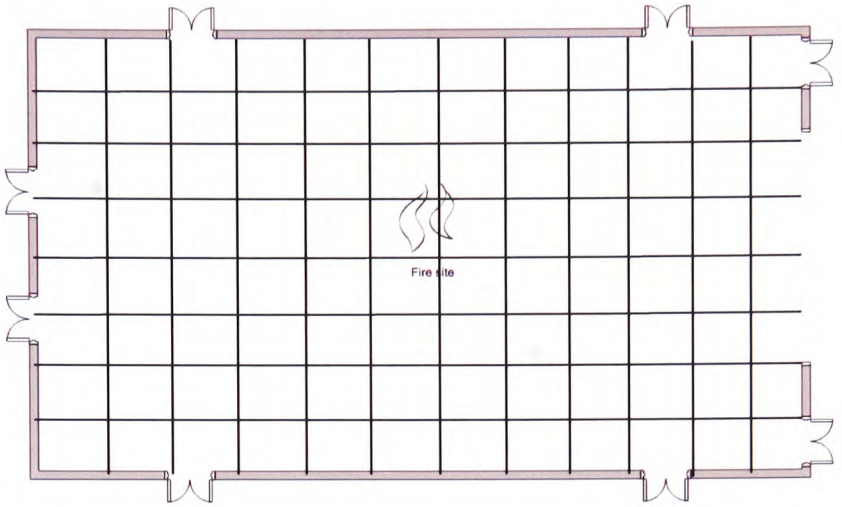

Figure 11-20 Mesh used in generating FMV

In calculating FMV, the floor is divided by a mesh of 12x8 as shown in Figure 11-20 (It is neither the CFD mesh nor the mesh for visibility simulation!). At each node of the mesh, images of all the exit signs are generated at average eye level (1.7m from the floor) and the best visibility is selected as the visibility of the node point. Figure 11-21 shows the created FMV after 3 minutes from the start of the fire. The visibility ranges from very good in the blue regions to very poor in the red regions. The dark red area in the centre of the map is the fire site. Close to the fire site, the visibility is the poorest.

Figure 11-22 shows the smoke concentration contours at the same floor level. The blue region represents soot volume fraction value equal or less than 1.0e-08 and the red region represent the value equal or great than 2.5e-08. Unlike optical density, the contours of visibility shown in Figure 11-21 do not resemble the distribution of smoke concentration. Near the top and bottom walls the local smoke concentration is relatively low but the visibility is also poor. This is contrary to the conclusion would be drawn from local optical density or simple line of sight. The explanation is that in these areas the observer is too far (in terms of optical depth) from the doors on the left, right and opposite side and the view angles are too large for the nearest doors on the same side.

FMV has taken into account smoke concentration, distance between the observer and the target, view angle as well as the luminance of the sign.

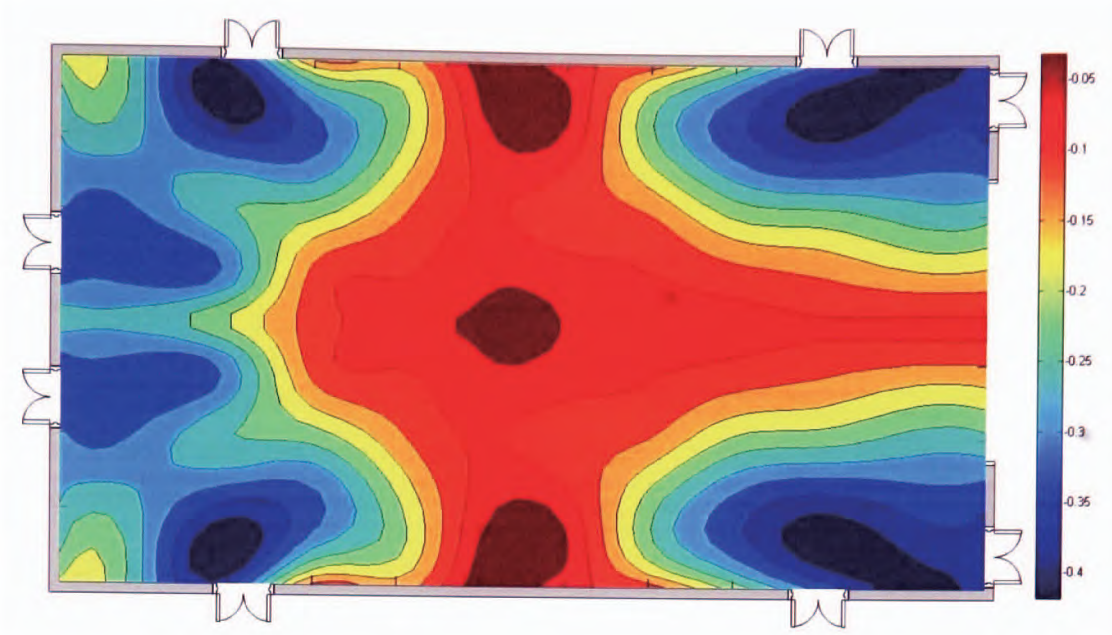

Figure 11-21 Floor map of visibility

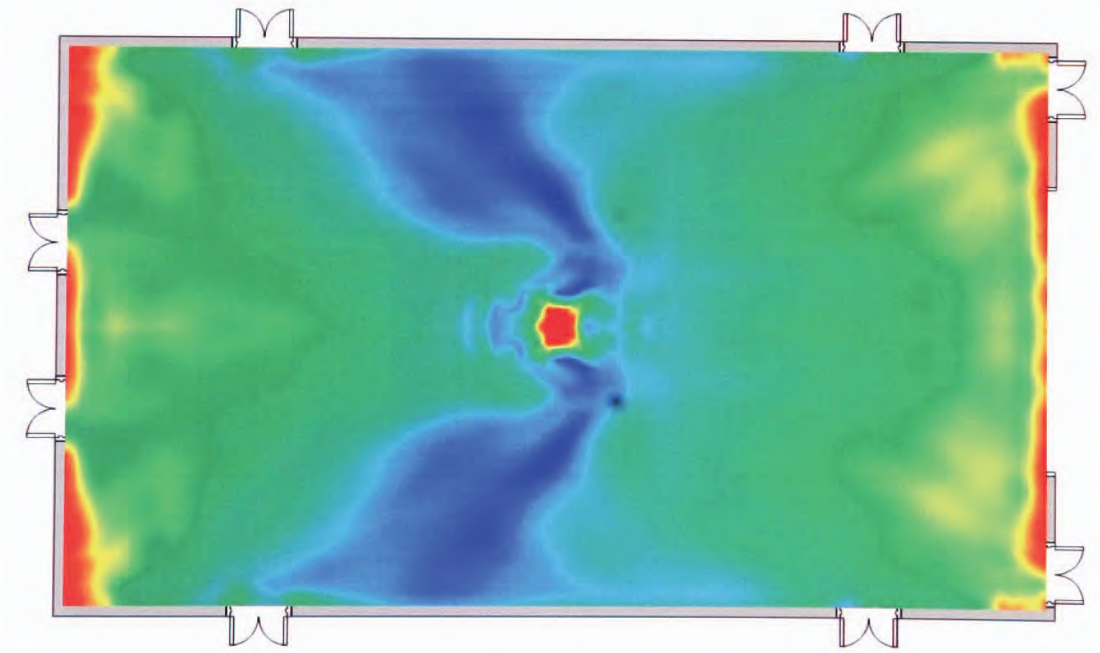

Figure 11-22 Smoke concentration

11.9 Summary

The proposed model for visibility in smoke laden environment has been verified with the analytical solution of an isotropic point light source. The verification has also shown that the simulation algorithm can fully converge to the analytical solution within 10 iterations even in a non-absorbing case.

Comparing with the experimental data in Chapter 8, the model prediction has been reasonably good. Discrepancies between the measurement and prediction come from deficiencies on both numerical model and experiment sides. On the modelling side, the isotropic scattering assumption has led to relatively large error of prediction in high scattering cases (low aspect ratio of barcodes or blue colour). Some uncertainties in determining the boundary conditions also contribute to the departure of prediction from experimental data.

The proposed floor map of visibility would be proven a useful tool assisting fire protection engineers in estimating overall visibility performance of a design. It is comprehensive in terms of the information that can be revealed (smoke density, view distance, view angle, optical properties of the sign etc.). At the same time it is much easier to understand than the contours of optical density.

Chapter 12. Discussion and conclusion

"Extremely small margins can mean the difference between life and death in catastrophes: a few more meters, a few seconds less, a single wrong choice of route, just a little less smoke or slightly better visibility, and lives could have been saved." (Jensen G. , 1994)

Today, fire safety engineers are facing the challenge of the ever rising safety standards against the ever expanding horizon of structural, architectural and ecological complexity. Meeting such challenge requires continuous research to improve our understanding of the environment surrounding us. The current study is a contribution to fire safety engineering research aimed at the better understanding of visibility in smoke environment. It is the author's wish that the results can eventually lead to the improvement of fire safety whatever small it might be.

12.1 Visibility in fire safety engineering

Losing visibility in building fire may lead to prolonged contact with toxic smoke and incite panic reaction among evacuees. It is arguably the most important indirect cause of fatality. In the existing building design codes, visibility is measured by the threshold visual distance that is inherited from meteorology and aviation industry. Such measurement of visibility largely ignored the context of the target object (colour, formation, light emission etc.), the relative angle between the target and the observer and the heterogeneity of media. These complexities do not exist in meteorology and aviation since they are dealing with target far from the observer (in kilometres) and homogeneous media under very stable conditions (the changes are measured in terms of minutes or even hours instead of seconds as in fire situation).

In fire safety, visibility is about the identification of exit sign. As long as the sign is visible, the distance between the sign and the evacuee is unlikely to be an issue. A sign may not be far away from the evacuee in terms of physical distance but it may be obscured by other objects, ambient lights, intermittent smoke cloud etc. It may be not facing the evacuee directly or become less obvious among other brighter objects (typical experience in departmental store). All such unfavourable visibility conditions may cause delay in evacuation particularly when people are in panic.

Improving visibility of an emergency sign even when it is still visible requires a measurement that is different from the current visual threshold. One such measurement has been proposed in the current study based on perceived image.

A perceived image is an image that is believed to be directly linked to the visual stimuli of human brain. In the current study, it has been created by applying the CIE photometric function to the incident image of the human eye.

The concept of image based visibility is close to its common understanding by ordinary people. When two images of the same object are presented, their relative visibility is judged by their contrast and brightness. An attempt has been made in the current study to quantify such judgement as a measurement of visibility. Chapter 7 and 8 described the procedure that converts a photograph taken with a commercial camera into a perceived image. Visibility in the image is measured in terms of its contrast and normalised brightness.

The measurement of visibility defined in this way does not concern with how the image was created and the factors that may affect it such as the distance of the target object or the media between the target and the eye (or camera), therefore can be applied in any circumstance.

12.2 Determination of visibility in smoke laden environment

12.2.1 Smoke concentration

Visibility in smoke laden environment depends on many factors. In the current study, some of them that are believed to be influential were tested in the smoke tunnel.

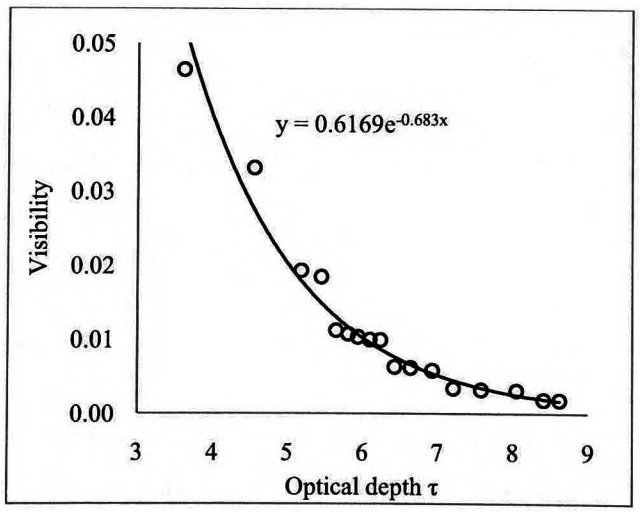

Figure 12-1 Red barcode (1:1) at power level 1

First of all, how visibility is affected by smoke concentration is our subject here and all the discussion in this thesis is around it. In the current study, smoke concentration is represented by its optical depth that is the product of the extinction coefficient of smoke and the distance over which the visibility is measured. It is the integrated optical characteristics of smoke over a particular line of sight. Its effect on radiation transport is determined by the Lambert-Beer's law in Chapter 2. As already known, the current definition of visibility is only based on photographical image and has no link with radiation transport theory. However Lambert-Beer's law is still satisfied in the results of the current experiment as shown in Figure 12-1. It is a proof that the new measurement of visibility does reflect the physical reality.

12.2.2 Luminance of the sign

According to the Handbook of Fire Protection Engineering by SFPE (2008), visibility is independent of the luminance of the emergency sign. Some researchers have shown the contrary and recommended the increase of the brightness of signs (Rea, Clark, & Ouellette, 1985). Experiments have been carried in the current study under three different luminance level and various colour and smoke conditions. Based on the results, the author has concluded that when the smoke concentration is low relative to the visual threshold, the visibility of the sign will improve as the luminance of the sign increases. As the smoke concentration increases toward the visual threshold, the effect of increasing luminance on the visibility of a sign diminishes therefore signs with different luminance will show the same visual threshold (Figure 8-6). In other words, both conclusions from previous researches are correct but under different conditions. The explanation is given in section 12.2.6.

12.2.3 Ambient light

Ambient light can reduce the visibility of a sign by increasing the brightness of the image background therefore decreasing the image contrast of the sign. This effect has been shown in Figure 8-10. When the ambient light is on, the visibility of the sign decreases rapidly and drops below the visual threshold before optical depth reaches 7. Although the obscured area remains the same but the image contrast is reduced by strong scattering of the ambient light. The current study has reiterated the conclusion from previous researches.

12.2.4 Colour of illumination

As the previous definition of visibility is based on Lambert-Beer's law, it can't offer any guidance on the use of colour in emergency sign. The current convention of using red colour for emergency sign in North America and green colour in Europe is largely based on the general knowledge of light transport (light with longer wavelength suffered from less loss during transmission) and the colour response of human eye. Limited research on this subject conducted in the US inconclusively favours red colour (Ouellette M. , 1993 and Rea, Clark, & Ouellette,

1985). The current experimental results, after being normalised by the luminance of the sign, have shown that the red and green colour signs are similar in visual performance under all smoke conditions but the performance of the blue colour sign is consistently poorer in comparison.

12.2.5 Format of the legend

In general, the legend with bulky strokes has shown better visibility. An explanation based on the current concept of visibility is shown in Figure 12-2.

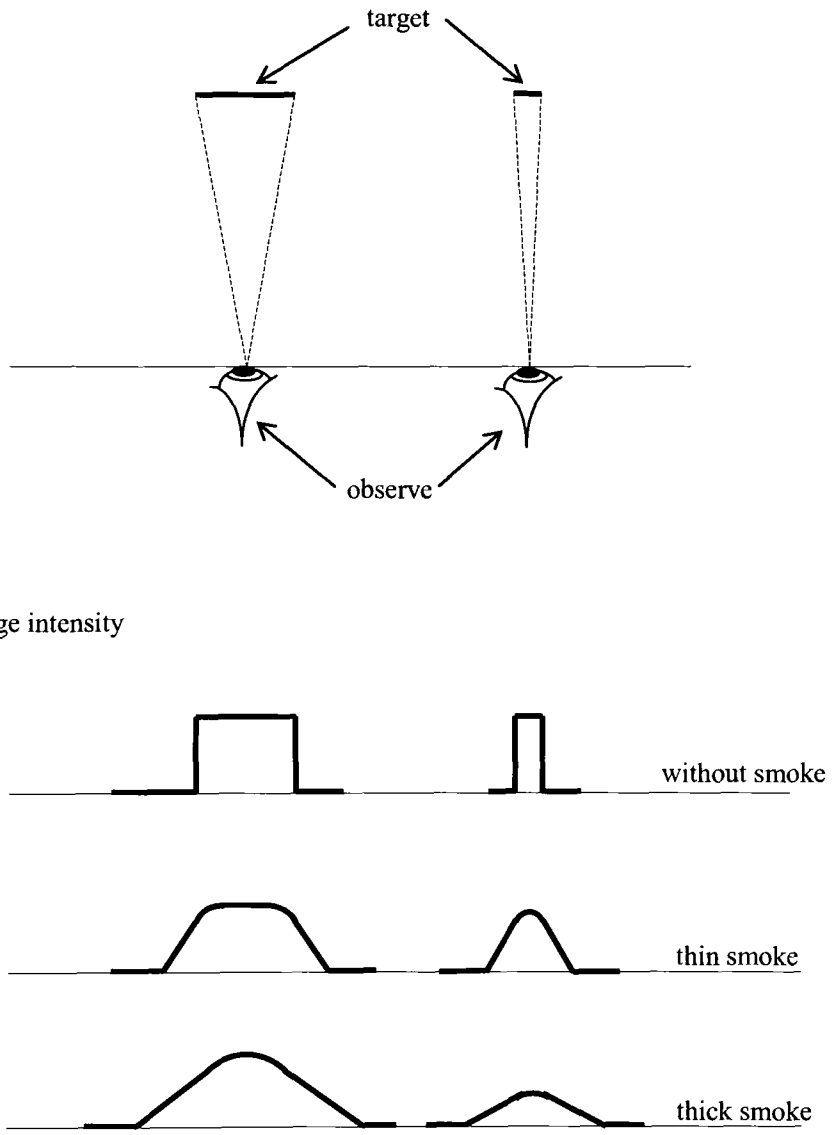

Figure 12-2

Light scattering is independent of the signs. As the optical depth of the smoke increases, the maximum image intensity of the bulkier sign (on the left) would be less affected than that of the thinner sign. As the image of the sign becomes wider due to scattering, energy conservation requires that the maximum image intensity is reduced therefore the overall contrast ratio of the image to be lower comparing with the bulkier sign.

12.2.6 The visual threshold

For non-irritant smoke, the current experiment has confirmed that Jin's constant visual threshold (=8.0) (Jin T. , 2008) stands in most cases except with ambient light. Same as in section 12.2.2, as the optical depth approaches the visual threshold, the difference seen in thin smoke diminishes and the sign disappears at the point of visual threshold regardless the other conditions.

The diminishing of sign luminance can be explained as the following. The image of a sign in smoke is formed by the incident light directly coming from the sign. Its intensity is proportional to the area that is not obscured by smoke. If the un-obscured area is not zero, the intensity of the direct incident light increases as the luminance of the sign increases. As the un-obscured area decreases, such effect also decreases. At the same time, the brightness of the background increases due to scattering. Once the un-obscured area becomes zero, no direct light can reach the image plane and the sign disappears. The visual threshold only depends on the un-obscured area.

12.3 Numerical modelling of visibility in smoke

This is the first quantitative direct numerical simulation of visibility in smoke. It has been made possible by the introduction of the image based concept of visibility so that visual stimuli can be estimated without the help of human field data. A number of unique features have been introduced in the numerical model in order to achieve the quantitative simulation based on synthetic image.

12.3.1 Hybrid zonal and Monte Carlo ray tracing algorithm

The zonal method in radiative heat transfer is an accurate but high cost numerical simulation method. It is capable of caching irradiance in 3D space. In a two pass algorithm as implemented in the current study, it is an efficient way to generate solutions of global illumination. The high cost of the zonal method lies in the computation of view factors.

Monte Carlo simulation is another accurate method widely accepted in neutron transport, nuclear medicine as well as computer graphics. In radiative heat transfer it is often referred as a benchmark method due to its accuracy and high cost. In computer graphic, the derived method

of photon-mapping has been used in the simulation with participating media. Photon-mapping generates a 3D irradiance cache similar, in function, to that in the zonal method. The highly unstructured photon-map has won the method a reputation of high cost even within the Monte Carlo community.

Although Monte Carlo ray tracing is a high cost method as said but it is also the one most suitable for parallel computing. The incoherent nature of light transport means that each ray being traced is autonomic therefore can be processed independently.

The new method proposed by the current author combines the above two methods and removed the high cost computation of view factor and unstructured photon-map. The cost of the new method is $O(mn^4)$. Comparing with $O(n^7)$ as in the case of zonal method, the current method is very efficient.

12.3.2 Dynamic adaptation

An important feature of the current simulation model is its capability of dynamic adaptation. Both 2D(surface) and 3D(space) meshes can be adaptive to the boundary conditions as well as the solution during iteration. The adaptation is in the form of mesh refinement and coarsening according to local gradient of the radiance. Mesh adaptation is based on the data structure of tree. For 2D surface mesh, it is a binary tree. In 3D space it is a Cartesian octree since Cartesian mesh is the most efficient one in terms of numerical operations and the octree mesh refinement keeps the aspect ratio of cells unchanged. Although the mesh is Cartesian in nature but the geometries are still adapted to its natural boundary curvature (see Figure 10-8).

As rays are issued from cached irradiance, the adaptation of the computational mesh leads to the adaptation of the ray tracing procedure. For the cases presented in this thesis, the number of rays issued at each emitting point is proportional to the local radiant power. It has made the cost of ray tracing more evenly distributed in space. This is a big improvement to the traditional Monte Carlo ray tracing method.

12.3.3 The two pass procedure

The simulation is carried out in a two pass procedure, namely shading and rendering. In the shading pass, the converged solution of global illumination is generated. The rendering pass utilises the global illumination solution and produces image from a particular viewing point. The procedure can efficiently generate high resolution images from many different viewpoints without recalculating global illumination.

12.3.4 Virtual camera

An image is only as good as the camera that produced it. This is also true for virtual camera. Previous virtual cameras are almost exclusively used in computer graphics and the images generated are only required to be visually acceptable or "realistic". In the current study, the synthetic images would be used in quantifying visibility therefore the virtual camera model must possesses the important features of the physical camera used in the experiment and reproduce the photographs from the physical camera. At the same time it should not decrease the accuracy of the overall algorithm. The new camera model has been built on these criteria and resultant synthetic images are indeed comparable to the photographs from the physical camera (Figure 10-18).

12.3.5 Accuracy of the model

The accuracy of the current model depends on the numerical algorithm and the physical model. The numerical algorithm being developed in the current study is based on the traditional zonal and Monte Carlo ray tracing models. Both of them are regarded as the most accurate models in their peer. Although there is no formal accuracy analysis, simulation of the simple point source solution has demonstrated that the algorithm is capable of accurately reproducing the analytical solution.

In physical modelling, the model has assumed that light scattering is isotropic. The model prediction of the smoke tunnel measurement has shown generally good agreement although discrepancies do exist in some cases. The analysis of the discrepancies points to the assumption of isotropic scattering.

12.3.6 Floor map of visibility

So far, a numerical model that is capable of generating accurate image for the measurement of visibility has been carefully built. What is needed is a way to interpret the simulation results and make it understandable to fire protection engineer. The image generated as the direct result of the simulation is good but it only gives the visibility at a particular viewpoint for a particular target. In the current study, the novel floor map of visibility (FMV) offers a comprehensive view of the visibility assessment of a design. The FMV is in the form of normal contours that clearly maps out the regions where visibility is poor.

In summary, the introduction of the image based visibility concept has significantly improved our understanding of the visibility of emergency sign in smoke laden environment. Application

of this concept in experiments has led to conclusions that are either consistent with previous research results or compensate/offer better explanation of them. In return, the experimental evidence also increased our confidence in the new concept itself.

The new concept of visibility also makes it possible to simulate visibility directly instead of relying on limited visual threshold data. Image based visibility simulation is suitable in almost any situation and the results are very easy to be interpreted. It will prove to be a useful tool in fire safety engineering.

12.4 Future research work in this area

- A new way of measuring visibility has been introduced in the current study. It has yield some useful results in the cases studied which has enhanced our understanding of the subject. The definition of visibility used is limited to the current experiments and computer simulation. More general concept of image based visibility is needed to cover wider range of applications.
- At the moment, the perceived image has been simulated assuming that the human eye has focus on the area limited to the target. More physiological research is need on the way human eye searching and locking the pre-defined target.
- The LED light source used in the current study is simple and less expensive but its non-uniformity has created some uncertainties in the experimental results. More uniform and controllable (luminance and spectrum) light source may offer better quality data in the future.
- Since the optical properties of soot have been extensively studied, real fire smoke should be tested. It would be closer to the design environment and can also demonstrate the effect of light absorption on visibility.
- Anisotropic scattering algorithm should be introduced into the simulation model to improve its accuracy.
- The objective of creating the current computer model is to offer a useful visibility simulation tool (VST) for fire engineers in their design verification. Therefore a graphic user interface would be necessary.

Bibliography

Akins, K. (Ed.). (1996). *Perception.* New York, Oxford: Oxford University Press.

Ashdown, I. (1994). *Radiosity: A Programmer's Perspective.* John Wiley & Sons, Inc.

Azad, F. H., & Modest, M. F. (1981). Evaluation of the radiative heat flux in absorbing, emitting and linear-anisotropic scattering cylindrical media. *Trans. ASME J. Heat Transfer* (103), pp. 350-356.

Bankston, C. P., Cassanova, R. A., Powell, E. A., & Zinn, B. T. (1978). *NBS-GCR G8-9000.* National Bureau of Standards, Washington, DC.

Bankston, C. P., Zinn, B. T., Browner, R. F., & Powell, E. A. (1981). *Combustion & Flame , 41,* 273.

Bartl, J., & Branek, M. (2004). Emissivity of aluminium and its importance for radiometric measurement. *Measurement Science Review , 4,* pp. 31-36.

Batten, C. (1985). Spectral optical constants of soots from polarized angular reflectance measurements. *Applied Optics , 24* (8).

Beard, A., & Carvel, R. (2005). *The Handbook of Tunnel Fire Safety.* London: Thomas Telford Publishing.

Beck, V. (1997). Performance-based Fire Engineering Design and its Application in Australia. *Fire safety science* (pp. 23-39). International Association for Fire Safety Science.

Bhate, N. (1993). Application of Rapid Hierarchical Radiosity to Participating Media. *Proceedings of ATARV-93: Advanced Techniques in Animation, Rendering and Visualization.*

Bhate, N., & Tokuta, A. (1992). Photorealistic volume rendring of media with directional scattering. *Third Eurographics Workshop on Rendering,* (pp. 227-245). Brishtol, UK.

Blaker, J. W., & Rosenblum, W. M. (1993). *Optics - An Introduction for Students of Engineering.* New York: Macmillan Publishing Company.

Bohren, C. F., & Huffman, D. R. (1998). *Absorption and Scattering of Light by Small Particles.* New York, Chichester, WeinHeim, Boston, Singapore, Toronto: John Wiley & Sons Inc.

Boudet, A., Pitot, P., Pratmarty, D., & Paulin, M. (2005). Photon Splatting for Participating Media. *GRAPHITE 2005* (pp. 197-204). Dunedin, New Zealand: ACM.

Bousis, C., Emfietzoglou, D., Hadjidoukas, P., & Nikjoo, H. (2008). A Monte Carlo study of absorbed dose distributions in both the vapor and liquid phases of water by intermediate energy electrons based on different condensed-history transport schemes. *Physics in Medicine and Biology , 53*, 3739-3761.

Building Research Establishment Ltd. (1998). *Emergency Guidance Lighting Systems, Phase 1.* HSE, UK.

CHAM. (2006). *TR326 – PHOENICS-VR Reference guide.* London: CHAM.

Chandrasekhar, S. (1960). *Radiative Transfer.* Dover Publications.

Chang, H., & Charalampopoulos, T. (1990). Determination of the Wavelength Determination of the Wavelength Dependence of Refractive Indices of Flame Soot. *Proceedings: Mathematical and Physical Sciences, 430*, pp. 577-591.

Charalampopoulos, T., & Chang, H. (1988). In Situ Optical Properties of Soot Particles in the Wavelength Range from 340nm to 600nm. *Combustion Science and Technology , 59*, 401-421.

Charalampopoulos, T., & Felske, J. (1987). Refractive Indices of Soot Particles Deduced from In-Situ Laser Light Scattering Measurements. *Combustion and Flame , 68*, pp. 283-294.

Chen, S. E., Rushmeier, H. E., Miller, G., & Turner, D. (1991). A Progressive Multi-Pass Method. *Computer Graphics , 25* (4).

Clark, F. (1988). *Strategies for Improving Visibility in Fires, CBD-246.* Institute for Research in Contruction, NRC, Canada.

Coelho, P. (2004). A modified version of the discrete ordinates method for radiative heat transfer modellin. *Computational Mechanics* (33), 375-388.

Cohen, M. F., & Wallace, J. R. (1993). *Radiosity and Realistic Image Synthesis.* Boston: Academic Press Professional.

Collins, B. L., Dahir, M. S., & Madrzykowski, D. (1992). Visibility of Exit Signs in Clear and Smoky Conditions. *Journal of the Illuminating Engineering Society , 21* (1), pp. pp. 69-84.

Collins, B. L., Dahir, M. S., & Madrzykowsky, D. (1990). *Evaluation of Exit Signs in Clear and Smoke Conditions, NISTIR 4399.* NIST.

Collins, B., & Lerner, N. (1983). *An Evaluation of Exit Sign Visibility, NBSIR 83-2675.* National Bureau of Standards.

Cook, R. L., Porter, T., & Carpenter, L. (1984). Distributed Ray Tracing. *Computer Graphics , 18* (3).

Dalzell, W., & Sarofim, A. (1969, 2). Optical Constants of Soot and Their Application ot Heat-Flux Calculations. *Journal of Heat Transfer, Trans. of ASME* , pp. 100-104.

Dennis, P. (1986). *Photodetectors.* New York: Plenum Press.

Dobbins, R. (1994). Comparison of a Fractal Smoke Optics Model with Light Extinction Measurements. *Atmospheric Environment , 28* (5), 889-897.

Dobbins, R., & Megaridis, C. (1991). Absorption and scattering of light by polydisperse aggregates. *Applied Optics , 30*, 4747-4754.

Dutré, P., Bekaert, P., & Bala, K. (2003). *Advanced Global Illumination.* Massachusetts: A K Peters.

EVANS, F. K. (1998). The Spherical Harmonics Discrete Ordinate Method for Three-Dimensional Atmospheric Radiative Transfer. pp. 429-446.

Fennell, D. (1988). *Investigation into the King's Cross Underground Fire.* Department of Transport, UK.

Fiveland, W. (1984). Discrete-Ordinate Solutions of the Radiative Transport Equations for Rectangular Enclosures. *ASME Journal of Heat Transfer , 106*, 699-706.

Fiveland, W. (1988). Three-Dimensional Radiative Heat-Transfer Solutions by the Discrete-Ordinates Method. *Journal of Thermophysics and Heat Transfer , 2* (4), 309-316.

Fleck, J. A. (1961). The calculation of nonlinear radiation transport by Monte Carlo method: Statistical physics. *Methods Comput. Phys.* (1), pp. 43-65.

Foley, J. D., Dam, v. A., Feiner, K. S., & Hughes, F. J. (1990). *Computer Graphics.* Addison-Wesley publishing company.

Forney, G. P., & McGrattan, K. B. (2006). *User's Guide for Smokeview Version 4 - A Tool for Visualizing Fire Dynamics Simulation Data.* NIST.

Forney, G. (2009). *Smokeview (Version 5) - A Tool for Visualizing Fire Dynamics Simulation Data Volume II: Technical Reference Guide.* NIST.

Gandhi, P. D. (1994). Validation of a Zone Model for Predicting Smoke Obscuration in Rooms. *Journal of Fire Science , 12* (3), pp. 313-325.

Habib, Z., & Vervisch, P. (1988). On The Refractive Index of Soot at Flame Temperature. *Combustion Science and Technology , 59*, pp. 261-274.

Heaslet, M. A., & Warming, R. F. (1963). Theoretical predictions of radiative heat transfer in homogeneous cylindrical medium. *J. Quant. Spectrosc. Radiat. Transfer* (6), pp. 751-774.

Horvath. (1993). Atmospheric Light Absorption - A Review. *Atmospheric Environment , 27A* (3), 293-317.

Hottel, H. C., & Sarofim, A. F. (1967). *Radiative heat transfer.* (New York: McGraw-Hill.

Hottel, H., & Cohen, H. (1958). Radiant heat exchange in a gas filled enclosure: Allowance for nonuniformity of gas temperature. *AIChE J.* (4), pp. 3-14.

Howell, J. R., & Perlmutter, M. (1964). Monte Carlo solution of radiant heat transfer in a nongray, nonisothermal gas with temperature-dependent properties. *AIChE J.* (10), pp. 562-567.

Howell, J. R., & Perlmutter, M. (1964). Monte Carlo solution of thermal transfer through radiant media between gray walls. *Trans. ASME J. Heat Transfer* (86), pp. 116-122.

HSE, UK. (1998). *Emergency Way Guidance Lighting Systems.* HSE, UK.

Hunt, R. (1992). *Measuring Colour* (2nd Edition ed.). New York, London, Toronto, Sydney, Tokyo, Singapore: Ellis Horwood Ltd.

Husted, B., Carlsson, J., & Göransson, U. (2004). VISIBILITY THROUGH INHOMOGENEOUS SMOKE USING CFD. *INTERFLAM 2004*, (pp. 697-702).

Ingason, H., & Persson, B. (1998). Prediction of visibility in tunnel fires. *Third International Conference on safty in road & rail tunnels*, (pp. 151-158). Nice.

ISO. (2007). Life-threatening components of fire - Guidelines for the estimation of time available for escape using fire data, ISO 13571.

Jarosz, W., Donner, C., Zwicher, M., & Jensen, H. W. (2007). Radiance Caching for Participating Media. *ACM Transactions on Graphics , 27* (1).

Jensen, G. (1994). *Evacuating in Smoke - Decisive Factors.* IGP AS. Trondheim, Norway: IGP AS.

Jensen, H. (1996). Global Illumination using Photon Maps. *Rendering Techniques'96, Proceedings of Seventh Eurographics Workshop on Rendering* , pp. 21-30.

Jensen, H. W. (2001). *Realistic Image Synthesis Using Photon Mapping.* A K Peters.

Jensen, H. W., & Christensen, P. H. (1998). Efficient Simulation of Light Transport in Scenes with Participating Media using Photon Maps. *Proceedings of SIGGRAPH'98*, (pp. 311-320). Orlando.

Jeon, G., & Wonhwa, H. (2009). Characteristic Features of the Behavior and Perception of Evacuees from the Daegu Subway Fire and Safety Measures in an Underground Fire. *Journal of Asian Architecture and Building Engineering , 8,* 415-422.

Jiang, E. X., Gao, K. M., & Wu, J. K. (1978). *Linear Algebra.* Shanghai: People's Education Press.

Jin, T. (2008). Visibility and Human Behavior in Fire Smoke. In SFPE, *The SFPE Handbook of Fire Protection Engineering* (pp. 2-54 - 2-66). NFPA.

Jin, T. (1978). Visibility through fire smoke. *Journal of Fire and Flammability , 9.*

Jin, T., & Yamada, T. (1985). Irritating Effects of Fire Smoke on Visibility. *Fire Science & Technology , 5,* 79-89.

Jin, T., Yamada, T., Kawai, S., & Takahashi, S. (1991). Evaluation of the Conspicuousness of Emergency Exit Signs. *Proceedings of the Third International Symposium of Fire Safety Sceince* (pp. 835-841). Boston: International Association for Fire Safety.

Jones, A. R. (1999). Light scattering for particle characterization. *Progress in Energy and Combustion Science , 25,* 1-53.

Kajiya, J. T. (1986). The Rendering Equation. *ACM, SINGGRAPH 86 , 20* (4), 143-150.

Kerker, M. (1969). *The scattering of light and other electromagnetic radiation.* New York and London: Academic Press.

Kirkland, C. (2002). The fire in the Channel Tunnel. *Tunnelling and Underground Space Technology* (17), 129-132.

Kobiyama, M. (1989). The reduction of computational time of the Monte Carlo method, applied to radiative heat transfer with variable properties, by using a fixed properties loop. *Computational Mechanics , 5* (1), 33-39.

Kolb, C., Mitchell, D., & Hanrahan, P. (1995). A Realistic Camera Model for Computer Graphics. *ACM-0-89791-701-4/95/008* .

Köylü, U. O., & Faeth, G. M. (1994). Optical Properties of Overfire Soot in Buoyant Turbulent Diffusion Flames at Long Residence Time. *Journal of Heat Transfer, ASME , 116*, 152-159.

Köylü, U. O., Faeth, G. M., Farias, T., & Carvalho, M. (1995). Fractal and projected structure properties of soot aggregates. *Combustion and Flame , 100*, 621-633.

Lathrop, K. (1966). Use of Discrete-Ordinate Medhod for Solution of Photon Transport Problems. *Nuclear Science and Engineering , 24*, pp. 381-388.

Lee, C. (1962). *The Discrete SN Approximation to Transport Theory.* Lawrence Livermore Laboratory.

Lee, S. &. (1981). Optical Constants of Soot in Hydrocarbon Flames. *Eighteenth Sympothsium (International) on Combustion* (pp. 1159-1166). The Combustion Institute.

Liou, B., & Wu, C. (1997). Ray effects in the discrete-ordinate solution for surface radiation exchange. *Heat and Mass Transfer* (32), 271-275.

Liu, J., Shang, H., & Chen, Y. (1999). Parallel simulation of radiative heat transfer using an unstructured finite-volume method. *Numerical Heat Transfer - Part B: Fundamentals , 36* (2), pp. 115-137.

Lougheed, G. (2000). Basic Principles of Smoke Management for Atriums. *Construction Technology Updates* (47), 1-5.

Lougheed, G., & Hadjisophocleous, G. (2001, June). Smoke hazards from fires in high places. *ASHRAE Journal, Smoke Management* , 1-5.

Mackowski, W. (1991). Analysis of radiative scattering for multiple sphere configurations. *Proceedings Royal Society London, A433*, pp. 599-614.

Mackowski, W. (1994). Calculation of total cross sections of multiple-sphere clusters. *Journal of the Optical Society of America* , 2851-2861.

Mackowski, W. (1995). Electrostatics analysis of radiative absorption by sphere clusters in the Rayleigh limit: application to soot particles. *Applied Optics , 34* (18), pp. 3535-3545.

Mather, G. (2009). *Fundations of Sensation and Perception* (Second Edition ed.). Hove and New York: Psychology Press.

McGrattan, K., Hostikka, S., & Floyd, J. (2009). *Fire Dynamics Simulator User's Guide.* NIST. NIST.

Menguc, M. E., & Viskanta, R. (1985). Radiative transfer in three-dimensional rectangular enclosures containing inhomogeneous, anisotropically scattering media. *J. Quant. Spectrosc. Radiat. Transfer* (33), pp. 533-549.

Metropolis, N. (1987). The beginning of the Monte Carlo method. *Los Alamos Science (1987 Special Issue dedicated to Stanislaw Ulam)* , 125-130.

Metropolis, N., & Ulam, S. (1949). The Monte Carlo Method. *Journal of the American Statistical Association , 44* (247), 335-341.

Meyer, C. (2000). *Matrix Analysis and Applied Linear Algebra.* SIAM.

Microsoft Encarta. (n.d.). *Visibility, Encarta.msn.* Retrieved 12 20, 2009, from Microsoft Encarta: http://encarta.msn.com/dictionary_/visibility.html

Mishra, S. C., & Blank, D. A. (1995). High to low optical thickness Monte Carlo solutions of the radiative heat transfer problems in 2-D rectangular enclosures with absorbing-emitting-isotropic scattering. In T. S. Mruthyunjaya, *In Advances in mechanical engineering* (pp. 1657-1668). New Delhi: Narosa.

Modest, M. F. (2003). *Radiative Heat Transfer* (Second Edition ed.). Singapore: Academic Press.

Mulholland, G. W. (2008). Smoke Production and Properties. In *SFPE Handbook* (4 ed., pp. 2-291 - 2-302). SFPE.

Mulholland, G. W., & Ohlemiller, T. J. (1981). Aerosol Characterization of a Smoldering Source. *Aerosol Science and Technology , 1*, pp. 59-71.

Nelson, H. F., Look, D. C., & Crosbie, A. L. (1986). Two-dimensional radiative back-scattering from optically thick media. *Trans. ASME J. Heat Transfer* (108), pp. 619-625.

NFPA. (2007). *NFPA 130: Standard for Fixed Guideway Transit and Passenger Rail Systems.* NFPA.

NFPA. (1999). *NFPA 170: Standard on Fire Safety Symbols.* NFPA.

Noble, J. J. (1975). The zone method: Explicit matrix relations for total exchange areas. *Int. J. Heat Mass Transfer* (18), pp. 261-269.

Office of the Deputy Preminister. (2004). *The Economic Cost of Fire: Estimates for 2004.* London: National Statistics.

Office of the Deputy Preminister, UK. (2004). *Fire Statistics, United Kingdom, 2004.* London: National Statistics.

Oppenheim, A. (1956). Radiation Analysis by the Network Method. *Transactions of ASME, Journal of Heat Transfer , 78*, 725-735.

Ou, S.-C. S., & Kuo-Nan, L. (1982). Generalization of the spherical harmonics method to radiative transfer in multi-dimensional space. *J. Quant. Spectrosc. Radiat. Transfer* (28), pp. 271-288.

Ouellette, M. J. (1988). Exit Signs in Smoke: Design Parameters for Greater Visibility. *Lighting Research & Technology , 20* (4), pp. 139 - 153.

Ouellette, M. (1993, 7). This way out. *Progressive Architecture* , pp. 39-42.

Potmesil, M., & Indranil, C. (1981). A LENS AND APERTURE CAMERA MODEL FOR SYNTHETIC IMAGE GENERATION. *Computer Graphics , 15* (3), pp. 297-305.

Pritchard, D. C. (1999). *Lighting.* (6, Ed.) London: Addison Wesley Longman Limited.

Rasbash, D. J. (1951). The Efficience of Hand Lamps in Smoke. *IFE Journal , 11* (1), p. 46.

Ratzel, A. C., & Howell, J. R. (1983). Two-dimensional radiation in absorbing-emitting media using the PN approximation. *Trans. ASME J. Heat Transfer* (105), pp. 333-340.

Ratzel, A., & Howell, J. (1982). Two-Dimensional Radiation in Absorbing-Emitting-Scattering Media Using P-N Approximation. *ASME Papper* .

Rea, M. (1985, 9). How good are emergency lighing systems. *Lighting and Application* , pp. 26-27.

Rea, M., Clark, F., & Ouellette, M. (1985). *Photometric and psychophysical measurements of exit signs through smoke.* NRCC 24627: National Research Council of Canada.

Robinson, A., & Burgoyne, J. (1999). The Scandinavian Star Incident, A Case Study. *IFE Journal* .

Rubini, P. A., Zhang, Q., & Moss, J. B. (2007). *Simulation of Visibility in Smoke Laden Enviornments.* London: InterFlame2007, 11th International Conference on Fire Science and Engineering.

Rubini, P., & Zhang, Q. (2007). SIMULATION OF VISIBILITY IN SMOKE LADEN ENVIRONMENTS. *InterFlam 2007, 11th International Conference on Fire Science and Engineering.* London, UK.

Rushmeier, H. E., & Torrance, K. E. (1987). The zonal method for calculating light intensities in the presence of participating media. *Computer Graphics , 21* (4), 293-302.

Rushmeier, H. E., & Torrence, K. E. (1990). Extending the Radiosity Method to Include Specularly Reflecting and Translucent Material. *ACM Transaction on Graphics , 9* (1).

Rushmeier, H. (1988). *Realistic Image Synthesis for Scense with Radiatively Participating Media.* PhD Dissertation, Cornell University, Computing Science.

Sacadura, J. (2005). Radiative heat transfer in fire safety science. *Journal of Quantitative Spectroscopy & Radiative Transfer* (93), pp. 5-24.

Schooley, L. C., & Reagan, J. A. (1980). Visibility and Legibility of Exit Signs, Part II: Experimental Results. *Journal of the IES , 10* (1), pp. 29-32.

Sekizawa, A. (1994). International Comparison Analysis on Fire Risk Among the United States, The United Kindom, and Japan. *Fire safety science, Proceedings of the fourth international symposium* (pp. 961-969). International Association for Fire Safety Sceince.

SFPE & NFPA. (2008). *NFPA SFPE - Handbook of Fire Protection Engineering* (4 ed.). NFPA.

SFPE. (2008). *The SFPE Handbook of Fire Protection Engineering.* (4, Ed.) SFPE.

Shirley, P. S. (1991). *Physically Based Lighting Calculations for Computer Graphics.* Computer Science. University of Illinois.

Siegel, R., & Howwell, J. R. (1992). *Thermal Raidiation Heat Transfer* (3 ed.). Hemisphere Publishing Corporation.

Simpson, G. (1948). *Visibility and the optical properties of the atmosphere.* Air Ministry, Meteorological Office. London: His Majesty's Stationery Office.

Smith, T. E., Sben, Z. E., & Al-Turki, A. M. (1985). Radiative and conductive transfer in a cylindrical enclosure for a real gas. *Trans. ASMEJ. Heat Transfer* (104), pp. 482-485.

Smyth, K. C., & Shaddix, C. R. (1996). The Elusive History of m=1.57-0.56i for the Refractive Index of Soot. *Combustion and Flame , 107*, 314-320.

Sonka, M., Hlavac, V., & Boyle, R. (1993). *Image Processing, analysis and Machine Vision.* International Thomson Computer Press.

Spanier, J., & Gelbard, E. M. (1969). *Monte Carlo Principles and Neutron Transport Problems.* Addison-Wesley.

Stull, V., & Plass, G. (1960). Emmisivity of dispersed carbon particles. *Journal of the Optical Society of America , 50*, 121-129.

Suo-Anttila, J., Gill, W., Gritzo, L., & Blake, D. (2005). An evaluation of actual and simulated smoke properties. *Fire and Materials , 29*, 91-107.

Sychta, Z. (1997). Contrast Attenuation Coefcient as a Parameter Enabling Determination of Range of Visibility in Smoke. *Fire and Materials , 21*, pp. 205-211.

Tessé, L., Francis, D., & Jean, T. (2004). Monte Carlo modeling of radiative transfer in a turbulent sooty flame. *International Journal of Heat and Mass Transfer , 47*, 555-572.

Tien, C. L. (1988). Thermal radiation in packed and fluidized beds. *Trans. ASME J. Heat Transfer* (110), pp. 1230-1242.

Truelove, J. S. (1987). Discrete-Ordinate Solution of the Radiation Transport Equation. *ASME Journal of Heat Transfer , 109* (4), 1048-1051.

Tuchin, V. (2007). *Tissue optics* (2 ed.). Bellingham, Washington: SPIE Press.

Tuomisaari, M. (1997). *Visbility of exit signs and low-location lighting in smoky conditions.* VTT Building Technology. JULKAISIJA-UTGIVARE-PUBLISHER.

van de Hulst, H. C. (1981). *Light Scattering by Small Particles.* New York: Dover Publications, Inc.

van Hulle, P., Talbaut, M., Weill, M., & Coppalle, A. (2002). Inversion method and experiment to determine the soot refractive index: application ot turbulent diffusion flames. *Measurements Science and Technology , 13*, 375-382.

Veach, E. (1997). *Robust Monte Carlo Methods for Light Transport Simulation.* Computer Science. Stanford University.

Vincent, D. (2009). Retrieved from NYFirestore.com: http://www.workingfire.net/misc3.htm

Viskanta, R. &. (1987). Radiation heat transfer in combustion systems. *Prog. Energy Combust. Sci.* (13), pp. 97-161.

Walton, W. D., & Thomas, P. H. (2008). Estimating Temperatures in Compartment Fires. In SFPE, & 4 (Ed.), *The SFPE Handbook of Fire Protection Engineering.* National Fire Protection Association.

Webber, G. M., & Aizelwood, C. (1994). Emergency lighting and wayfinding systems in smoke. *Proceedings of the CIBSE National Lighting Conference* (pp. pp. 131-143). Cambridge: CIBSE.

Weicheng, F., & Li, S. (1994). Fire Research in China. *Fire safety sceince, Proceedings of the fourth international symposium* (pp. 27-45). International association of fire safety science.

Werner, C., Jurgen, S., Leike, I., & Munkel, C. (2005). Visibility and Cloud Lidar. In *Electromagnetic Wave Scattering on Nonspheircal Particles* (pp. 165-186). Springer Berlin / Heidelberg.

Whitted, T. (1980). An Improved Illumination Model for Shaded Display. *Communications of ACM , 23* (6), 343-349.

wikipedia/eye. (n.d.). Retrieved from http://en.wikipedia.org/wiki/Eye

Williams, J., & Gritzo, L. (1998). In situ sampling and transmission electron microscope analysis of soot in the flame zome of large pool fires. *Proceedings of the 27th International Symposium on Combustion, 2*, p. 2707.

WITZ, F. J. (2008). *http://en.wikipedia.org/wiki/Digital_single-lens_reflex_camera.* Retrieved from Wikipedia.

Wu, J., Krishnan, S., & Faeth, G. (1997, 5). Refractive Indices at Visible Wavelengths of Soot Emitted from Buoyant Turbulence Diffusion Flames. *Journal of Heat Transfer, Trans. of the ASME , 119*, pp. 230-237.

Wyszecki, G., & Stiles, W. S. (1982). *Color Science: concepts and methods, quantitative data and formulae* (2 ed.). New York: Wiley.

Zhang, Q., & Rubini, P. (To be published in 2010). Modelling of Light Extinction by Soot Particles. *Fire Safety Journal* .

Zhang, Q., & Rubini, P. (2009). Simulation of perceived visibility in smoke laden environment. *Proceedings of Human Behaviour in Fire 2009.* Cambridge, UK.

Appendix A Measurement of barcode visibility

A1 Barcode with aspect 2:1

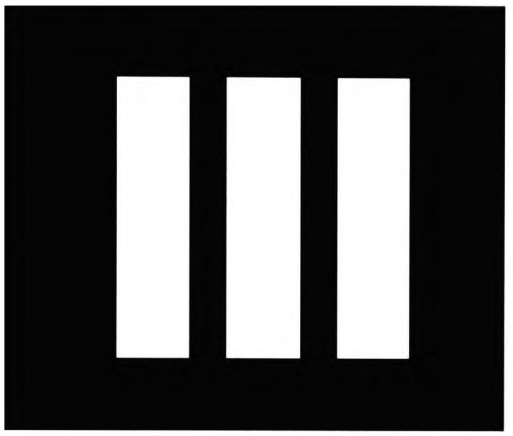

Barcode with aspect ratio 2:1

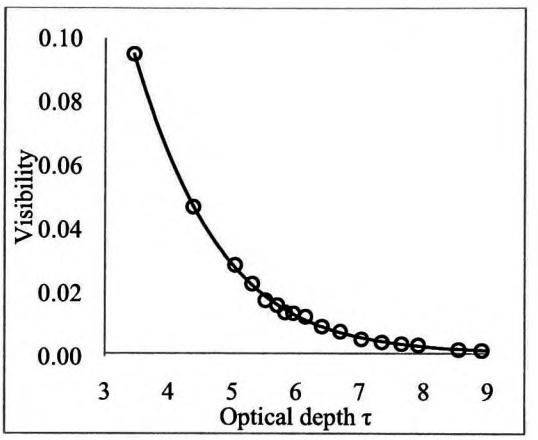

(1) red, power level 1

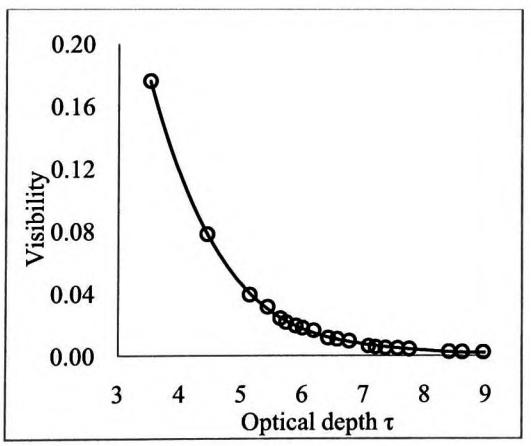

(2) green, power level 1

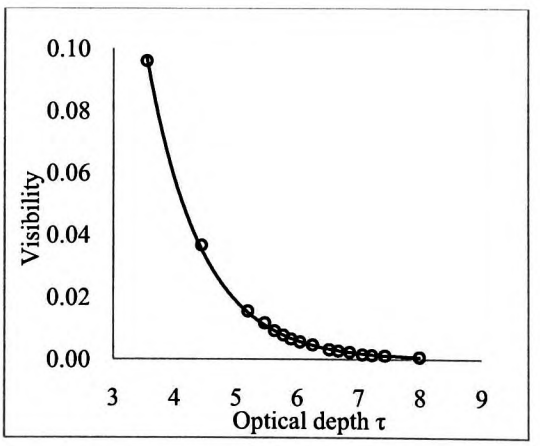

(3) blue, power level 1

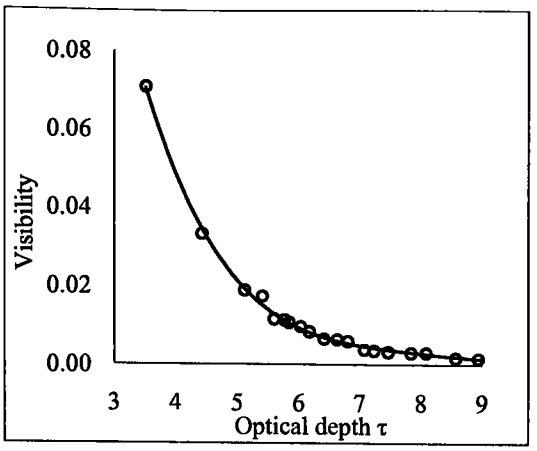

(4) red, power level 2

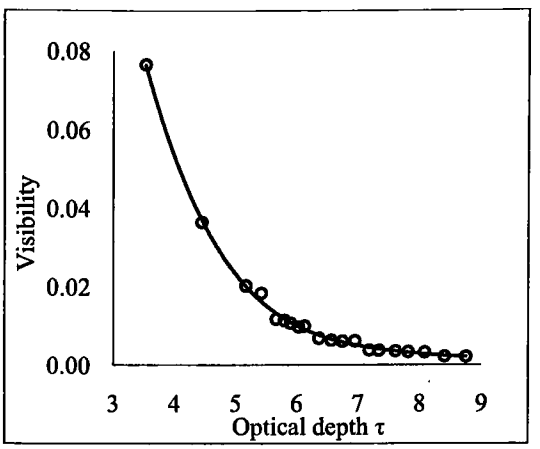

(5) green, power level 2

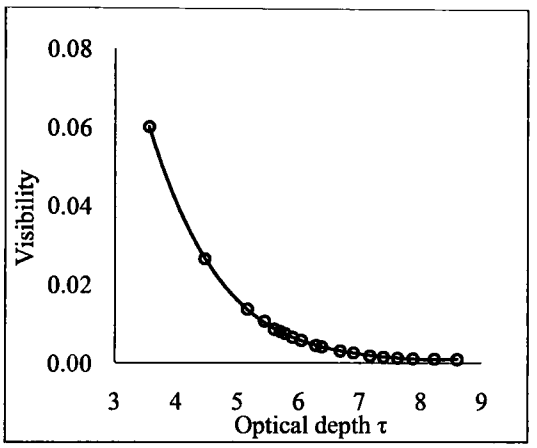

(6) blue, power level 2

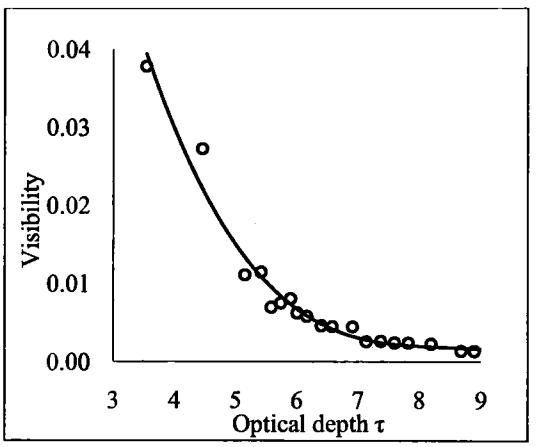

(7) red, power level 3

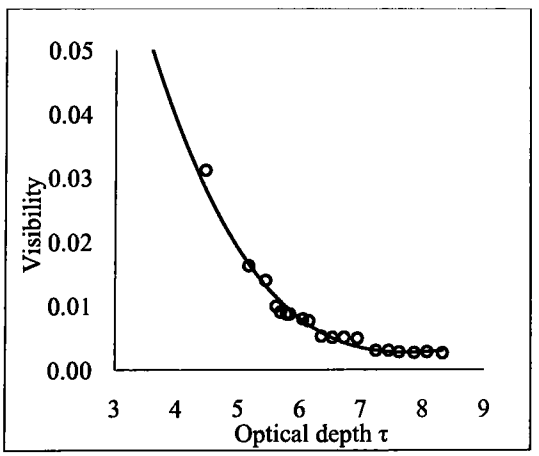

(8) green, power level 3

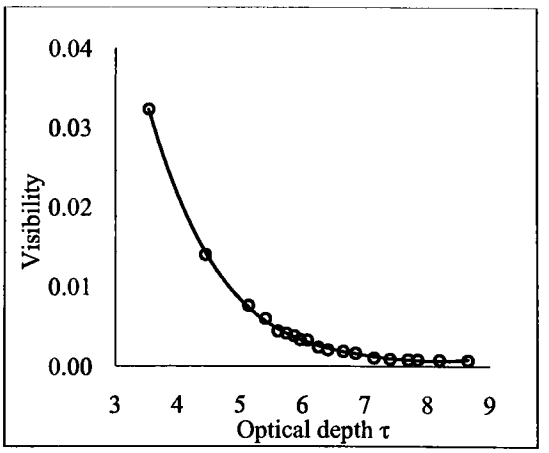

(9) blue, power level 3

A2 Barcode with aspect ratio 1.5:1

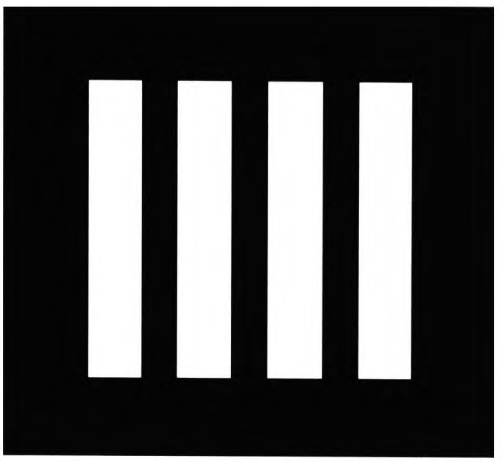

Barcode with aspect ratio 1.5:1

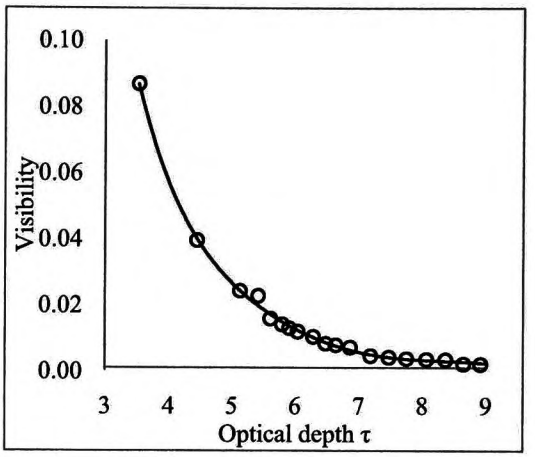

(1) red, power level 1

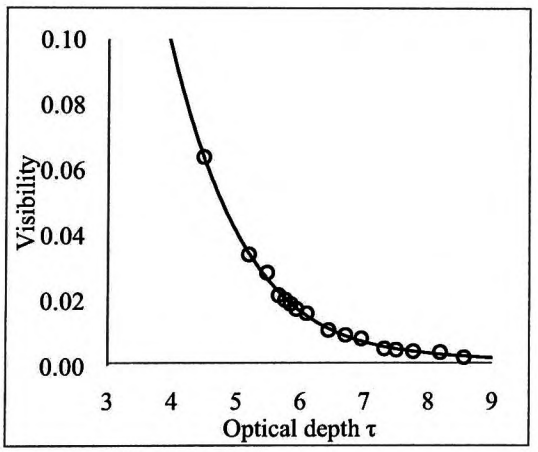

(2) green, power level 1

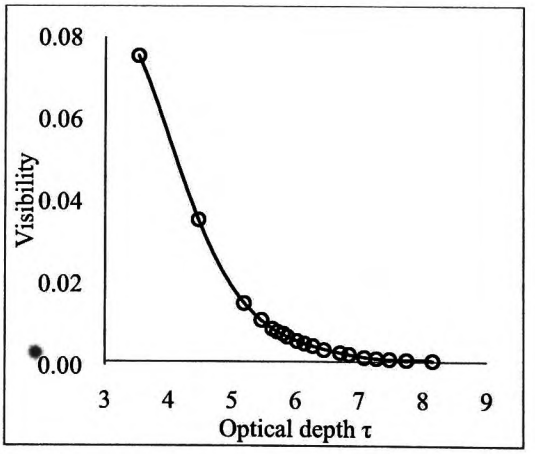

(3) blue, power level 1

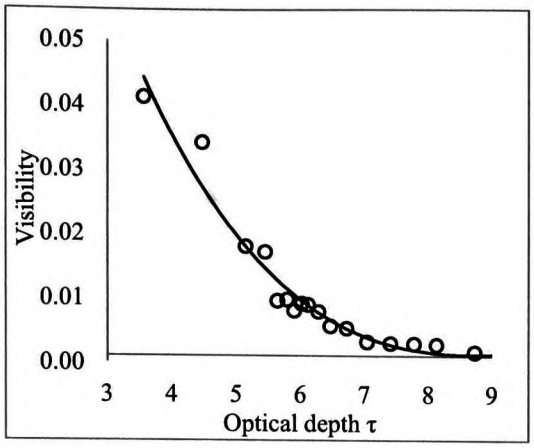

(4) red, power level 2

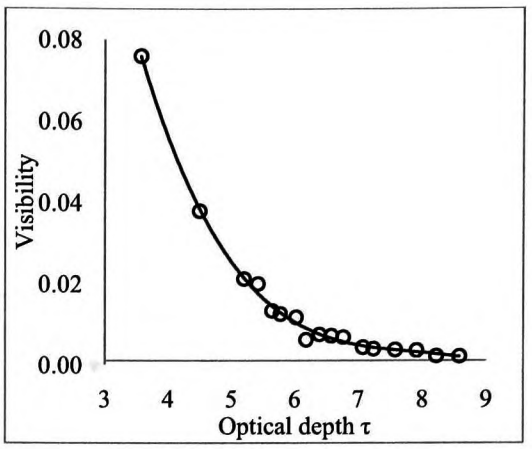

(5) green, power level 2

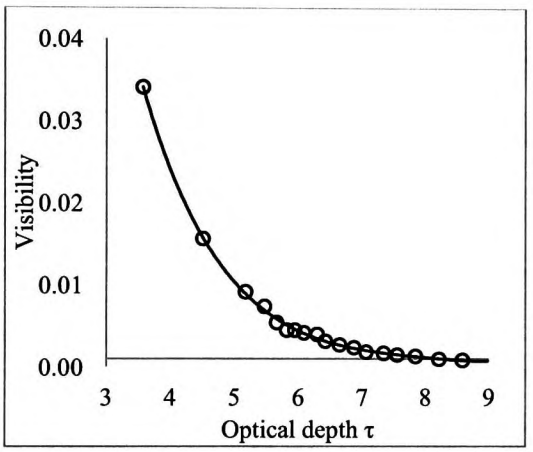

(6) blue, power level 2

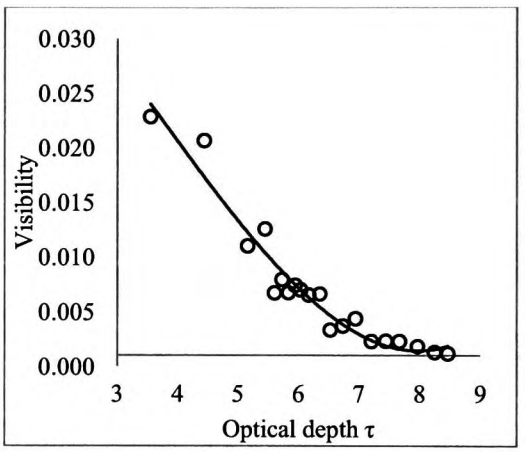

(7) red, power level 3

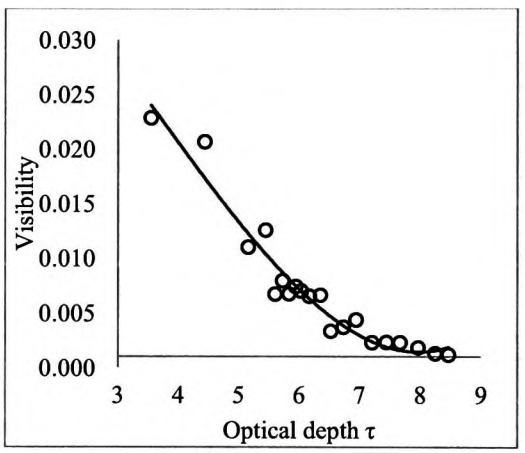

(8) green, power level 3

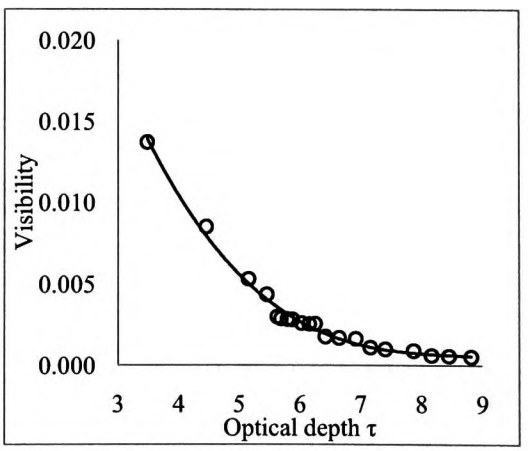

(9) blue, power level 3

A3 Barcode with aspect ratio 1:1

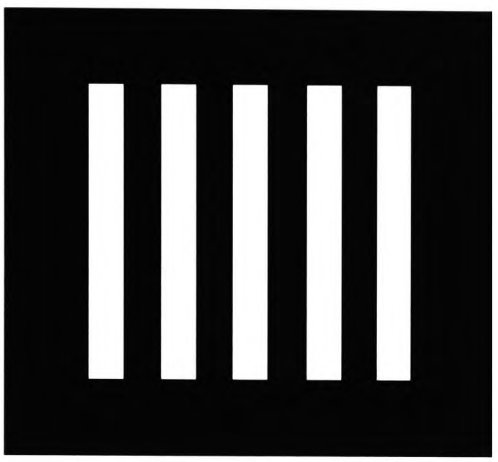

Barcode with aspect ratio 1:1

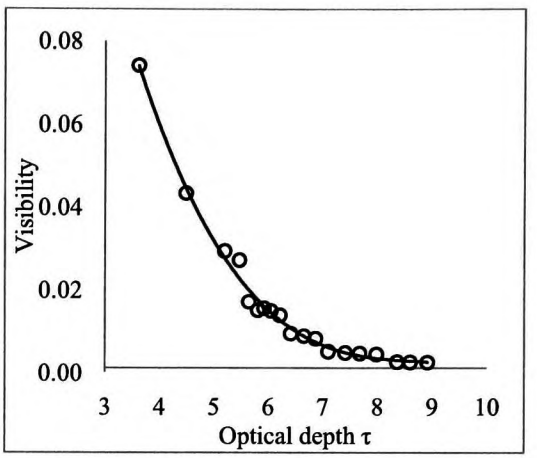

(1) red, power level 1

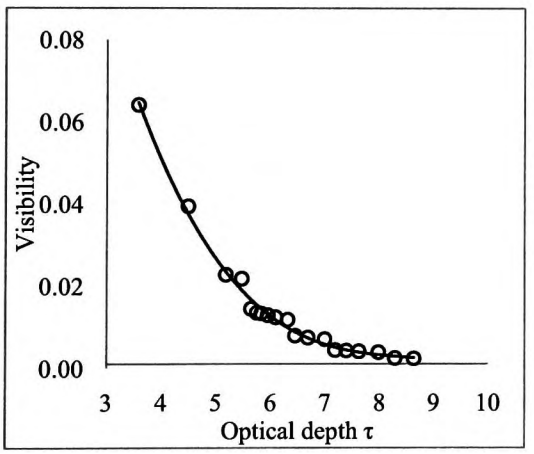

(2) green, power level 1

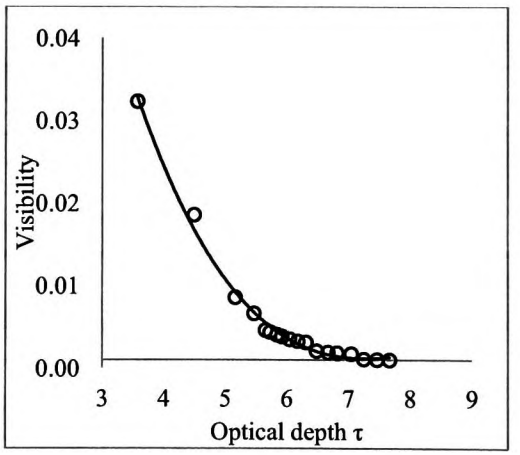

(3) blue, power level 1

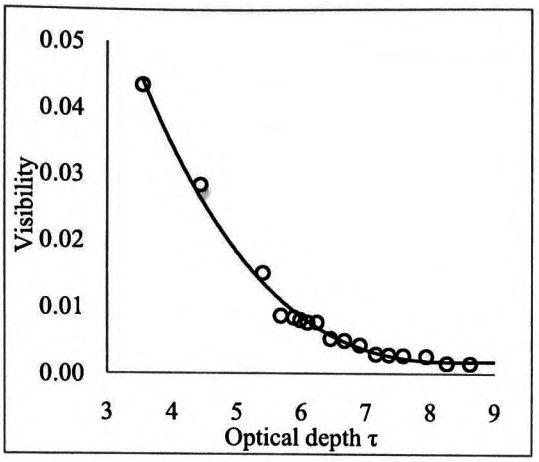

(4) red, power level 2

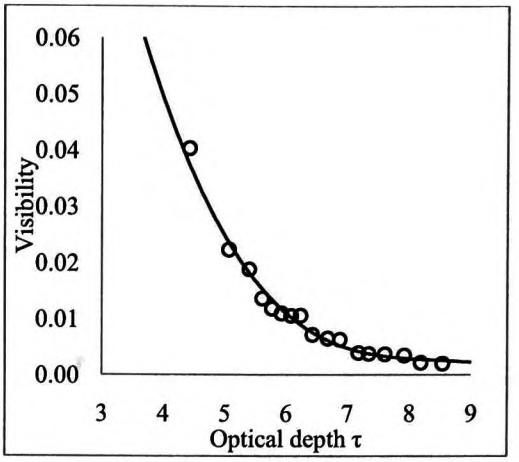

(5) green, power level 2

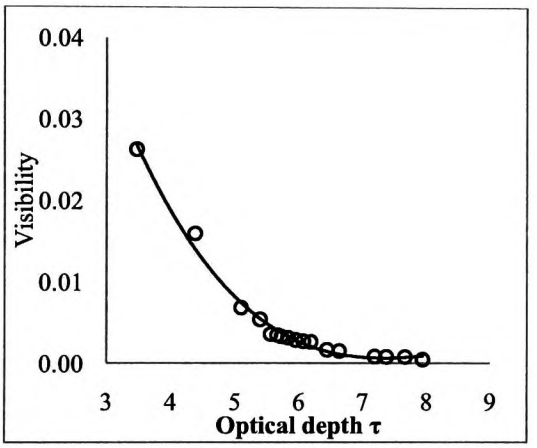

(6) blue, power level 2

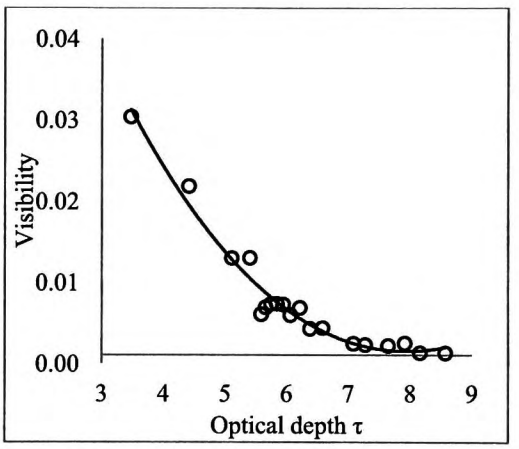

(7) red, power level 3

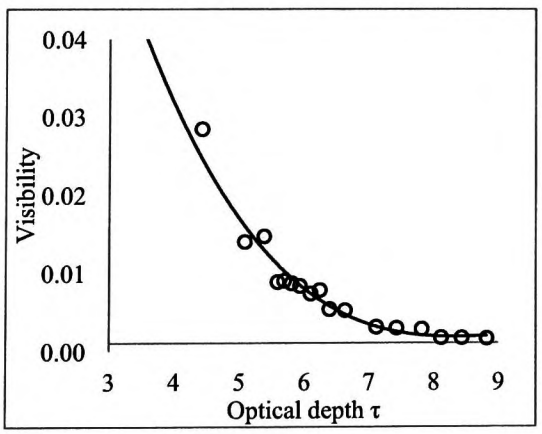

(8) green, power level 3

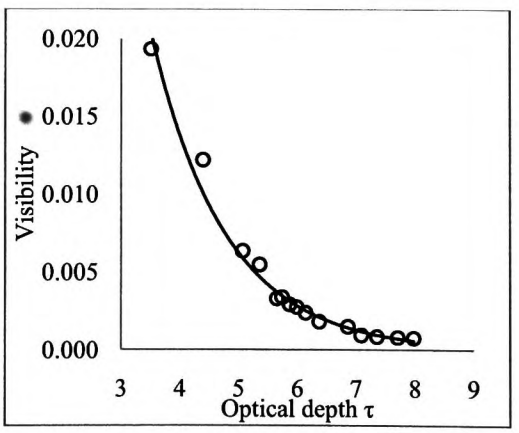

(9) blue, power level 3

A4 Barcode with aspect ratio 1:0.5

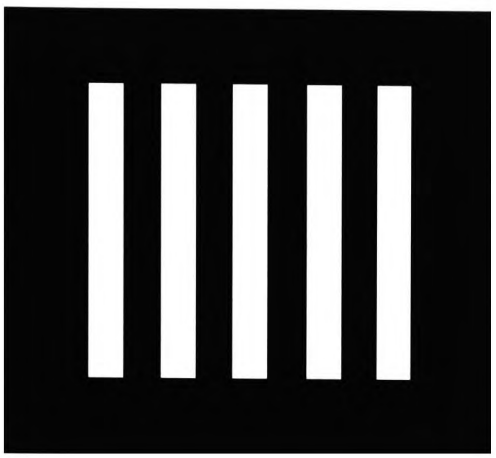

Barcode with aspect ratio 1:1

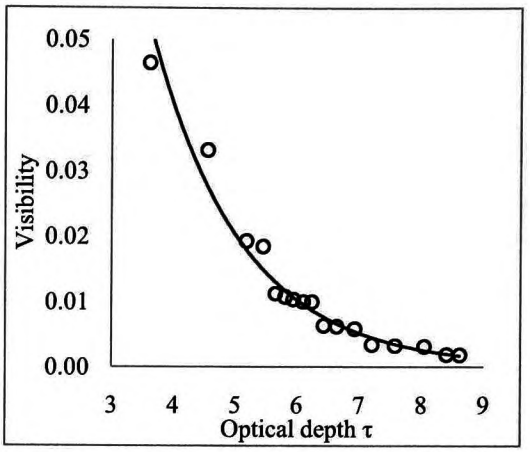

(1) red, power level 1

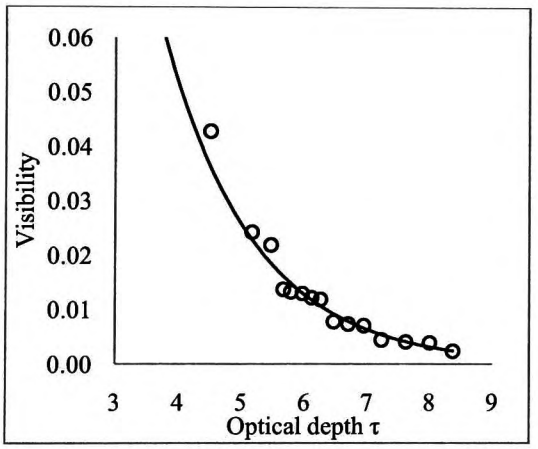

(2) green, power level 1

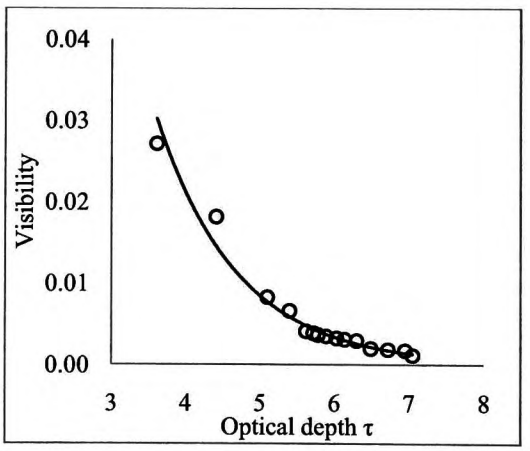

(3) blue, power level 1

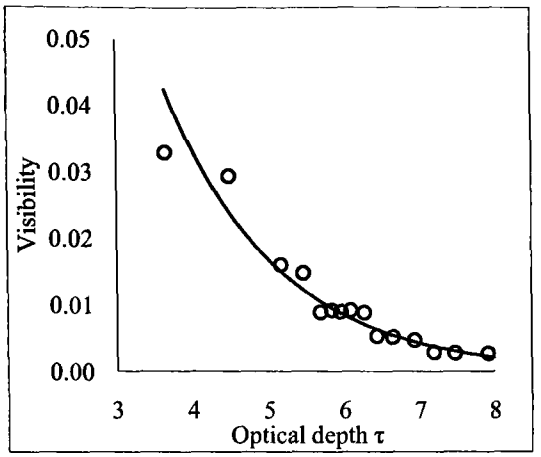

(4) red, power level 2

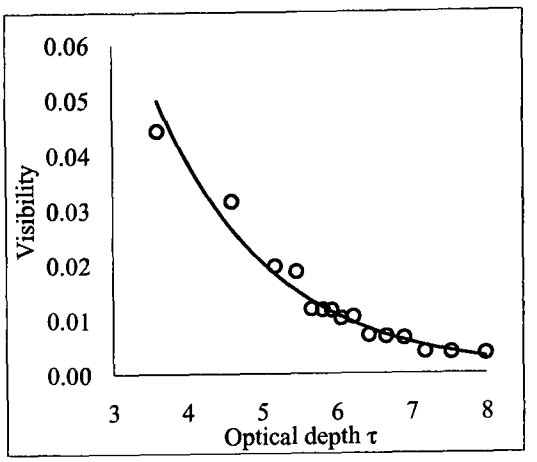

(5) green, power level 2

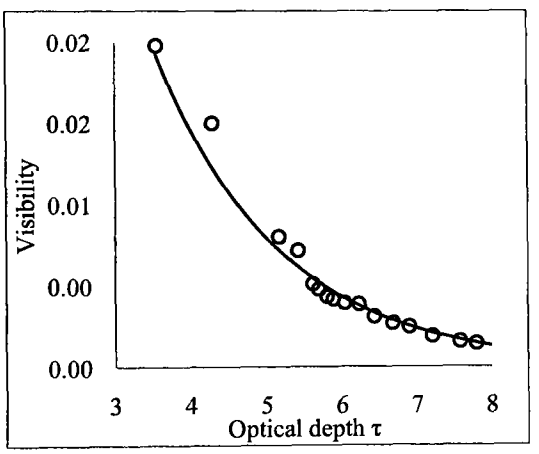

(6) blue, power level 2

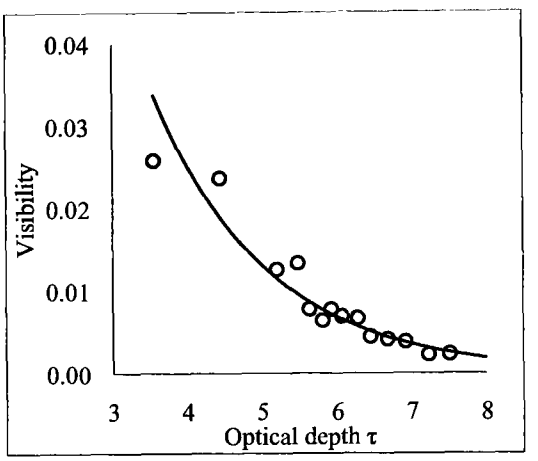

(7) red, power level 3

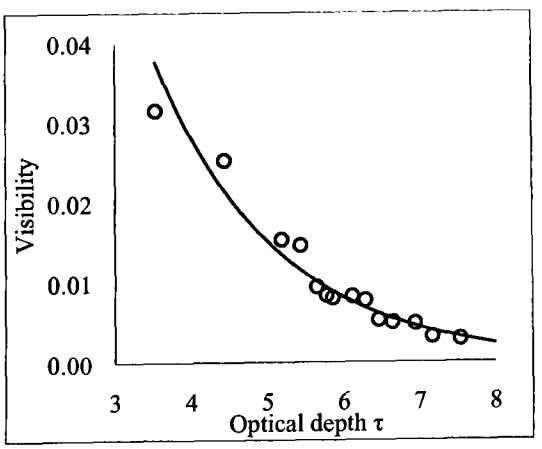

(8) green, power level 3

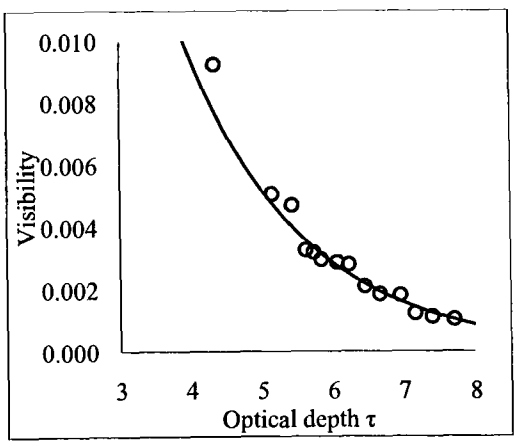

(9) blue, power level 3

Appendix B *Visibility of different barcodes*

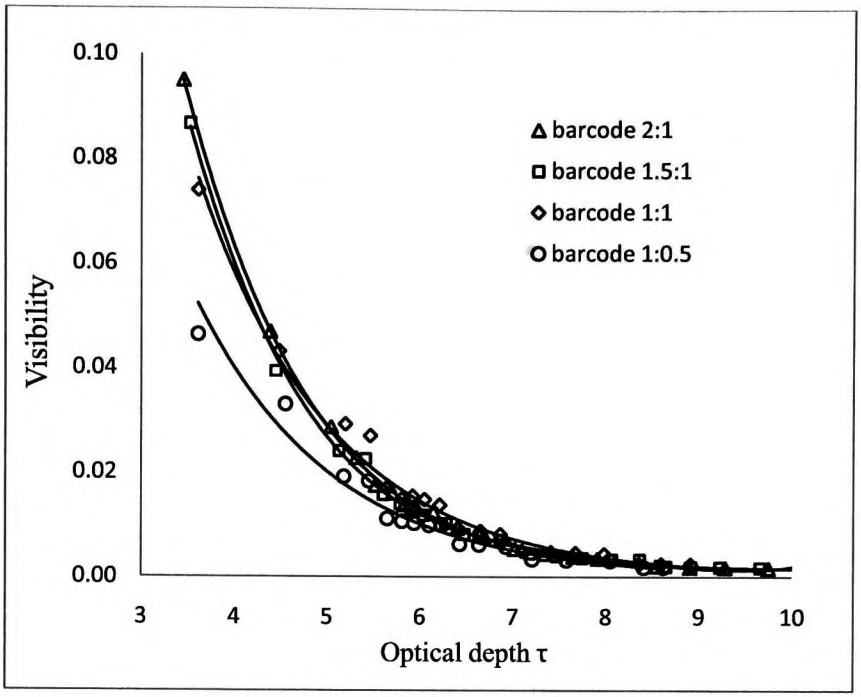

(a) red

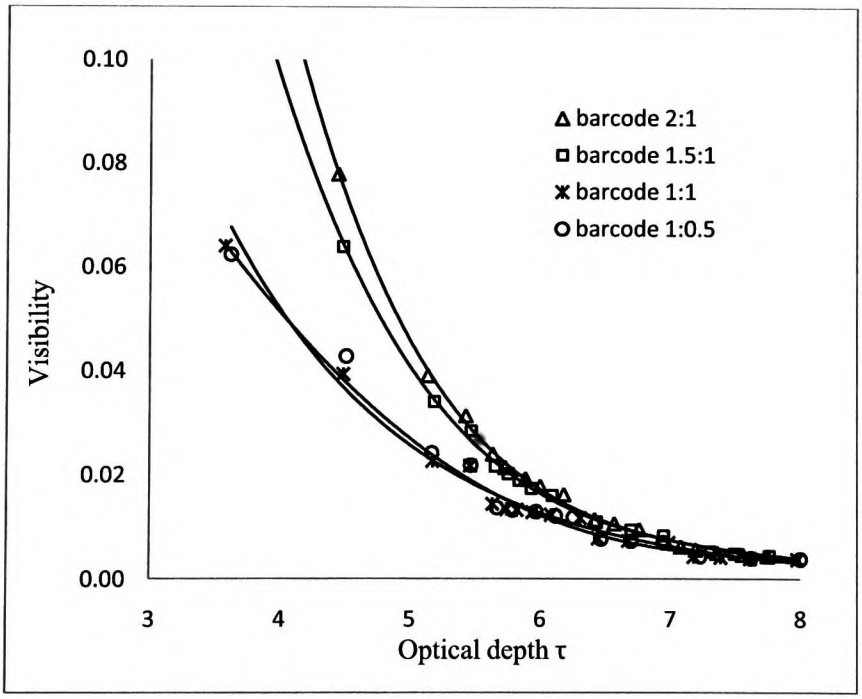

(b) green

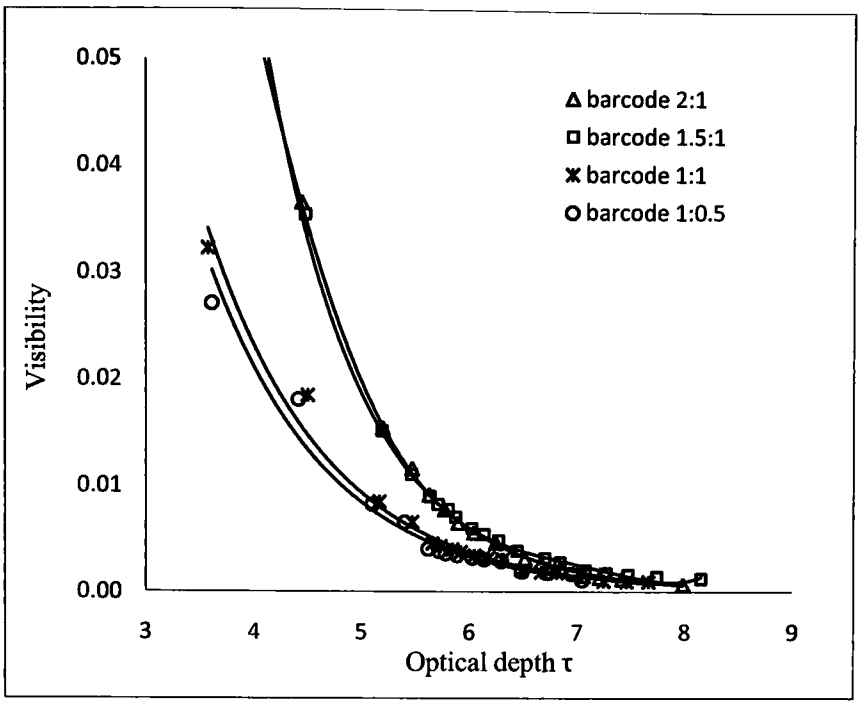

(c) blue

B-1 Visibility of different barcodes at power level 1

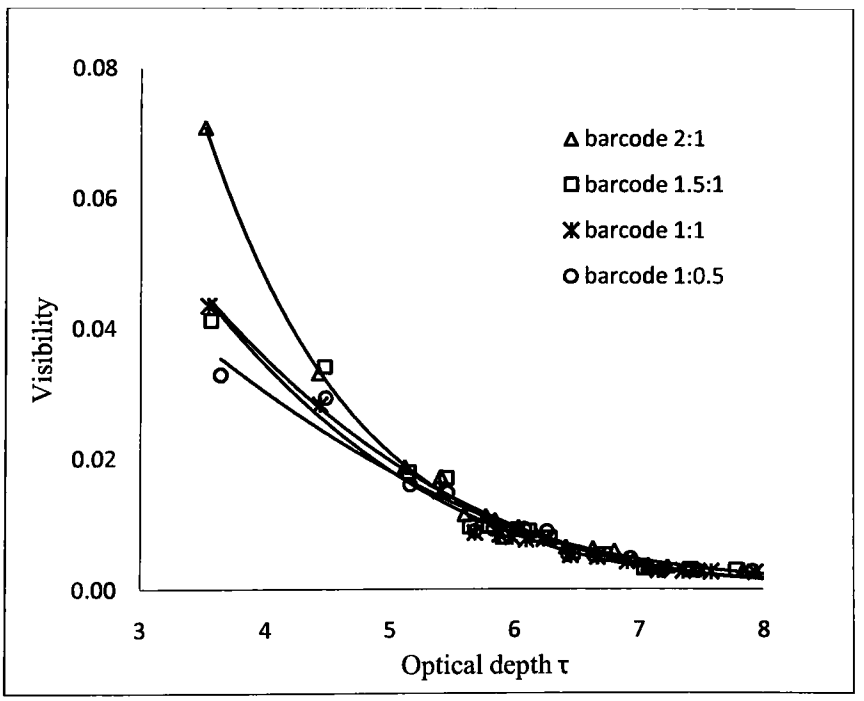

(a) red

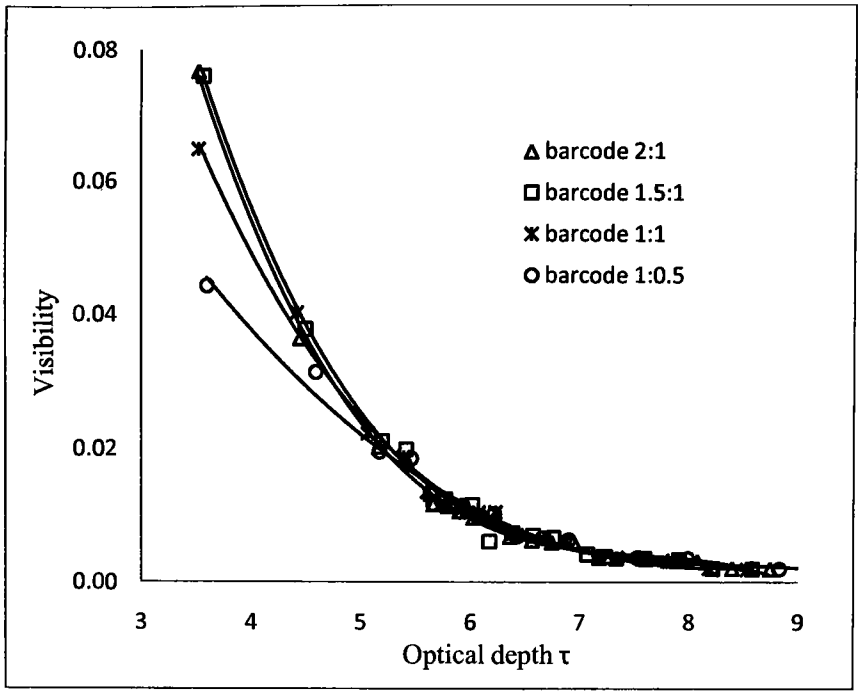

(b) green

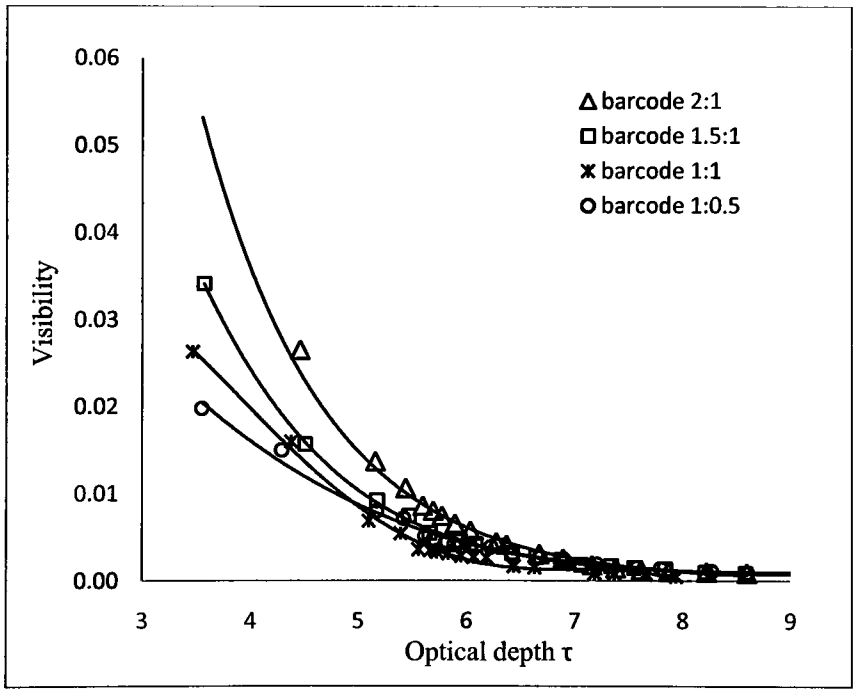

(c) blue

B-2 Visibility of different barcodes at power level 2

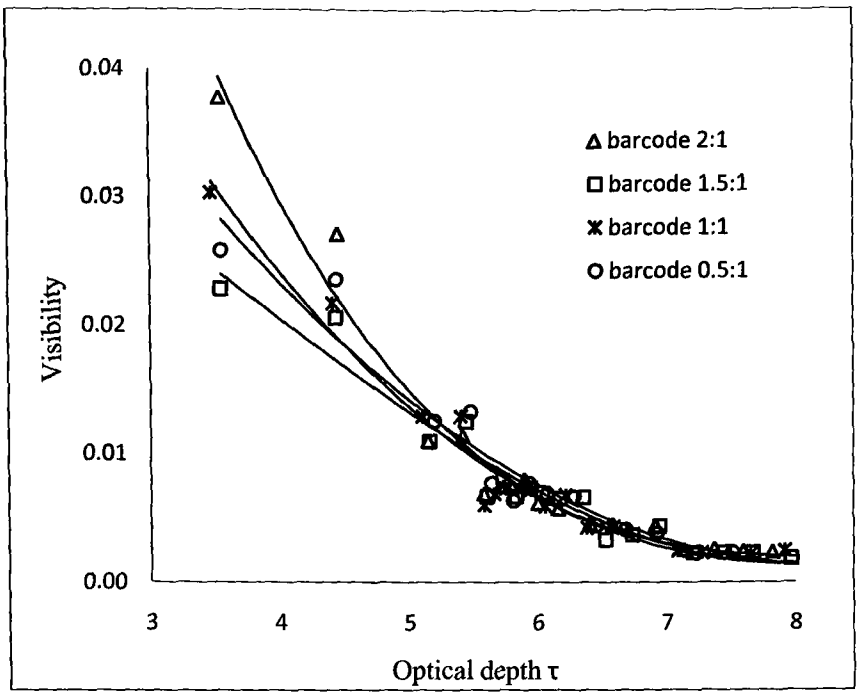
0.04
0.03
0.02
0.01
0.00
Visibility
3
4
5
6
7
8
Optical depth τ
barcode 2:1
barcode 1.5:1
barcode 1:1
barcode 0.5:1

(a) red

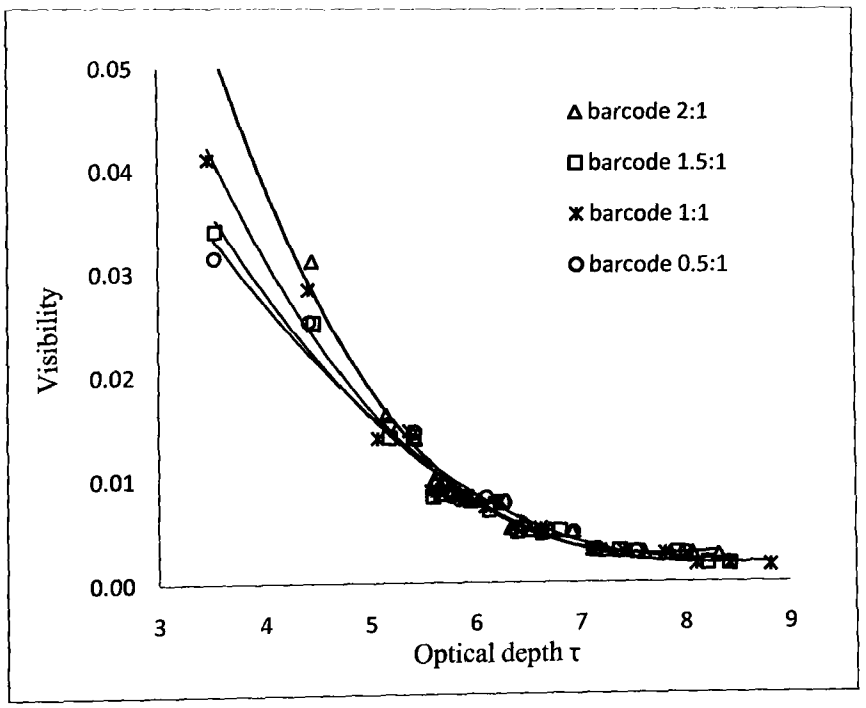
0.05
0.04
0.03
0.02
0.01
0.00
Visibility
3
4
5
6
7
8
9
Optical depth τ
barcode 2:1
barcode 1.5:1
barcode 1:1
barcode 0.5:1

(b) green

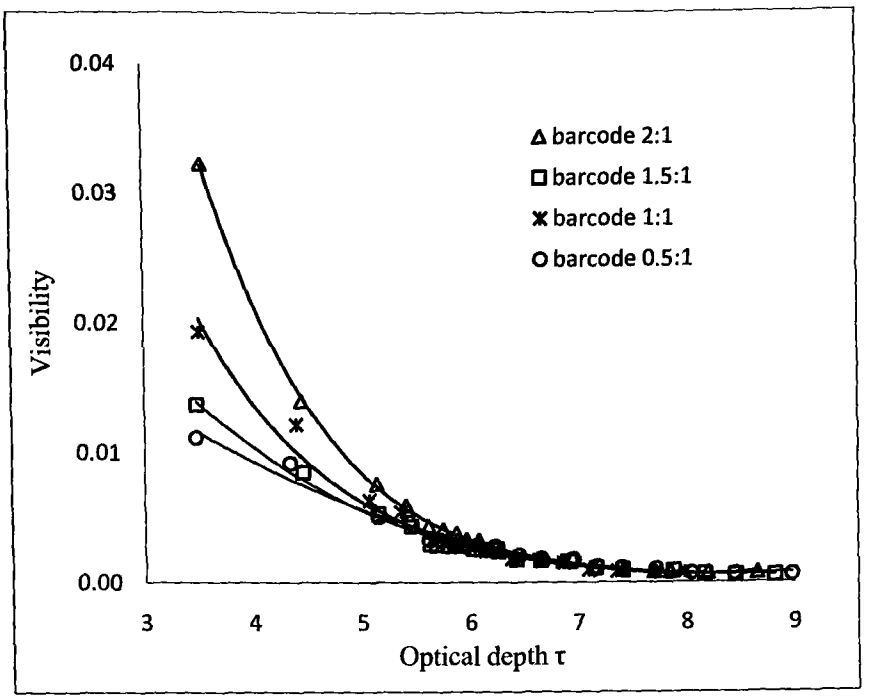

(c) blue

B-3 Visibility of different barcodes at power level 3

Appendix C *Visibility of barcodes with different light power*

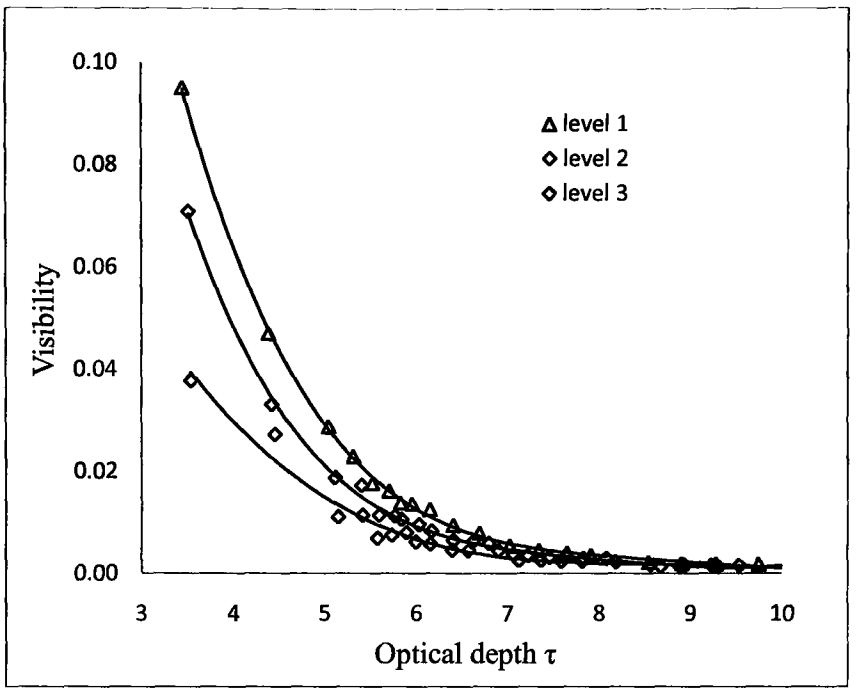

(a) Red

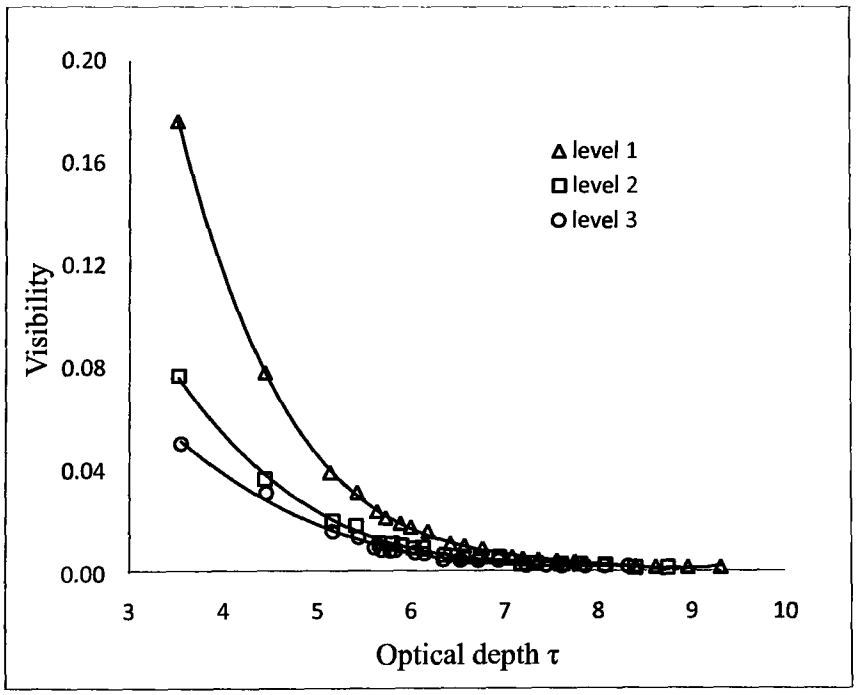

(b) Green

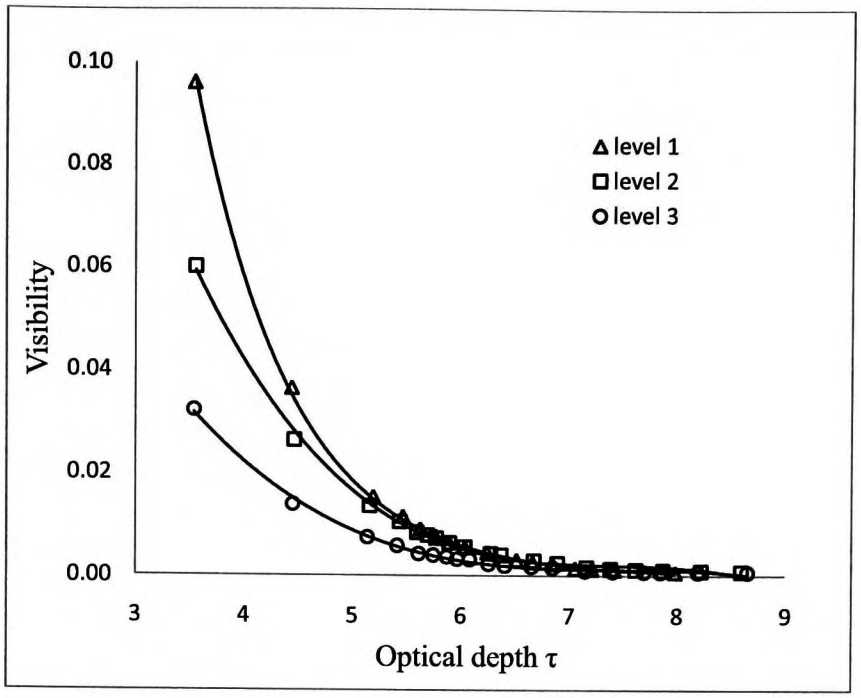

(c) Blue

C-1 Visibility of barcode (2:1) with different light power

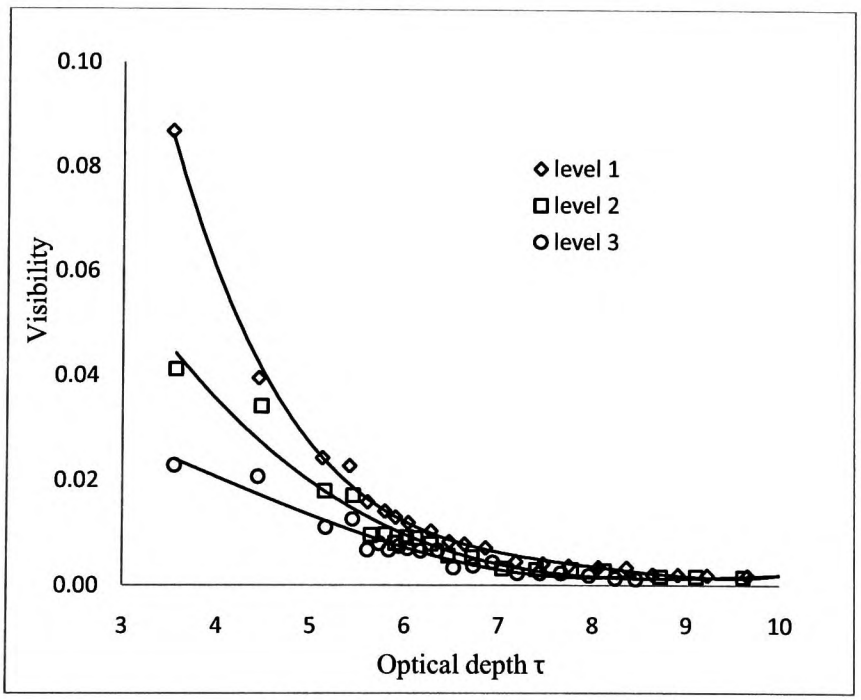

(a) Red

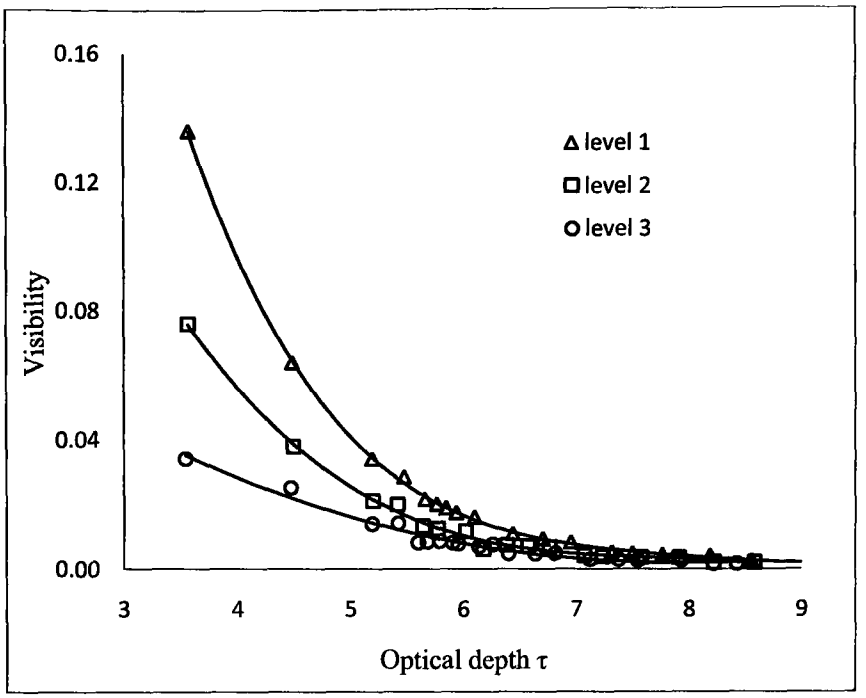

(b) Green

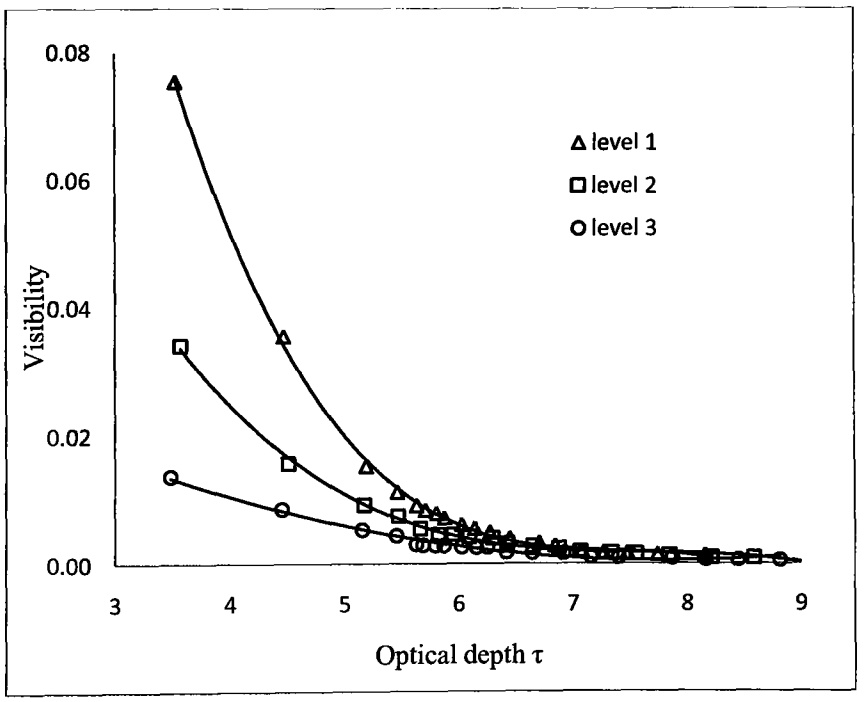

(c) Blue

C-2 Visibility of barcode (1.5:1) with different light power

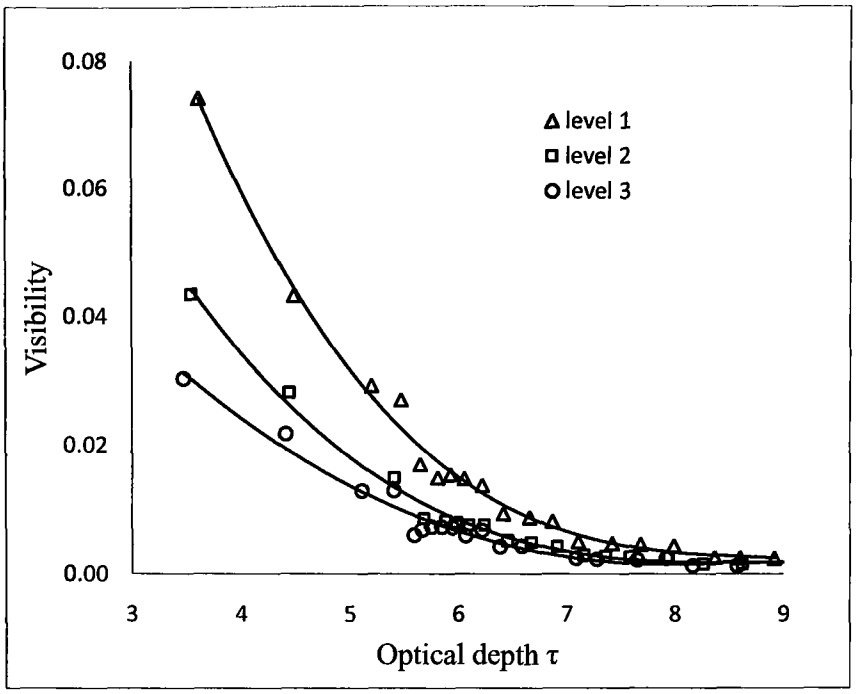
0.08
0.06
0.04
0.02
0.00
Visibility
level 1
level 2
level 3
3
4
5
6
7
8
9
Optical depth τ

(a) red

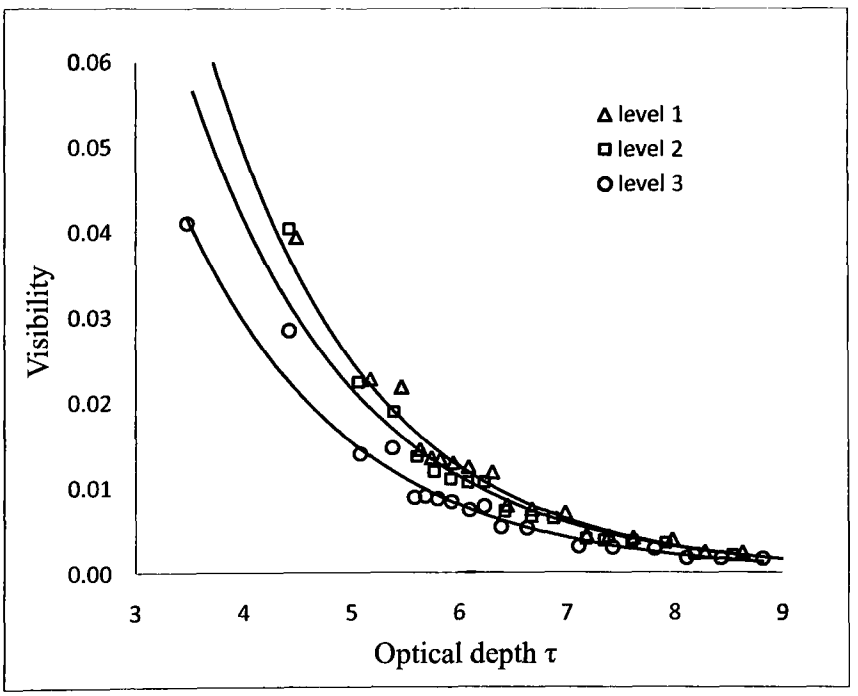
0.06
0.05
0.04
0.03
0.02
0.01
0.00
Visibility
level 1
level 2
level 3
3
4
5
6
7
8
9
Optical depth τ

(b) green

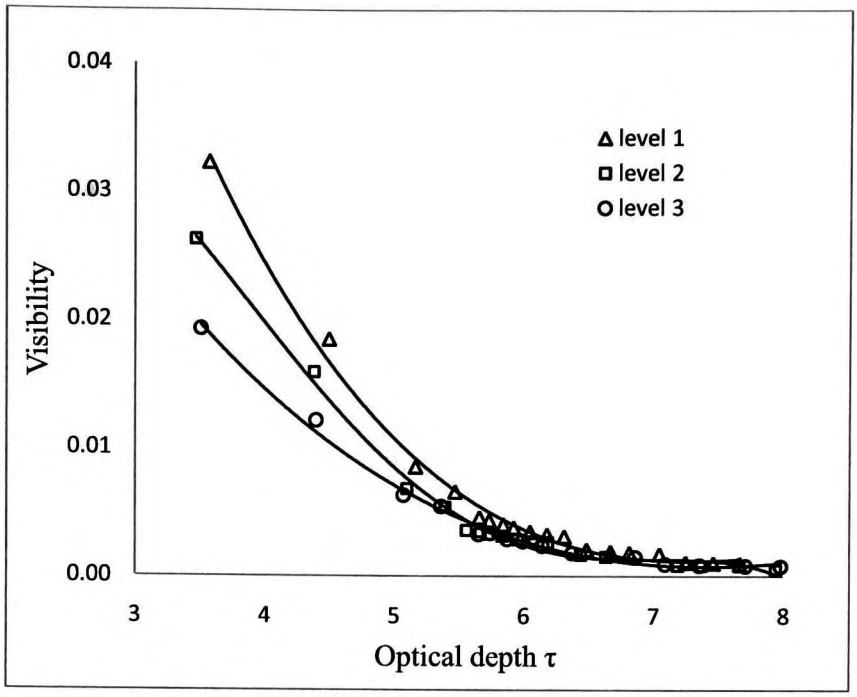

(c) blue

C-3 Visibility of barcode (1:1) with different light power

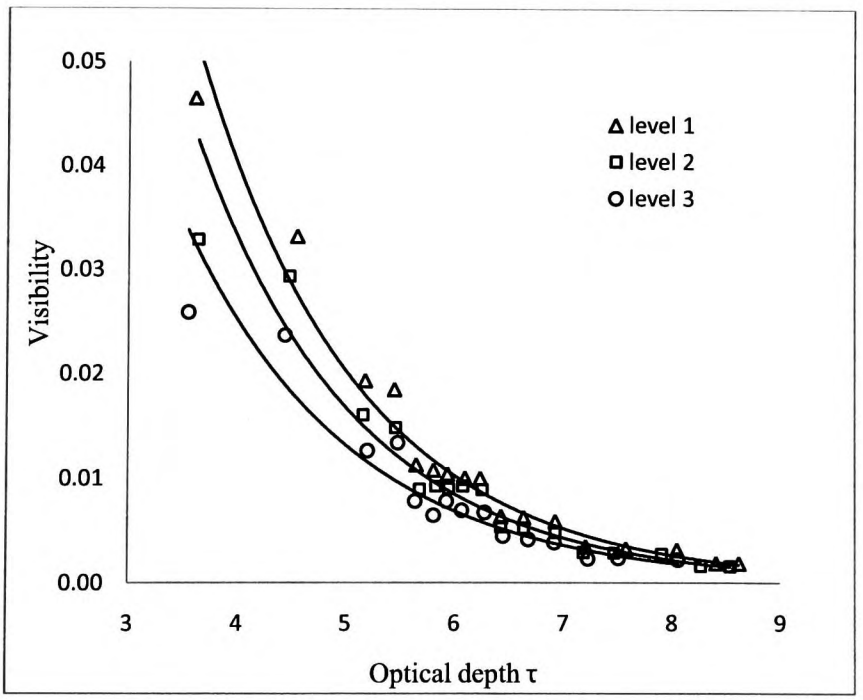

(a) red

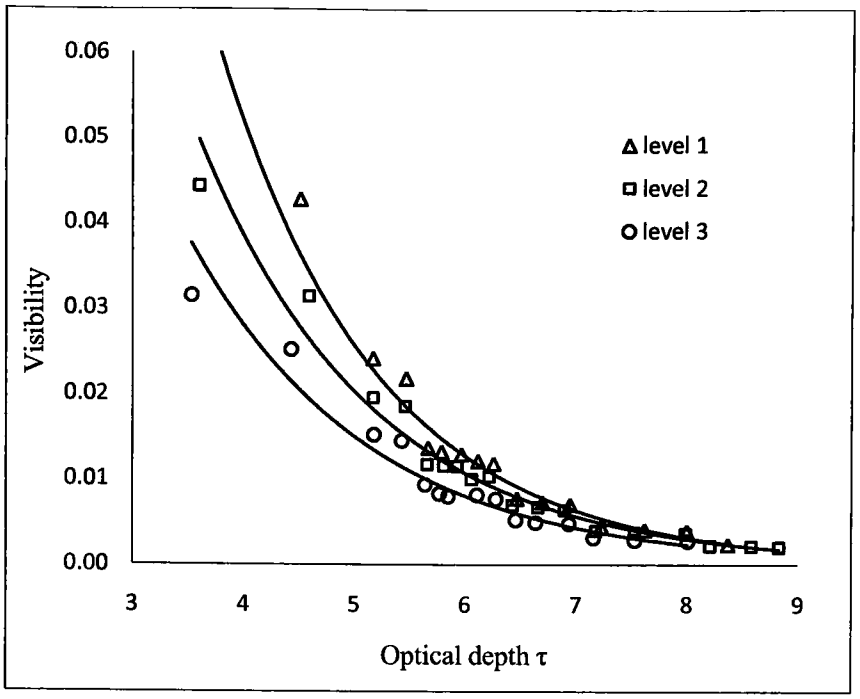

(b) green

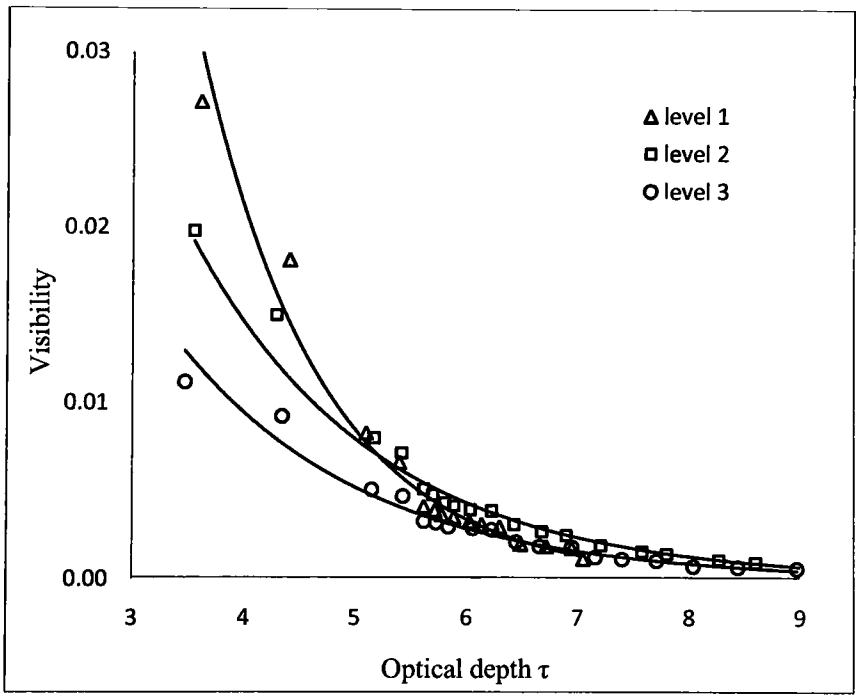

(c) blue

C-4 Visibility of barcode (1:0.5) with different light power

Appendix D *Normalised visibility of barcodes with different colour light source*

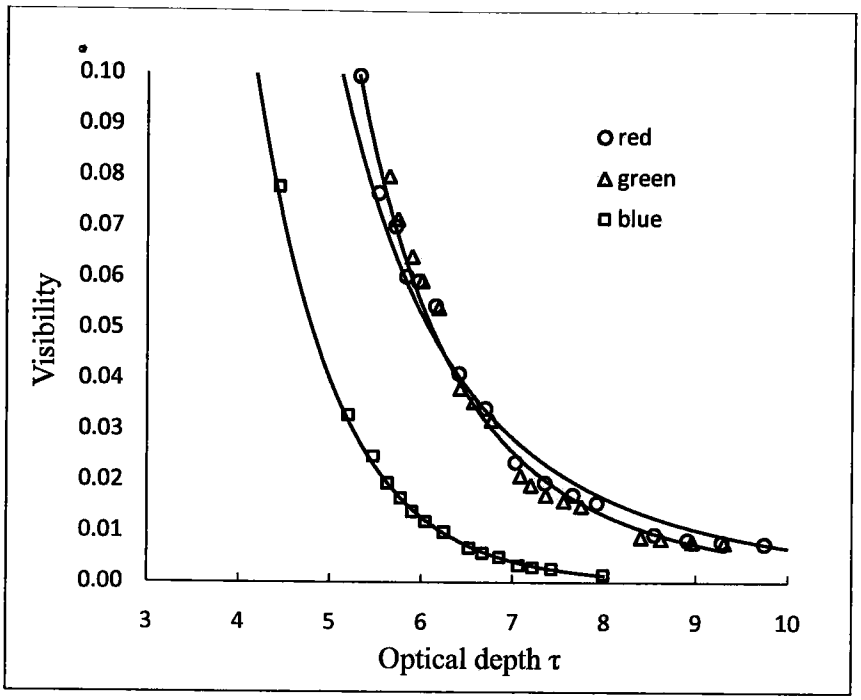

(a) Power level 1

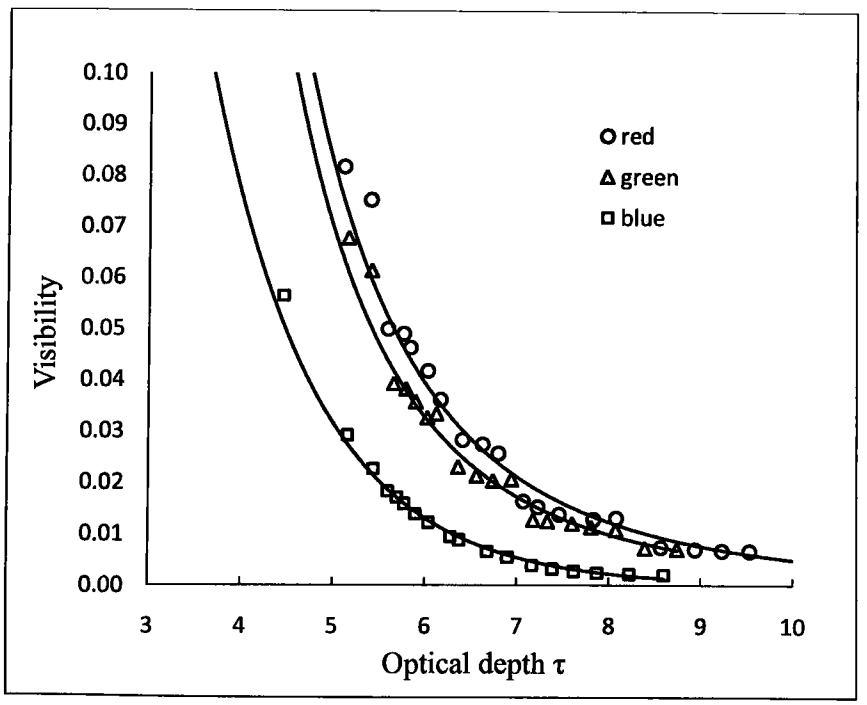

(b) Power level 2

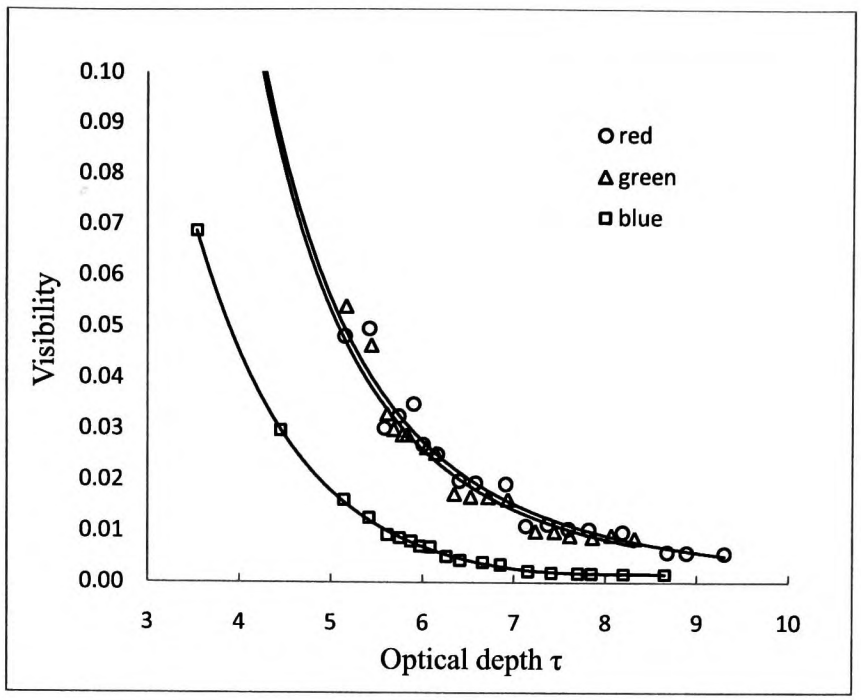

(c) Power level 3

D-1 Visibility of barcode (2:1) with different colour light sources

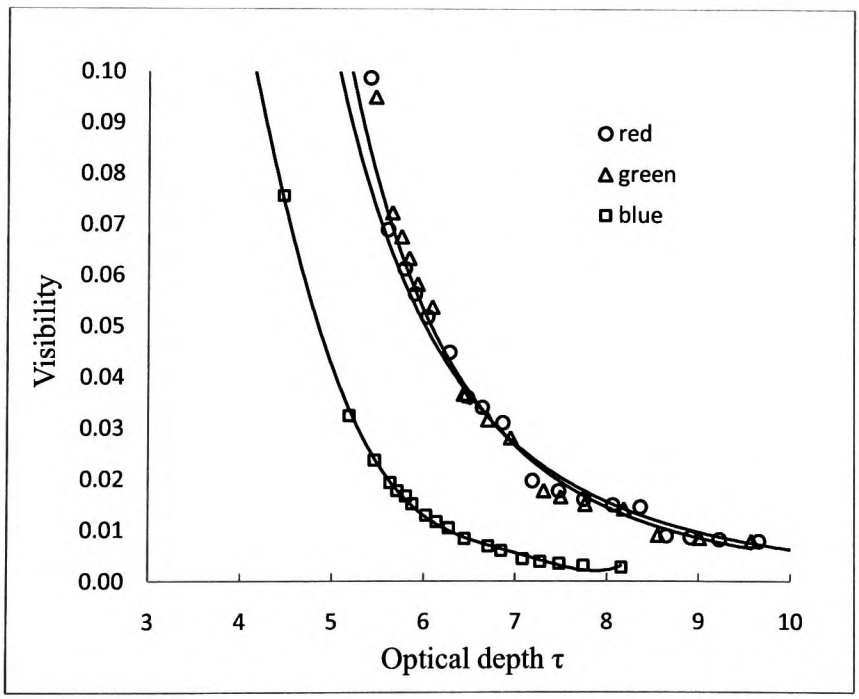

(a) Power level 1

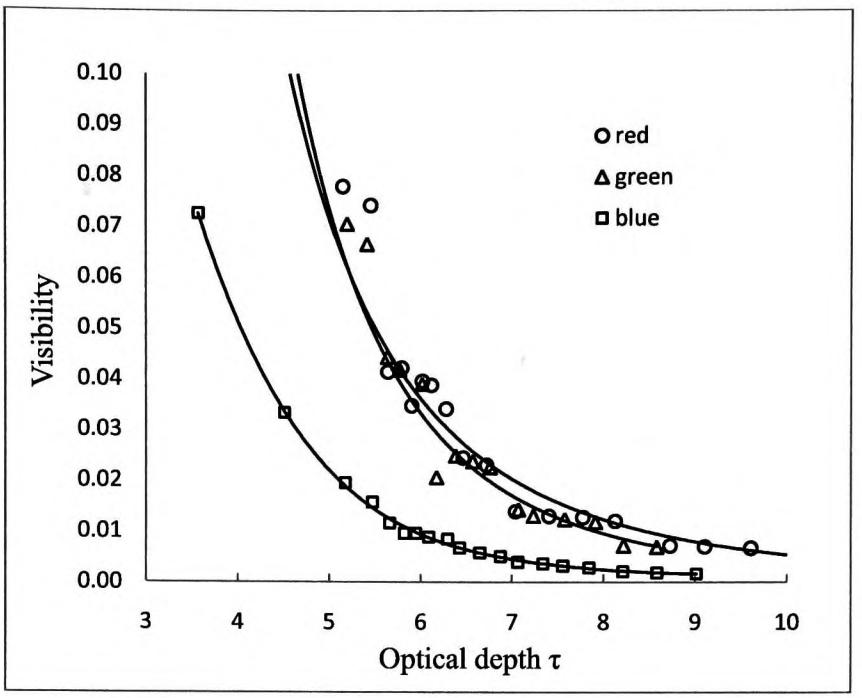

(b) Power level 2

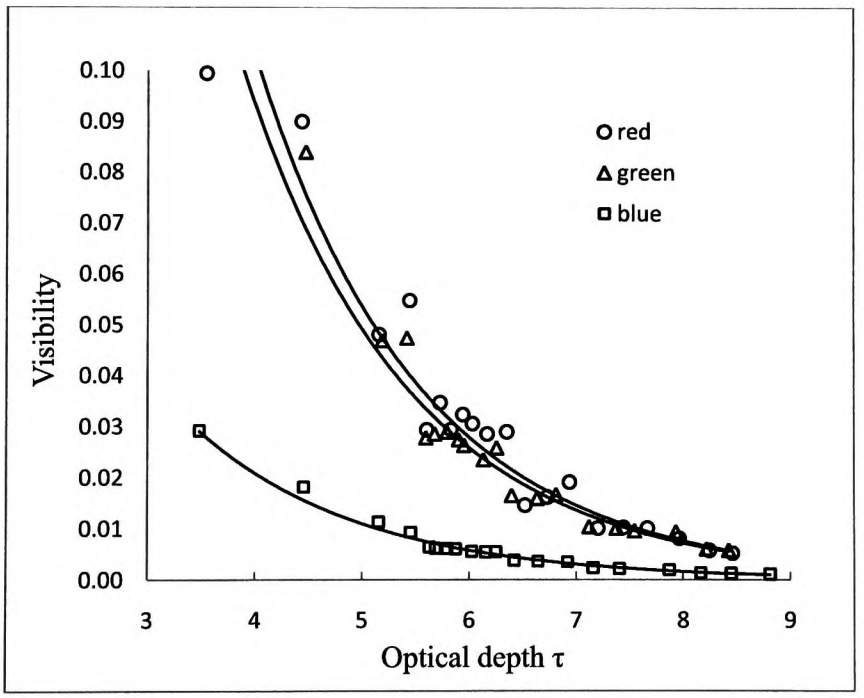

(c) Power level 3

D-2 Visibility of barcode (1.5:1) with different colour light sources

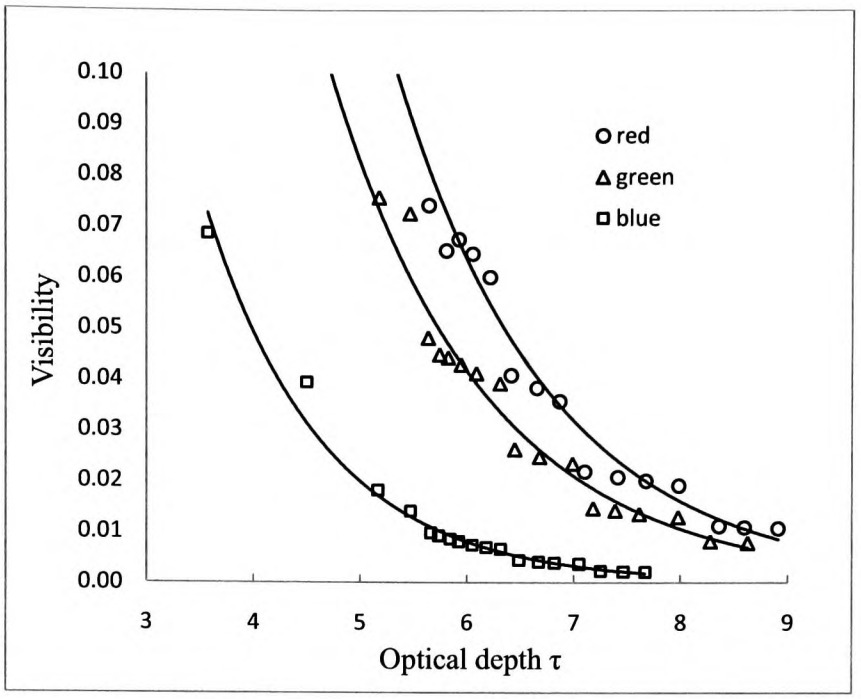

(a) Power level 1

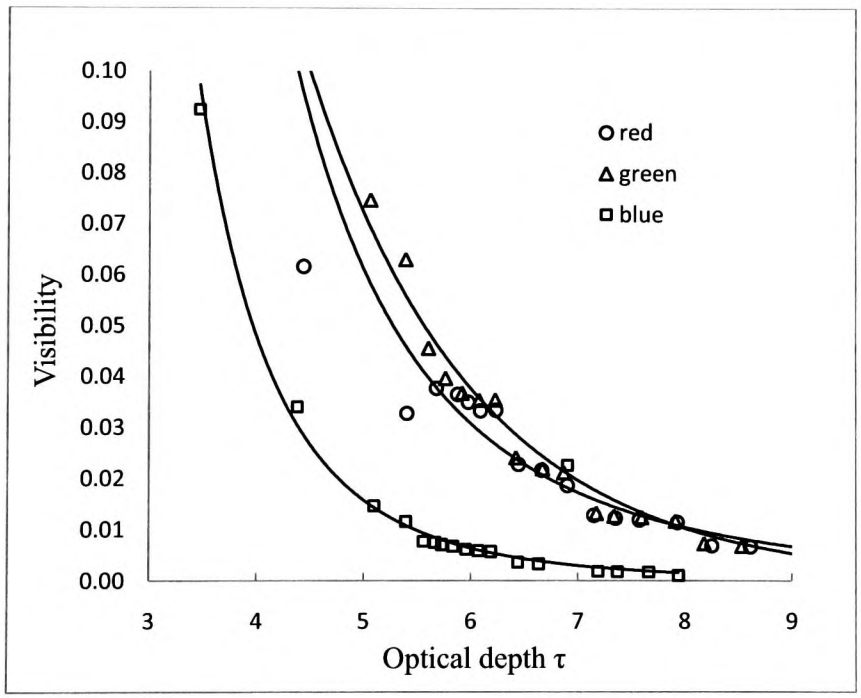

(b) Power level 2

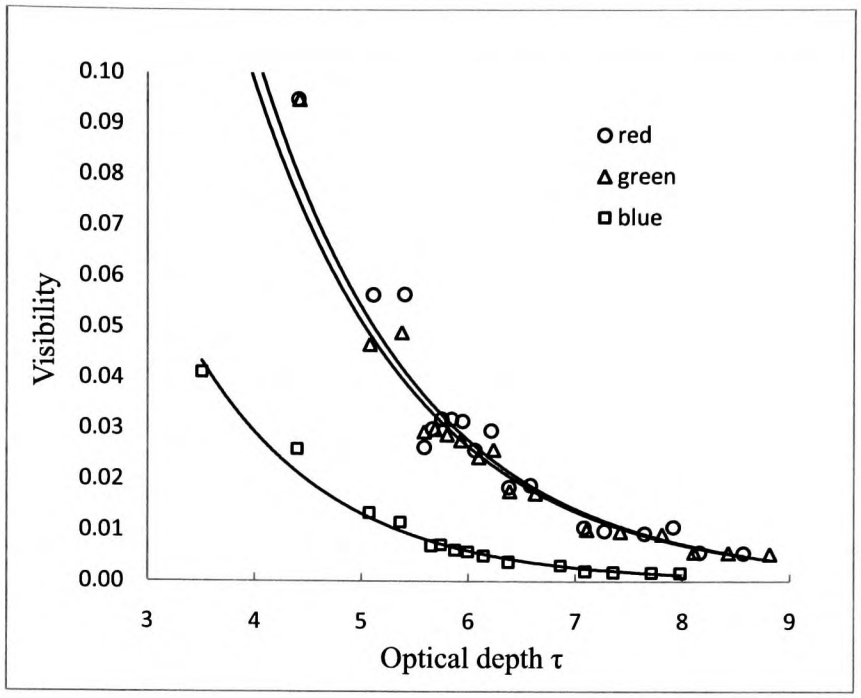

(c) Power level 3

D-3 Visibility of barcode (1:1) with different colour light sources

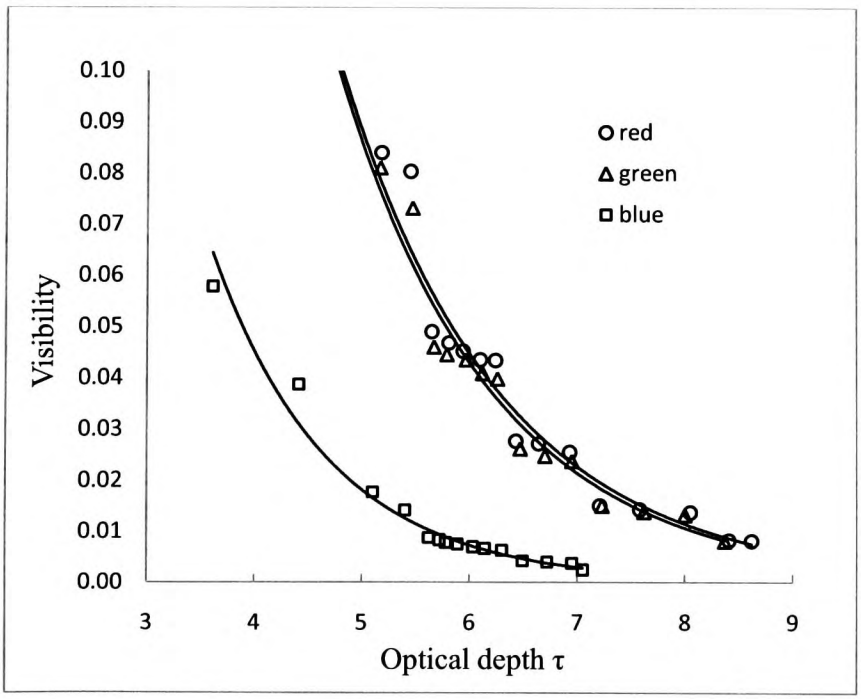

(a) Power level 1

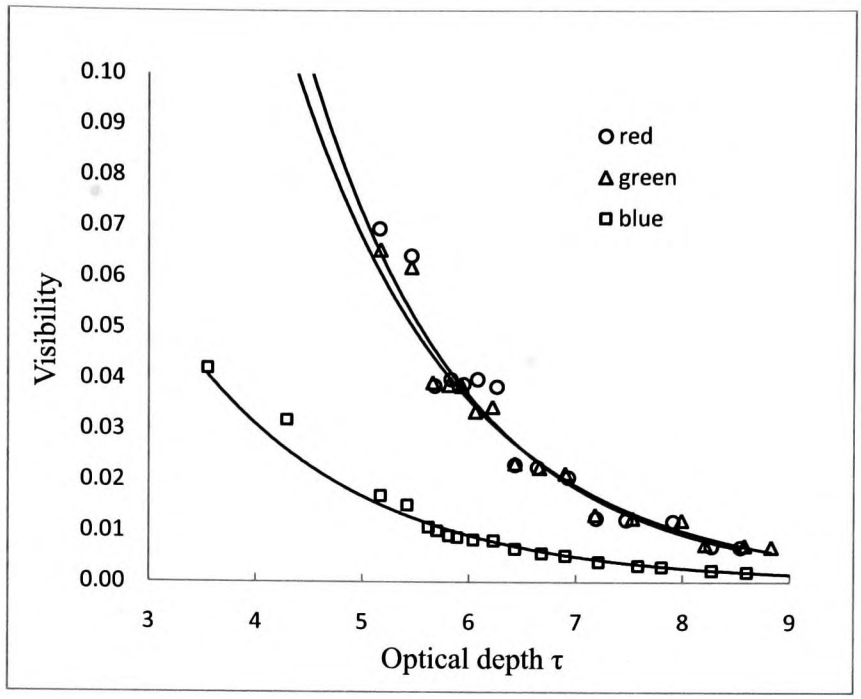

(b) Power level 2

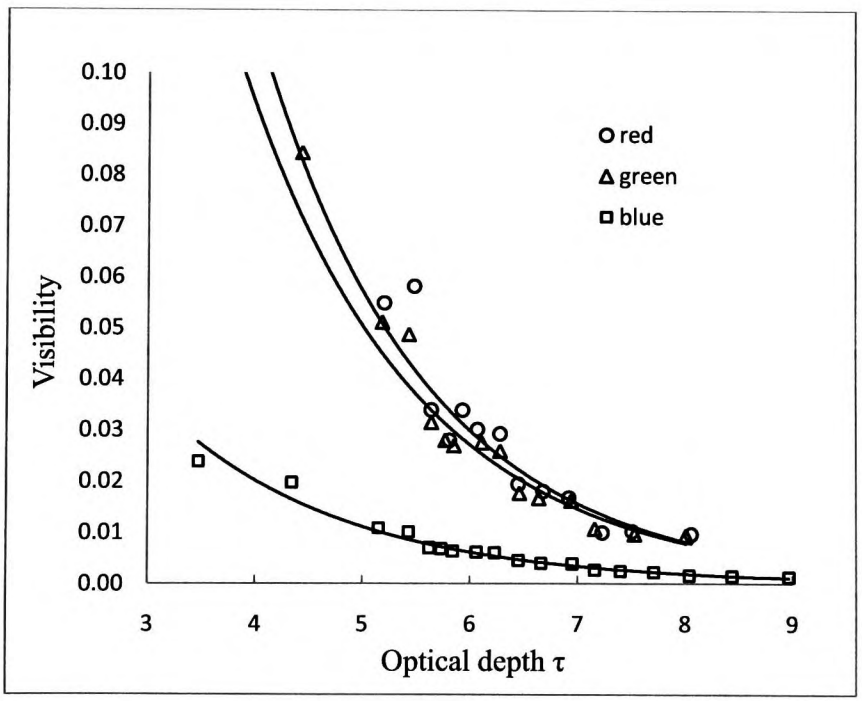

(c) Power level 3

D-4 Visibility of barcode (1:0.5) with different colour light sources

Appendix E *Effect of ambient light on the visibility of barcodes*

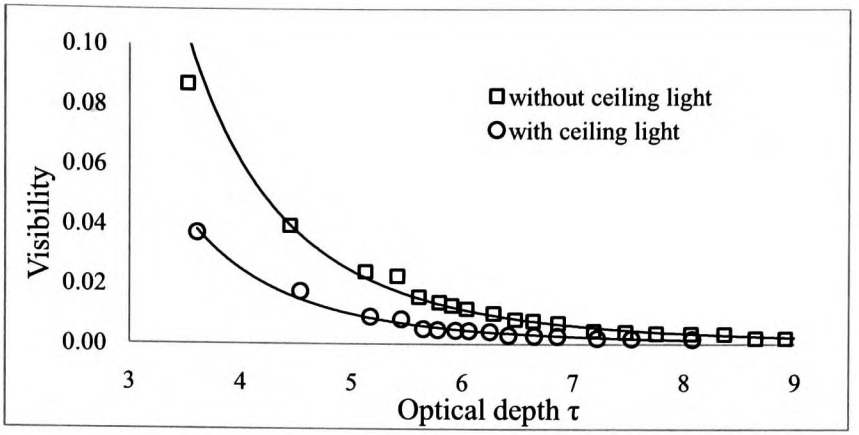

(red)

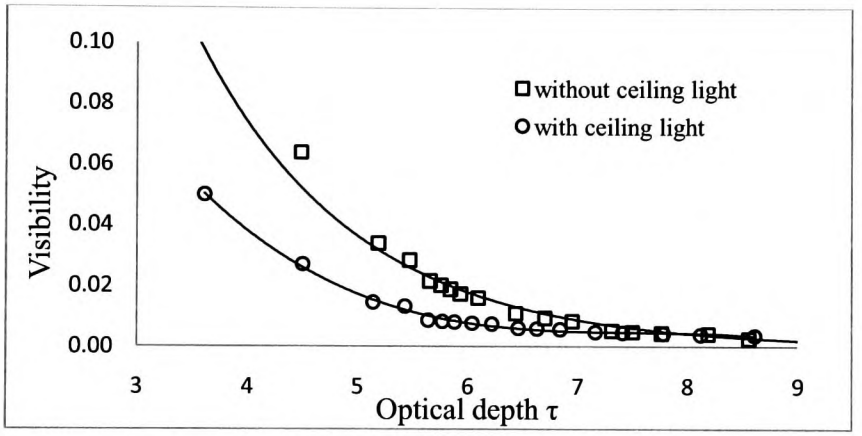

(green)

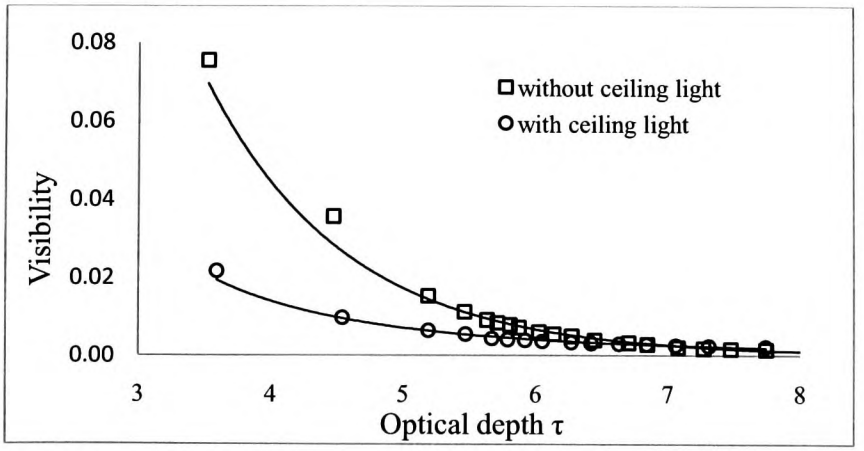

(blue)

E-1 Visibility of barcode (1.5:1) at power level 1

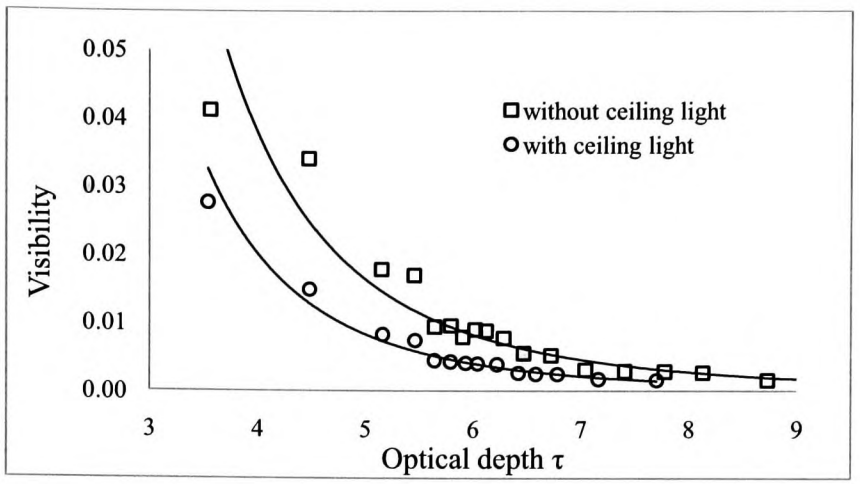

(red)

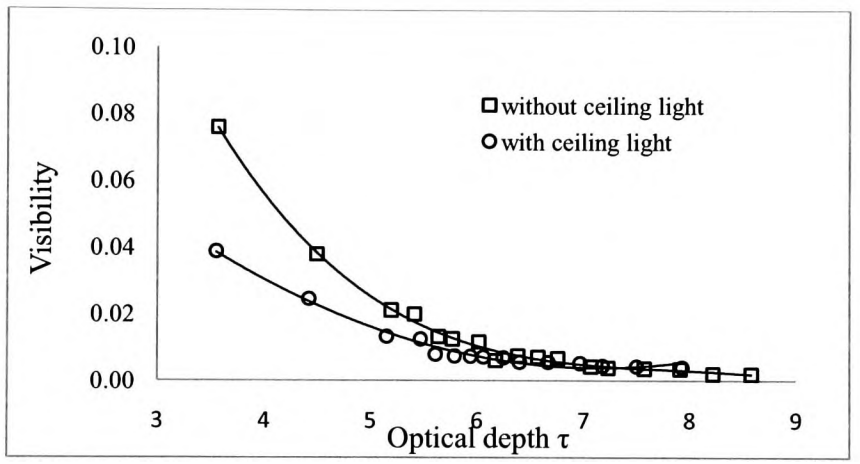

(green)

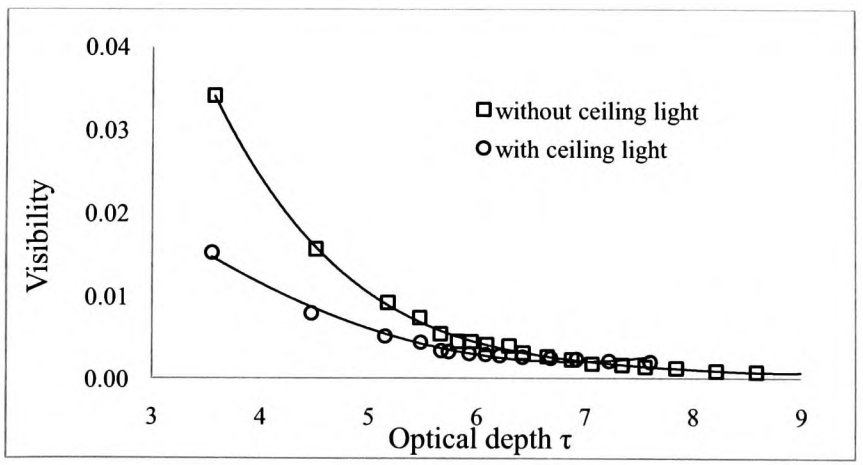

(blue)

E-2 Visibility of barcode (1.5:1) at power level 2

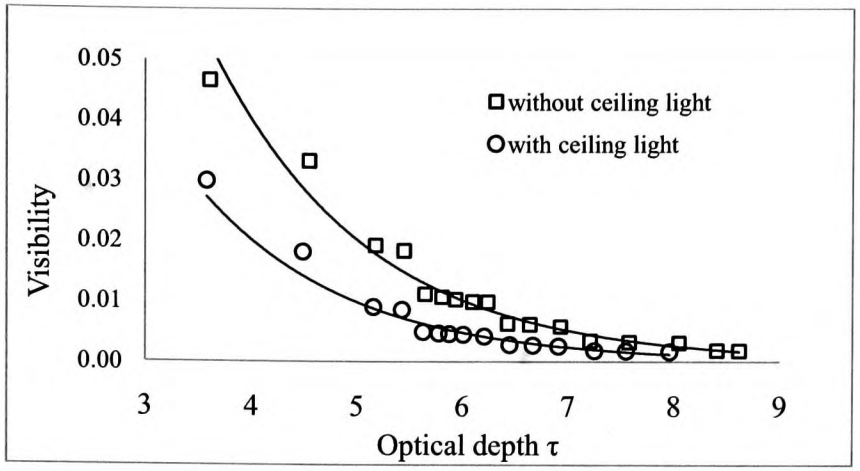

(red)

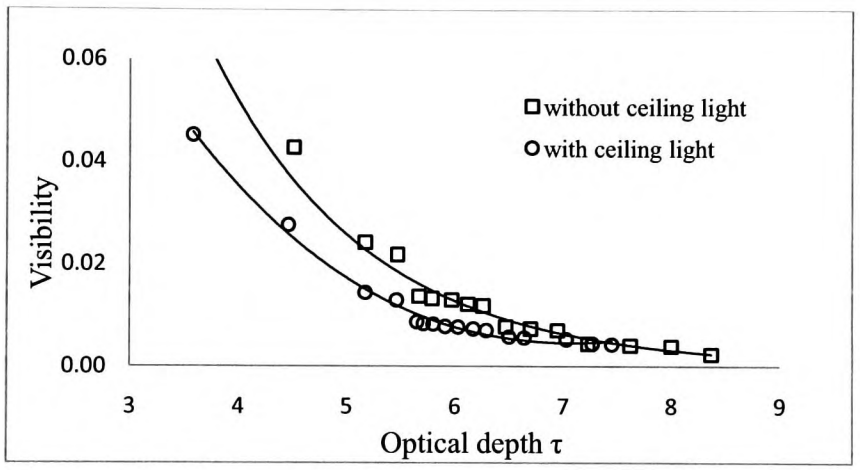

(green)

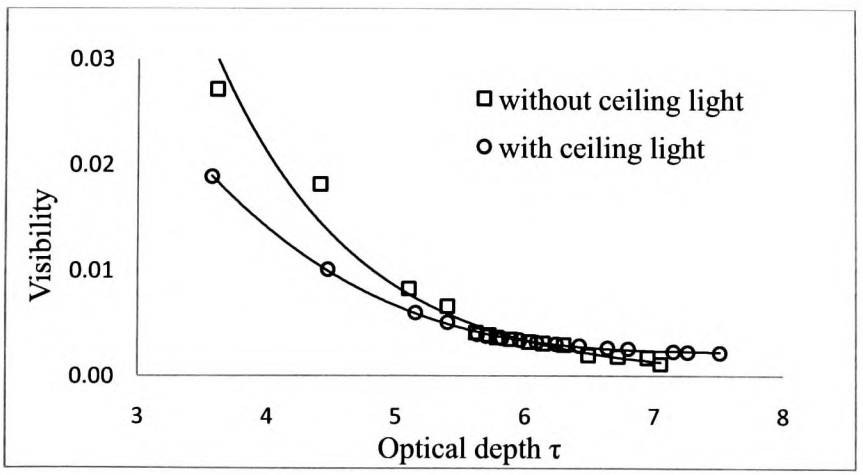

(blue)

E-3 Visibility of barcode (0.5:1) at power level 1

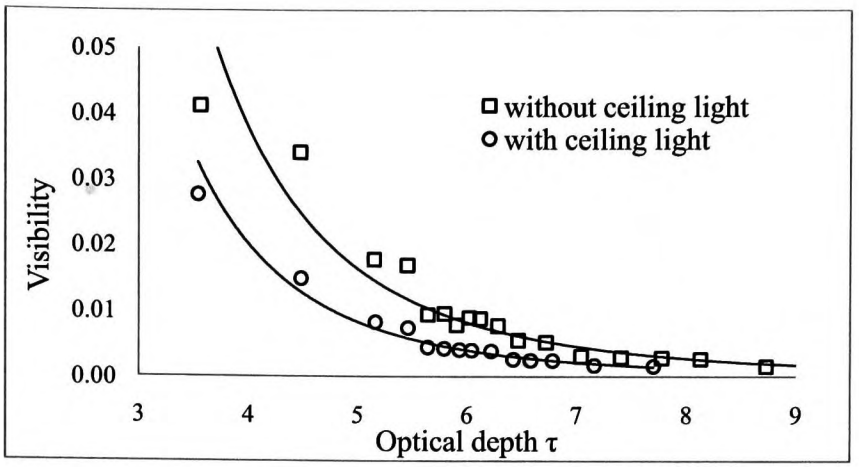

(red)

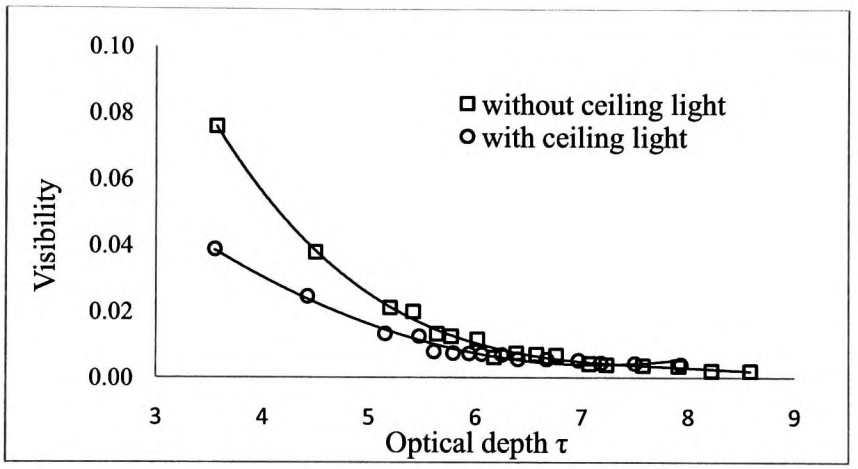

(green)

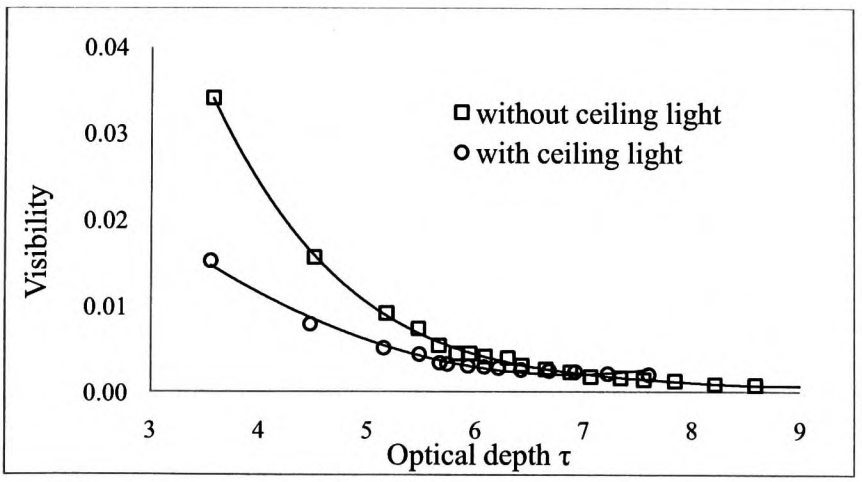

(blue)

E-4 Visibility of barcode (0.5:1) at power level 2

Appendix F *Prediction of barcode visibility*

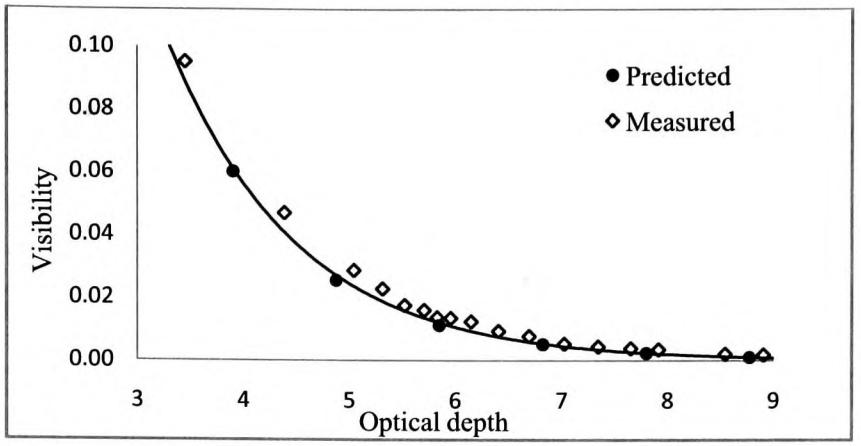

(red)

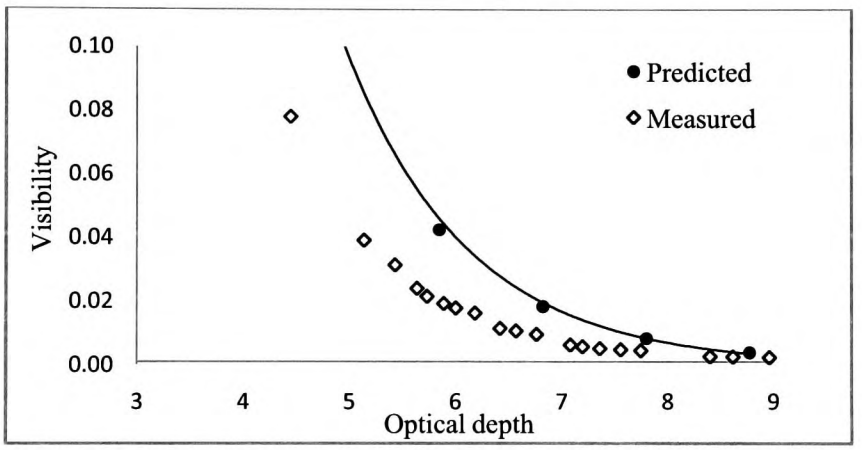

(green)

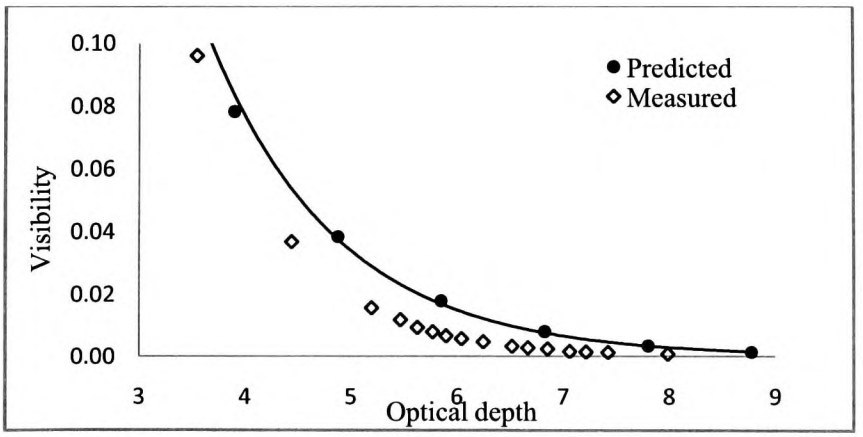

(blue)

F-1 Visibility of barcode (2:1) at power level 1

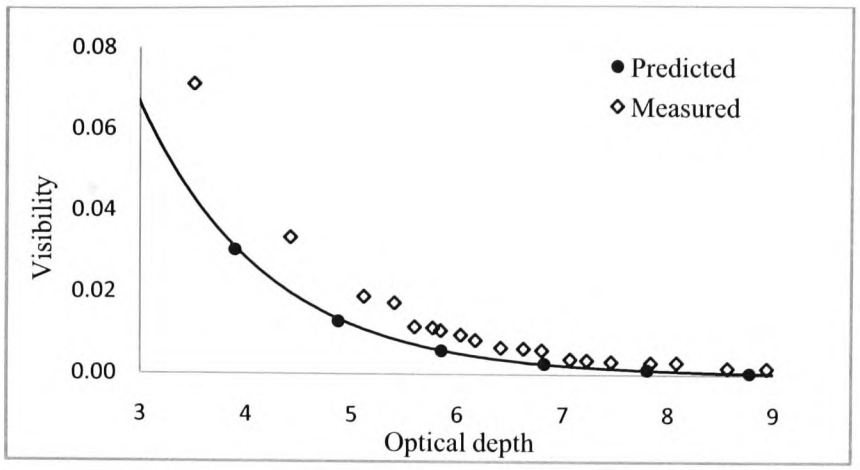

(red)

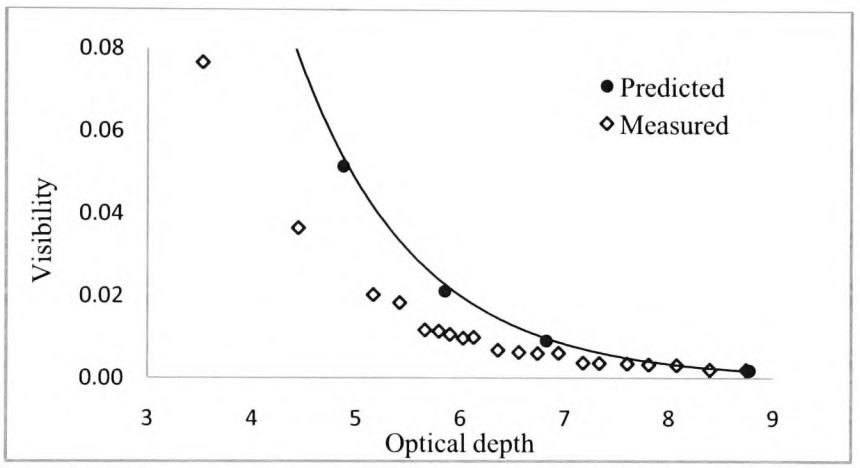

(green)

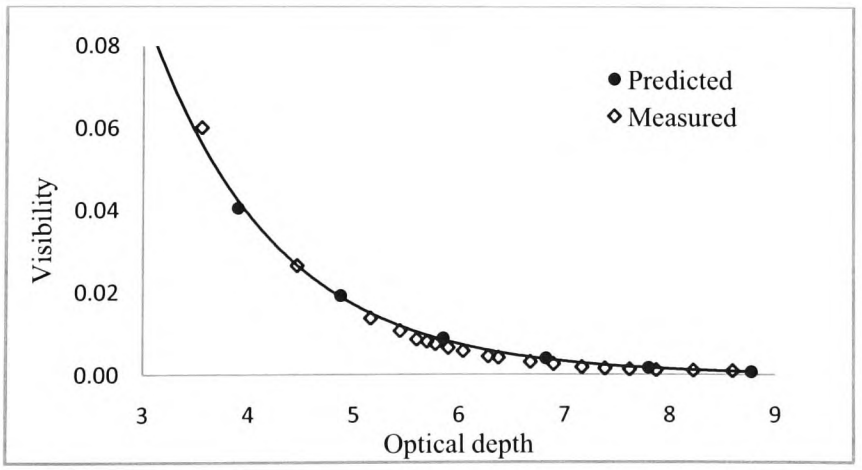

(blue)

F-2 Visibility of barcode (2:1) at power level 2

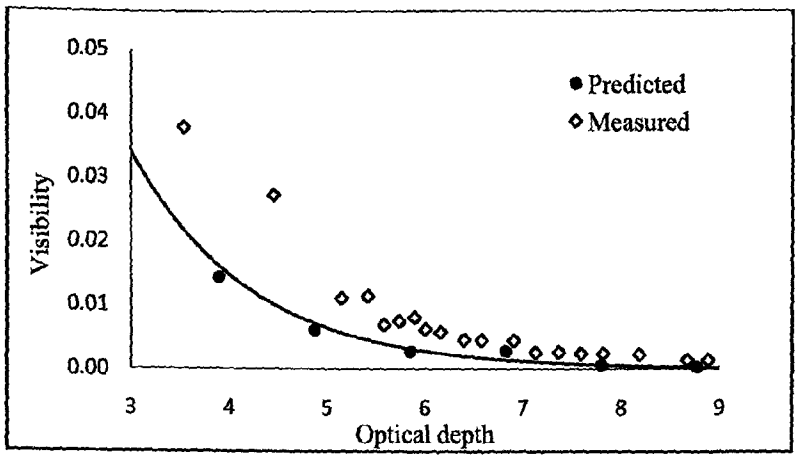

(red)

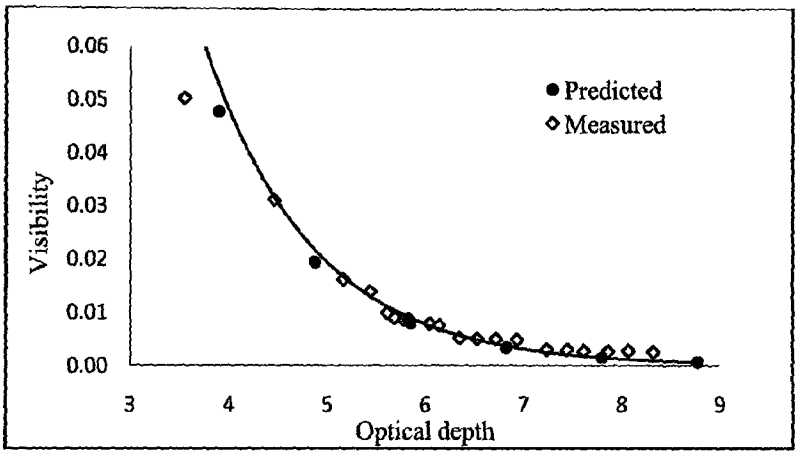

(green)

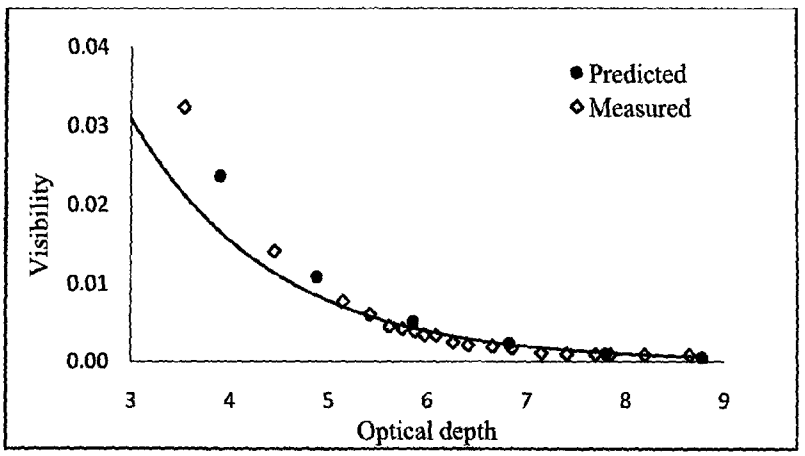

(blue)

F-3 Visibility of barcode (2:1) at power level 3

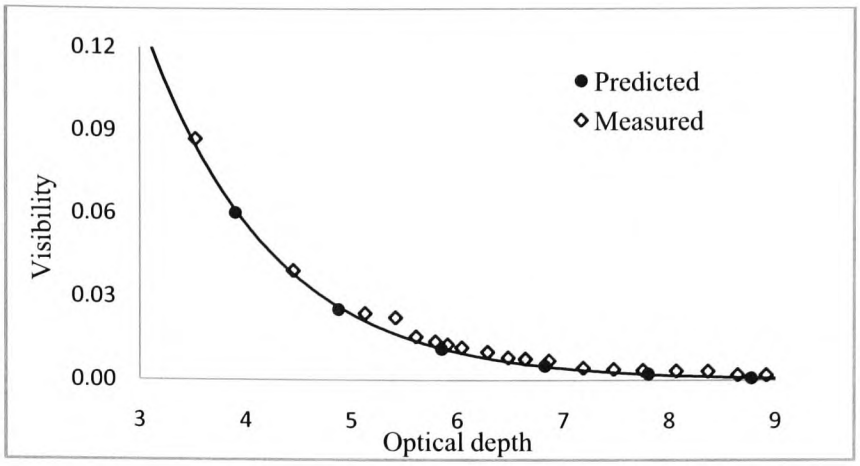

(red)

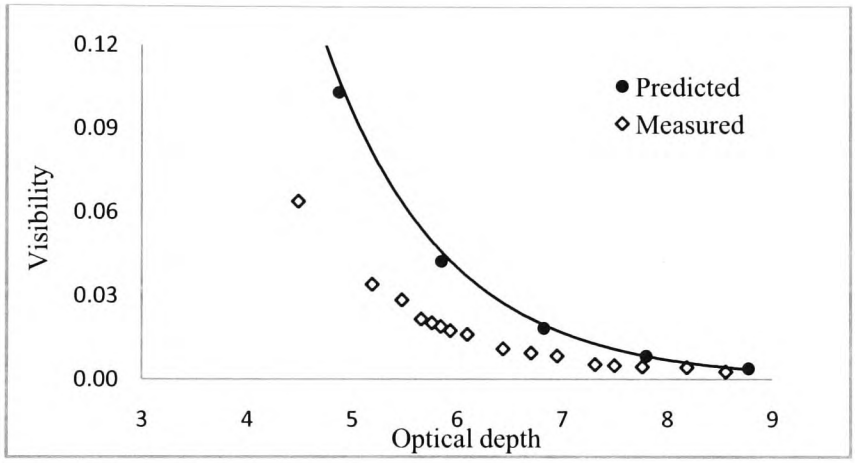

(green)

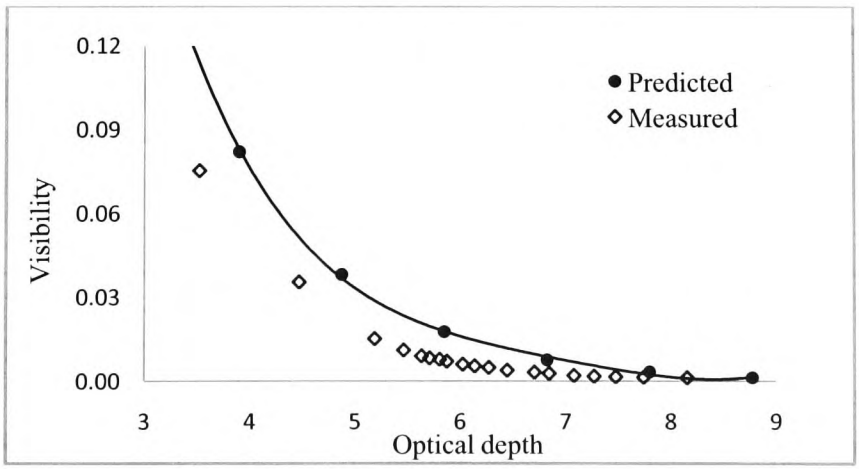

(blue)

F-4 Visibility of barcode (1.5:1) at power level 1

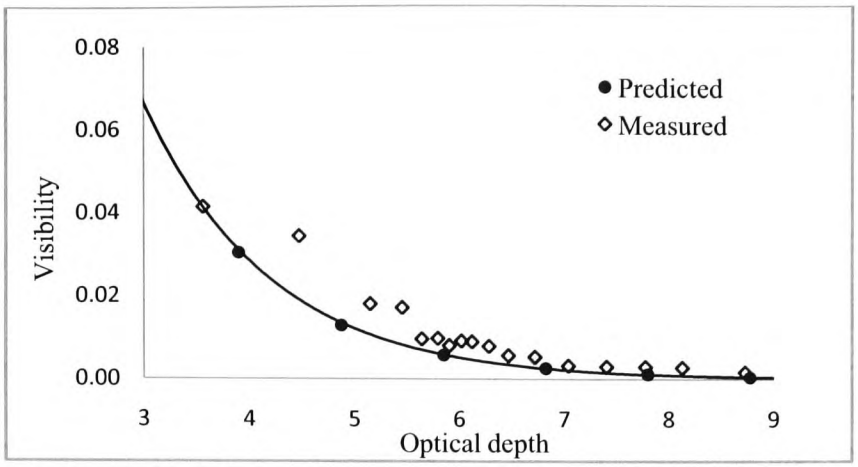

(red)

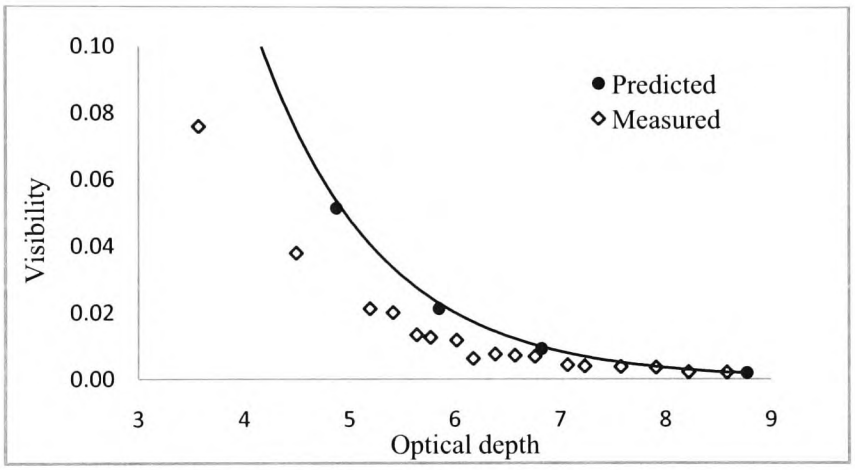

(green)

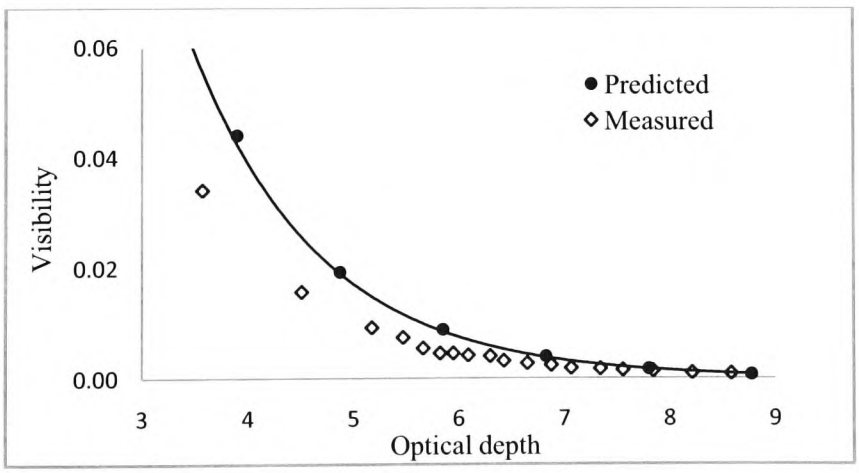

(blue)

F-5 Visibility of barcode (1.5:1) at power level 2

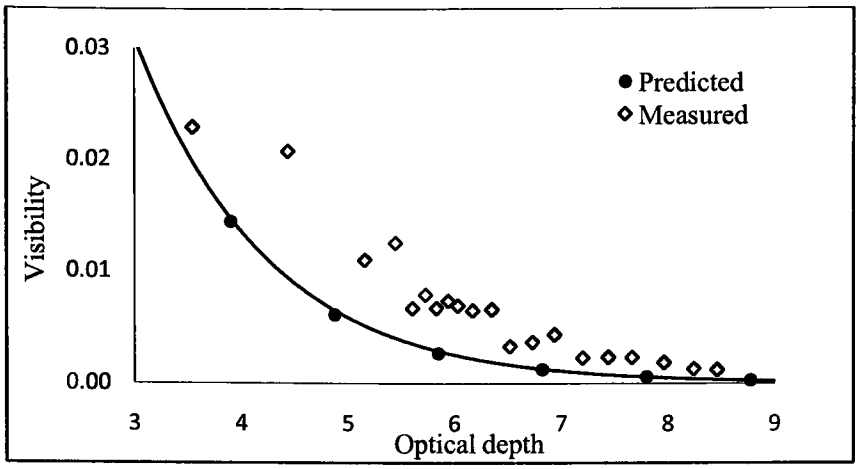

(red)

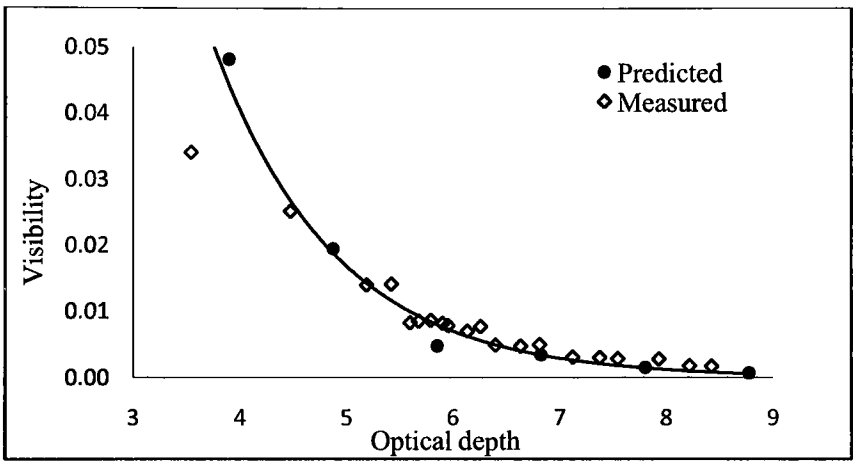

(green)

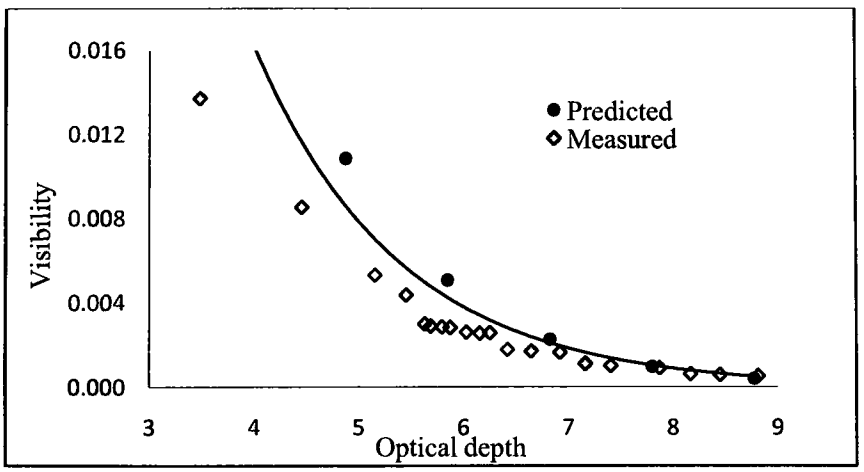

(blue)

F-6 Visibility of barcode (1.5:1) at power level 3

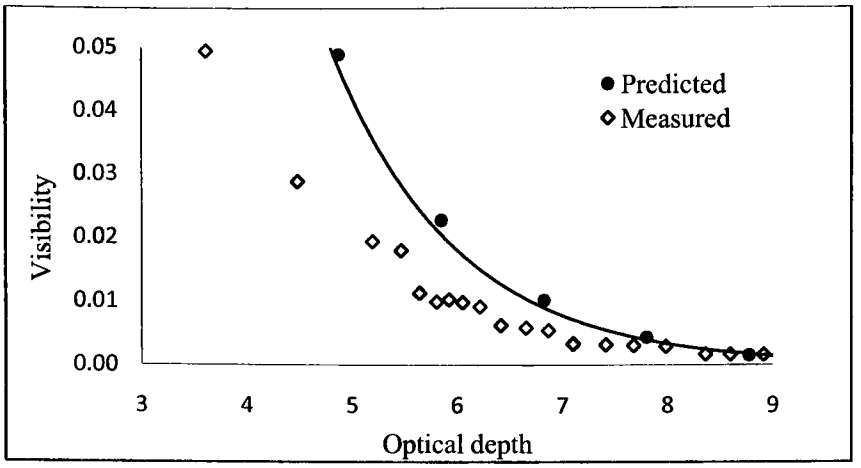

(red)

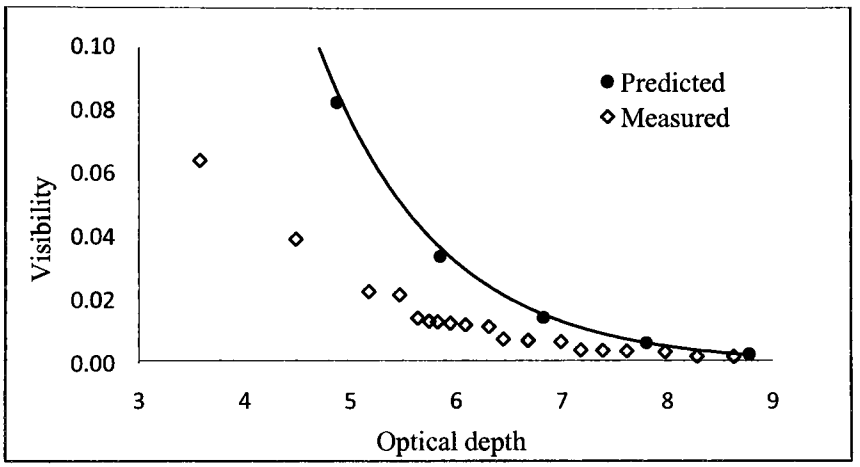

(green)

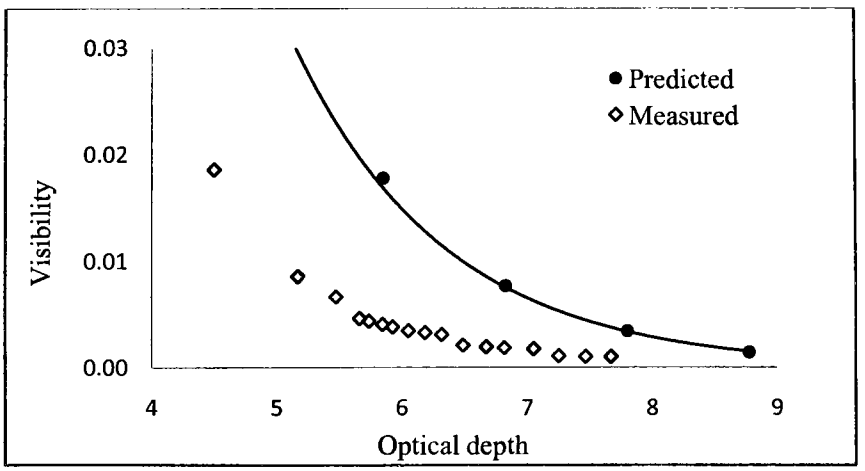

(blue)

F-7 Visibility of barcode (1:1) at power level 1

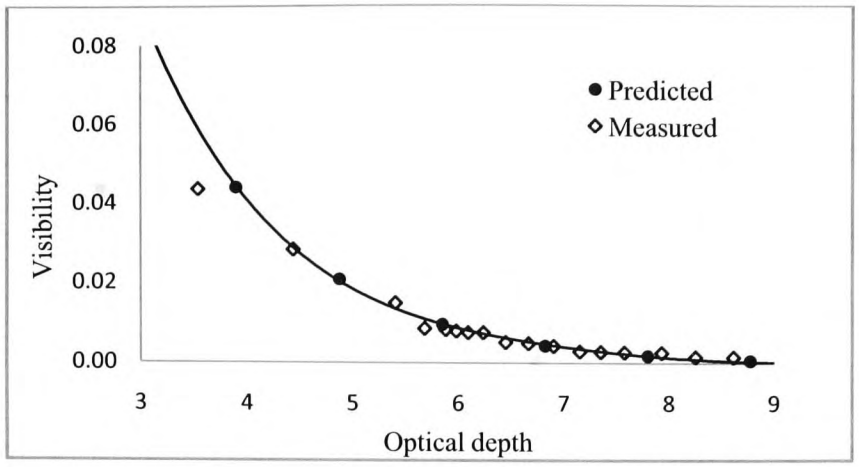

(red)

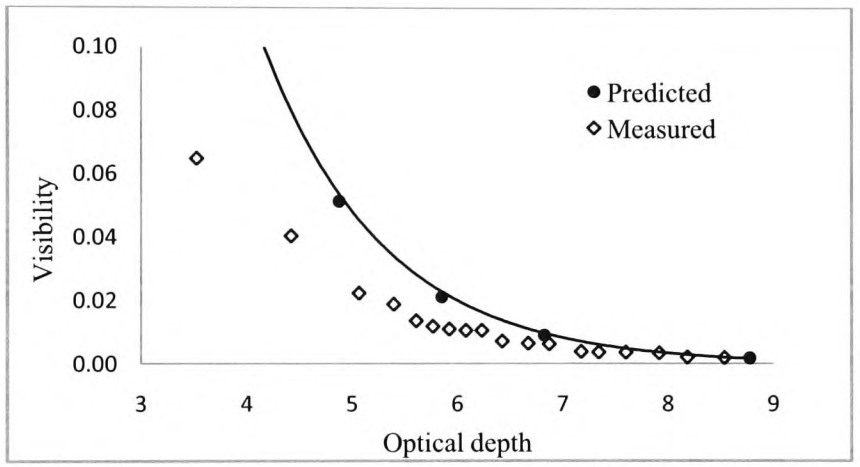

(green)

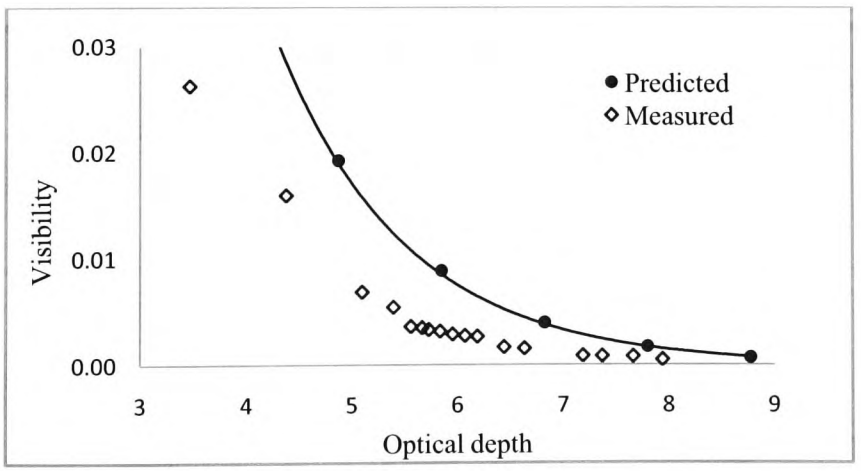

(blue)

F-8 Visibility of barcode (1:1) at power level 2

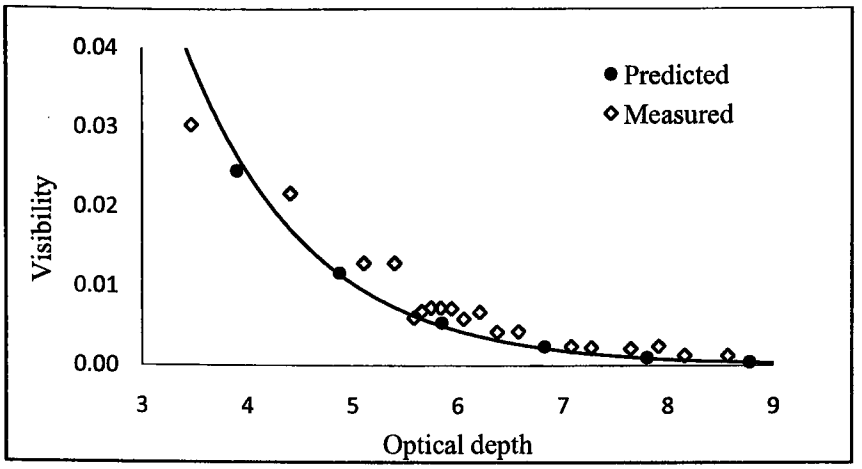

(red)

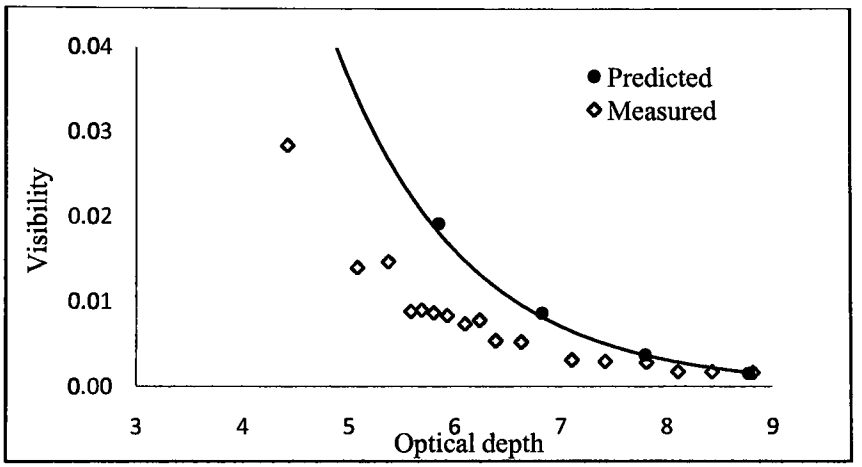

(green)

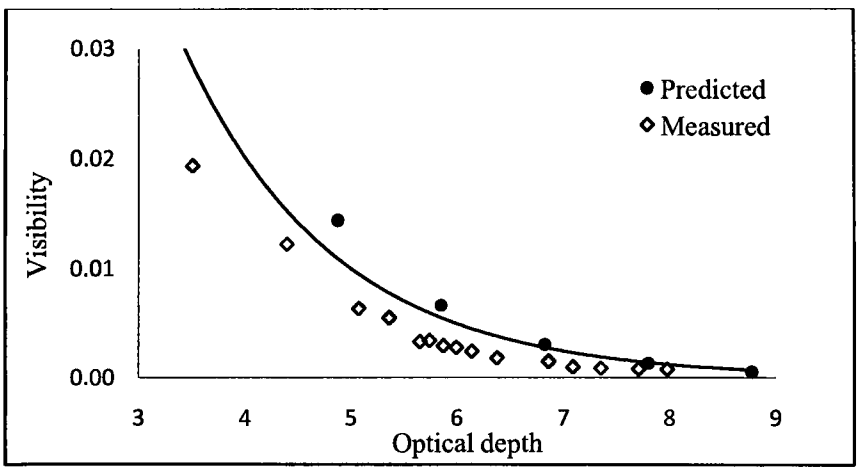

(blue)

F-9 Visibility of barcode (1:1) at power level 3

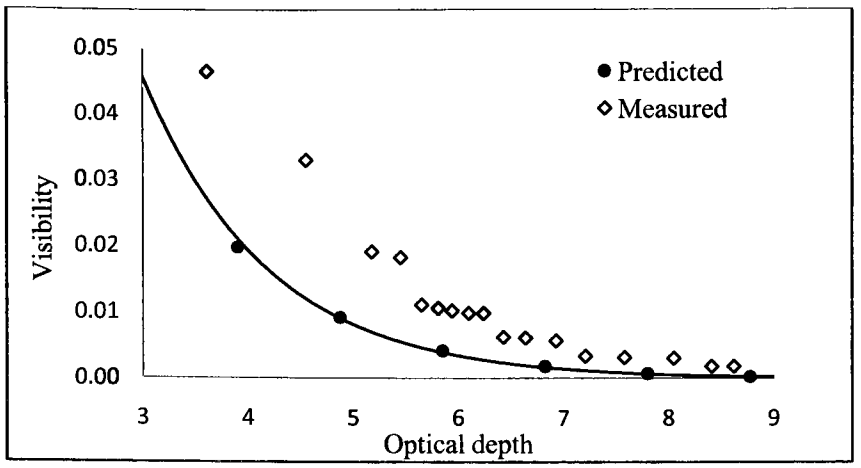

(red)

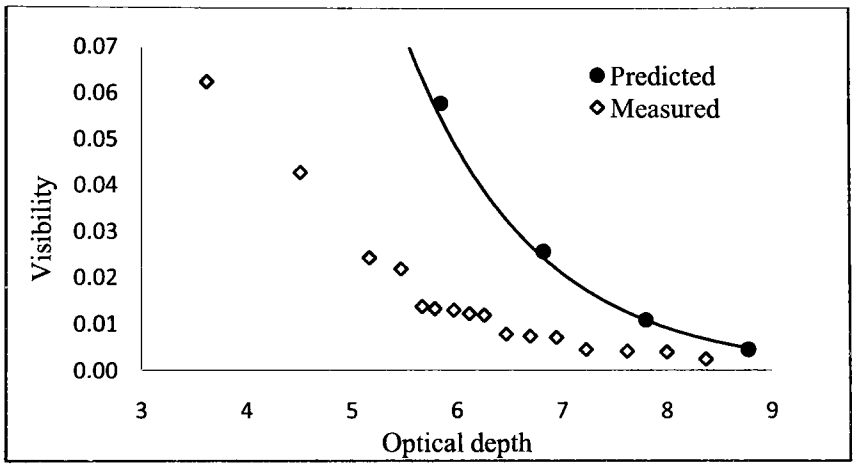

(green)

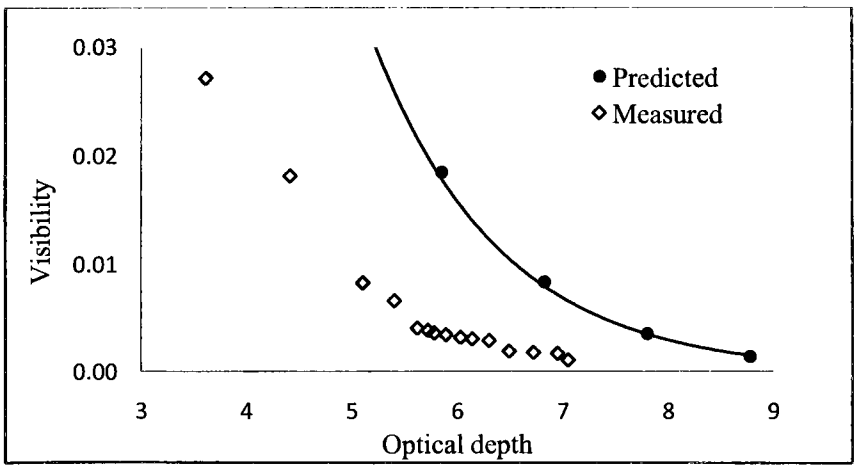

(blue)

F-10 Visibility of barcode (1:0.5) at power level 1

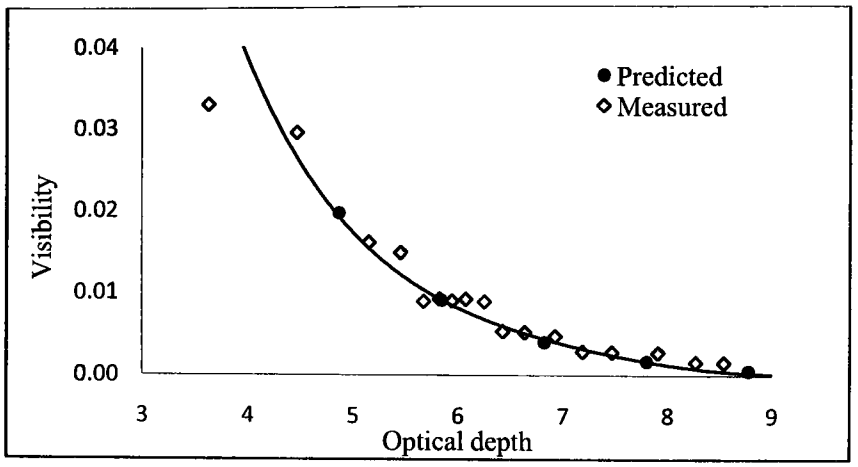

(red)

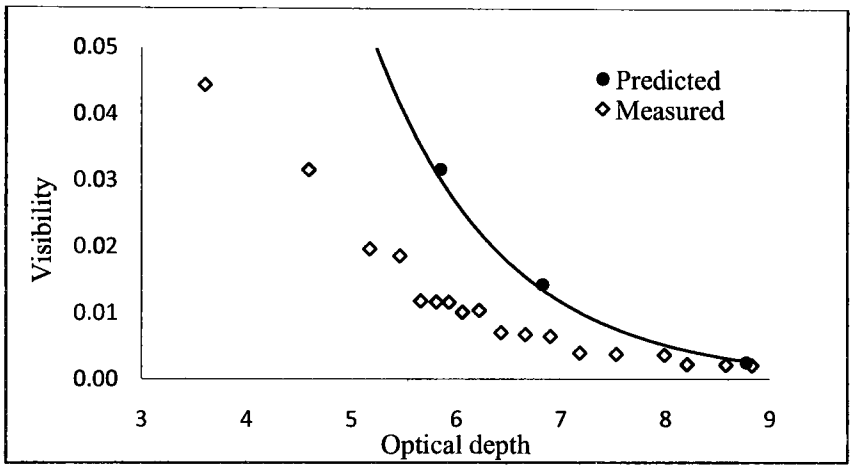

(green)

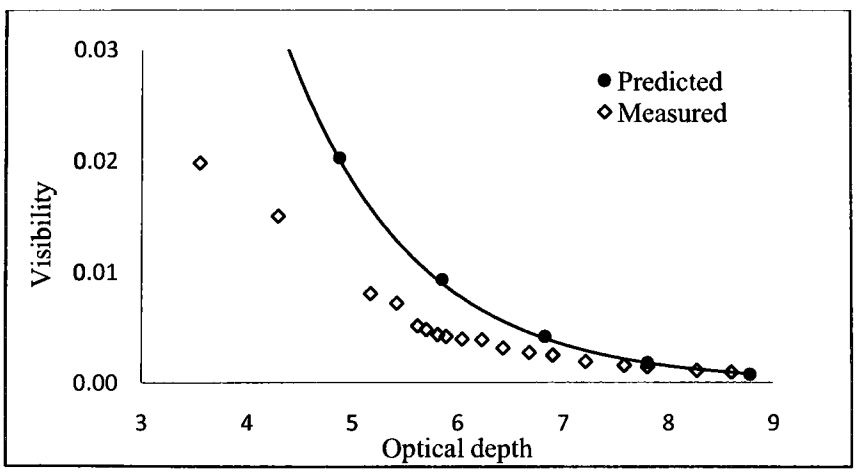

(blue)

F-11 Visibility of barcode (1:0.5) at power level 2

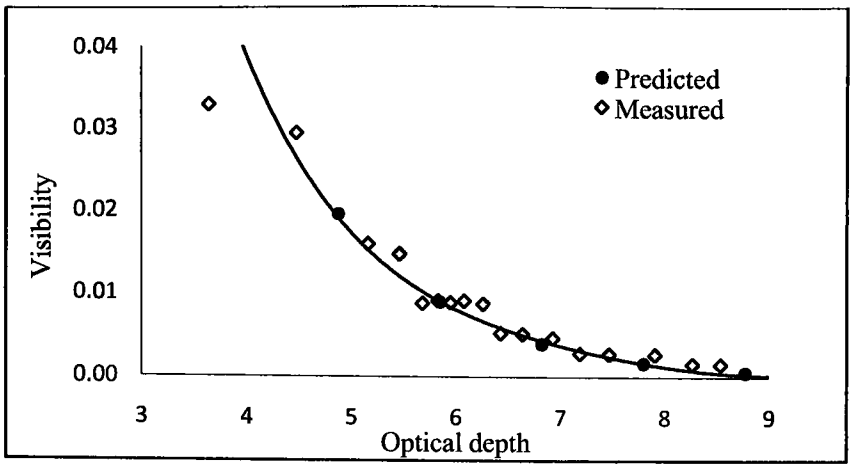

(red)

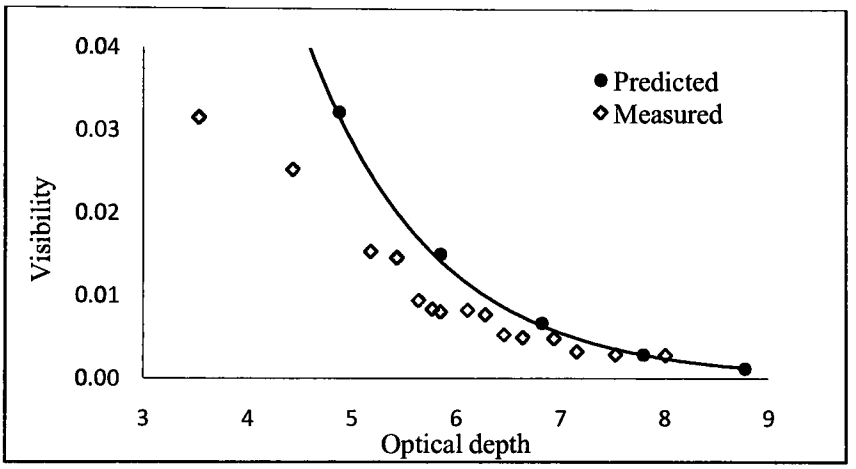

(green)

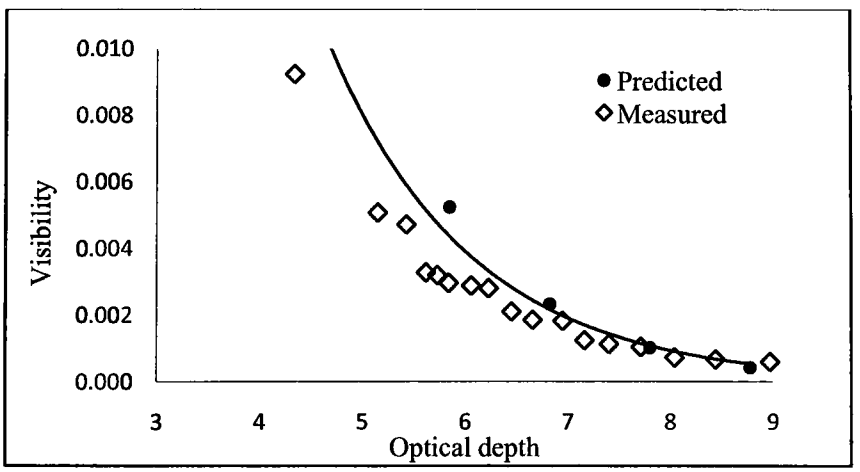

(blue)

F-12 Visibility of barcode (1:0.5) at power level 3